MODELLING THE SPECTRA OF DISTRIBUTED FEEDBACK LASERS

By

GORDON MORRISON, B.A.Sc. Engineering Physics

A Thesis

Submitted to the School of Graduate Studies

in Partial Fulfillment of the Requirements

for the Degree

Doctor of Philosophy

McMaster University

MODELLING THE SPECTRA OF DISTRIBUTED FEEDBACK LASERS

DOCTOR OF PHILOSOPHY McMaster University

(Engineering Physics) Hamilton, Ontario

TITLE: Modelling the Spectra of Distributed Feedback Lasers

AUTHOR: Gordon B. Morrison, B.A.Sc, Eng. Phys. (Simon Fraser University)

SUPERVISOR: Professor Daniel T. Cassidy

NUMBER OF PAGES: xviii, 238

Abstract

Distributed feedback (DFB) semiconductor lasers have a periodic modulation of refractive index, or Bragg grating, in the active region of the device. The Bragg grating causes a wavelength dependent distributed feedback of light. This thesis develops a below-threshold model for the spectra of DFB lasers. The model is shown to treat spontaneous emission in a manner that is quantum mechanically correct. Most other models in the literature do not treat spontaneous emission correctly, and are shown to yield spurious spectral predictions for truncated quantum-well DFB lasers. Techniques for fitting the model to spectral data are explained, and the model is demonstrated to be a useful diagnostic tool for understanding the performance and behaviour of DFB lasers. The effects of facet phase on DFB laser spectra are documented and explained. The model is then expanded to the above threshold regime, and is used to predict correctly spatial hole burning phenomena in DFB laser spectra.

Acknowledgements

The past four years have been great, and I need to thank the people who have made them so. I owe so much, to so many people, that proper acknowledgements would be longer than this thesis.

I would like to thank my supervisor, Dr. Daniel T. Cassidy, for his time, expertise, encouragement, moral support, and enthusiasm. I cannot imagine a better mentor for graduate studies. More that anything, I have appreciated his insatiable appetite for answers to the questions "why?" and "how?". He has given me confidence when I needed it, and is a constant and exemplary role model.

Thanks to David Adams for taking me under his wing at Nortel and helping me get a fantastic start to my graduate studies. He gave me a desk and a computer, a direction to start in, access to a lab, and never laughed out loud at any of my ideas.

Thanks to Doug Bruce for taking the scanning photoluminescence data and for helping me to understand the results. And many thanks to Dr. Jessop and Dr. Luke for their time and input, as members of my supervisory committee. Thanks also to Linda Benson, Fran Allen, and Anne Green for helping me in the Eng. Phys. office.

Thanks to the 7 dwarfs, for giving me the friendship and the adventure I needed. Thanks to Peter Mascher for letting me finish what I'd started.

Thanks also to all my friends who have gone on those low budget, big mountain ski trips with me in the past years. And thanks to Karl and my sister for becoming even closer friends since their marriage. I hadn't expected that, or even thought it possible.

I owe a great deal to Mike Hamp. In the past 4 years he has helped me out of almost as much trouble as he has helped me into. All those days of soccer, karate, cycling, skiing, traveling, and research would have been way less enjoyable without him. More like a brother than a friend.

Mike, Sean Woodworth, and Dave Deforge have lived part of my life with me. They have been room mates, lab mates, and great friends simultaneously. Thanks also to my other room mates over the years, especially: Andrzej, Joel, Sara, Sandra, Brian, Jamal, Catherine and Dana. And thanks to all my lab mates, you've all been great.

Thanks to Sensei McColl for teaching me Karate and keeping me fit.

Special thanks to Rob Johnson and Bodo Littman: the friends who ventured to move "out east" at the same time I did. Thanks to the Mike and Jen, Mike O'Brian, Kerwin, Kassia, Elena, Neil and Karen, Bill DaSilva, Patricia, Horatiu, and Johnny Hazell and all my other new friends for the many, many fun times.

Thanks to Sandra for the best of all adventures, the patience, the understanding. Thanks for putting up with me when I've been stressed out, and for never letting me forget about the beautiful things in every day life.

And biggest thanks of all to Mum and Dad. Their encouragement, support, and respect for education have helped me find this path on which I have had no regrets. I believe that good parents are invaluable to a young person, and that I have been blessed with the best.

Lastly, but by no means least (except perhaps in stature) thanks to Ruaridh: Friend, Comrade, Daschund.

Table of Contents

Table of Figures

1. Introduction

1.1. Overview of Distributed Feedback Lasers

The word "laser" is an acronym for Light Amplification by Stimulated Emission of Radiation. A basic laser consists of an active region, and two mirrors, as shown in Fig. 1-1 below. Light is generated by spontaneous emission in the active region. The spontaneous emission is then amplified by stimulated emission as it passes through the active region. The end reflectors of the laser allow some light to leak out (i.e., the laser beam) while the rest is reflected back through the active region for further amplification.

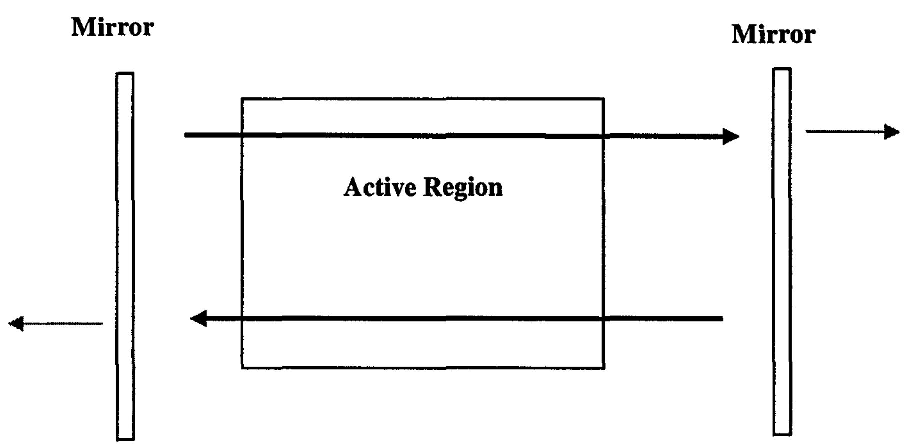

Fig. 1-1 The basic layout of a simple laser, showing an active region with light circulating through it from two end mirrors.

Distributed feedback (DFB) lasers incorporate a Bragg reflector into their active region, so that light is reflected everywhere within the cavity, rather than only at the end mirrors. The Bragg reflector is a small periodic modulation of the index of refraction of the laser cavity. This periodic modulation is referred to as the Bragg grating. Semiconductor distributed feedback lasers consist of a Bragg reflector internal to the laser in addition to two end reflectors (facets). The end mirrors, or facets, are a necessary result of the change in index as light passes from the semiconductor into the outside environment, i.e., air. The facets can be AR (anti-reflection) coated, to minimize their impact on the laser performance, or can be HR (high-reflection) coated, to create extra feedback into the laser cavity. The position of the facet reflector with respect to the phase of the grating has very important effects on the performance of the laser. This is a concept that will be examined in depth in this thesis. A very basic illustration of the design of a semiconductor DFB laser is demonstrated in Fig. 1-2.

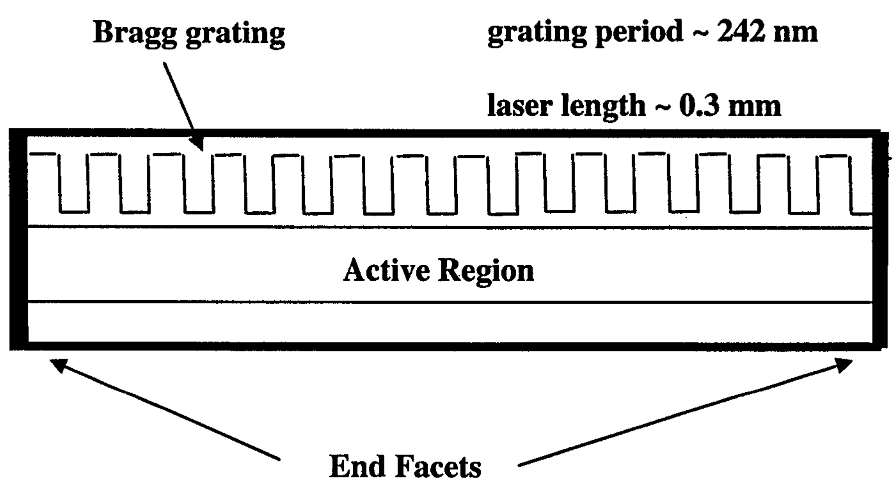

Fig. 1-2 The basic concept of a semiconductor DFB laser.

The active region of a semiconductor laser is a narrow cavity designed to maintain a single spatial mode of light. In Fig. 1-2, the Bragg grating is outside of the active region, but near enough to it that the evanescent tail of the single spatial mode of light in the cavity is in the grating region. Thus, the light experiences a modulation in the index of refraction. This type of DFB laser is referred to as an index-coupled laser. Gain-coupled lasers consist of gratings that occur within the active region, thereby modifying not only the real part of the index of refraction, but also the imaginary part of the index of refraction (i.e., a periodic modulation is introduced into the gain, or amplification of the active region). In general, gain-coupled lasers are also index-coupled because creating a periodic modulation of the gain in the active region inherently induces a periodic modulation in the real part of the index.

Many modern DFB lasers use quantum well technology for their active regions. Quantum wells create active regions with better efficiency than bulk material due to the discrete density of states [1],[2],[3],[4],[5]. A popular design of gain-coupled DFB lasers uses a periodic etching (removal) of the quantum wells in the active region. In this design, etched regions have less gain than not-etched regions. A device that is fabricated in this manner is called a truncated-well DFB laser.

1.2. Brief History of Physics and Development of DFB Lasers.

Bragg diffraction of radiation was heavily studied by Sir William Lawrence Bragg, and his father, Sir William Henry Bragg, at Trinity College, Cambridge. The father and son team used x-ray diffraction as a tool for studying crystal structure. They were awarded the Nobel Prize for their research in 1915 [6].

The first maser (microwave amplification through stimulated emission of radiation) was developed and demonstrated by nobel laureates Charles Townes and his colleagues in 1953. He shared the nobel prize for development of maser-laser oscillators and amplifiers with N.G. Basov, and A. M. Prokhorov [7]. The concepts used in the design of the first maser were later applied by Schawlow and Townes to optical frequencies, and reflecting mirrors were used to form a cavity with reflective feedback for the first laser in 1958. Semiconductor lasers were demonstrated shortly thereafter in 1962 by Basov *et al*, Hall *et. al*, Bernard *et. al*, and Nathan *et. al.* [8].

The distributed feedback (DFB) laser was first demonstrated in an optically pumped gelatine medium by Kogelnik and Shank in 1971 [9]. In conjunction with their demonstration, Kogelnik and Shank developed the coupled wave theory of distributed feedback lasers [10]. Their coupled-wave model was based on theory that had been successfully developed for the fields of Bragg diffraction of x-rays, acoustic diffraction of light, and diffraction in volume holograms.

1.3. Literature Review

This section presents a review of published work on models for semiconductor DFB lasers. Much experimental and theoretical work pertaining to DFB lasers has been performed over the past 30 years, but not all of it is directly relevant to this thesis. This thesis primarily deals with spectral properties of DFB lasers, above and below-threshold. Fitting models to spectral data has not been the primary goal of most of the existing literature. Nonetheless, a brief overview of much of the existing work is presented in this section.

The two most frequently cited approaches for modeling distributed feedback lasers are coupled-wave theory, and layered-structure transfer-matrix theory. Both methods are satisfactory tools for predicting many aspects of DFB lasers, though it has been shown that the transfer-matrix approach is slightly more accurate [11]. A comparison between coupled mode theory, the Bloch wave approach, and transfer-matrix analysis is also given in [12], which concluded that the transfer-matrix approach is the simplest, most insightful and most accurate of the three models. Often, the coupled wave theory is combined into transfer matrices, whereby a laser active region is broken into several large parts, each of which is represented by a coupled-wave transfer-matrix [13].

Shortly after the work of Kogelnik and Shank, an eigenmode model was developed by S. Wang for investigation of distributed feedback lasers[14]. Wang's eigenmode theory was later expanded on for an in-depth analysis of the coupling of spontaneous emission into lasing modes [15]. Streifer *et. al.* were some of the earliest researchers to investigate the effect of facet reflectances on distributed feedback lasers [16]. C. Henry, expanded on this work and investigated threshold gain of a band gap mode in DFB laser structures with varying facet reflectivities and coupling coefficients

[17]. At the same time, S. McCall *et. al.* investigated theoretical facet effects on the external reflective properties of phase shifted DFB lasers [18]. Perhaps the only experimental method for measuring facet phase, other than fitting models to spectra, was much later proposed in 1996 by D. M. Adams *et. al.*[19]. Some of the earliest work done on simulating semiconductor distributed feedback laser spectra was performed by Soda and Imai, in 1986. Their analysis was applied to phase shifted DFB lasers, and the effects of the magnitude of phase shift and of the position of the phase shift in the cavity were examined [20]. In 1987, Björk and Nilssön proposed a numerical transfer-matrix theory for analysis of phase shifted DFB lasers [21]. The following year, T. Makino and J. Glinski reported a transfer-matrix analysis of amplified spontaneous emission of DFB Lasers [22]. Hamasaki *et. al.* proposed a gain-coupled DFB structure in 1988 and presented a travelling-wave based transfer-matrix approach to analysis of such structures. Their paper included some interesting transmission intensity distributions for short gain-coupled cavities, which demonstrated the tendency of long wavelength Bragg standing waves to be in phase with high index regions of the Bragg grating [23]. In 1994, E. Berglind *et. al.* presented a simple classical electrical network approach for modelling DFB lasers, the most interesting result of which was a powerful short-cut method for rapidly calculating amplified spontaneous emission in sub-threshold index guided lasers [24].

By the late 1980s, the above-threshold effects of spatial hole burning in DFB lasers were being considered, and one of the earliest detailed models of this phenomenon was presented in 1989 by Whiteaway *et. al.* [25]. In 1990 Vankwikelberge, Morthier, and Baets, introduced their highly sophisticated model CLADDIS. This model was capable of threshold analysis, linewidth calculation, and AC response [26][27]. Since then, a comprehensive text book on DFB Lasers has also been written by Morthier and Vankwikelberg [28]. Two years later Whiteaway *et. al.* published a paper that included analysis of dynamic behaviour [29]. Whiteaway *et. al.* had predominantly used coupled-mode theory for their analysis and similar papers were produced shortly thereafter by Hansmann *et. al.* [30][31], who used a transfer-matrix approach. Similar work was also performed by R. Schatz, who developed a purely rate equation model for analysis of frequency response of DFB lasers [32]. An overview of several above-threshold quarter-wave-shifted DFB laser models was published by A. J. Lowery *et. al.* in 1992, who in the same paper proposed a transmission line laser model [33]. A Greens function approach to linewidth analysis, and a theoretical explanation for the impact of standing waves on non-linear gain has also been proposed by B. Tromborg *et. al.* [34][35]. Detailed above-threshold modelling has also been performed by Montrosset *et. al.*, who have included thermal effects in their above-threshold model [36][37]. An exceptionally rigorous model for above-threshold gain-coupled DFB lasers, was published by A. Champagne *et. al.* in 1999 [38]. Their model used a full Poisson solver coupled with transfer-matrix based intensity distributions and a look-up table. The effect of the standing wave on spatial hole burning was given special attention in this paper.

Of special relevance to this thesis are groups which have attempted to fit spectral simulations to data. To fit a complex model to data is an arduous task and few researchers have approached the problem. R. Schatz *et. al.* produced one of the earliest papers that demonstrated the use of a below-threshold model for parameter extraction [39]. Morthier *et. al.* was also one of the first to demonstrate the potential power of parameter extraction by fitting a model to data [40]. Data and simulation for amplified spontaneous emission were also compared by Hansmann *et. al.* [41]. An evaluation of the ability for a DFB model to extract grating coupling coefficients from DFB lasers was later made by J. Skagerlund *et. al.* [42]. W. Fang *et. al.* produced an interesting paper in 1997 that attempted to fit an above-threshold model to spectral data, and also verified calculations of the longitudinal intensity distribution by measuring spontaneous emission from the side of the laser cavity [43].

1.4. Thesis Outline and Objectives

This thesis is organised into nine chapters. Chapters 2,3,4,5 are based on previously published work [44],[45],[46][47],[55],[66]. Chapter 2 introduces the probability amplitude transfer-matrix model for below-threshold DFB lasers. The probability amplitude model is different from other models that have been used to extract parameters from DFB lasers in that it treats spontaneous emission in a correct, quantum mechanical manner. The model is shown to fit to spectral data from truncated-well DFB lasers with more success than a model that does not correctly account for spontaneous emission. Chapter 3 describes useful spectral features for fitting a below-threshold DFB laser model to data, and demonstrates that in contrast to work that has been published in the literature in the past, relatively wide bandwidth spectra from both facets of a DFB laser must be used to eliminate the possibility of degenerate solutions. In Chapter 4, the facet phases of a group of truncated-well DFB lasers are extracted by fitting the probability amplitude model to data. The Scanning Photoluminescence technique, [19], is then used to experimentally determine the facet phase for these same lasers, and is shown to yield the same results, within experimental error, as the spectral fitting method. Qualitative explanations are presented for the spectral features that allow the model to extract correctly facet phases from spectral data. Chapter 5 demonstrates the practical nature of the below-threshold probability amplitude model by applying it to two projects sponsored by Nortel Networks of Ottawa. The first project uses the model to extract gain parameters from truncated-well DFB laser spectra over a range of different injection currents. The results are used to help explain the exceptionally high yield and side mode suppression ratio of truncated-well devices. The second project uses a modified version of the model to analyse and explain the performance of two-section tuneable DFB laser devices. Chapter 6 presents a probability amplitude model for longitudinal intensity distributions within DFB laser cavities. An advantage of the probability amplitude model for intensity distribution is that it correctly includes spontaneous emission in its formulation. The probability amplitude model also has the advantage of correctly predicting the standing wave component of intensity distributions in laser cavities. Various simulations are performed, and are found to be in agreement with other models. Physical explanations are given for several noteworthy features of longitudinal intensity distributions in DFB lasers. Chapter 7 describes a carrier rate-equation model for above-threshold DFB lasers. Algorithms for rapidly finding equilibrium between carrier rate equations and longitudinal intensity distributions are developed. In chapter 8, the above-threshold model is shown to predict correctly the above-threshold spectral features of truncated-well DFB lasers, starting with parameters extracted from below-threshold spectra using the below-threshold model. Brief explanations for the above-threshold spectral features are given, and the importance of the standing wave in truncated-well DFB lasers is verified. Chapter 9 contains a summary of the work reported in this thesis, and some suggestions for future work.

2. A Probability-Amplitude Transfer-Matrix Model for Distributed-Feedback Laser Structures

2.1. Introduction

I developed an amplified spontaneous emission transfer-matrix model for distributed feedback (DFB) lasers. This model has been used to extract parameters such as modal gain, the phase of the DFB grating at the facet (i.e., facet phase), and the reflectance of the facet. The model is similar to the one proposed by J.P Weber and S. Wang [15]. I have shown that there is a startling difference between the model described by Weber and Wang, and many others reported in the literature. The difference lies in the classical vs. quantum mechanical treatment of single spontaneous emission events in the laser cavity, and results in a noticeable difference in the predictions for spectra of truncated-well gain-coupled DFB lasers.

This chapter first presents my approach to modelling DFB lasers, and then demonstrates that my model is similar in its treatment of spontaneous emission to the model proposed by Weber and Wang. A fundamental difference between Weber and Wang's treatment of spontaneous emission [15] and other models available in the literature is investigated, and the impact of this difference on the predicted below-threshold spectra for index-coupled DFB lasers, Fabry-Perot lasers, and truncated-well gain-coupled DFB lasers is observed. Finally, experimental evidence for the validity of one model over the other is presented.

2.2. The Probability Amplitude Model

This model treats a DFB laser as an amplifier of spontaneous emission. The spectrum from each end of a DFB laser is obtained by summing the amplified outputs of single photon spontaneous emission events. In this thesis the term "photon" is used to describe a single quantum of electromagnetic radiation. I acknowledge that a photon is not a material particle that can be localised in any meaningful manner, and that a photon is best described by a waveform [48]. However, the wave mechanics that apply to the probability amplitudes of particles are analogous to the wave mechanics of light, and so one may think of the photon as a fictitious particle that obeys boson statistics and is associated with the waveform for a single quantum of radiation. This use of the term "photon" is, in my opinion, in accordance with much of the literature in the field of laser physics [48].

To begin, consider the probability of a single spontaneous emission event resulting in photon detection at either the left or right facet of the laser. This is accomplished by employing transfer matrices to calculate the probability of transmission of a photon through the facets of a DFB laser [11].

Any single interface between two materials of differing refractive index will cause a photon to reflect or to transmit. The coefficients t_{12} and r_{12} are defined as the probability amplitude coefficient for transmission from material 1 across an interface into material 2, and the probability amplitude coefficient for reflection back into material 1 from material 2, respectively. The probability amplitude reflection coefficient is therefore written as

$$r_{12} = \frac{n_1 - n_2}{n_1 + n_2}$$

Eq. 2-1

where n_1 and n_2 are the indices of refraction for materials 1 and 2, respectively. Similarly, the probability amplitude transmission coefficient is

$$t_{12} = \frac{2n_1}{n_1 + n_2}.$$

Eq. 2-2

From these fundamental relations, the following transfer-matrix relates the reflection and transmission of input fluxes E_1^+ and E_2^- on either side of the interface:

$$\begin{bmatrix} E_1^+ \\ E_1^- \end{bmatrix} = \begin{bmatrix} \frac{1}{t_{12}} & \frac{r_{12}}{t_{12}} \\ \frac{r_{12}}{t_{12}} & \frac{1}{t_{12}} \end{bmatrix} \bullet \begin{bmatrix} E_2^+ \\ E_2^- \end{bmatrix}$$

Eq. 2-3

where E is the probability amplitude of the photons, the subscript "1" or "2" signifies at which side (left or right) of the interface the photons are, and the superscript "+" or "–" signifies the direction (to the right or to the left) in which the photons are travelling.

The probability amplitude of a photon is a complex number with a phase that varies spatially. Thus, the relative probability amplitudes of left and right-going photons at either side of a distance l can be described using the following phase-shifting transfer-matrix:

$$\begin{bmatrix} E_1^+ \\ E_1^- \end{bmatrix} = \begin{bmatrix} e^{jKnl} & 0 \\ 0 & e^{-jKnl} \end{bmatrix} \bullet \begin{bmatrix} E_2^+ \\ E_2^- \end{bmatrix}$$

Eq. 2-4

where $K = \dfrac{2\pi}{\lambda}$ is the wavenumber and $n = n_R + jn_I$ is the complex refractive index, with n_I the extinction coefficient, or imaginary part of n, and n_R the real part of n.

The transfer-matrix for any series of films (e.g., any part of the DFB grating) can be obtained by multiplying a series of the above propagation and interface matrices [11]. The resulting 2×2 transfer-matrix is of the form:

$$\begin{bmatrix} E_1^+ \\ E_1^- \end{bmatrix} = \begin{bmatrix} T_{11} & T_{12} \\ T_{21} & T_{22} \end{bmatrix} \bullet \begin{bmatrix} E_2^+ \\ E_2^- \end{bmatrix}.$$

Eq. 2-5

From this matrix, one can obtain the effective probability amplitude transmission and reflection coefficients as

$$\frac{E_2^+}{E_1^+} = [T_{11}]^{-1} = t \qquad \frac{E_1^-}{E_1^+} = \left[\frac{T_{21}}{T_{11}}\right] = r \ .$$

Eq. 2-6

Each grating segment in a DFB can now be treated as an individual Fabry-Perot cavity, with facets defined using effective probability amplitude reflectivity and transmission coefficients, as shown in Fig. 2-1.

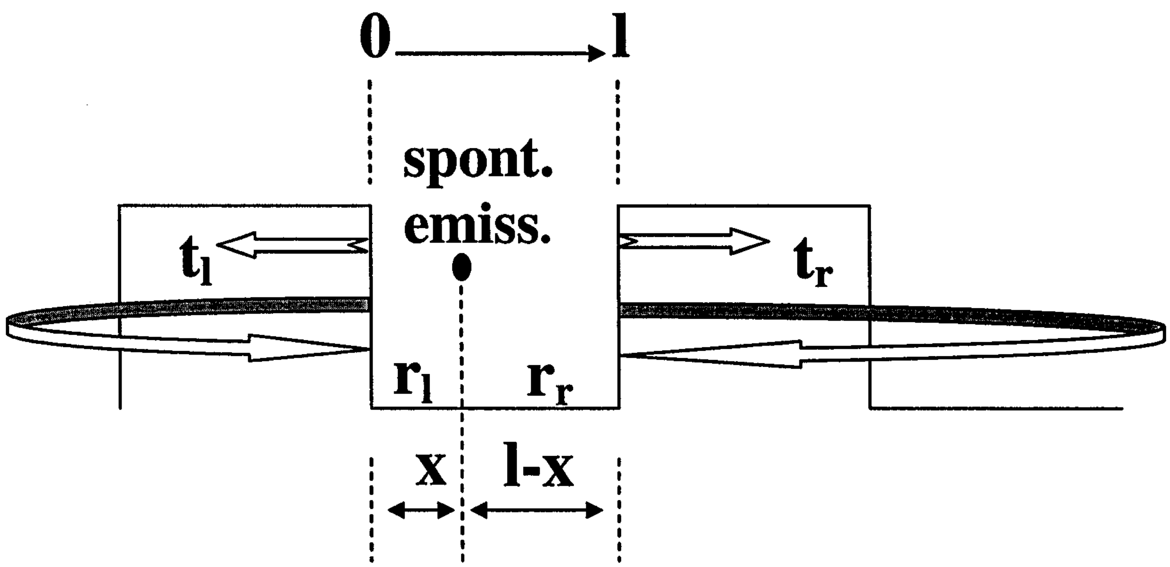

Fig. 2-1 A section of a DFB laser containing 4 segments (2 high index and 2 low index) is shown with associated reflection and transmission definitions looking outwards from the spontaneous emission event.

The standard procedure of summing an infinite number of reflections in a convergent geometric series is used to obtain the probability that a photon that was initially emitted in the direction of the right-hand facet will result in photon detection at the right-hand facet. This is given by $\left|\langle P_r | right \rangle\right|^2$ where

$$\langle P_r | right \rangle = \frac{t_r e^{-jKn(l-x)}}{1 - r_r r_l e^{-j2Knl}}$$

Eq. 2-7

is the probability amplitude.

The same procedure is again used to obtain the probability of photon detection at the right-hand facet if a photon was initially emitted in the direction of the left-hand facet. This is given by $\left|\langle P_r | left \rangle\right|^2$ where

$$\langle P_r | left \rangle = \frac{r_l t_r e^{-jKn(l+x)}}{1 - r_r r_l e^{-j2Knl}}.$$

Eq. 2-8

The above equations deal with the probability amplitudes of photons. A fundamental general principle of quantum mechanics states that "when a particle can reach a given state by two possible routes, the total amplitude for the process is the sum of the amplitudes for the two routes considered separately" [49]. This fundamental principle is responsible for the phenomena of a single particle in a Bragg grating being able to interfere with itself, which is a well-known quantum mechanical effect [49]. In a DFB laser, the "given state" is one in which the photon exits a specific facet for detection. There are two separate genres of routes to this state that are available to a spontaneously emitted photon. These are the routes that start with the emitted photon travelling initially in the direction of the right facet, and the routes that start with the emitted photon travelling initially towards the left facet. If the photon initially travels towards the left facet, obviously it will have to be reflected at least once if it is to exit the right facet. Certainly each genre of routes (left-starting and right-starting) contains an infinite series of possible individual routes, but these probability amplitudes have already been summed together in the form of effective reflectivity and transmission coefficients, and in the form of a convergent infinite geometric series of reflections.

Using the above argument, the total probability amplitude for detection of photons at the right-hand facet, due to emission of a single photon at point x in a segment of a DFB laser, is

$$\langle P_r \rangle = \langle P_r | right \rangle + \langle P_r | left \rangle .$$

Eq. 2-9

Thus the total probability, or light intensity, detected at the right-hand facet due to a single photon emitted at point x in a grating segment, will be

$$I_r = \left| \langle P_r \rangle \right|^2 = \left| \frac{t_r e^{-jKnl}}{1 - r_r r_l e^{-j2KnL}} \right|^2 \times \left| e^{jKnx} + r_l e^{-jKnx} \right|^2 .$$

Eq. 2-10

Note that I_r is proportional to the square of the sum of the amplitudes of an initially left going photon, and of an initially right going photon, at the right-hand facet. The square of the sum is found in the second term of Eq. 2-10, which clearly allows two probability amplitudes to interfere with each other. The physical concept of a single photon travelling by two different paths and interfering with itself may seem unreasonable, but it has been well documented in other experiments. For instance, it is well known that single photons passing individually through a double slit apparatus will produce an interference pattern.

Assuming a continuum of spontaneously emitting atoms in any given grating segment, one can integrate the sum of all contributing spontaneous emission events at points separated by *dx* within a given grating segment. The total light intensity at the right-hand facet due to all the spontaneous emission in a single segment is then

$$I_r^{seg} = \int_0^l I_r dx = \left| \frac{t_r e^{-jKnl}}{1 - r_r r_l e^{-j2Knl}} \right|^2 \times \frac{1}{2} \left[\frac{1 - e^{-2gl}}{g} + j \frac{r_l^*}{Kn_R} \left(1 - e^{2jKn_R l}\right) + j \frac{r_l}{Kn_R} \left(e^{-2jKn_R l} - 1\right) + \frac{r_l r_l^*}{g} \left(e^{2gl} - 1\right) \right]$$

Eq. 2-11

The above equation for I_r is for the total light intensity output at the right facet due to all the spontaneous emission in a single grating segment. Here g is defined as $K_o n_I$. There are hundreds or thousands of segments in a DFB laser, so to obtain the spectrum at the right-hand facet, one must sum contributions from all N segments. Thus,

$$I_r^{tot} = \sum_{seg=1}^{N} I_r^{seg} .$$

Eq. 2-12

Notice that for every grating segment, the effective reflectivity and transmission coefficients will be different, and must be recalculated using the transfer-matrix method. Eq. 2-12 assumes that each segment has the same spontaneous emission rate. If this is not the case then each term in the sum of Eq. 2-12 must be appropriately weighted by the spontaneous emission rate for the segment. Also, the probability for a single photon to go in a given direction is ½, so equation Eq. 2-11 should be multiplied by a factor of ½ for precise photon counting purposes.

2.3. Comparison with Other Models Found in the Literature.

Weber and Wang developed an eigenmode-based model for DFB lasers [15]. They derived the equation

$$A_1 = \frac{1}{T_{11}}\left[L_{11} - L_{12}\right]$$

Eq. 2-13

based on 3×3 transfer matrices, where T_{11} is defined in Eq. 2-5, and is the result of multiplying transfer matrices from left to right for all layers in the DFB laser. L_{11} and L_{12} are equivalent to T_{11} and T_{12} but relate only to the layers to the left of the spontaneous emission source, which is somewhere within the laser cavity. A_1 is the field emitted from the right-hand facet. Weber and Wang redefined their transfer matrices and reflection coefficients for application to eigenmodes to make a detailed study of spontaneous emission coupling, but for purposes of comparison, one can substitute the probability amplitude transfer-matrix model into their equation.

It is simple to show for a Fabry-Perot cavity, that

$$T_{11} = \frac{1 - r_l r_r e^{-j2Knl}}{\vec{t}_l t_r e^{-jKnl}}$$

Eq. 2-14

Here the notation $\vec{t}_l$ is used for a transmission coefficient that is in the opposite direction of t_l (i.e., from outside of the left facet to the location of the spontaneous emission event inside the laser). The transmission matrix for the left-hand side of the Fabry-Perot cavity, from outside of the cavity to the spontaneous emission event, yields the coefficients:

$$L_{11} = \frac{e^{jKnx}}{\vec{t}_l} \qquad L_{12} = \frac{-r_l e^{-jKnx}}{\vec{t}_l}.$$

Eq. 2-15

Substituting these terms into the equation (Eq. 2-13) used by Weber and Wang gives

$$A_1 = \frac{t_r e^{-jKn(l-x)}}{1 - r_l r_r e^{-2jKnl}} + \frac{t_r r_l e^{-jKn(l+x)}}{1 - r_l r_r e^{-2jKnl}}.$$

Eq. 2-16

Thus the intensity at the right-hand facet due to a single spontaneous emission event is

$$I_r = |A_1|^2 = \left|\frac{t_r e^{-jKnl}}{1 - r_r r_l e^{-j2Knl}}\right|^2 \times \left|e^{jKnx} + r_l e^{-jKnx}\right|^2$$

Eq. 2-17

and is identical in form to the probability amplitude model for a single spontaneous emission event. The square of a sum is clearly present in the second term of Eq. 2-17.

Integrating Eq. 2-17, but using the notation of Wang and Weber, one obtains an alternative notation for Eq. 2-11:

$$I_r^{seg} = \int_0^l I_r dx = \left|\frac{1}{T_{11}}\right|^2 \times \frac{1}{2}\left[\frac{L_{11}L_{11}^*(1-e^{-2gl})}{g} - j\frac{L_{11}L_{12}^*(1-e^{2jKn_Rl})}{Kn_R} - j\frac{L_{11}^*L_{12}(e^{-2jKn_Rl}-1)}{Kn_R} + \frac{L_{12}L_{12}^*(e^{2gl}-1)}{g}\right]$$

Eq. 2-18

Weber and Wang assumed that a spontaneous emission event would contribute to the eigenmodes of the laser at the point of emission, and incorporated this assumption into their 3×3 spontaneous emission transfer-matrix approach. As shown in the mathematical comparison above, their approach turns out to be equivalent to assuming that a spontaneous emission source emits a single photon that travels in two opposite directions at once, but this assumption is concealed in the mathematics of the 3×3 transfer-matrix approach. Weber and Wang gave no detailed explanation for their reasoning on this subject. Furthermore, no experimental evidence for the validity of their treatment was presented [15].

On a classical level, it seems intuitive that a photon must be emitted in *either* one direction *or* the other. If one were to make this assumption, then the light intensity due to spontaneous emission from a point source would be

$$I_r = |A_1|^2 = \left| \frac{t_r e^{-jKnl}}{1 - r_r r_l e^{-j2Knl}} \right|^2 \times \left(\left| e^{jKnx} \right|^2 + \left| r_l e^{-jKnx} \right|^2 \right)$$

Eq. 2-19

which clearly does not allow cross-correlation of a photon emitted from a single source in two different directions, and produces a mathematically different solution (i.e., the two terms in parentheses are individually squared, then added, rather than added and then squared).

The formulation of Eq. 2-19 is the same as the one that Hansmann [30][31] obtained, except that the probability amplitude model is integrated over the thickness of each grating segment, while Hansmann takes the spontaneous emission to originate entirely from the centre of each subsection. Hansmann assumes that photons emitted from a point source are emitted in different directions at different times. Therefore, he assumes that the photon emitted in one direction is incoherent with the photon emitted in the other direction. This makes a great deal of intuitive sense but does not agree with basic quantum mechanics, or with spectral data collected from truncated-well DFB lasers (which is presented later in this chapter). According to quantum mechanics, a spontaneous event can emit a photon in either direction, and it is impossible to determine upon detection of the photon in *which* direction the photon was originally emitted. Thus, according to the rule of [49][50], one must add the probability amplitudes for each case before squaring the absolute value. This results in additional, self-interference, or cross-correlation terms in the mathematical model. Weber and Wang obtained this result [15], but Hansmann [30][31] did not. There are other laser models in the literature that treat the spontaneous emission source in the same manner as Hansmann, but to the best of my knowledge, there are none that agree with Weber and Wang. The intensity distribution calculations developed for the simulator CLADDIS [26] , however, do use a system of propagator matrices that appear to include correctly forward and backward going spontaneous emission for DC analysis of the longitudinal intensity distribution of a lasing mode.

H. Soda and H. Imai [20], for instance, apply coupled mode theory to the same multiple reflection method as Hansmann for obtaining the output due to a single spontaneous emission source at a point $-z_o$. Their equation is

$$U(-z_o) = \frac{|tr_1(-z_o)|^2 + |tr_1(-z_o) ref_2(-z_o)|^2}{|1 - ref_1(-z_o) ref_2(-z_o)|^2}$$

Eq. 2-20

which clearly neglects the cross-correlation between the two different paths available to a photon, as in Eq. 2-10.

Makino and Glinski state [22] that they use the same multiple reflection technique as Soda and Imai [20] and present the same equation for multiple reflections of a spontaneous emission source. T. Makino [51] shows that the result obtained by applying the equation for spontaneous emission derived by Henry using a Green's function approach [52], gives the same result as his multiple reflection analysis, which as previously noted, is based on Eq. 2-20. Whiteaway *et. al.* [25] also use a version of Eq. 2-20.

The work of Berglind and Gillner [24] circumvents the problem of directly addressing the initial directions of spontaneously emitted photons by applying classical electric network theory using scattering matrices and their associated theorems. Their mathematical formalism is entirely in agreement with classical microwave theory, and certainly provides a much faster computational method for obtaining laser spectra for *some* types of DFB lasers (i.e., where n_{sp}/n is longitudinally constant). However, their equation [24] simply sums a power reflection with a power transmission coefficient, which does not properly address the phenomenon of self-interfering spontaneous emission. In this sense the classically derived equation of Berglind and Gillner treats a spontaneous emission event in the same manner as Hansmann, Makino, Soda and Imai.

I believe that only the model that incorporates quantum mechanical treatment of the self-interference of a photon is correct. I am not sure why the discrepancy between the model by Weber and Wang, and the models by other widely referenced groups, has not been pointed out previously. Even Weber and Wang only noted and investigated one key difference between their model and other existing models. That difference was their extension of the use of Petermann's somewhat controversial coupling coefficient [53][54], which yielded their "S" factor, which was not experimentally verified.

The next sections describe the effect that the self-interference, or cross-correlation terms have on the spectra of index-coupled DFB lasers, Fabry-Perot lasers, and truncated-well DFB lasers, and compare the results to experimental data.

2.4. Effects of the Cross-Correlation Terms on Laser Spectra

If Eq. 2-19 is integrated along a grating segment length instead of Eq. 2-10, one obtains

$$I_r^{seg} = \int_0^l I_r dx = \left| \frac{t_r e^{-jKnl}}{1 - r_r r_l e^{-j2Knl}} \right|^2 \times \frac{1}{2}\left[\frac{1 - e^{-2gl}}{g} + \frac{r_l r_l^*}{g}\left(e^{2gl} - 1\right) \right]$$

Eq. 2-21

which is missing the two self-interference, or cross-correlation terms that are within the square parentheses of Eq. 2-15.

For computational purposes it is simpler to use the less intuitive notation of Weber and Wang. Using their notation, integration of Eq. 2-19 yields an equation that is only different from Eq. 2-18 in that the following cross-correlation terms are missing:

$$\left[-j\frac{L_{11}L_{12}^{*}(1-e^{2jKn_R l})}{Kn_R}-j\frac{L_{11}^{*}L_{12}(e^{-2jKn_R l}-1)}{Kn_R}\right].$$

Eq. 2-22

The effects of the cross correlation terms can now be analysed in detail. Noting that the term ($1/T_{11}$) in Eq. 2-18 is constant for all segments in Eq. 2-12, one is able to move it outside of the summation. Thus, the spontaneous emission spectrum is given by

$$I_r^{tot}=\frac{1}{2}\left|\frac{1}{T_{11}}\right|^2\times\sum_{seg=1}^{N}\left[\frac{L_{11}L_{11}^{*}(1-e^{-2gl})}{g}-j\frac{L_{11}L_{12}^{*}(1-e^{2jKn_R l})}{Kn_R}-\right.$$
$$\left.j\frac{L_{11}^{*}L_{12}(e^{-2jKn_R l}-1)}{Kn_R}+\frac{L_{12}L_{12}^{*}(e^{2gl}-1)}{g}\right]$$

Eq. 2-23

and is clearly just the power transmission coefficient of the DFB multiplied by the summation of the terms in the square brackets. Therefore, one should be able to see the effect of the self-interference, or cross-correlation terms on a spectrum by examining the shape of

$$c.c.\_effect=\sum_{seg=1}^{N}\left[-j\frac{L_{11}L_{12}^{*}(1-e^{2jKn_R l})}{Kn_R}-j\frac{L_{11}^{*}L_{12}(e^{-2jKn_R l}-1)}{Kn_R}\right].$$

Eq. 2-24

2.4.1. Index-coupled DFB Lasers

A fit to the front and back facets of an index-coupled laser is shown in Fig. 2-2. The fit was performed over a bandwidth of 72 nm, to the spectra from the front and back facets simultaneously.

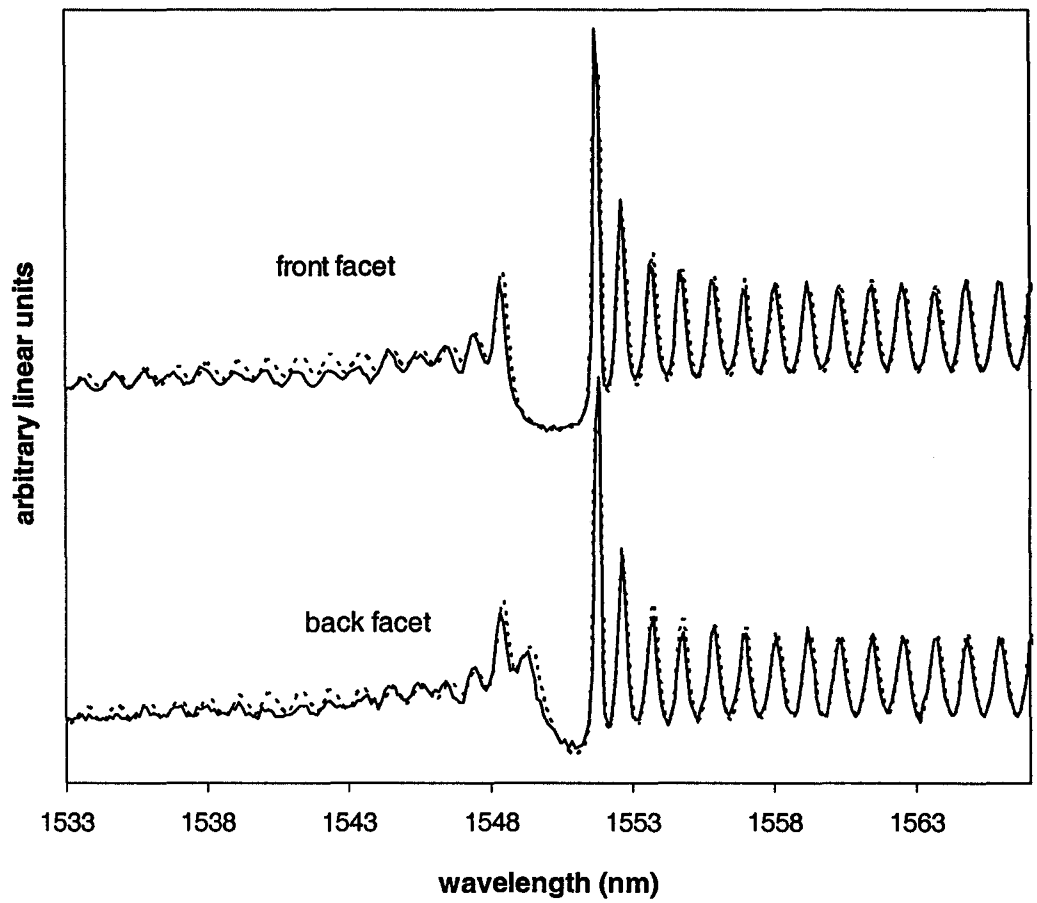

Fig. 2-2 Best fit to an index-coupled laser front facet spectrum using the probability amplitude model. The fit is shown using a dashed line. A solid line is used for the experimental data. Parameters for the laser are listed in Table 2-1. The bottom of the y-axis marks light intensity. The front facet spectrum has been offset for comparison.

To demonstrate the quality of the fit, bandwidths of 40 nm are plotted Fig. 2-2, rather than the full 72 nm of the fit. It is worth noting that all sub-threshold spectra in this thesis are plotted on a scale with x-axis intercepting the y-axis at the 0 point, unless an obvious offset has been added to one of the spectra for purposes of comparison. Some important parameters that determine the characteristics of the laser are shown in Table 2-1.

Table 2-1 List of Parameters for index-coupled laser of Fig. 2-2.

Front Facet Reflectance	0.040 ± 0.004
Front Facet Phase	$203 \pm 1°$
Back facet reflectance	0.31 ± 0.01
Back facet phase	$241° \pm 1°$
Real index step of grating	0.00870 ± 0.00001
Average modal effective index	3.2000 ± 0.0001
Average modal group index	3.5569 ± 0.0002
Length of a single grating period	242.2 nm assumed
Length of Laser	0.3050 mm ±0.0005mm
Coupling coefficient κ_r	$112\ cm^{-1} \pm 1\ cm^{-1}$

The effects of Eq. 2-24 on the spectrum of the laser can now be analysed. For analytical purposes, the result of summing all the cross-correlation terms for the low index segments is compared with the result of summing all the cross-correlation terms for the high index segments in Fig. 2-3. Both figures relate only to the front, low reflectivity facet. Similar results were obtained for the back facet.

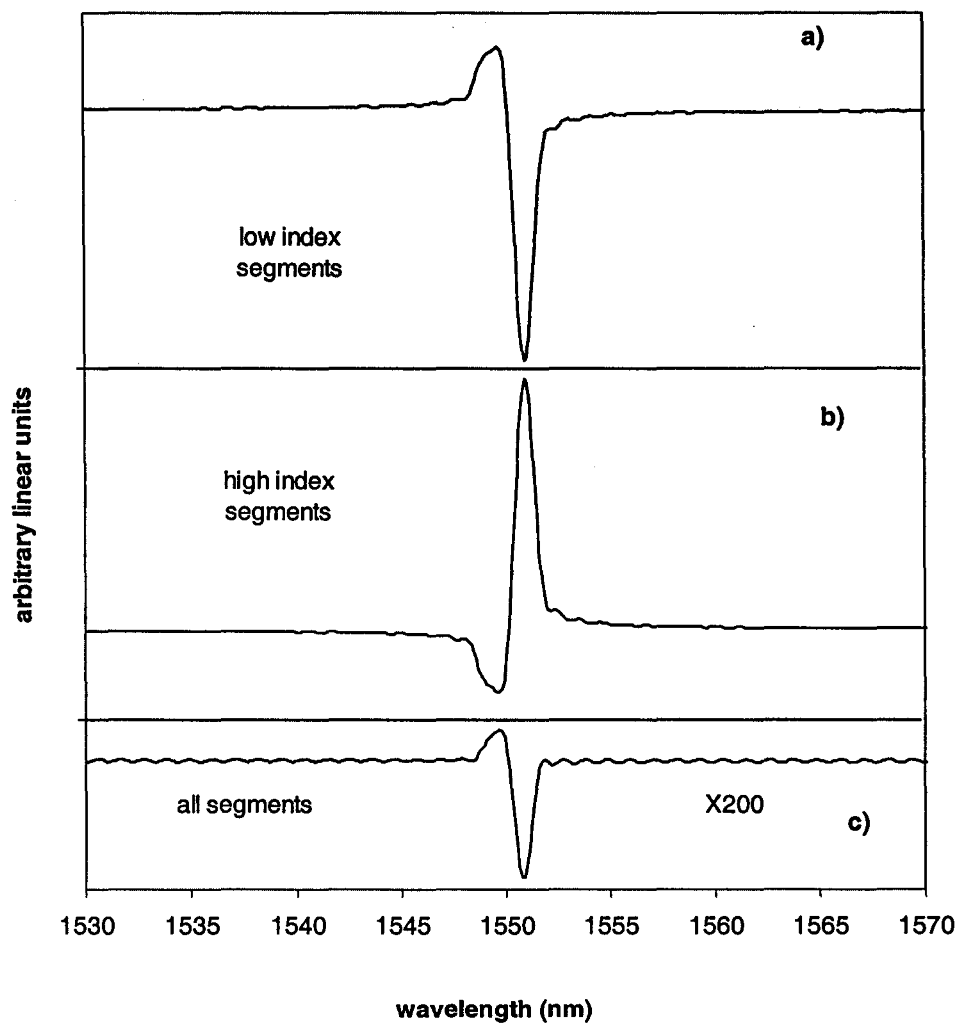

Fig. 2-3 a) The front facet cross-correlation sum from the low index segments of the laser of Fig. 2-2 . b) The cross-correlation sum from the high index segments. c) The net cross-correlation sum at the front facet, magnified ×200 on the vertical scale.

The effect of the cross-correlation terms from the low index segments (Fig. 2-3 a) is opposite in sign to the effect of the cross correlation terms in the high index areas (Fig. 2-3 b). The figure also shows, using a ×200 expanded vertical scale, the net effect of the cross-correlation terms from both the high and low index segments. The net effect is relatively small in magnitude because of the cancelling effect resulting from the addition of Fig. 2-3 a) and Fig. 2-3 b).

The difference in the absolute magnitudes of the maxima and minima found in the Bragg regions of Fig. 2-3 are due to the facet phases of the laser. Facet phases with spectrum-symmetric values of 90° or 270° (see chapter 4), would cause the absolute magnitudes of the maxima and minima to be the same.

The shape of the cross-correlation contribution is also dependent on the mark-to-space ratio of the DFB laser grating. If the high index segments of the laser have a duty cycle > 50%, then the maximum/minimum on the long wavelength side will have greater magnitude than the maximum/minimum on the short wavelength side. If the high index segments of the laser have a duty cycle <50%, then the maximum/minimum on the long wavelength side will have a smaller magnitude.

The simulated spectra from Fig. 2-2 were compared with simulated spectra that were obtained without including the cross-correlation terms. The simulations could not be distinguished from one another. This is due to the cancellation effect between the high-index cross-correlation terms and the low-index cross-correlation terms, which makes the net cross-correlation terms negligible in comparison to the other terms in Eq. 2-23. The sum of the cross-correlation terms was found to be at most 0.04% of the magnitude of the other terms.

2.4.2. Fabry-Perot Lasers

In an index-coupled laser with a decreased coupling coefficient, the effects in the Bragg region of the high and low index cross-correlation terms cancel each other out to an even greater degree. In the zero coupling-coefficient limit of a Fabry-Perot laser, the individual "low-index" and "high-index" segments produce shapes similar to Fig. 2-3 a) and Fig. 2-3 b), which have very distinct maxima and minima in the stop band region of the DFB. Note that the refractive index of the "high index" segment is exactly equal to the refractive index of the "low index" segment in a Fabry-Perot laser. The addition of the "high" and "low" index cross-correlation contributions in a Fabry-Perot laser results in total cancellation of the maxima and minima found in Fig. 2-3 a) and Fig. 2-3 b). The sum of the cross-correlation terms for a Fabry-Perot laser thus has a uniform, approximately sinusoidal shape that matches the mode spacing of the actual Fabry-Perot spectrum. There was no noticeable difference between spectral predictions (based on parameters of Table 2-1 but with no coupling coefficient) generated with and without the cross-correlation terms because the magnitude of the cross-correlation terms were at most 0.02% of the magnitude of the other terms in Eq. 2-23.

2.4.3. Truncated-Well DFB Lasers

In a truncated-well DFB, there will be more spontaneous emission in the high index region than the low index region because there are a greater number of quantum wells in the high index region. A truncated-well DFB design is depicted in Fig. 2-4, which also demonstrates my definition for facet phases. Because there is more spontaneous emission from the high index segments than from the low index segments, the contributions of the cross correlation terms from the high index segments and the low index segments are not as effective at cancelling each other out. Hence, one expects to see a noticeable effect in the stop band region of the spectrum.

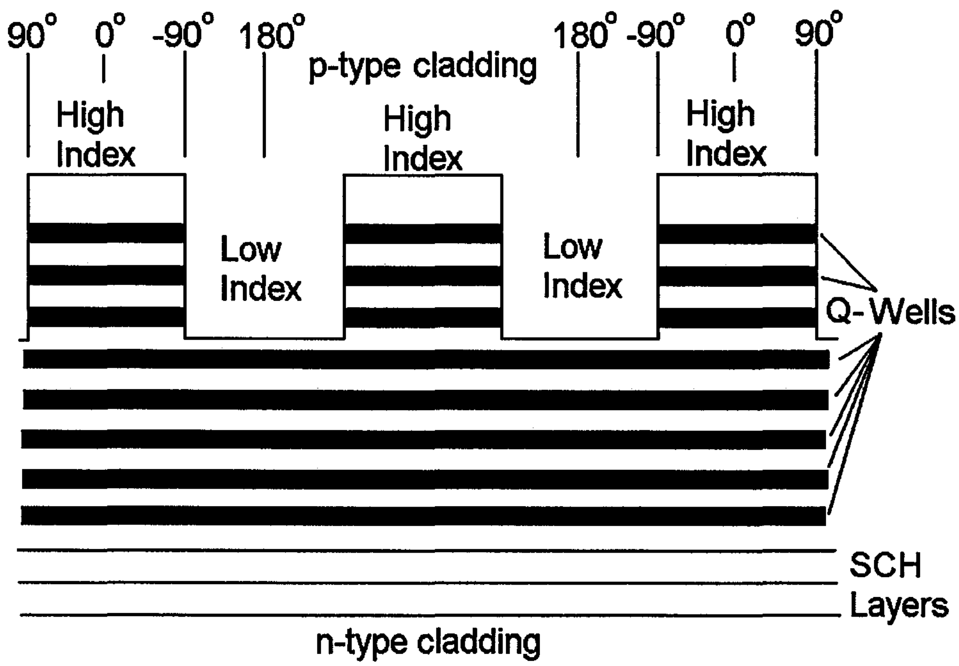

Fig. 2-4 Structure of a truncated-quantum-well laser with 8:5 high-index to low-index quantum well ratio. Also shown is my definition of facet phases.

Predictions for the front and back facet spectral output of a truncated-well DFB laser with and without the cross-correlation terms are given in Fig. 2-5. The laser of Fig. 2-5 has five quantum wells in the high index region, and no quantum wells in the low index region, so one can make the assumption that there is no spontaneous emission in the low index areas. Some important parameters for this laser are listed in Table 2-2. All parameters were extracted from a real laser. The spectra that were predicted without inclusion of the cross-correlation terms are shown using dashed lines. Clearly, in a laser where spontaneous emission only occurs in the high index region, the cross-correlation terms have a distinct effect on the laser spectrum.

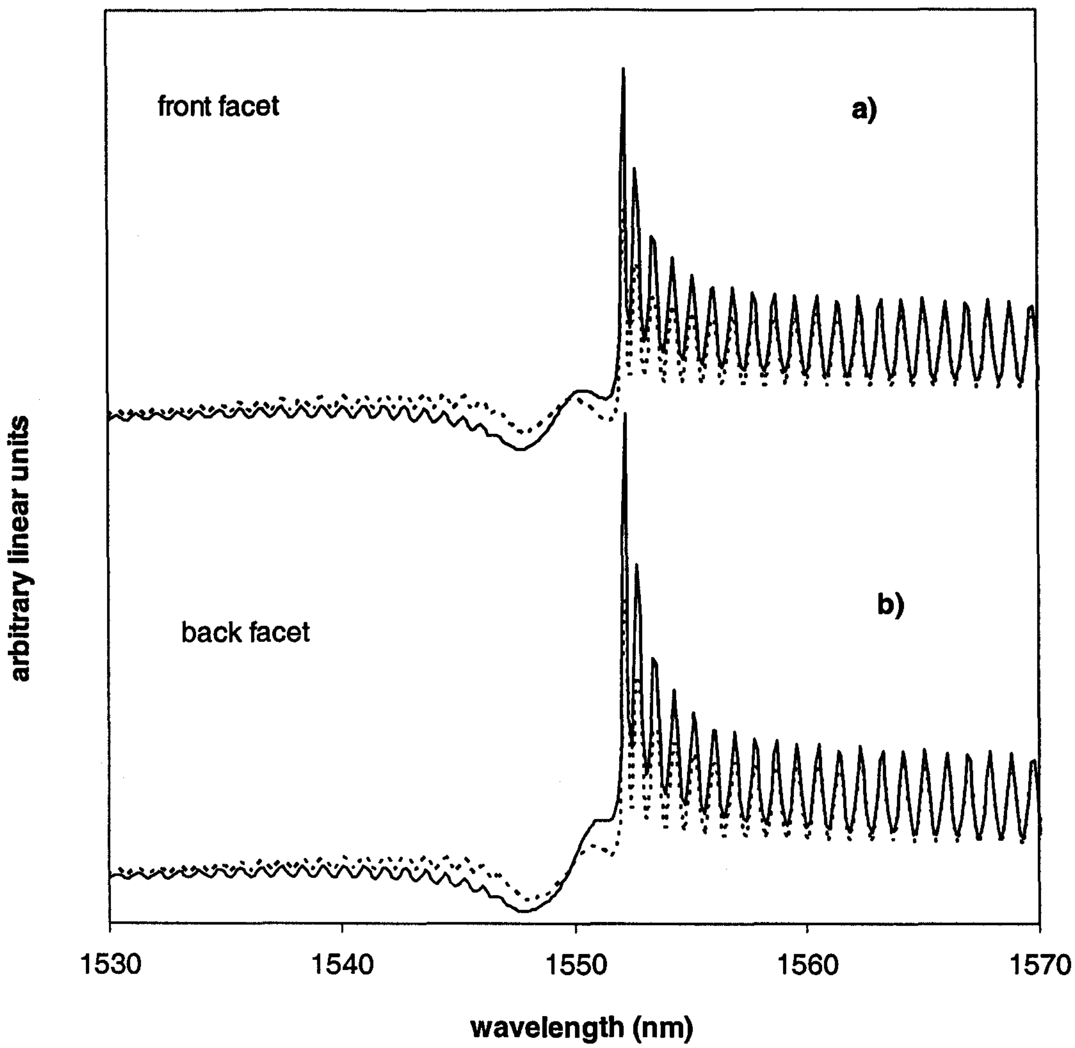

Fig. 2-5 a) Comparison of front facet spectra for the truncated-quantum-well DFB laser described by Table 2-2, with and without inclusion of the cross-correlation terms. b) Comparison of back facet spectra for the same laser. The solid lines are spectra that were generated with inclusion of the cross-correlation terms. The dotted lines were generated with the cross-correlation terms omitted.

Table 2-2 List of Parameters for truncated-well DFB laser of Fig. 2-5.

Front facet reflectance	0.31 ± 0.01
Front facet phase	$274.1° \pm 1°$
Back facet reflectance	0.31 ± 0.01
Back facet phase	$291.3° \pm 1°$
Real index step of grating	0.01573 ± 0.00001
Average modal effective index	3.2000 ± 0.0001
Average modal group index	3.466 ± 0.009
Length of a single grating period	242.1 nm assumed
Length of Laser	0.3800 mm $\pm$ 0.0005 mm
Coupling coefficient κ_r	203 cm^{-1} $\pm$ 1 cm^{-1}

2.5. Experimental Evidence of the Cross Correlation Effect

As has already been noted in this chapter, the cross-correlation effect is observable in truncated-well DFB lasers. This section examines two different designs of truncated-well DFB laser, and in both cases, the effects of the cross-correlation terms have been appreciable. The first design that is examined in this section is one in which the high-index segments have 8 quantum wells and the low index segments have 5 quantum wells. The other design has a ratio of 5 quantum wells in the high index segments to 0 quantum wells in the low index segments.

2.5.1. High-Index to Low-Index Quantum Well Ratio 8:5

In other applications, the probability amplitude model was used to study the evolution with respect to injection current of modal gain in the high and low index segments of a truncated-well DFB laser (see chapter 5). During this study, laser spectra were fitted to over a wide range of currents, with and without the cross-correlation terms. All fits were performed over a bandwidth of 72 nm, and in all cases both the front and back facet spectra were fitted simultaneously.

The graphs in Fig. 2-6 show that the model with no cross-correlation terms predicts that as the injection current approaches 0, the five quantum-well, low-index segments will have approximately the same absorption as the 8 quantum-well, high index segments. Other lasers of the same design and from the same wafer produced similar results. These results do not agree with the intuitive observation that at low currents, the ratio of modal loss is expected to approach (at least approximately) 8:5 in the high index and low index segments.

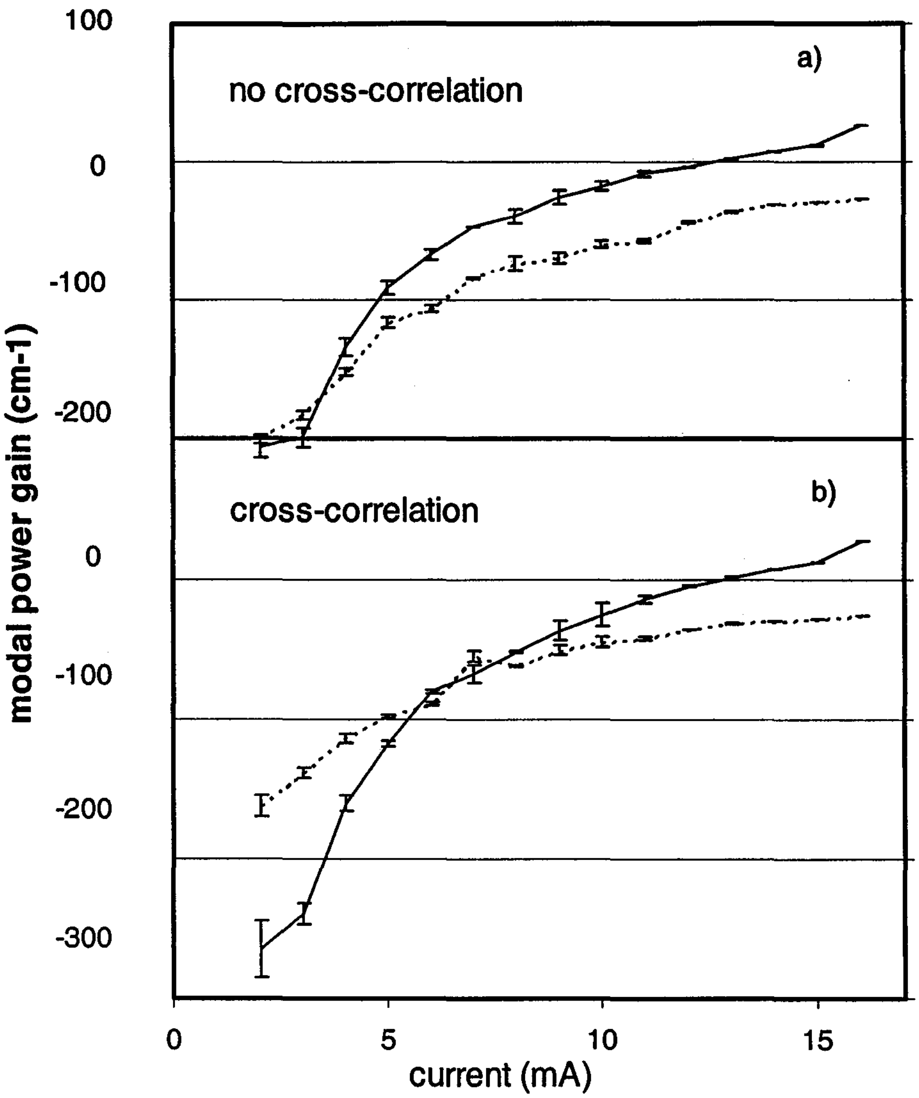

Fig. 2-6 a) Evolution of gain in the 8 well and 5 well segments, extracted using the model that is missing the cross-correlation terms. The dashed line represents 5 well segments. The solid line is for the 8 well segments. The values obtained at low currents make very little intuitive sense, based on the 8:5 ratio of quantum wells. b) The equivalent graph obtained by the model that included the cross-correlation terms.

When the cross-correlation terms were incorporated, an absorption ratio of 8:5 was obtained as the laser injection current approached zero. The cross-correlation counterpart of Fig. 2-6 a) exhibited the expected 8:5 absorption ratio, and is shown in Fig. 2-6 b). The model without the cross-correlation effect most likely compensates for error by selecting unrealistic values for the gains, and also by slightly adjusting other variables. Note that both models agree with the observation that there is enhanced gain coupling in the DFB laser as threshold is approached [55]. This is clear because both models reveal a loss in the low index segments, compared to the gain in the high index segments, and both models produce a slope ratio that is greater than 8:5.

2.5.2. High-Index to Low-Index Quantum Well Ratio of 5:0

Fig. 2-7 a) and Fig. 2-7 b) show the best front facet fits to data for a truncated-well semiconductor DFB laser which had a ratio of quantum wells in the high and low index segments of 5:0. Some important parameters for this laser were shown in Table 2. Fig. 2-7 a) was obtained using the model that neglects cross-correlation and Fig. 2-7 b) was obtained using the model that includes cross-correlation. In a 5-0 truncated-well laser no spontaneous emission is emitted in the low index regions, and so the cross correlation terms from the high index segments are not cancelled out by the cross-correlation terms from the low index segments. Thus, there could be a noticeable difference in the ability of the models to fit to spectra.

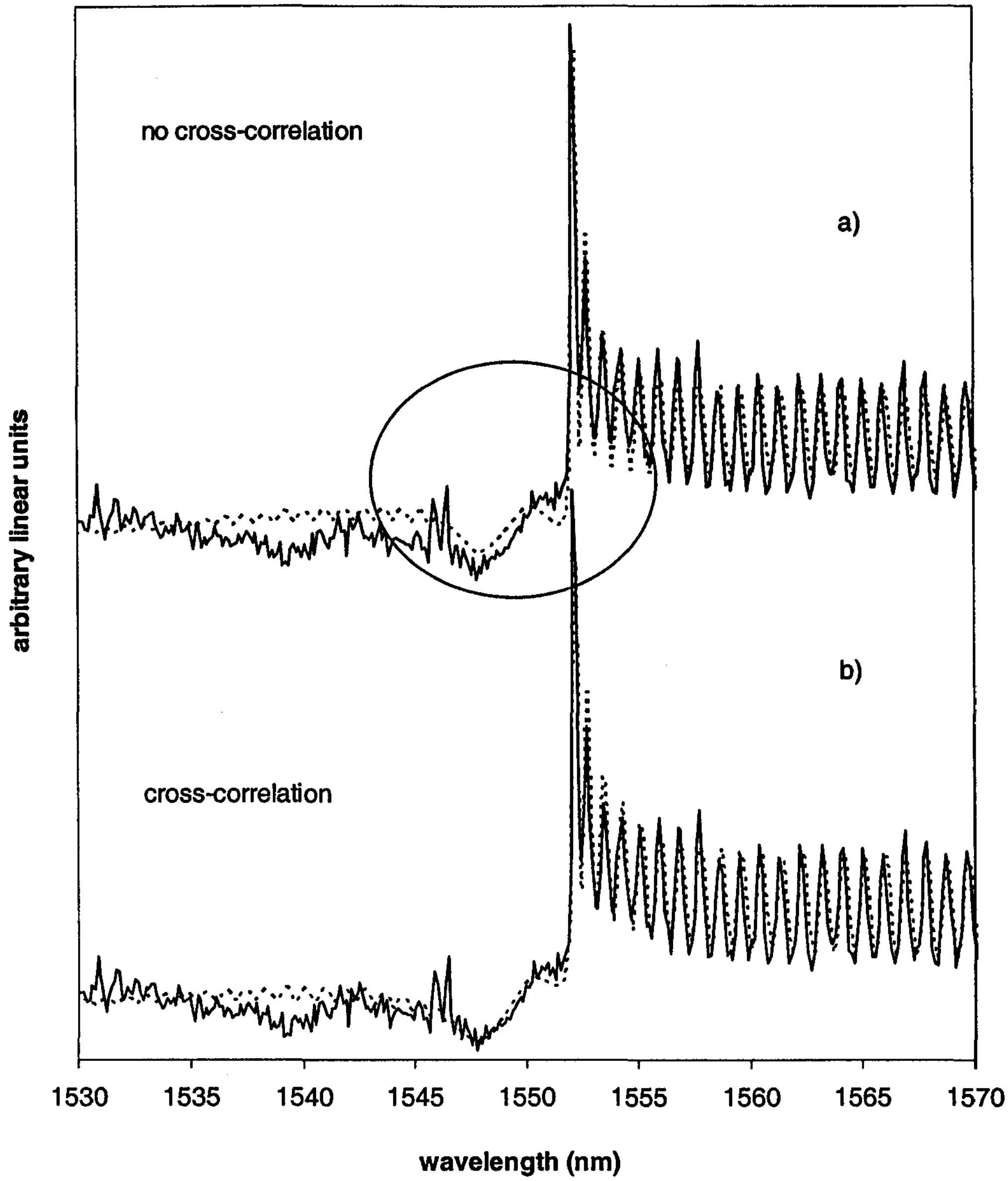

Fig. 2-7 a) The best fit to the front facet of the truncated-well laser of Table 2, using the model without the cross-correlation terms. Dashed lines show the fits. Solid lines show the data. The problem area of the fit is circled, and appears to be a result of the missing cross-correlation terms. b) The best fit to the front facet of the same laser, using the model that includes the cross-correlation terms.

Fig. 2-7 a) and b) show that the model that includes the cross-correlation terms was able to fit the data better than the one that does not include the cross-correlation terms. The problematic region in the fit missing the cross-correlation terms is circled, and examination of the shape of the high-index cross correlation terms in Fig. 2-3 b) reveals that these problem regions are most probably due to the missing cross-correlation terms. Similar results were obtained for the rear facet spectra.

Fig. 2-8 shows the mean-squared-errors of the best fits, with and without the cross-correlation terms, for a sample of eight different 5-0 truncated-quantum well lasers. All fits were performed over a bandwidth of 72 nm, and in all cases both the front and back facets were fitted simultaneously. Clearly the model with the cross-correlation terms is most often able to make the best fit. The observation that the model lacking cross-correlation usually makes a less good fit is especially important because parameters such as the gain curves, spontaneous emission curve, and the facet phases, were all allowed to vary during the fit so as to best conceal the effects of the missing cross-correlation terms.

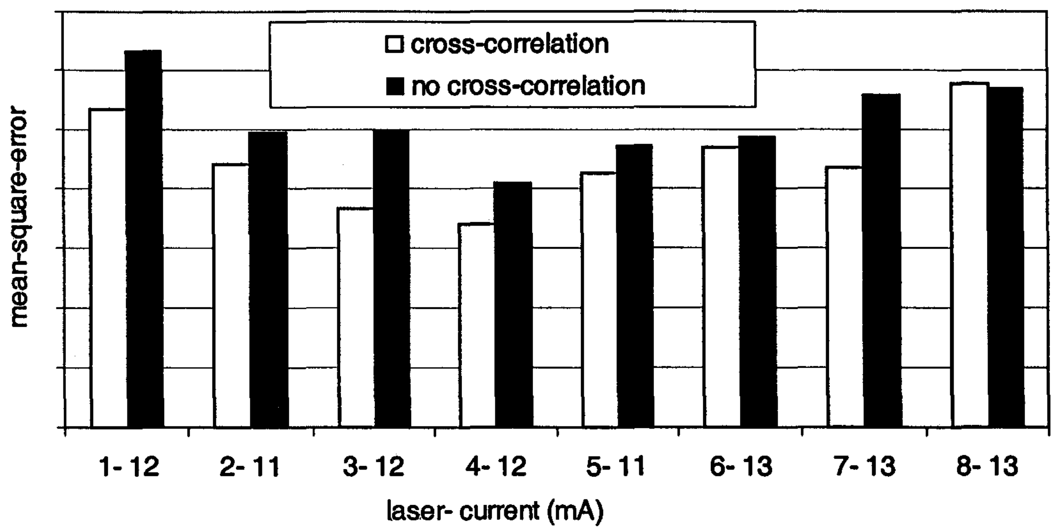

Fig. 2-8 Comparison of fit quality with and without the cross-correlation terms for 8 different truncated-well lasers. Each of these lasers has 5 quantum wells in the high index segments and 0 quantum wells in the low index segments. The best fits, represented by the white bars, were obtained with inclusion of the cross-correlation terms.

2.6. Conclusion

Existing models for DFB lasers do not appear to use a proper quantum mechanical treatment of spontaneous emission events within the grating. This has resulted in models that do not sum the probability amplitudes of a photon travelling in each available direction from a spontaneous emission point. While this apparent error has no noticeable effect on simulated spectra for index-coupled DFB lasers with mark-space ratio of 50%, or on Fabry-Perot lasers, it is clearly noticeable in simulated spectra for truncated-well DFB lasers. Especially interesting is the fact that a quantum mechanical phenomenon (which by the standards of classical physics is not necessarily intuitive) directly leads to spectral shaping in truncated-well DFB lasers.

3. Fitting a Distributed Feedback Laser Transfer-Matrix Model to Spectra from Distributed Feedback Lasers.

3.1. Introduction

The previous chapter described a probability amplitude transfer-matrix model for distributed feedback (DFB) lasers. This model is useful for extraction and examination of laser parameters by fitting predicted spectra to the spectra from DFB lasers [55]. The Marquardt-Levenberg numerical recipe is used for all fits in this thesis [56][57][58].

This chapter demonstrates that fitting to spectra from *both* facets simultaneously, over a wide bandwidth, is extremely important for obtaining quick, accurate and consistent results. To make accurate fits to spectra over wide bandwidths, various parameters such as gain, index of refraction, and spontaneous emission must be considered as wavelength dependant. The equations that are used by the probability amplitude model to approximate these wavelength dependencies are also presented in this chapter.

The position of a DFB laser facet with respect to the phase of the internal Bragg grating is known as the facet phase. The facet phase at one facet of a DFB has effects on the spectra collected at both facets, though the nature and magnitudes of the effects can differ. Because the spectra are different at the front and back facets, together they provide more information for the model to fit to. Knowledge of the relationships between front and back facet spectra can greatly assist in choosing starting facet phase parameters when fitting the model to data.

Fitting a model to data over a wide bandwidth (e.g., 72 nm) is important for accurate determination of laser parameters. Most fits in the literature use a bandwidth of approximately 10 to 12 nm, often only fitting to four or five modes on either side of the stop band [39],[40],[41],[42]. This chapter argues that it is important to fit over a wide bandwidth to obtain information about the frequency dependence of the modal gain and spontaneous emission, so that these parameters are set correctly. Incorrect gain or spontaneous emission curves could lead to false values for other parameters. Furthermore, facets with low reflectances can affect the spectrum up to 30 nm from the stop band region. The Fabry-Perot type modes that are far from the stop band are very useful in helping to determine facet reflectances and refractive indices. Information about laser parameters can be contained in spectra at wavelengths far from the stop band, and so wide bandwidths should be used if accurate, quick, and non-degenerate solutions are desired.

3.2. Gain, Spontaneous Emission, and Index of Refraction Vs Wavelength

The equations for gain in a quantum well that are commonly cited in the literature [4],[5] can be approximated with a modified parabola of the form

$$gain(\lambda) = gain\_peak - \frac{1}{gain\_width}[gain\_position - \lambda]^2$$

Eq. 3-1

An additional condition is sometimes used whereby the parabola is set to a constant value starting somewhere on the long wavelength side of the peak of the parabola. This allows the model to simulate the transparent behaviour of the quantum well at energies below the band gap. Note that Eq. 3-1 is for modal gain, and thereby is assumed to include scattering losses inherent to the waveguide cavity. The gain is a result of the sum of scattering loss, stimulated emission, and stimulated absorption from quantum wells in the active region. The gain can, therefore, take on negative (absorptive) values.

Spontaneous emission has a different functional form because it is never negative. The equation used in this model is of the form

$$spont(\lambda) = \frac{spontmax}{1 + \frac{(peaklambda - \lambda)^2}{|spontwidth|}}.$$

Eq. 3-2

In truncated-well DFB lasers, a spontaneous emission rate, and a gain, is assigned to the quantum wells in the low index area, which also appear in the high index area. Separate gain and spontaneous emission curves are assigned to the extra quantum wells that are in the high index region only, and the total gain or spontaneous emission in the high index area is then the sum of two equations. This procedure is useful in that it incorporates into the mode a physically valid relationship between the high and low index regions of the laser.

The equation for index of refraction that is used in the model is

$$n(\lambda) = n_g + \lambda \frac{dn}{d\lambda}$$

Eq. 3-3

where

$$\frac{dn}{d\lambda} = \frac{1}{2}\left(\frac{n_e - n_g}{\lambda_1} + \frac{n_e - n_g}{\lambda_2} \right).$$

Eq. 3-4

and λ_1 and λ_2 are the shortest and longest wavelengths in the spectrum that is being modelled. In Eq. 3-3 and Eq. 3-4, n_e is the effective index, and n_g is the group index. The index of refraction is then modified according to the index step of the grating, such that

$$n_h(\lambda) = n(\lambda) + \frac{\Delta n}{2} \qquad n_l(\lambda) = n(\lambda) - \frac{\Delta n}{2}$$

Eq. 3-5

where n_h is the index of refraction in the high index segment, and n_l is the index of refraction in the low index segment. The term Δn describes the magnitude of the index step between the low index and high index segment.

3.3. Example of Degenerate Solutions

Fig. 3-1 compares two fits to spectra from the front facet. The fits are of approximately equal quality over the 12 nm wide region shown. Fig. 3-2 shows that the first fit, Fig. 1a), is valid both at the front and back facet, over a bandwidth of 72 nm. Fig. 3-3 shows that the fit of Fig. 3-1 b) produces erroneous results when examined over a wider bandwidth and at the back facet, which indicates that the parameters obtained from the fit of Fig. 3-1 b) are incorrect. Together, these figures highlight the necessity of fitting to both facets over a wide bandwidth in order to ensure that the correct parameters are extracted.

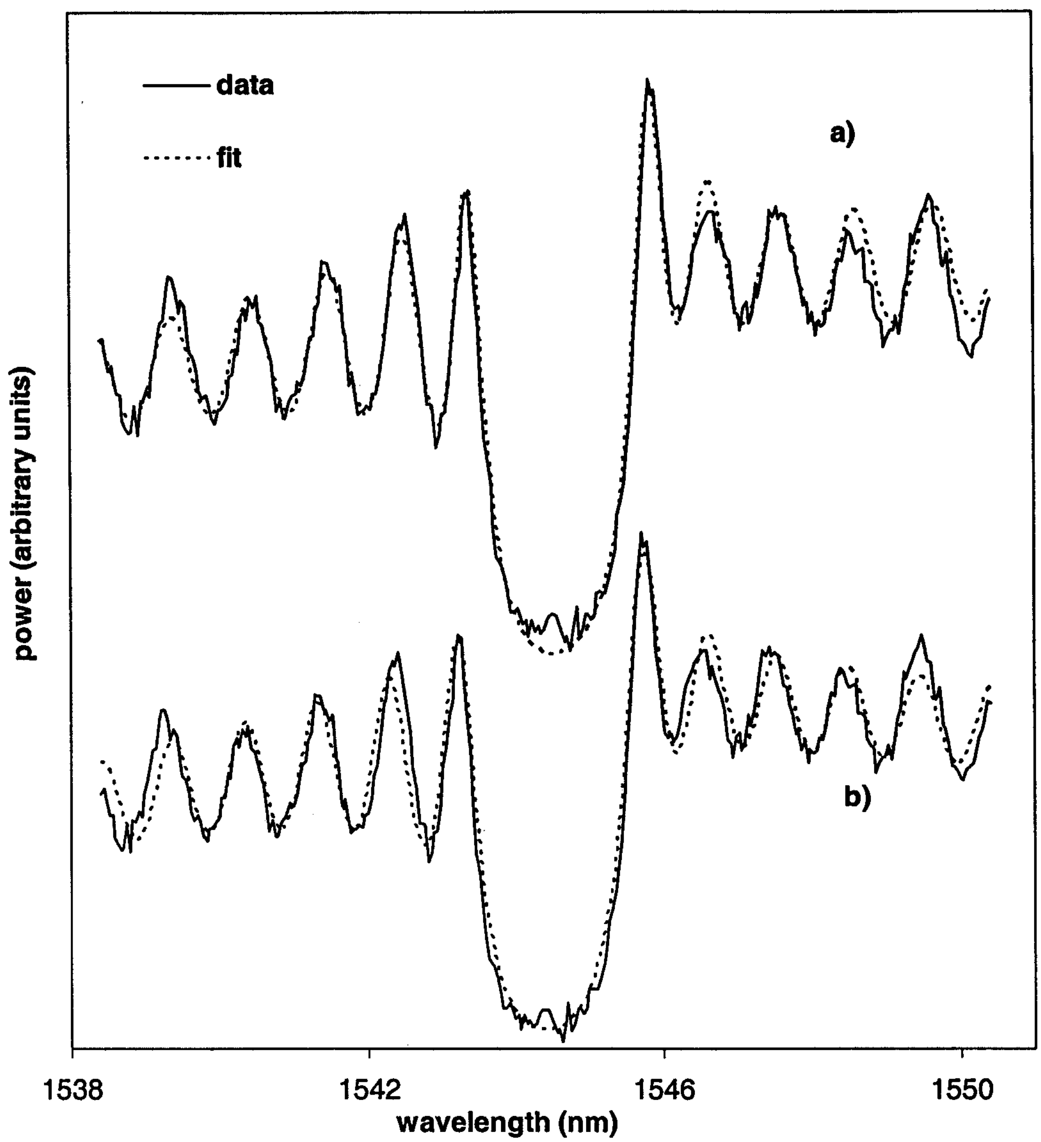

Fig. 3-1 Two fits of approximately equal quality. Plot a) was obtained by fitting to spectra from both facets over a 72 nm range. Plot b) was obtained by fitting to the spectrum from the front facet over 12 nm.

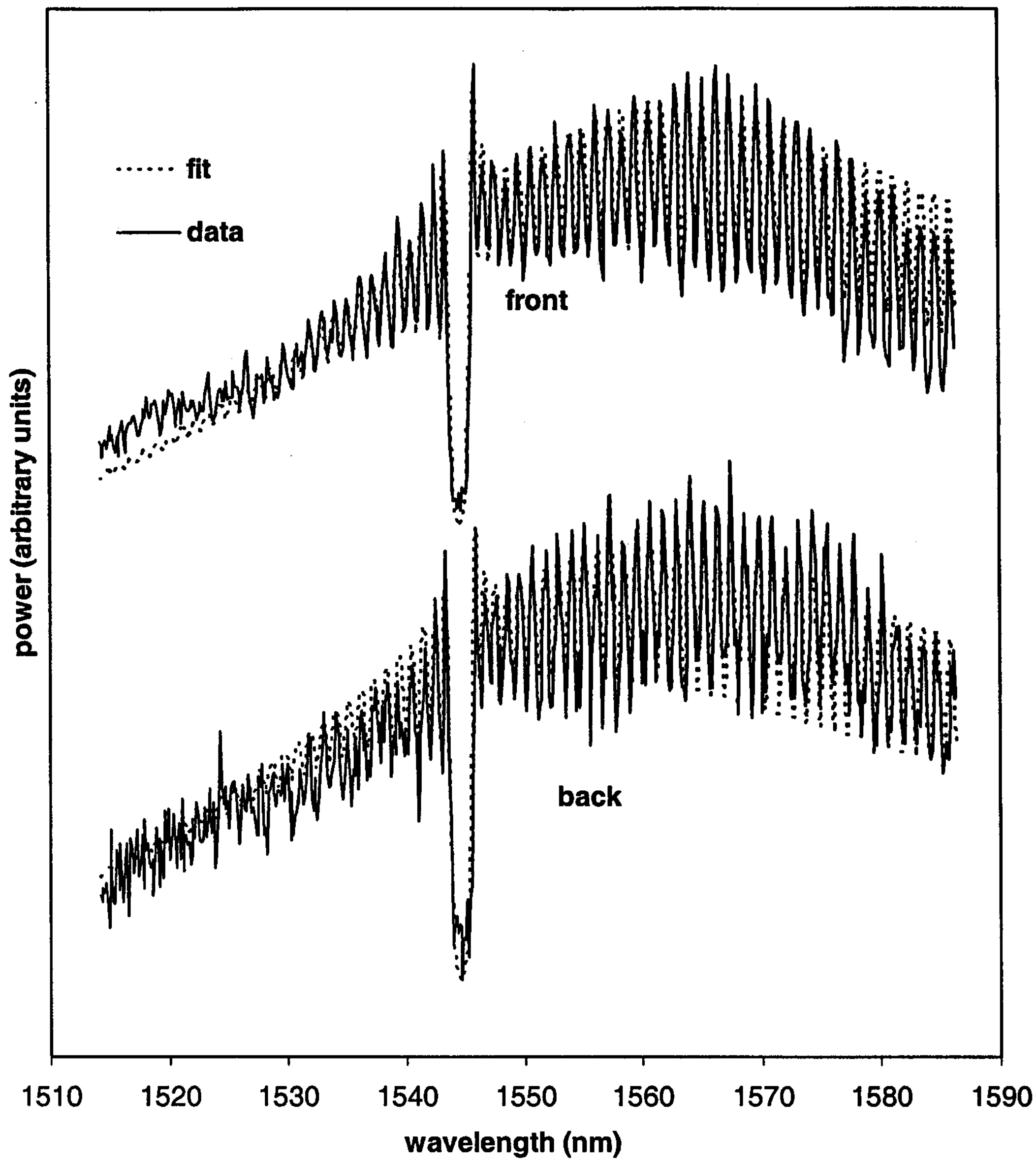

Fig. 3-2 A 72 nm wide display of the fit to the front and back facet spectra from Fig. 3-1 a).

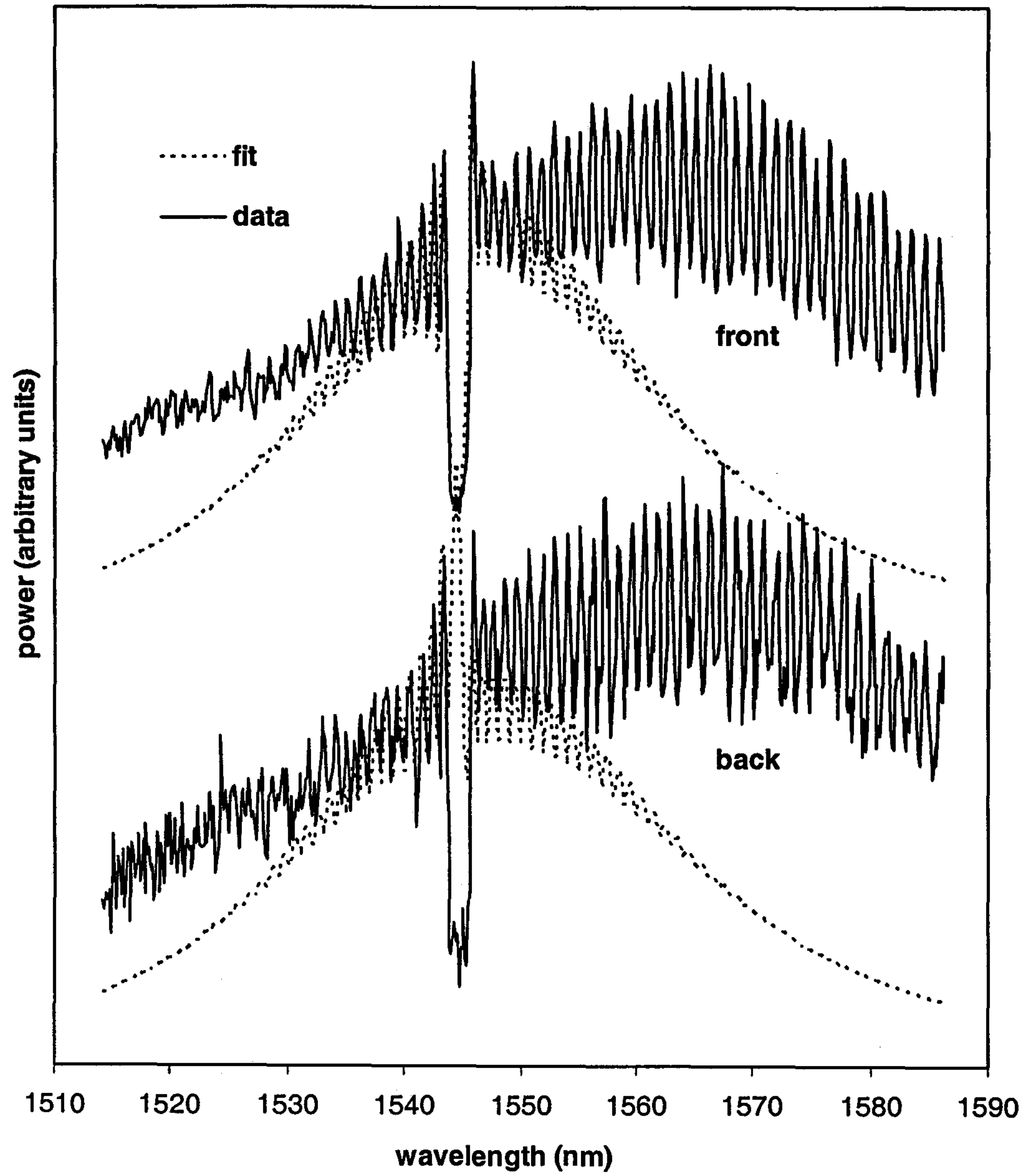

Fig. 3-3 A 72 nm wide display of the fit to the front and back facet spectra from Fig. 3-1 b).

Fig. 3-4, below, compares magnitudes of a few of the most important parameters that were extracted from this laser. The modal gain was modelled using the simple parabolic function of Eq. 3-1. Discrepancies between the results obtained from the fit of Fig. 3-1 a) and the fit of Fig. 3-1 b) are clear. The uncertainty calculated for the parameters is obtained by multiplying the mean-squared error with the diagonals of the error matrix [56]. This provides an estimate of the precision with a confidence level of 68%, assuming that the local minimum of χ^2 in parameter space is the correct solution. Unfortunately, if data is limited to a narrow bandwidth and single facet, then there may be several different minima in k-space with approximately equal χ^2 values.

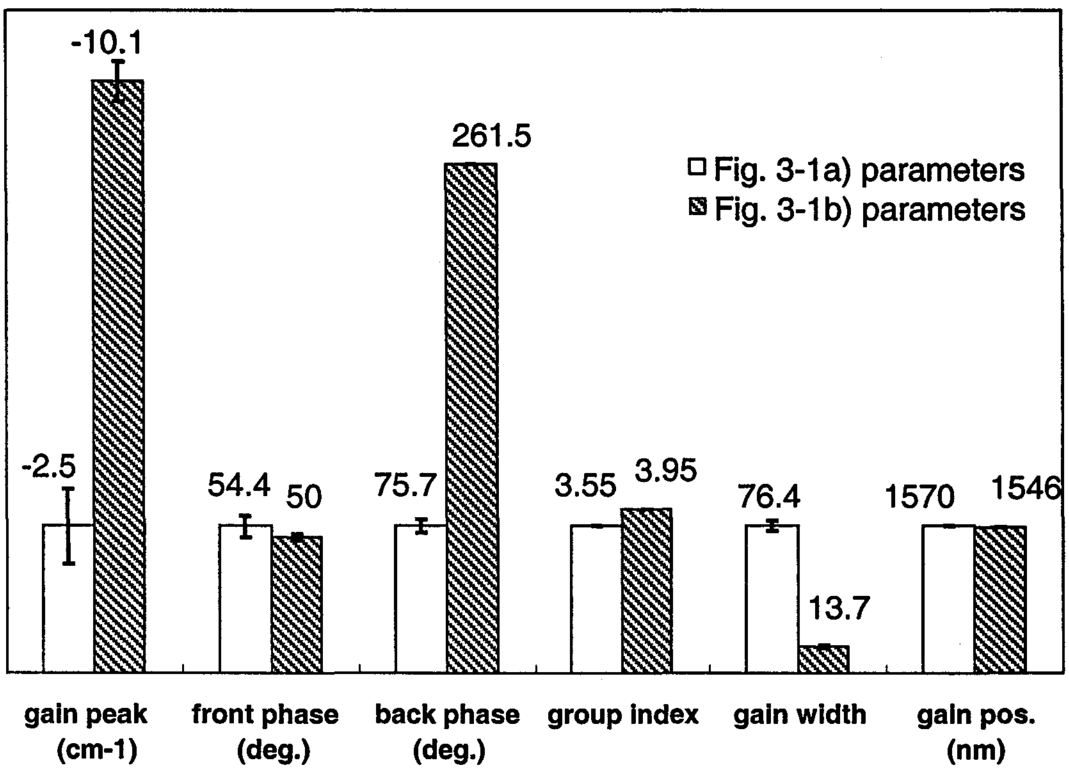

Fig. 3-4 A comparison of the relative magnitudes of some important laser parameters obtained from the fits of Fig. 3-1a) and Fig. 3-1b).

3.4. An Easily Identifiable Facet Phase Trend

When fitting to data it is useful to fit to both the front and back facet at the same time. The effects of gain profile and facet phase can appear very similar if only one facet is examined. Modes near the stop band can be suppressed or enhanced by the spontaneous emission and gain profile, or they may be suppressed or enhanced by the facet phases. It is often difficult to determine which parameters are responsible for the shape of the spectrum. However, comparison of the differences between the front and back facet spectrum will immediately separate gain effects from facet effects. Fig. 3-5 shows the front and back facet spectra of a truncated-well DFB laser, and an obvious facet effect is marked as "ramping". Front and back facet spectra are labelled. The small anomaly that appears in the spectra at 1567 nm is believed to be the stop band of a much weaker secondary transverse mode. This secondary transverse mode has negligible power output and is not accounted for in the model.

Without comparing spectra from the two facets, it is difficult to determine the role of the facets in shaping the spectra. This problem is amplified in gain-coupled lasers, where the gain ratio between high and low index segments can severely affect the modes near the stop band. For instance, if one were to only examine the front facet spectrum of Fig. 3-5, one might obtain erroneously high absorption values for the low index segments of the DFB grating, when in reality the modes are suppressed by the rear facet phase.

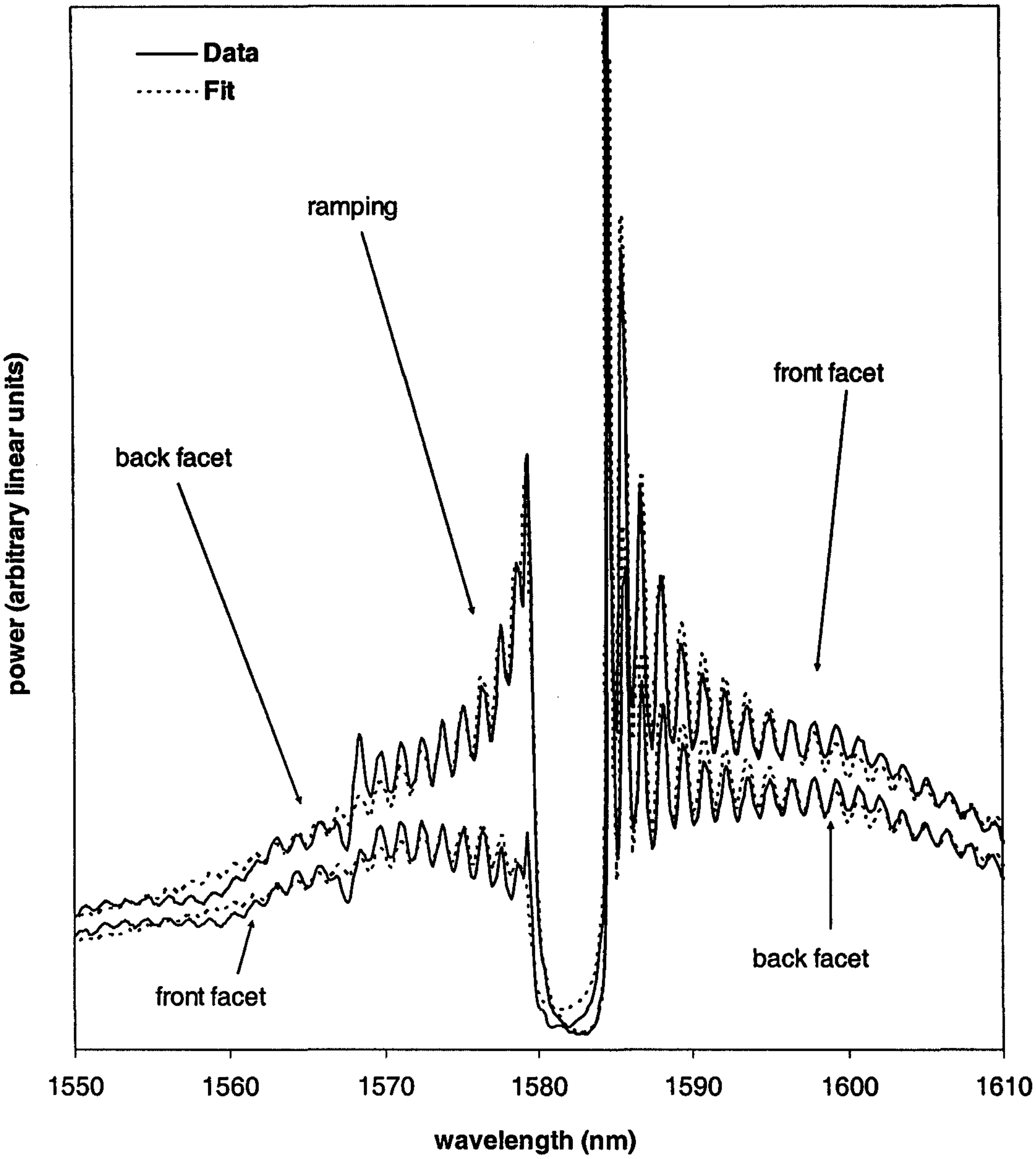

Fig. 3-5 Data (solid line) collected from the front and back facets of a truncated-well DFB laser, with best fit (dashed line). This data clearly demonstrates the facet dependent phenomenon of ramping.

The phenomenon marked "ramping" in Fig. 3-5 indicates a rear facet phase of 175°±5°, where the centre of the high index segment is considered to be 0°, as shown in Fig. 6. With increasing facet phase the ramping phenomenon gradually pushes into the stop band and at 270° will result in symmetric spectra, with the back facet spectrum exhibiting a much shallower stop band (or even a weak mode at the base of the stop band if the facet reflectance is sufficiently large [17][18]). At 0°, the ramping phenomena will appear at the right-hand side of the stop band. The ramping effect is commonly found in DFB lasers, and can easily be used to make an accurate first estimate of a facet phase. The facet that emits a spectrum with a ramping effect is responsible for the ramping effect. For example, in Fig. 3-5 the back facet is responsible for the ramping effect seen in the rear facet spectrum. The opposite facet yields a different spectrum, with suppressed modes in the wavelength band that exhibited ramping at the first facet (see Fig. 3-5).

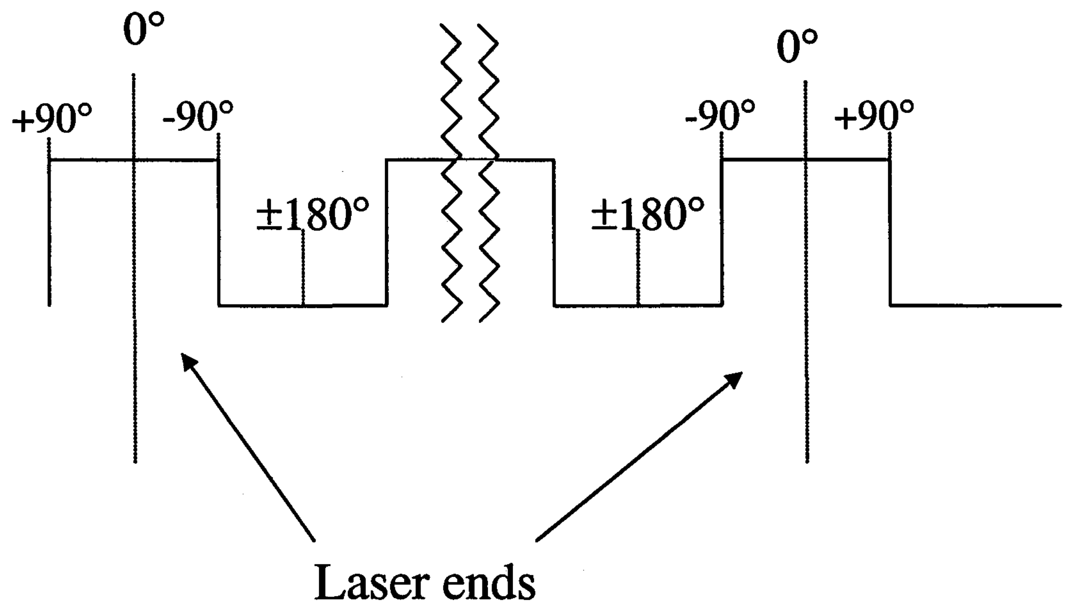

Fig. 3-6 Facet phase definition for a 50% duty cycle grating.

Ramping effects caused by AR coated facets are negligible because the AR coating reduces the feedback from the facet into the grating. The spectrum in Fig. 3-5 was fitted using a rear facet reflectance of 31%, which agrees with the expected reflectance for a cleaved facet. The fit used a reflectance of 0.2% for the AR coated front facet, which was found to have a phase of -33°±15°.

3.5. Fitting Far from the Stop Band

Fitting far from the stop band is necessary for three reasons. Firstly, it is important to obtain the correct shapes for the gain and spontaneous emission curves, so as to separate these effects from facet phase effects. Secondly, modes *very* far from the stop band are only weakly affected by the grating and by facet phases, and so are particularly useful for estimating the correct effective and group indices, and for estimating the facet reflectances if such parameters are not known in advance. Lastly, mode flattening facet effects can often be observed up to 30 nm from the stop band, if one of the facet reflectances is very low (i.e., AR coated). I am not aware of any previous reports of facet effects this far removed from the Bragg wavelength.

If the flattening occurs to the left of the stop band, (shorter wavelengths) then the AR coated facet must have a phase in the vicinity of 180°. If the flattening occurs to the right of the stop band, (longer wavelengths) then the AR coated facet must have a phase of approximately 0°. The distance of the flattening effect from the stop band is determined not by the phase, but by the relative magnitudes of the AR coated reflectance, and the coupling coefficient. A higher coupling coefficient will force the flattening effect further from the stop band. A higher reflectance will force it nearer the stop band. Fig. 3-7 shows a series of simulated rear facet spectra that have been generated for lasers with different front facet reflectances (rear facet reflectance = 31 %). The front facet spectra (not shown) displayed the same flattening phenomena. The rear facet was set to a constant phase of 90°, which prevented the rear facet feedback from causing spectral shaping such as ramping or flattening. As the reflectance decreases, the flattening phenomenon moves further from the Bragg wavelength. Spectra that exhibit these effects in both index-coupled and truncated-well gain-coupled DFB lasers have been observed and fitted to.

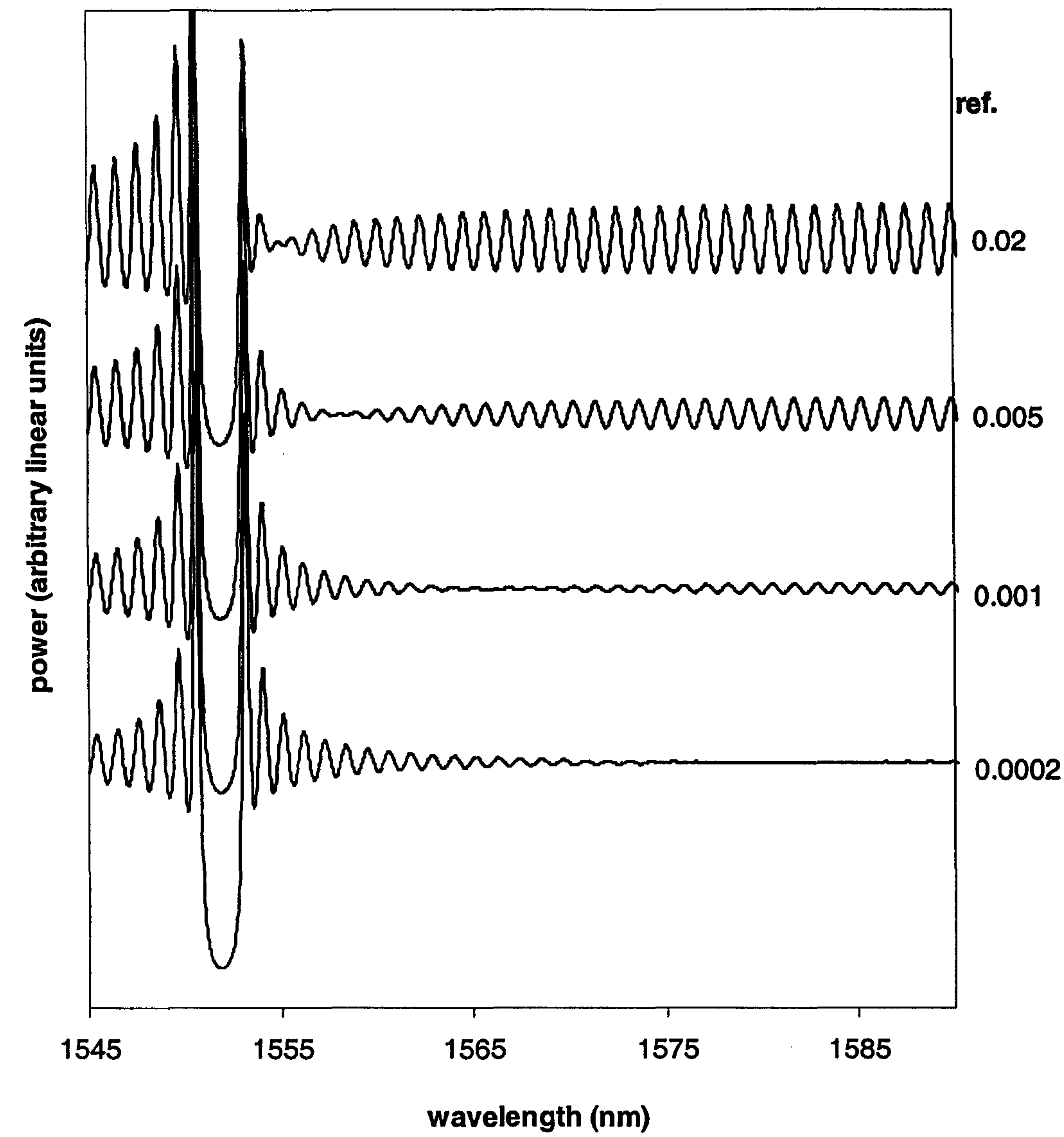

Fig. 3-7 The modal flattening phenomenon shifts outwards from the stop band with decreasing front facet reflectance. For this laser the coupling coefficient was 82 cm^{-1}, the rear facet had a reflectance and phase of 0.31 and 90°, respectively, and the front facet phase was set to 0°.

3.6. Conclusion

Accurate estimates of distributed feedback laser parameters have been extracted by fitting a transfer-matrix model to laser spectra. Simple facet phase trends commonly found in DFB laser spectra have been discussed. These trends are useful for choosing initial facet phases with which to begin the fitting routine. The trends are common to both index-coupled and index-coupled gain-coupled DFB lasers, and are especially useful in fitting to truncated-well DFB lasers.

The necessity of fitting over a wider bandwidth and to both facets simultaneously has been demonstrated. Simple wavelength dependencies for important parameters in the model have been presented. When the guidelines in this chapter are followed, overly complicated fitting algorithms are not necessary, and relatively simple least squares fitting procedures such as the Marquardt-Levenberg fitting algorithm can be employed [57][58]. These simple approaches to quickly obtaining accurate and non-degenerate results have not been well documented in any existing literature.

4. Facet Phases and Sub-Threshold Spectra of DFB Lasers: Spectral Extraction, Features, Explanations, and Verification.

4.1. Introduction

In distributed feedback (DFB) lasers, the phases of the internal grating at each of the two partially reflecting facets (i.e., the facet phases) have distinct effects on static and dynamic laser characteristics. The facet phases of DFB lasers have measurable effects on the threshold gain, linewidth, differential quantum efficiency, side-mode suppression ratio (SMSR), and single mode yield [16],[59],[60],[61],[62],[63],[64]. Effects of facet phase on DFB laser spectra have been modelled using transfer-matrix and coupled mode theories of light propagation [13],[40]. Direct experimental evidence of the facet phase affecting laser characteristics has been obtained by ion beam etching of the cleaved facets of second order DFB lasers. The behaviour of the lasers was seen to change periodically with etching depths equal to one half of the oscillation wavelength in the laser cavity [65].

This chapter examines and explains the effects of facet phase on sub-threshold spectra of DFB lasers. Spectral fitting and scanning photoluminescence (PL) measurement techniques were used. Section 4.2 describes the fit of the probability-amplitude transfer-matrix model to 6 truncated-well DFB lasers. The probability-amplitude model treats spontaneous emission correctly by allowing for self-interference of probability amplitude waveforms. This treatment of spontaneous emission appears to be correct quantum mechanically and results in better fits to spectral data than other contemporary models [66].

In sub-threshold spectra, facet phases are responsible for many distinctive patterns. These are discussed in section 4.3 of this chapter where the probability amplitude model is used to isolate and explain some of the more obvious effects that facet phases have on DFB laser spectra. Many effects of facet phases have been noted in the literature, but have not been isolated nor explained in detail. Most spectral features are unique to certain combinations of the front and back facet phases. It is the uniqueness of these spectral features that allows determination of facet phases in a laser by fitting to spectral data. A few facet effects were documented in the previous chapter, but this chapter explains how these effects, and others, arise.

The facet phase for truncated-well DFB lasers can be determined independently of fits to the spectra by analysis of PL data collected from the facet. This allows for validation of the facet phases (and the concurrent explanations of spectral effects) that were obtained by fitting the probability amplitude model to spectra. The photoluminescence method for determining facet phases of truncated-well lasers was developed and first demonstrated by Adams *et. al.* [67]. Section 4.4 of this chapter describes use of the PL method to measure the facet phases of the 6 truncated-well lasers that were fitted to in section 4.2.

Finally, in section 4.5, the results from the PL technique in section 4.4 and the spectral fitting method of section 4.2 are compared and found to yield the same results for facet phases, within estimated experimental error. The agreement between the two methods validates, in my opinion, the use of the transfer-matrix model for estimating, documenting, isolating, and explaining sub-threshold facet phase effects.

4.2. Fitting to Spectra

The design of the truncated-well lasers used in this experiment is shown in Fig. 4-1. Truncated-well DFB lasers are fabricated by periodically etching through some, or all, of the quantum wells in the active region. The advantage of this design is that it results in gain coupling, which leads to a high single mode yield and side mode suppression ratio. The ratios of quantum wells in the not-etched to etched segments of the truncated-well DFB lasers of this chapter are 5:0, and 8:5.

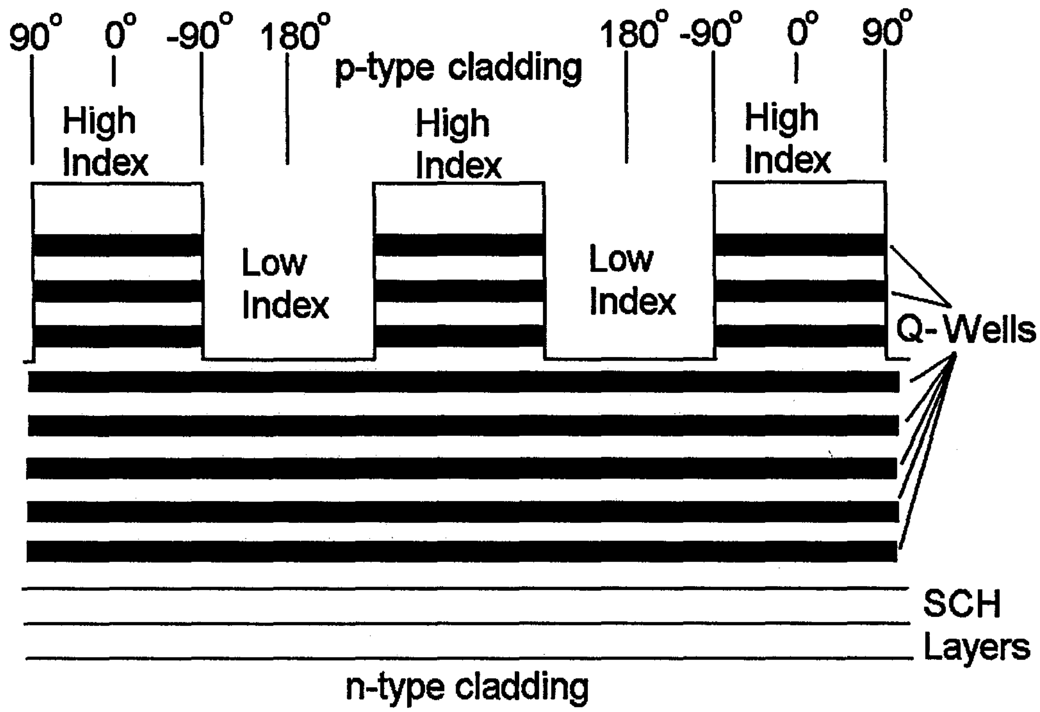

Fig. 4-1 Schematic of the 5:0 (not-etched to etched ratio) truncated-well DFB lasers analysed in this chapter. My convention for facet phase measurement is also depicted.

Sub-threshold spectra were gathered from the front and back facets of 6 truncated-well (5:0) lasers. A Marquardt algorithm [56],[57],[58] was used to fit the transfer-matrix model to the front and back facet spectra of the lasers simultaneously, and to estimate the uncertainties. The fits were performed over a bandwidth of 72 nm. Estimates for the facet phases were extracted from the best fits to the sub-threshold spectra. Fig. 4-2 and Fig. 4-3 demonstrate typical fits of the laser model to front and back facet data. The fits in Fig. 4-2 are for laser 3, and the fits in Fig. 4-3 are for laser 4. The fits are good in the sense that all features are explained with the exception of some unexplained intensity spikes on the short wavelength side of the stop band. These anomalous spikes are unique to the bar of lasers used for this experiment, and have little effect on the spectral fitting results. All 6 truncated-well lasers are from the same bar, and thus have similar fit parameters. Parameters for lasers 3 and 4 are documented in Table 4-1, as examples of typical values. The fits of Fig. 4-2 and Fig. 4-3 were easily obtained by starting with good estimates of facet phase. Spectral phenomena that can be easily identified to obtain good initial estimates of facet phase are discussed in section 4.3, below.

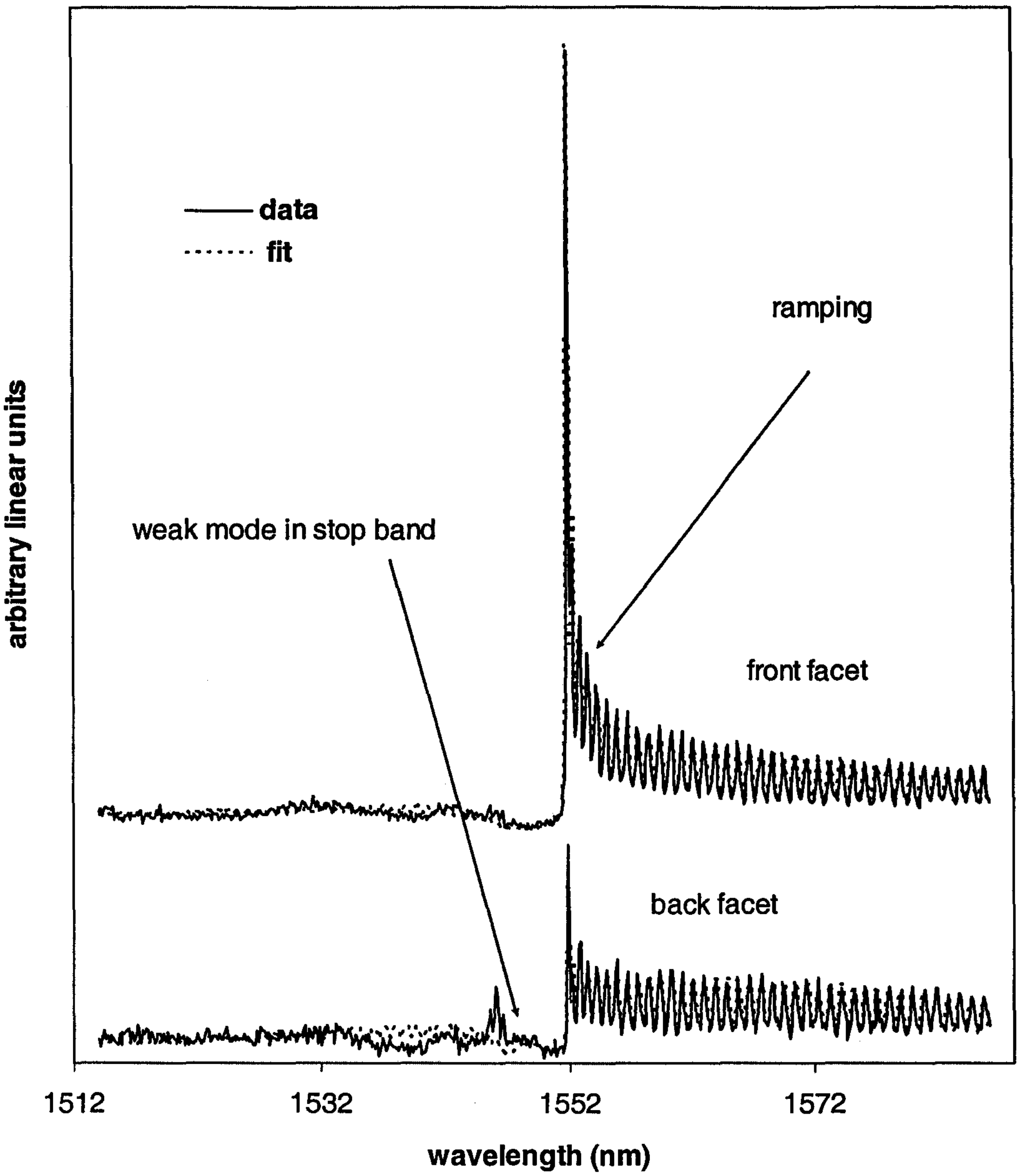

Fig. 4-2 Data from the front and back facets of laser 3, together with the best fits of a transfer-matrix model. Fits to the front and back facets were made simultaneously using the same set of parameters. Interesting facet phase effects are labelled.

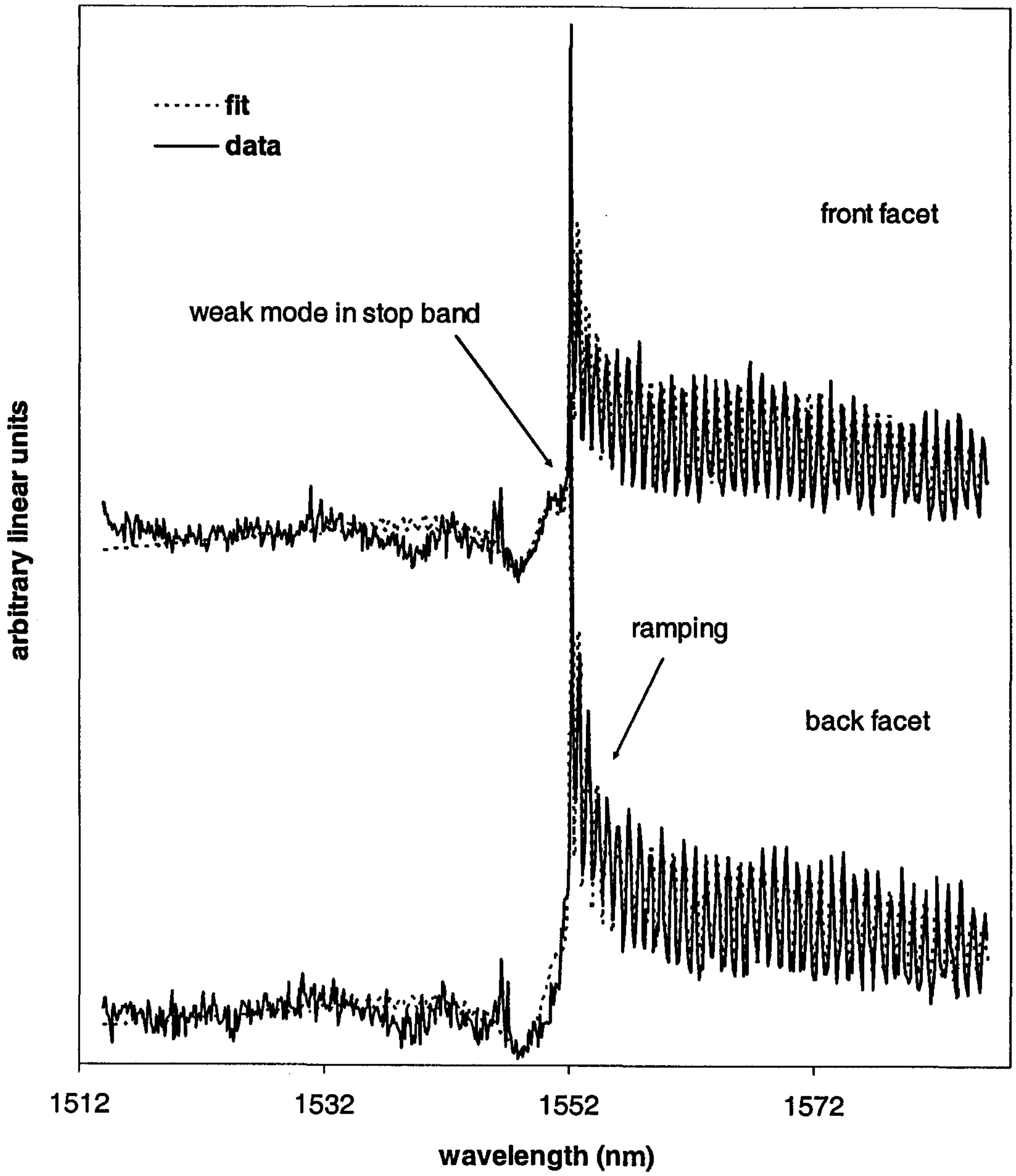

Fig. 4-3 Data from the front and back facets of laser 4, together with the best fits of a transfer-matrix model. Fits to the front and back facets were made simultaneously using the same set of parameters. Interesting facet phase effects are labelled.

Table 4-1 Sample of parameters from lasers 3 and 4.

Parameter	Laser 3	Laser 4
Facet Reflectances	0.31	0.31
Front facet phase	17° ± 5°	274° ± 5°
Back facet phase	250° ± 5°	291° ± 5°
Real index step of grating	0.01778 ± 0.00001	0.01572 ± 0.00001
Average modal effective index	3.1988 ± 0.0001	3.2000 ± 0.0001
Average modal group index	3.4600 ± 0.0001	3.4665 ± 0.0001
Length of a single grating period	242.15 nm assumed	242.15 nm assumed
Mark/Space Ratio	0.5	0.5
Length of Laser	0.3799 mm ± 0.0005 mm	0.3799 mm ± 0.0005 mm
Coupling coefficient κ_r	229 cm^{-1} ± 1 cm^{-1}	203 cm^{-1} ± 1 cm^{-1}

4.3. Facet Phase Phenomena Useful for Spectral Fitting

The features seen in DFB laser spectra can be understood as the superposition and interaction of various different cavity resonances. A good starting value for a spectral fitting routine can usually be offered in advance if one understands the role of the laser facet phase in creating these cavity resonances.

In this section theoretical spectra are systematically generated and compared to real spectra, including those of section 4.2. An understanding of the physics of spectral shaping leads to estimations of facet phases and facet reflectances by visual observation of the spectrum. The arguments in this section are also useful for showing that when fitting a model to spectral data both facets should be fit to over a relatively wide bandwidth if accurate laser parameters are to be extracted.

For the sake of clarity, in this chapter the term “mode” is used to describe any local maximum in a laser spectrum. Kogelnik and Shank [10] showed that for a laser with zero reflectance facets, strong symmetrical Bragg modes exist on the edges of the stop band but the magnitudes of Bragg modes diminish rapidly with increased deviation from the stop band. For non-zero facet reflectance, modes that would be created by Fabry-Perot resonance are unable to exist in and around the stop band owing to dominance of Bragg reflection. However, in regions well outside of the stop band, Fabry-Perot resonant modes determine the shape of the spectrum.

A third type of mode can also exist in the DFB spectrum. This mode is not a resonance between Fabry-Perot facet mirrors, nor is it a resonance within the DFB laser. It results from a resonance between a single facet and the DFB grating. One example of such a mode has been studied extensively by Henry [17] and McCall and Platzman [18]. McCall *et. al.* noted the similarity between a $\pi/2$ shifted DFB grating and a facet positioned at 270° with respect to the grating (in my convention for facet phase, 0° is the centre of a high index tooth, and the length of one grating period is considered to be 360°, as shown in Fig. 4-1). Either condition in a DFB laser creates a mode in the centre of the stop band. The condition for the existence of this centre mode resonance is

$$\phi_{RT} + \phi_M + \phi_{DF}(\omega) = 2n\pi$$

Eq. 4-1

where n is an integer, ϕ_{RT} is the phase difference $2l(2\pi/\lambda)$ between the grating and the facet (i.e., the facet phase), ϕ_M is the phase change upon reflection at the facet (often 0), and ϕ_{DF} is the frequency dependant phase of the Bragg grating reflection. The magnitude of the reflectance of the facet determines the relative magnitude of the facet-grating resonances in comparison to pure DFB grating resonances. The frequencies and relative strengths of the various Fabry-Perot, DFB grating, and facet-grating resonances are the clues that allow a spectral fitting algorithm to extract facet phases from laser spectra. The spectral shapes that result as a superposition of the various possible resonances will be briefly explained in the following sections.

4.3.1. Low Reflectance Facet Effects

4.3.1.1. Mode Flattening

Mode flattening was observed on both the long and short wavelength sides of the stop band in index-coupled and truncated-well DFB laser spectra. Fig. 4-4 shows as an example the front facet spectrum from a truncated-well DFB laser, with the best fit, in a least-squares sense, to the data. The spectrum exhibits flattening of the longitudinal mode profile on the long wavelength side of the stop band. It became apparent during the fitting of the model to the spectrum that the flattening of the modes could only be explained by assuming a certain front facet phase for the model. That front facet phase was -15° ± 5°.

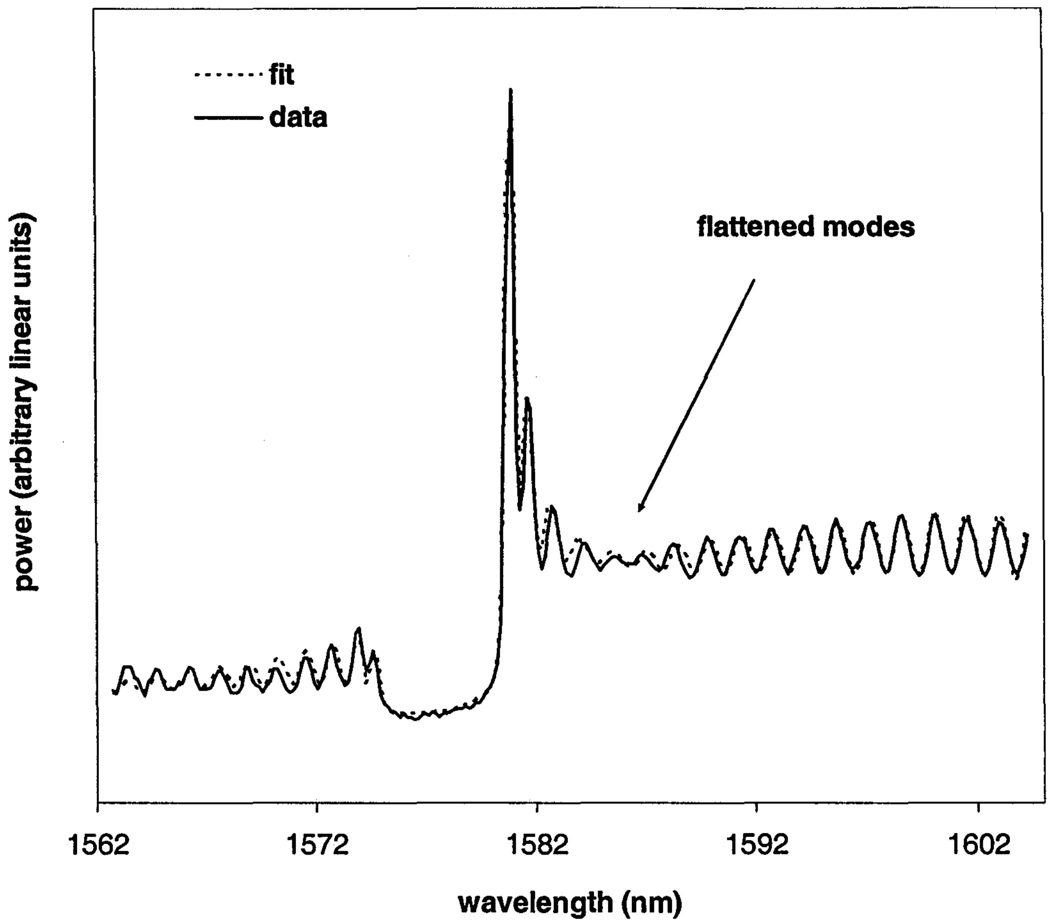

Fig. 4-4 A good example of mode flattening in an 8:5 (not-etched to etched ratio) truncated-well gain-coupled DFB laser. The data is shown with a solid line and the fit is shown with a dashed line.

For further analysis of the flattened mode phenomenon, Fig. 4-5 shows a series of simulated back facet spectra for lasers in which the front facet reflectance was set to 0.04. The reflection from the back facet was removed (i.e., reflectance set to 0) to isolate the effects of a single facet. From the bottom spectrum upwards, the phase of the grating at the front facet has been increased from 0° to 330° in 30° increments. The uppermost spectrum in the graph is for the same laser but with the reflectances for both facets set to zero. This uppermost spectrum provides, for comparison with the spectra below it, an indication of the frequencies of the natural Bragg grating modes (i.e., the modes that are selected by the Bragg grating exclusively, in the absence of facet reflectors).

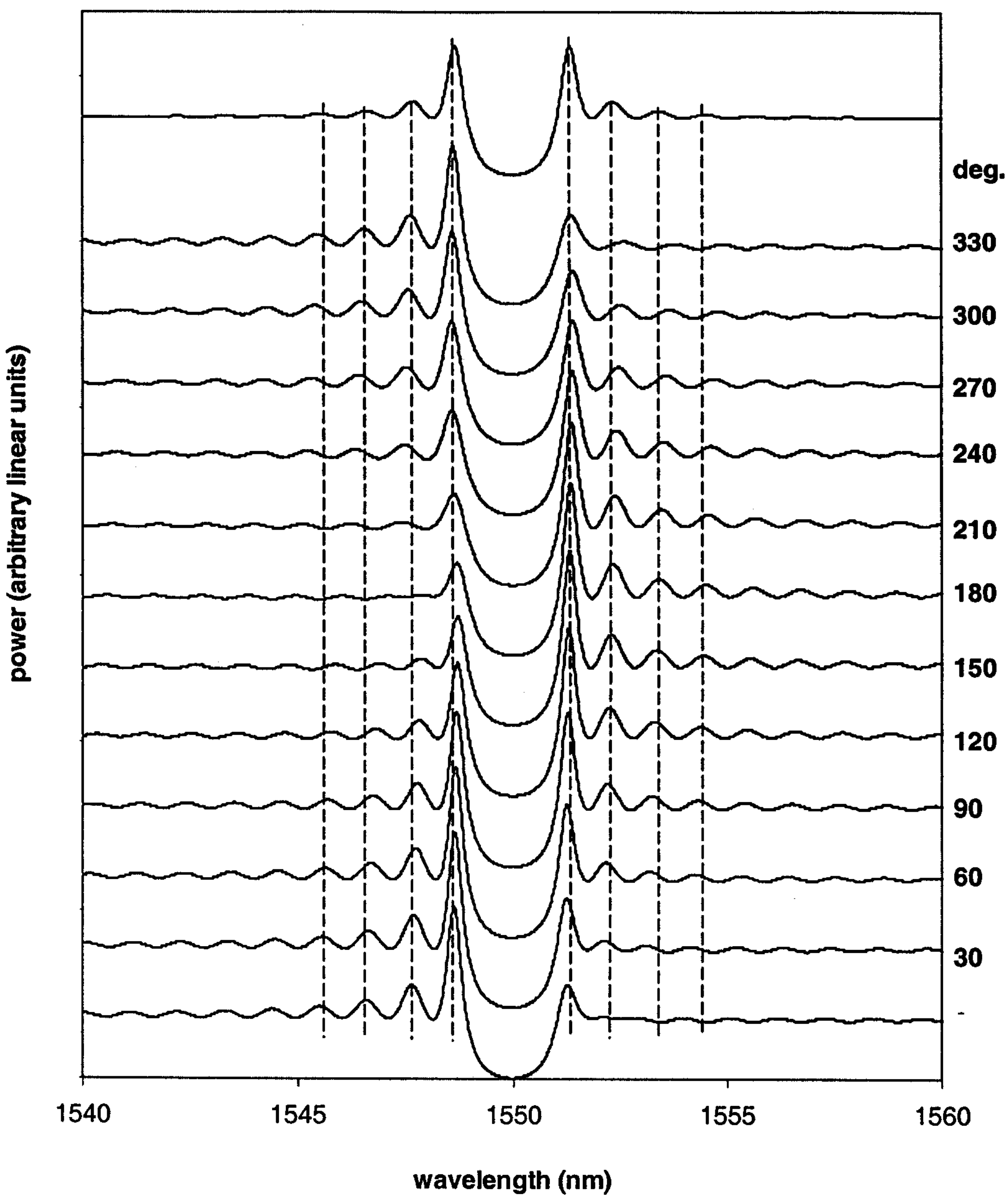

Fig. 4-5 A series of back facet spectra for front facet phases ranging from 0° (bottom) to 330°(top) in 30° increments. The front facet reflectance is set to 0.04, and the uppermost spectrum demonstrates where the natural Bragg modes (dashed lines) lie. The back facet reflectance was set to 0 in these simulations.

Table 4-2 contains the parameters of the simulated lasers of Fig. 4-5. All simulated lasers described in this chapter have the same parameters, unless otherwise specified. To ensure that the simulations would be relevant and practical, the parameters of Table 4-2 were extracted from the measured spectra of a bar of index-coupled lasers. Fig. 4-6 shows a typical fit that was made to a laser from this bar. The laser of Fig. 4-6 has a front facet phase and reflectance of 55° ± 5° and 0.04, and a back facet phase and reflectance of 94° ± 5° and 0.31 respectively. It is gratifying to note that the spectra of Fig. 4-6 clearly resemble the basic shapes of the theoretical 90° curves presented in Figs 8 and 9, which assume reflectances of 0 and 0.5 and not 0.04 and 0.31 as for Fig. 4-6. Note also that a very small amount of modal flattening is visible at the long wavelength side of the spectrum of Fig. 4-6, as is predicted by the 60° curve of Fig. 4-5.

Table 4-2 List of Parameters for simulated lasers.

Real index step of grating	0.00637
Gain	0.3 cm^{-1}
Average modal effective index	3.1998
Average modal group index	3.5438
Length of a single grating period	242.2 nm
Mark/Space Ratio	0.5
Length of Laser	0.305 mm
Coupling coefficient κ_r	82 cm^{-1}

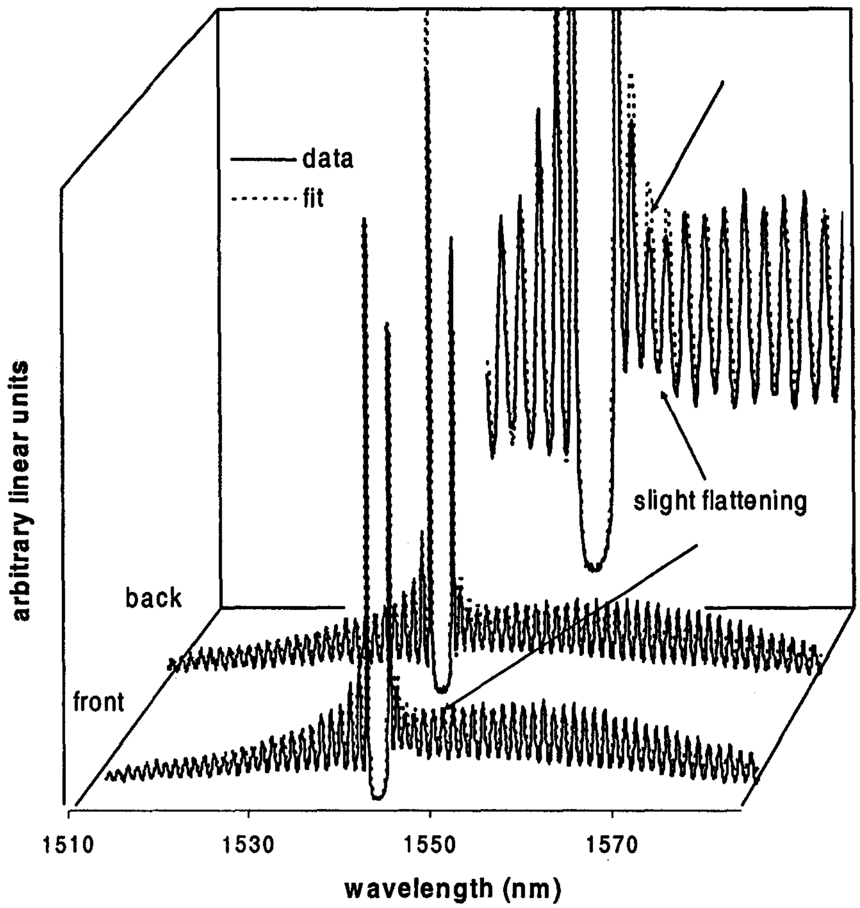

Fig. 4-6 A fit to the index-coupled laser from which parameters were extracted (see Table 4-2) for use in the simulations of Fig. 4-5, Fig. 4-7, Fig. 4-8 and Fig. 4-9,. The general shape of the data (and fit) is particularly interesting to compare to Fig. 4-5, Fig. 4-8, and Fig. 4-9. Weak modal flattening due to a front facet phase of 55° (compare to 60° in Fig. 4-5) is visible, and the front and back spectra are roughly symmetric, as is predicted by the 90° curves of Fig. 4-8 and Fig. 4-9.

Flattened modes owe to the dominant facet-grating resonances (as described by Eq. 4-1) occurring at frequencies exactly between the natural Bragg resonances. Fig. 4-5 shows that when facet-grating resonances coincide with the minima between Bragg resonance peaks, a flattened spectrum is the result. A relatively low front facet reflectance (e.g., 0.04) is needed for mode flattening to be visible. Higher reflectances can have stronger spectral shaping effects, such as spectral ramping (which is discussed further in this chapter), but do not cause such visible mode flattening effects, because the Bragg grating resonances are greatly overwhelmed by the grating-facet resonances. Higher reflectances may cause mode flattening effects if the coupling coefficient of the grating is proportionally stronger.

In Fig. 4-5, flattening of the modes can occur at either the short or long wavelength side of the stop band, depending on the facet phase. Mode flattening is also visible in the spectra obtained at the front facet. In both the front and back spectra, long wavelength modes are most flattened when the front facet phase is at 0°, and short wavelength modes are flattened when the front facet phase is at 180°.

There is one aspect of mode flattening that is not addressed by Fig. 4-5. This is that the flattening effect is of finite length. After a few flattened modes, larger modes reappear, as can be seen in the spectrum of Fig. 4-4 (and upon careful inspection, in Fig. 4-6 also). These larger modes, even further from the stop band than the flattened region of the spectrum, are the result of Fabry-Perot type resonance. They are not present in the simulations of Fig. 4-5 where the back facet was removed (i.e., assumed to be perfectly transmitting) by setting the reflectances to zero.

4.3.1.2. Positioning of Flattened Modes

The modes that are flattened can be further selected by adjustment of the facet reflectivity. Fig. 4-7 shows a series of simulated spectra for the back facets of lasers having front facet reflectance ranging from 0.24 to 0.01, and front facet phase of 0°. Front facet spectra are not shown but the effect of changing the reflectance is the same for both front and back facet spectra. All the spectra in Fig. 4-7 have a back facet reflectance of 0.3 (as cleaved) and back facet phase of 90°. It is clear that a smaller front facet reflectance moves the mode flattening phenomena further from the stop band, and that a larger front facet reflectance moves the mode flattening closer to the stop band. Fig. 4-7 is similar to Fig. 3-7 of the previous chapter, which varied smaller facet reflectances against a weaker coupling coefficient. The coupling coefficient in the simulations of Fig. 4-7 is 307 cm^{-1}, compared to 82 cm^{-1} in Fig 3-7. These two figures, taken together, demonstrate the importance of the balance between coupling coefficient and facet reflectance that determines the positioning of the flattened modes.

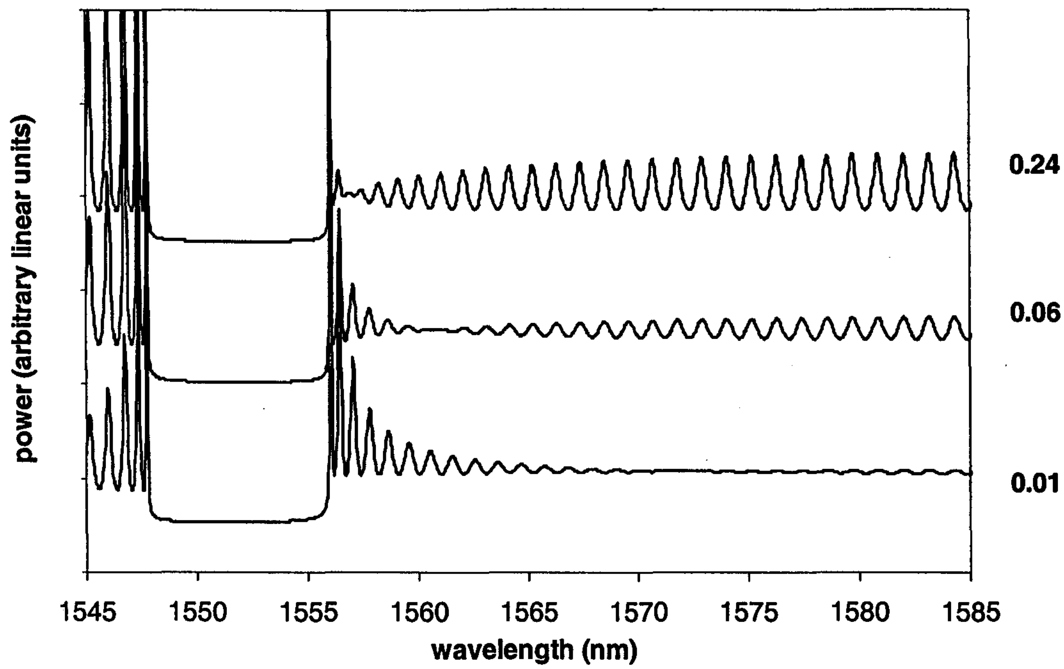

Fig. 4-7 The modal flattening phenomena shifts outwards from the stop band with decreasing front facet reflectance. For this laser the coupling coefficient was 370 cm^{-1}, the back facet had a reflectance of 0.31 and phase 90°, and the front facet phase was set to 0°.

The effect of reflectance on the position of mode flattening can be explained easily. In Fig. 4-7, the modes that are outside of the flattened region and away from the stop band are predominantly Fabry-Perot modes. Modes resonating between the grating and front facet, and Fabry-Perot modes resonating primarily between the front and back facets, both become more dominant when the front facet reflectance is increased. For an increased front facet reflectance, stronger Fabry-Perot modes can dominate in regions closer to the stop band. Similarly, the stronger facet-grating resonances can compete with Bragg grating resonances at wavelengths nearer the stop band. Thus the flattened mode region in the spectrum appears at wavelengths closer to the stop band when there is a larger facet reflectance. Although Bragg resonance, grating-facet resonance, and Fabry-Perot resonance are all responsible for shaping the spectra in Fig. 4-4, Fig. 4-5, and Fig. 4-7, the final laser modes are defined only by the spectral maxima that result from the combination of these resonances. The stimulated emission rate is directly proportional to intensity, and so as gain increases the sub-threshold maxima will continue to be maxima, and will develop into larger, sharper modes. Thus, the Bragg resonances, Fabry-Perot resonances, and facet-grating resonances do not all create peaks in the laser spectra.

Because the flattened region of spectrum is a result of competition between Bragg grating resonances and facet-grating resonances, the coupling coefficient of the grating is also responsible for the position of the flattened modes. For a given facet reflectance, the flattened modes will be seen further from the stop band if the coupling coefficient is increased. The same trends are apparent on the short wavelength side of the spectrum if a front facet phase of 180° is chosen.

4.3.2. High Reflectance Facet Effects.

4.3.2.1. Mode in Stop Band

A superposition of resonances also occurs when the facet reflectance is strong, but the effect on the shape of the spectrum is somewhat different from the low reflectance case. Fig. 4-8 and Fig. 4-9 are the same types of plot as Fig. 4-5 but with the front facet reflectance raised to 0.5. In accordance with the format of Fig. 4-5, the Bragg resonance spectrum is shown at the top of Fig. 4-8 and Fig. 4-9. Spectra from the front facet are displayed in Fig. 4-8 and Fig. 4-9 displays spectra from the back facet, which has zero reflectance. With strong reflectance, the effects of the facet phase on the laser spectra are very noticeable. Mode flattening is less prominent because the facet-grating resonances are significantly larger than the Bragg resonances and are of substantial size regardless of the facet phase.

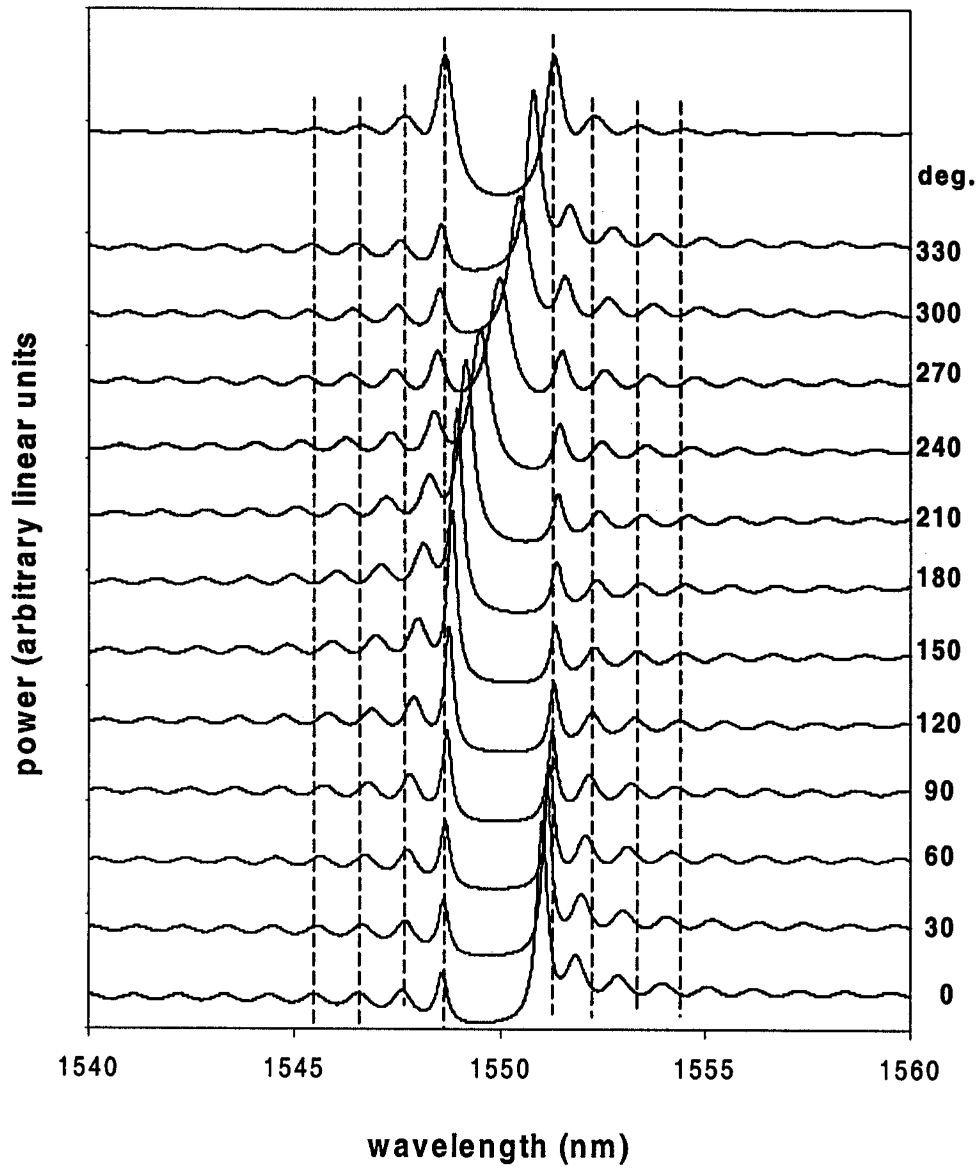

Fig. 4-8 A series of front facet (0.5 reflectance) spectra for facet phases ranging from 0° (bottom) to 330° (top) in 30° increments. The back facet reflectance was set to 0 (thereby preventing effects from more than one facet from being confused), and the uppermost spectrum demonstrates where the natural Bragg modes (dashed lines) lie.

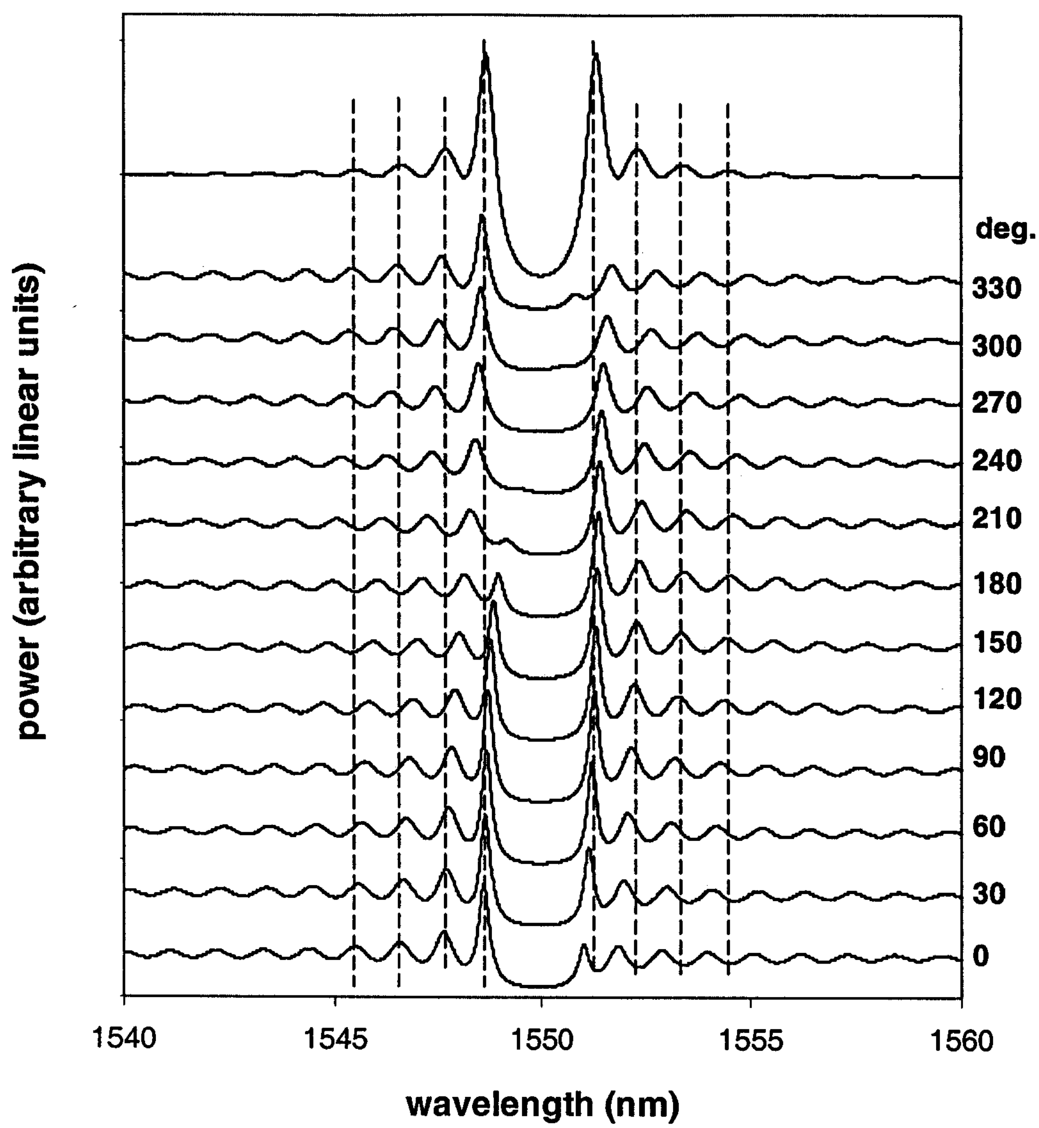

Fig. 4-9 A series of back facet spectra for front facet phases ranging from 0° (bottom) to 330°(top) in 30° increments. The front facet reflectance is set to 0.5, and the uppermost spectrum demonstrates where the natural Bragg modes (dashed lines) lie. The back facet reflectance was set to 0 in these simulations in order to prevent confusion of effects from more than one facet.

In Fig. 4-8 the spectrum with a front facet phase of 90° is very similar to the Bragg spectrum. This is also apparent in Fig. 4-6, in which the reflecting facet had a phase of 94° ± 5°. The effect of a facet phase of 90° on the Bragg grating spectrum is small. With a phase of 90° the reflective facet feeds light back into the laser cavity in much the same way that an extended grating would. In the limiting case of a perfectly reflecting facet, the laser spectrum would be similar to one from a laser with double the cavity length and perfectly anti-reflection coated facets. The only difference between the two cases is that a mirror reflection does not have the same frequency dependent phase as a Bragg grating.

At a facet phase of 270°, the facet-grating mode analysed by McCall and Platzman [18] is visible. For the Bragg wavelength, the standing wave created by reflection from the 270° facet is exactly in phase (spatially) with standing waves that are created by reflection of light from the Bragg grating in a direction away from the centre of the laser. Thus for a facet phase of 270°, there is a resonance at the Bragg wavelength created between the grating and the facet, as is predicted by Eq. 4-1.

As the facet phase changes from the 270° (-90°) position towards 360° (0°), the mode in the centre of the stop band shifts to longer wavelengths. The reason for this is best understood if one considers light circulating in the laser between the facet and the

DFB grating. For a grating phase that is larger than 270°, the standing wave resonance between the facet and the Bragg grating that causes the central mode is reduced at the Bragg wavelength. Eq. 4-1 no longer holds at the Bragg wavelength because the term ϕ_{RT} has been increased. At slightly larger wavelengths (detuned from the Bragg wavelength), the standing wave resonance will exist because the frequency dependant term ϕ_{DF} is decreased at this frequency and Eq. 4-1 is then satisfied. Parallel arguments can be used to explain why shorter wavelengths are favoured by the centre mode as the facet phase approaches 180° from 270°. Lasers 3 and 4 of Fig. 4-2 and Fig. 4-3 provide actual examples of modes within the stop band. A weak mode in the stop band can be seen in the back facet spectrum of laser 3 (Fig. 4-2). This weak mode indicates a back facet phase of 249° ± 5°. There is also weak mode within the stop band of the front facet spectrum of laser 4 (Fig. 4-3), which was shown to have a front facet phase of 274° ± 5°.

Fig. 4-9 shows a series of simulated spectra collected from the 0 reflectance back facet of a laser with a 0.5 reflectance front facet. Again, front facet phases range from 0° to 330° in 30° steps from bottom to top. At wavelengths near the stop band, transmittance of the Bragg grating is low. As a result, the effects of the front facet are smaller in and around the stop band of the back facet spectrum.

4.3.2.2. *Ramping*

A spectrum collected from a facet with phase of approximately 180° exhibits increasing amounts of power on the short wavelength side of the stop band as the wavelength deviation from the stop band region decreases. At a front facet phase of 0°, the same effect is visible on the long wavelength side. Examples of this ramping power effect can be seen in the front facet spectrum of laser 3 (Fig. 4-2) on the long wavelength side of the stop band, and in the back facet of laser 4 (Fig. 4-3). The ramping effect in Fig. 4-2 is due to the 0.31 reflectance (as cleaved) front facet phase of 16° ± 5°. Laser 4, in Fig. 4-3, has a back facet phase of 291° ± 5°. Obtaining a good fit to lasers 3 and 4 was not difficult because reasonable initial estimates for the facet phases were made, based on the ramping phenomena.

Facet phases of 0° and 180° create facet-grating resonant modes that are at frequencies different from those of the natural Bragg resonances (Fig. 4-8). In these cases, Bragg resonance wavelengths that are fed back into the laser by the facet are rejected because they are out of phase with grating-reflected standing waves. The Bragg grating also inhibits propagation of the facet-grating resonant modes because the facet-grating modes lie at frequencies that are at minima between Bragg resonant peaks (Fig. 4-8). The grating has an increased effective reflectance for light reflected back from the facet, and an increased amount of light is forced out of the facet. Thus a ramping effect on one side of the stop band is visible in the spectrum. Under close inspection the ramping effect is visible in the 0° and 180° spectra of Fig. 4-8. The ramping effect in Fig. 4-8 would be more noticeable in a laser with higher coupling coefficient, such as a truncated-well DFB laser. The reduced feedback from a facet that exhibits ramping causes spectral power to be lower at the other facet over the same wavelength range as the ramping. Comparison of Fig. 4-8 to Fig. 4-9 reveals this effect.

4.3.2.3. Front and Back Modes

In the front facet spectra of Fig. 4-8, the long wavelength mode dominates the below-threshold spectral output when the front facet phase is 0°, and the short wavelength mode dominates when the front facet phase is 180°. In the back facet spectra of Fig. 4-9, however, the short wavelength mode dominates when the front facet phase is 0° and the long wavelength mode dominates when the facet phase is 180°. A front facet phase of 0° or 180° selects the dominant mode in the front facet spectrum at a frequency that is not compatible with the Bragg grating (i.e., is partially within the stop band). This dominant front facet mode is unable to propagate to the back facet without being reflected and diffracted by the Bragg grating, unless the front facet reflectance is very high and the grating coupling coefficient is relatively low, or the laser length is quite short. Conversely, the mode on the other side of the stop band, i.e., the one that was not favoured at the front facet, is in good alignment with the Bragg resonant frequencies of the grating and is able propagate its power through to the back facet, where it dominates in the below-threshold back facet spectrum. The relative heights of peak modes at the long and short wavelength sides of the stop band will, of course, also depend on the shape of the gain curve in that region of the spectrum. In Fig. 4-2 for instance, the modal gain is much larger on the long wavelength side of the stop band, and the long wavelength mode dominates at both facets. Nonetheless, for laser 3 in Fig. 4-2, the dominant mode is much stronger at the front facet than at the back.

4.3.2.4. Asymmetry

Fig. 4-8 and Fig. 4-9 reveal that at 270°, the facet dependant modes are partially misaligned with the Bragg resonance peaks. To satisfy Eq. 4-1 on the long wavelength side of the stop band, modes selected by the facet-grating interference are at slightly longer wavelengths than the Bragg resonance peaks. On the short wavelength side of the stop band, modes selected by the facet-grating resonance are at slightly shorter wavelengths than the Bragg resonance peaks. As the facet phase moves away from 270°, the higher-order facet-grating modes are shifted in the same direction as the central facet-grating mode in Fig. 4-8 (due to the behaviour of the frequency dependant term ϕ_{DF} in Eq. 4-1). If the facet-grating resonant modes on one side of the stop band move away from the Bragg resonant peaks, then the facet-grating resonant modes on the other side of the stop band move *towards* the Bragg resonance peaks. Thus Bragg resonances and facet-grating resonances can only compete and produce the aforementioned flattening and ramping effects on one side of the stop band at a time.

Having used the model to identify and explain facet effects in DFB laser spectra, it is important to verify that the model is making correct predictions. There are examples in the literature of transfer-matrix models making fits to spectral data, and thereby surmising the facet phase. Unfortunately there has been no way of directly measuring the actual facet phase for comparison, and so the accuracy and reliability of the technique has not been studied. These issues are addressed in the following sections.

4.4. Photoluminescence Method

The scanning photoluminescence technique for measuring facet phases in truncated-well DFBs is made possible by a small and unintentional misalignment of angle α between the grating grooves (of period Λ_{Bragg}) and the facet cleavage plane [67]. The intensity of photoluminescence measured along the facet of a cleaved bar of truncated-well DFB lasers varies in an approximately sinusoidal manner (with period Λ_{Facet}) that corresponds to the etched and not-etched segments of the grating. The not-etched, high index segments of the grating yield a greater amount of photoluminescence because they contain a larger number of quantum wells than the etched segments. Fig. 4-10 graphically depicts the photoluminescence technique and its use in measuring facet phase. The period of photoluminescence measured along the facet of the laser bar is defined by the equation

$$\Lambda_{facet} = \frac{\Lambda_{Bragg}}{\sin\alpha}$$

Eq. 4-2

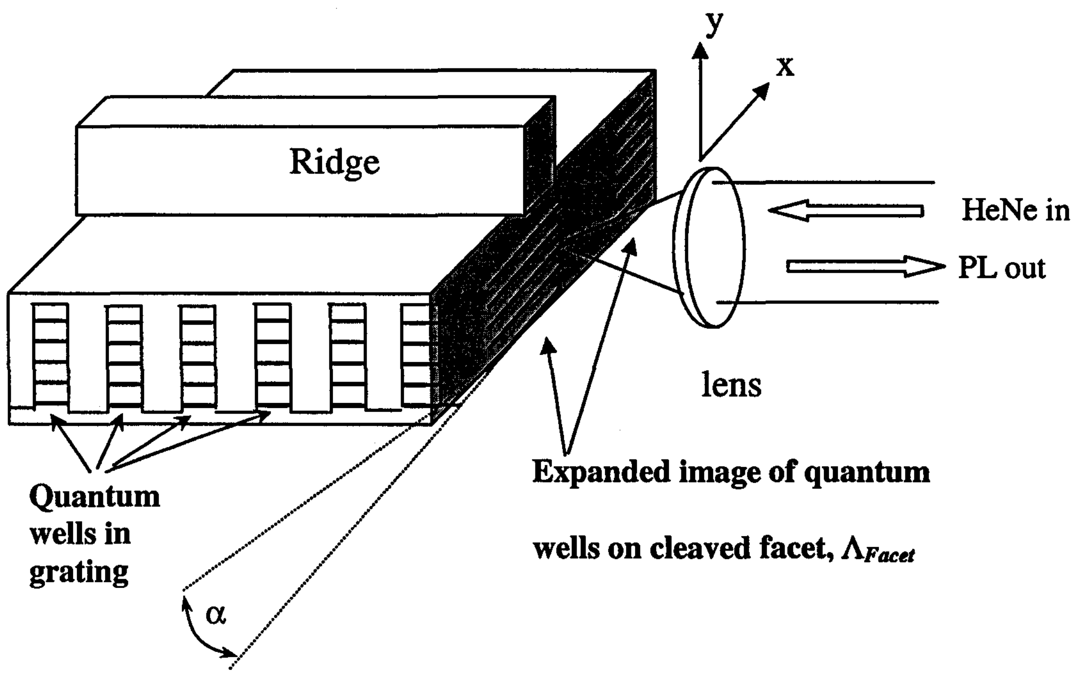

Fig. 4-10 An illustration of the scanning photoluminescence method for determining facet phases, as applied to a truncated-well laser with a not-etched:etched quantum well ratio of 5:0. The unintentional misalignment between the cleaved facet and grating is labelled α.

To find the facet phase, the location of the laser cavity ridge must be determined. Most PL scans obtained for the 6 lasers in this study revealed a distinct dip in PL yield at the ridge point. PL scans from different heights on the facet were processed using a high pass digital filter. DC offsets and low frequency noise were thereby removed. The best scans were averaged together and a simple sinusoid was fitted to the resulting data. Noisy regions were excluded from the fit. Fig. 4-11 shows a typical sinusoidal fit to PL data for the back facet of laser 5. This fit yielded a facet phase of 141° ± 20°. The primary source of uncertainty was the accuracy with which the position of the laser ridge could be determined. Error bars were calculated according to the estimated accuracy of the laser ridge position.

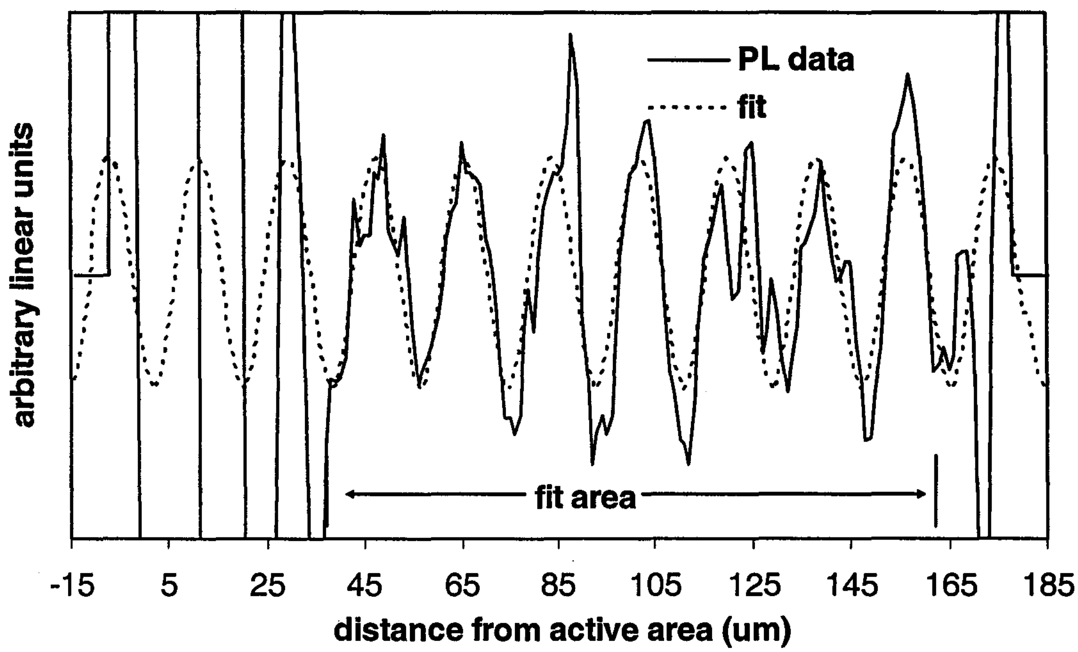

Fig. 4-11 The sinusoidal fit to PL data for the back facet of laser 5, which yielded a facet phase measurement of 141° ± 20°. Noisy regions were excluded from the fit.

4.5. Comparison of methods

This section of the chapter compares the facet phases that were predicted by spectral fitting described in secton 4.2 of this chapter with facet phases measured using the photoluminescence technique. Fig. 4-12 compares extracted facet phases with measured facet phases. Extracted facet phases and measured facet phases are within experimental uncertainty for 11 of the 12 laser facets.

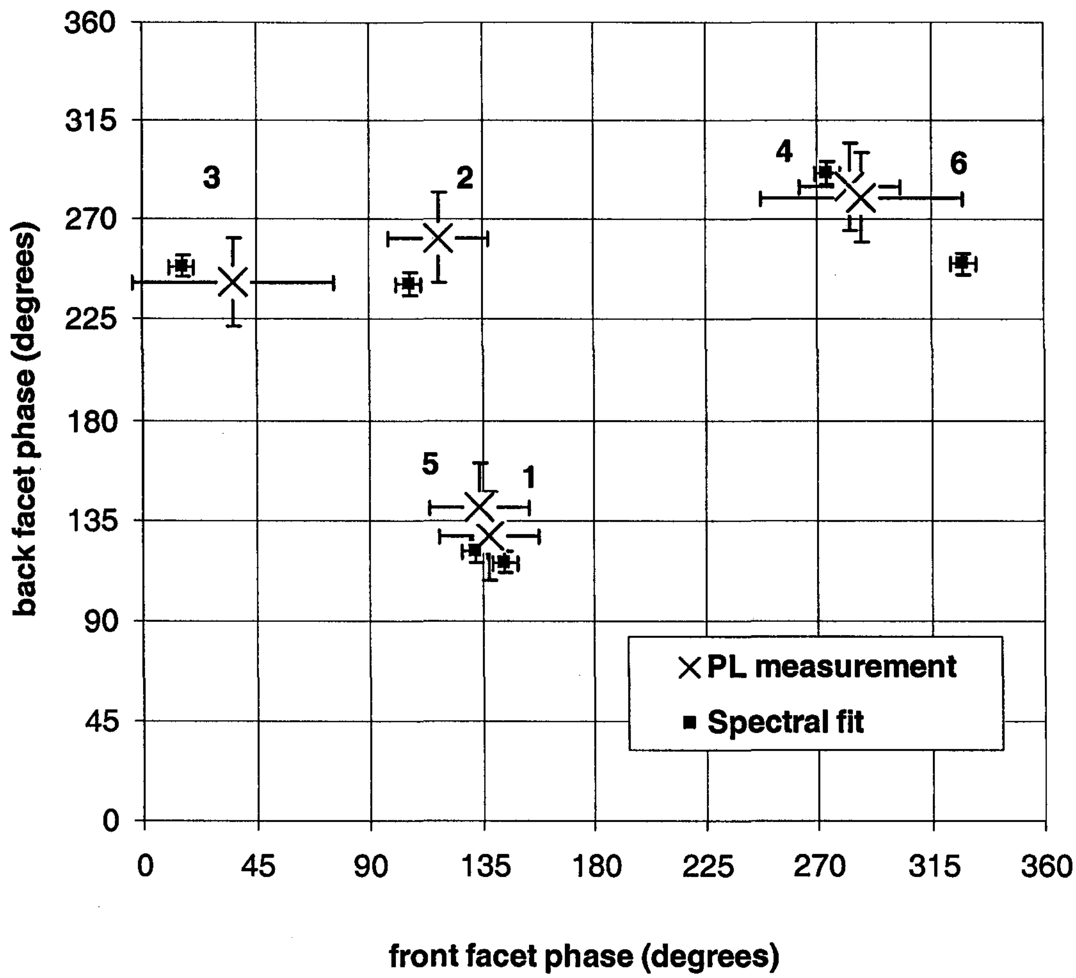

Fig. 4-12 A plot of front and back facet phases for the 6 lasers examined in this chapter. An agreement between the PL measurements and the values determined by spectral fitting is clear.

PL data near the ridge for the front facets of lasers 3 and 6 were not obtainable because of damage to the cleavage plane around (but not on) the light emitting ridge area. To find the phase of the grating at the ridge for these two cases, PL scans were performed 100 μm from the ridge. For this reason the error bars are twice as large (i.e., 40°) for the front facets of laser 3 and 6. The PL scans of the back facet of laser 6 were also problematic. Values ranging from 280° to 350° could be obtained for the facet phase, depending on the altitude on the facet from which the PL scan was obtained. Scans that were relatively low on the facet were chosen. A broad fault (complete lack of photoluminescence) was observed 14 μm from the ridge, and may have been responsible for the difficulty in measuring the back facet phase of this laser. The two methods of facet phase determination yielded results for this facet that were slightly (5°) outside of the standard estimations of uncertainty. This is probably due to the fault that was observed near the ridge.

The lasers in this experiment had uncoated facets that exhibited reflectances of approximately 0.31. Reflectances of 0.31 are large enough to have substantial effect on the laser spectrum so that a precise facet phase (± 5° is standard) must be assumed if reasonable fits to the spectra are to be obtained. The difficulty in identifying the exact location of the ridge in the PL scans results in a much larger uncertainty of ± 20°. The accuracy obtainable using the PL method will vary for different laser bars, and depends on both the clarity of ridge location, and the misalignment α of the grating relative to the cleaved facet of the bar.

There are aspects to spectral fitting that may make extraction of facet phases from spectral measurement the preferred method over the PL technique. For the lasers that were tested, agreement was found between the two techniques. The spectral fitting technique can be applied to index guided structures whereas the PL technique is limited to truncated-well DFB lasers. Also, the spectral fitting technique is simpler to implement owing to the ease with which a spectrum can be obtained using commercially available optical spectrum analysers. Nonetheless, the PL technique is a more direct measurement of facet phase and there may be occasions where a more direct measurement is required.

4.6. Conclusion

This chapter has described the successful fitting of the probability amplitude transfer-matrix model to 6 truncated-well distributed feedback lasers. Obtaining good fits was made easy by using knowledge of facet phase effects in sub-threshold spectra. The transfer-matrix model was then used to isolate, document, and explain the various sub-threshold spectral phenomena that are unique to certain facet phases and reflectances. The results clearly demonstrate the advantages of fitting a physical model to front and back facet spectra simultaneously over a broad spectral range. Finally, the validity and accuracy of using a transfer-matrix model to analyse facet phase effects in spectral data has been demonstrated by making a comparison with results from the scanning PL technique. The spectral fitting method may often be more convenient and more accurate than the PL technique, but the PL technique may provide a more direct measure of the facet phase than spectral fitting.

5. Application Examples

5.1. Introduction

This chapter demonstrates two practical projects in which the probability amplitude model has been applied. In each application, important information that was useful to DFB laser designers in the telecommunications industry was extracted. The success with which the model has been applied in industry helps to highlight the importance of the work in this thesis. The first project described in this chapter examines the behaviour of gain coupling in truncated quantum well lasers as the injection current approaches threshold. The second project that will be described uses a modified version of the probability amplitude model to examine the yield of multi-section tuneable truncated-well DFB lasers.

5.2. Extraction of Gain Parameters for Truncated-Well DFB Lasers

5.2.1. Overview of Gain Analysis Project

Truncated-quantum-well gain-coupled distributed feedback lasers have a periodic modulation of the real and imaginary parts of the index of refraction of the active region. As shown in Fig. 5-1, the Bragg grating in these devices is fabricated by periodically etching away a number of the quantum wells in the active region of the device. Gain-coupled distributed feedback lasers (GC-DFB) that are fabricated in this manner show a high yield of single frequency lasers with a large side mode suppression ratio (SMSR) and excellent performance under modulation [68][69]. The high index to low index quantum well ratio in the lasers studied in this section is 8:5.

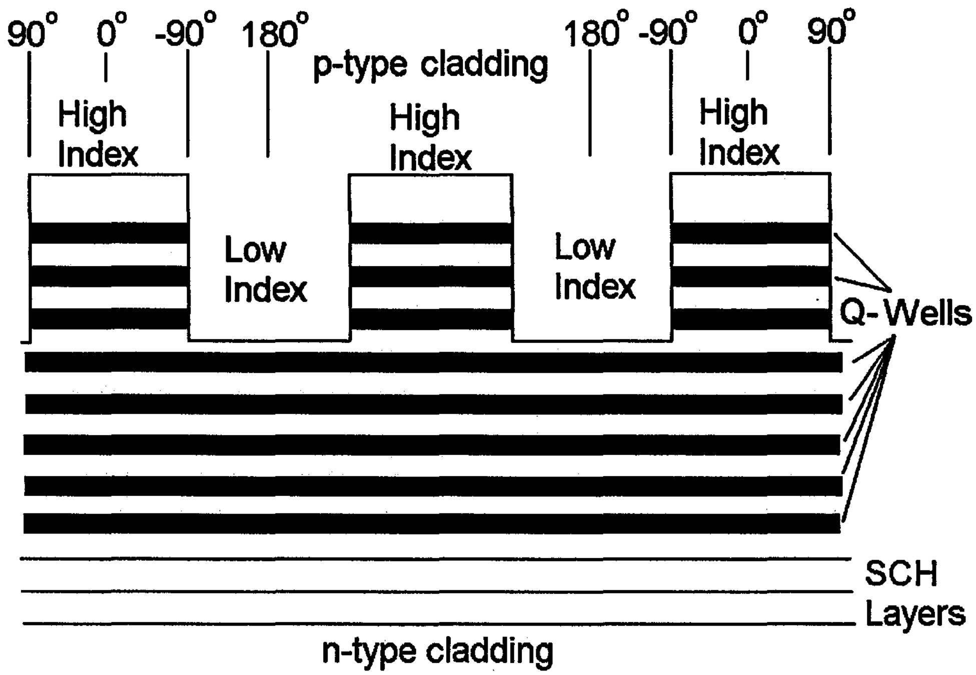

Fig. 5-1 Depiction of a portion of the Bragg grating in a truncated-well gain-coupled DFB. For clarity, the grating phase definition is also depicted.

The favourable modulation characteristics of truncated-well GC-DFB lasers have been attributed to the efficiency of injection of carriers owing to the increased surface area between the quantum wells and the cladding layer [70]. It has also been suggested that non-uniform injection into the wells causes an additional difference in the gain between the etched and not etched segments of the grating, and that this accounts for the exceptionally high single mode yield and side mode suppression ratio (SMSR) of truncated-well GC-DFBs [71],[72],[73]. The non-uniform injection is thought to be a consequence of the low mobility of holes [74]. According to this theory, quantum wells that are adjacent to the n-side of an InGaAsP/InP active region are less populated and do not contribute as much to the gain as do wells that are adjacent to the p-side of the active region [75],[76].

The next three sections of this chapter describe a study of the ratio of the modal gains of high gain, high index segments to low gain, low index segments of the Bragg grating in truncated-well DFBs as determined by least squares fits to the below-threshold steady state spectral output. The gain ratios are shown to be higher than would be expected from simple consideration of the ratio of quantum wells in the high and low index segments.

5.2.2. Extraction of DFB Parameters for Gain Analysis Project

Nonlinear least-squares fits of a transfer-matrix model to sub-threshold spectral data were performed using a Marquardt-Levenberg algorithm [56],[57],[58]. Best estimates of the gain profiles, effective indices, group indices, grating phases at facets, facet reflectances, and spontaneous emission profiles were extracted from the fits. Each grating segment is represented by a 2×2 transfer-matrix. Accordingly, the fits to the spectra directly yield values for the average net modal gains in the high index, high gain segments, and in the low index, low gain segments. Uncertainties in fit parameters were estimated using the error matrices that were generated during the fitting routine.

The spectrally resolved emissions from the front and back facets were fitted simultaneously using the same parameter sets, as recommended in chapter 3 of this thesis. For each laser, values of the grating phase at the facets remained consistent over the complete range of currents for which spectra were fitted. The spectra were obtained with 0.04 nm separation between data points using an Anritsu MS9710B Optical Spectrum Analyzer having a resolution of 0.07 nm.

The grating mark to space ratio (i.e., length of high gain segments to length of low gain segments) had little effect on the quality of fits or the resulting parameter trends. Transmission electron microscopy indicated that the gratings are of uniform depth and that the mark to space ratios are $\approx$ 1:1. The top (p-side) 3 wells of the 8 wells in the active region were etched out in the low gain segments of the truncated-well ridge wave-guide GC-DFB laser (see Fig. 5-1).

Fig. 5-2 and Fig. 5-3 show examples of data and best fits (in a least squared error sense) of the front and back facets of GC-DFB laser 3 at 13 mA. The quality of the fits is very good in that the data and model predictions are difficult to distinguish over a wide range (72 nm) of wavelengths. The small anomaly that appears in the spectra at 1567 nm is the stop band of a much weaker secondary transverse mode. This secondary transverse mode has negligible power output and is not accounted for in the model. Fig. 5-4 and Fig. 5-5 show that a reasonable quality of fit was also obtained at very low currents (4 mA). The reflectances of the facets of laser 3 were found to be (0.2 $\pm$ 0.1) % at the front facet and (31.1 ± 2) % at the cleaved back facet. Facet phases, which were defined with zero degrees at the center of the high index grating segment (seeFig. 5-1), were -33° ± 15° and 175° ± 5° for the front and back facets respectively (one grating period = 360 degrees). The laser was taken to be 250 μm in cavity length and the grating period was taken to be 246.8 nm. The effective index at 13 mA was 3.2049 ± 0.0001. The difference in the real index between etched and not etched segments in the grating was determined to be 0.01676 ± 0.00001, which translates to a real coupling coefficient of κ_r = 211.8 cm^{-1} ± 0.2 cm^{-1}.

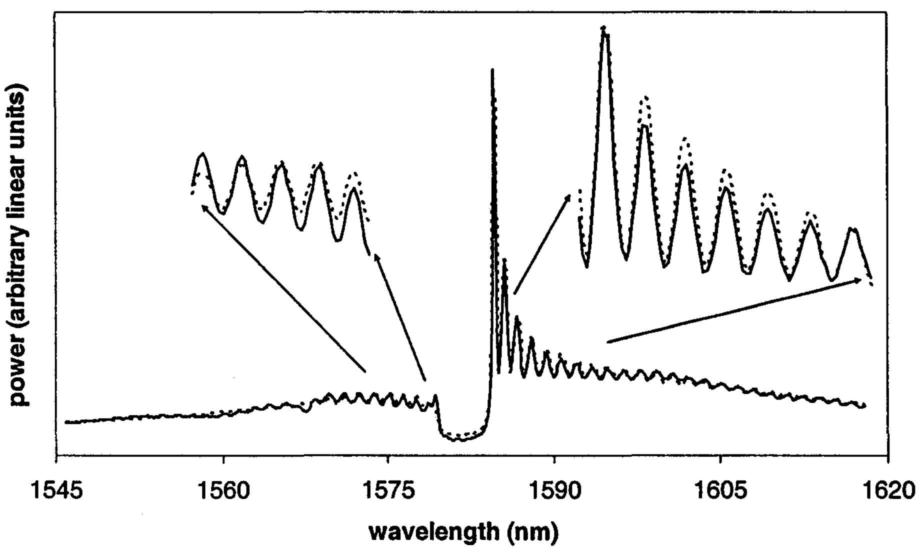

Fig. 5-2 Measured spectra (solid line) and best least squares fit (dashed line) of the front facet emission of laser 3 at 13 mA. Fig. 5-2 was fitted simultaneously using the same parameter set.

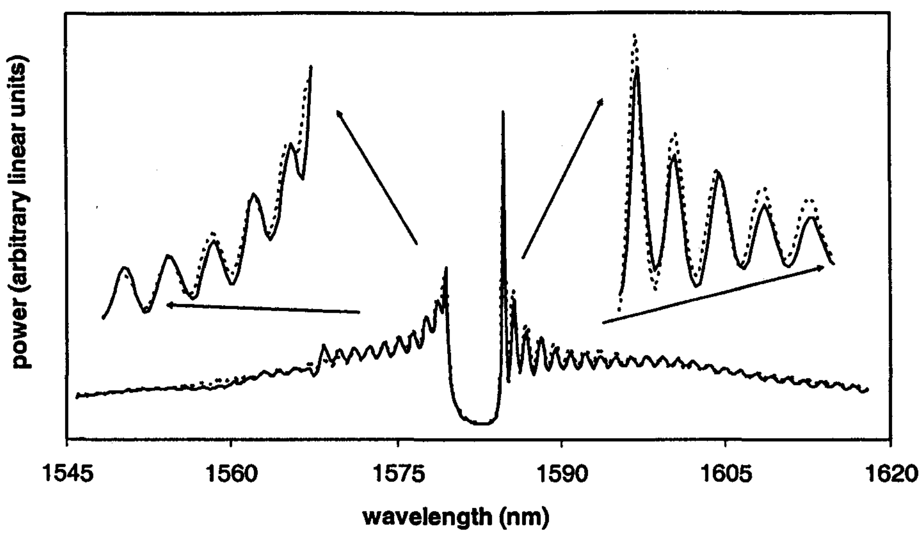

Fig. 5-3 Measured spectra (solid line) and best least squares fit (dashed line) of the back facet emission of laser 3 at 13 mA. Fig. 5-2 was fitted simultaneously using the same parameter set.

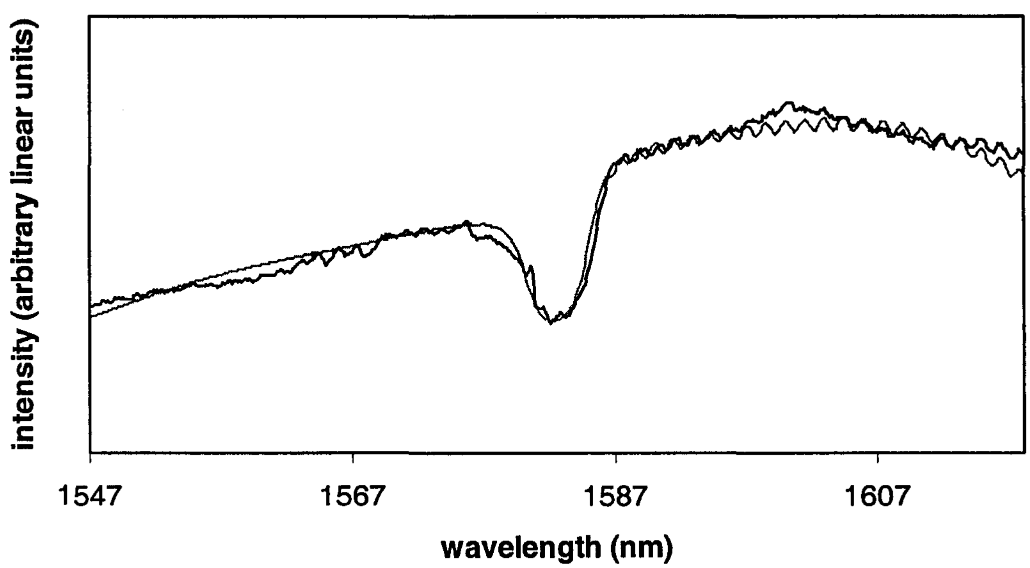

Fig. 5-4 Measured spectra (dark line) and best least squared fit (grey line) of the front facet emission of laser 3 at 4 mA.

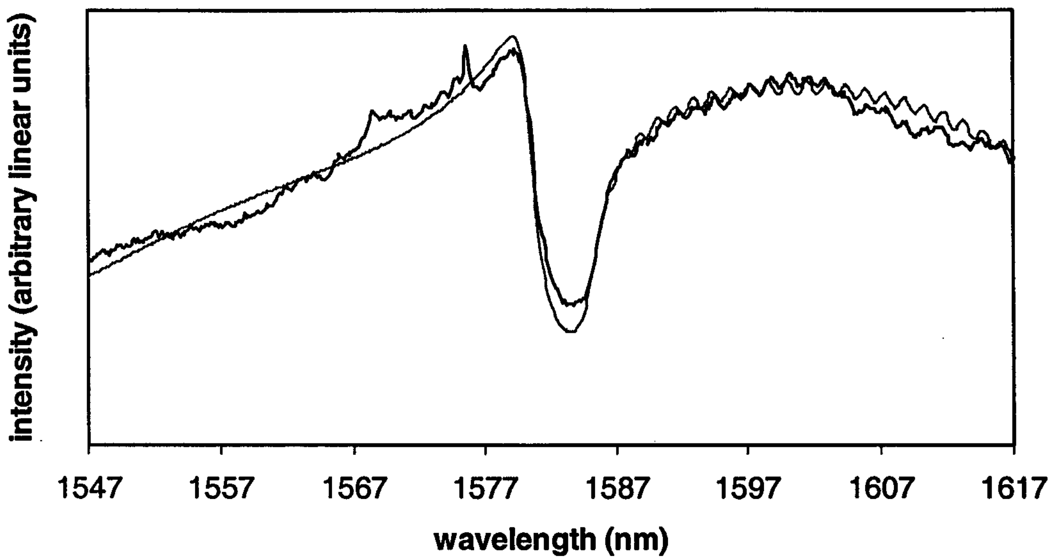

Fig. 5-5 Measured spectra (dark line) and best least squared fit (grey line) of the front facet emission of laser 3 at 4 mA.

5.2.3. Discussion of Results of the Gain Analysis Project

Fig. 5-6 and Fig. 5-7 are plots of the modal gains in the 8 quantum well and 5 quantum well grating segments (i.e., the high gain and low gain segments), for laser 2, and laser 3, respectively. Both plots were obtained by parameter extraction from spectral fits at a series of different injection currents. Examination of Fig. 5-6 and Fig. 5-7 reveals the evolution of the net modal gain in the high and low gain segments of the grating with increasing injection current. At very low bias levels (2 mA) the laser is absorbing (negative gain), with a ratio of modal losses in the high and low gain segments which is approximately equal to the ratio of the number of quantum wells in each segment. As the injection current is increased, the gain in the 8 well segments is seen to increase much more rapidly than the gain in the 5 well segments. The curves cross at approximately 8 mA, while the laser is still well below transparency. In the region above the crossover point, where the curves can be approximated with straight lines, the ratio of the slopes of the plots of modal gain vs. current is 2.2 ± 0.2. The slope ratio after the crossover point in laser 2 was found to be 2.2 ± 0.1. The ratio of gain curve slopes (= 2.2) clearly exceeds the ratio of the number of quantum wells in the two segments (8/5 = 1.6). The high slope ratio (=2.2) indicates that the average rate of increase of carrier density per well is larger for the 8 wells of the high gain segments than for the 5 wells of the low gain segments. For currents approaching the laser threshold, the 5 well segments continue to exhibit net modal loss. The longitudinal profile of the net modal gain at threshold (17.5mA $\pm$ 0.5 mA) is expected, based on the data shown in Fig. 5-6 and Fig. 5-7, to alternate between gain and loss in the high and low index grating segments, respectively. Accordingly, the modal gain contrast in the grating at threshold will significantly exceed the ratio of the number of quantum wells in the high and low index grating segments. The enhanced modal gain contrast is consistent with the exceptionally high single mode yield of these lasers [71].

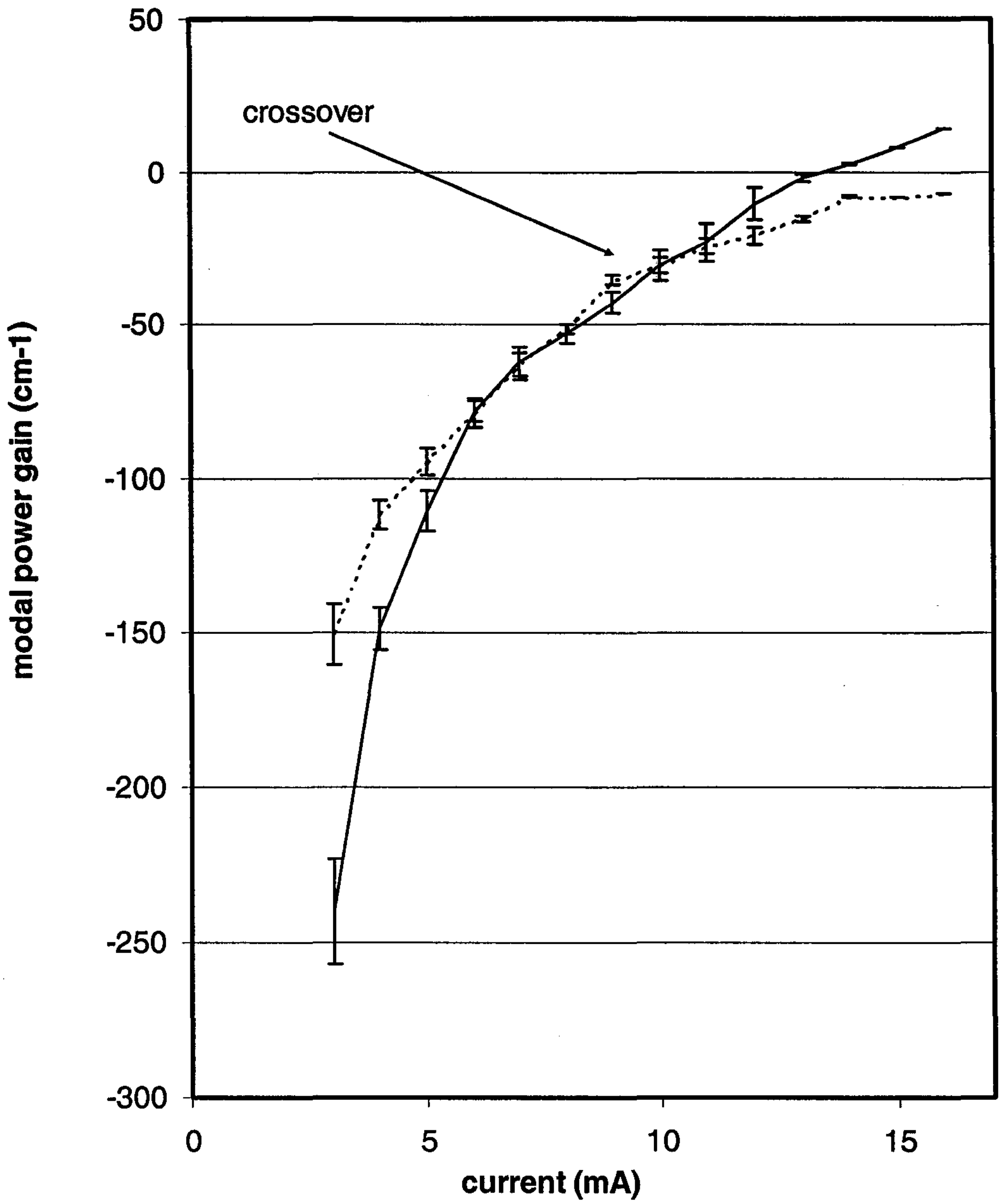

Fig. 5-6 Net modal gain as a function of current in the 8 well segments (solid line) and 5 well segments (dashed line) of the grating for laser 2.

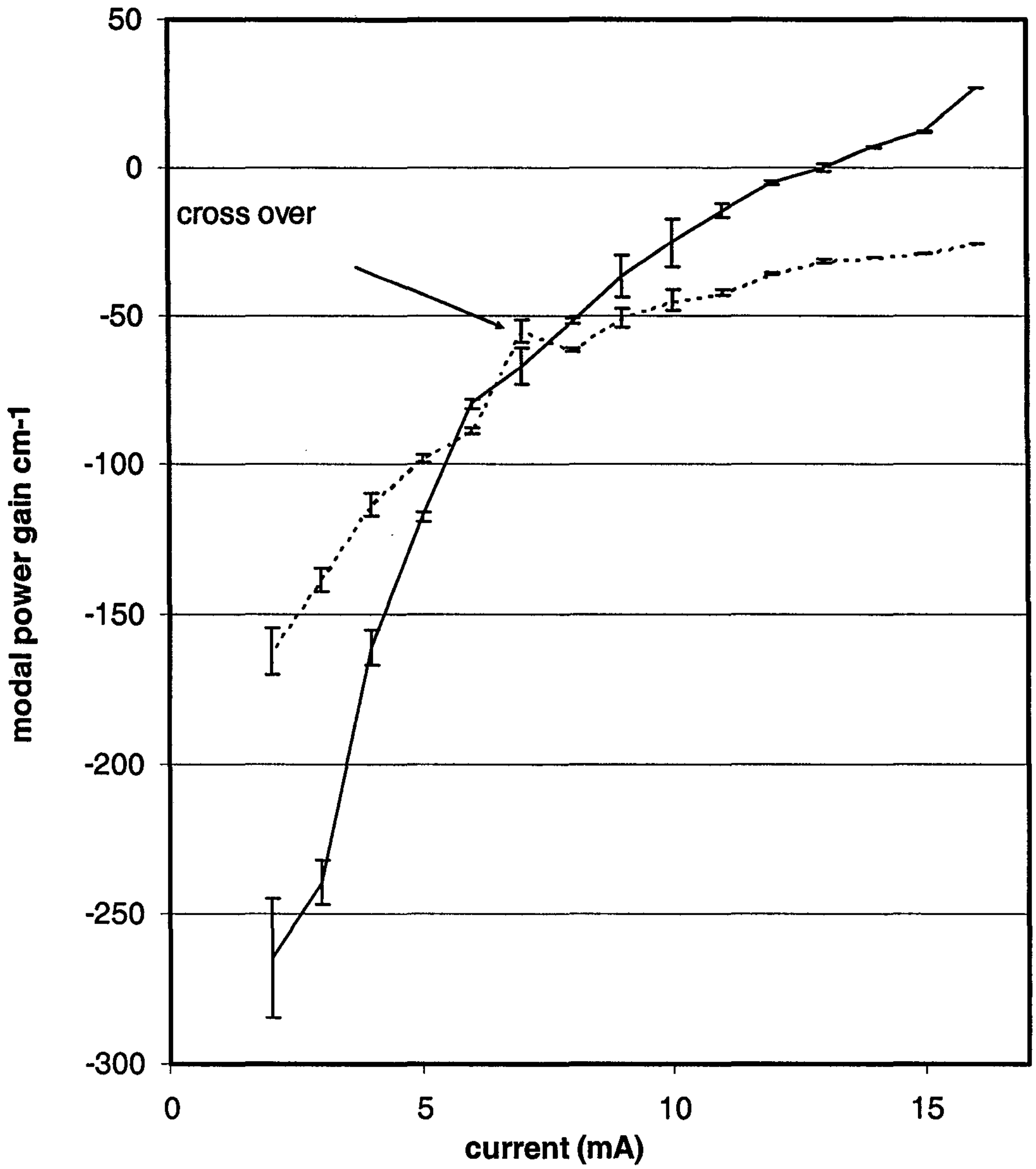

Fig. 5-7 Net modal gain as a function of current in the 8 well segments (solid line) and 5 well segments (dashed line) of the grating for laser 3.

5.2.4. Summary of Gain Analysis Project

Least squares fits of an amplified spontaneous emission transfer-matrix model to measured spectra reveal that the net modal gain contrast at threshold in truncated-well GC-DFB's is significantly enhanced. The simulations were simultaneously fitted to front and back facet spectra over a wide spectral range using a single set of laser parameters, which not only provided a self-consistent verification of the model, but also allowed accurate parameter extraction. The gains of the high and low gain segments of the GC-DFB lasers were extracted from the fits and plotted as a function of current. It was found that the average modal gain per quantum well of the high gain segments increases faster with current than the average modal gain per quantum well of the low gain segments. This is presumably due to the non-uniform injection of carriers into quantum wells of the laser. The top three wells (i.e., the wells nearest the p-side) in the high gain segments are probably highly populated in comparison to the lower 5 wells that are common to both the high and low gain segments [71],[72],[73],[74],[75],[76]. The enhanced dominance of the high gain segments in these truncated-well GC-DFB lasers, likely caused by non-uniform injection of carriers into the quantum wells, is concluded to contribute significantly to the exceptionally high yield of single frequency lasers and to the large SMSRs.

5.3. Analysis of Two Section DFB Lasers

5.3.1. Overview of the Two Section DFB Laser Project

Multi-section truncated quantum well DFB lasers have been developed in order to allow a single DFB device to be used over an exceptionally wide range of wavelengths [77][78]. A multi-section DFB device essentially consists of several DFB lasers seamlessly joined together so that they share the same waveguide. The different DFB gratings have periods that are different enough so that if one of the section is turned on, other sections transmit the light from the powered section with very little feedback. The stop band of each section of the device is designed to appear at approximately the lasing wavelength (long Bragg mode) of the section in front of it. This scheme means that each section experiences a very high effective reflectivity at its rear, and a very low reflectivity at its front. Each section is temperature tuneable over a small range of wavelengths that overlaps the range that the section in front and the section behind. The device as a whole can therefore tune over a range several times wider than a standard DFB device. An interface between two DFB sections in the waveguide is depicted in Fig. 5-8 below.

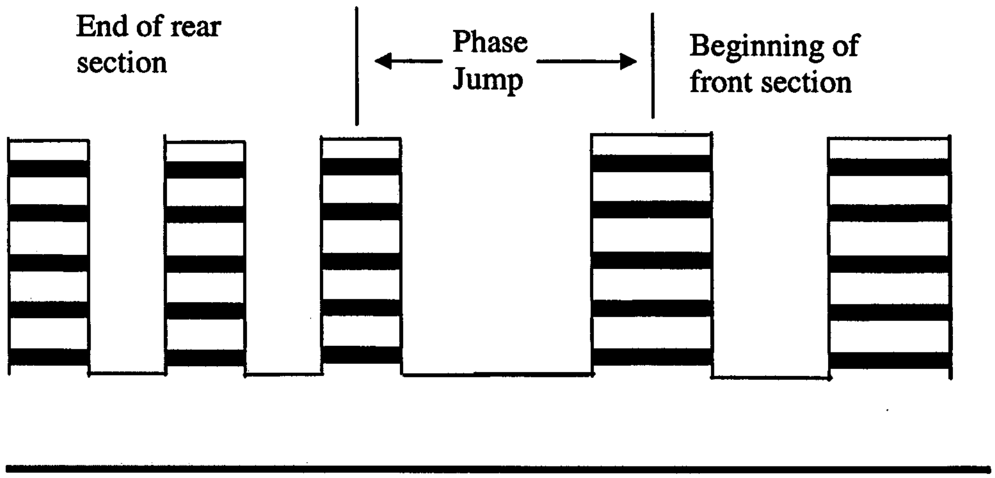

Fig. 5-8 An interface between two sections in a multi section tuneable DFB device.

5.3.2. Extraction of Parameters in the Two Section DFB Project

The probability amplitude model has been expanded for use with two-section tunable truncated-well DFBs. The main purpose of the two-section tunable DFB laser model is parameter extraction by fitting the model to data. The two-section model uses transfer-matrix mathematics to obtain the complex reflectivity of a grounded (i.e., no injection current) distributed feedback section. The complex reflectivity of the dark section is then used as an effective facet reflectivity. In a standard DFB laser model, parameters are needed to describe gain and spontaneous emission curves, group index, effective index, facet phase and reflectivity, and magnitude of index step. In a two section model, the second section needs an additional set of parameters to describe its grating.

An important practical observation is that fitting the model to data can be greatly simplified by defining certain parameters of section 2 with respect to the values in section 1, rather than as entities unto themselves. The period, effective index, grating index step, and group index were all defined in section 2 as an offset from the values of the grating in section 1. The primary reason for this is that when fitting to data, the relative wavelength of the section two stop band with respect to the section one lasing wavelength is very important in determining the shape of the below-threshold spectrum. Thus, the parameters pertaining to stop band shape or mode position should be defined relative to one another.

5.3.3. Discussion of Results from the Two Section DFB Project

Of special interest to multi-section tunable laser designers is the optimal relative phase (phase jump) between the grating sections (see Fig. 5-8). The phase jump describes the distance between the last high index (not etched) segment of the rear section, and the first high index segment of the front section. By fitting the model to data one can show that two-section tunable laser performance is strongly dependent on the choice of phase jump.

Fig. 5-9 and Fig. 5-10 show good fits to the front and back facet spectra of a two-section tunable DFB. In each case the section nearest the facet was activated, whilst the other was left dark (no injection current). Fitting to data from both the front and rear facets of a tunable DFB is important in obtaining more accurate parameter estimates. A useful method for finding a good starting point in the fitting process is to measure a spectrum with both sections turned on simultaneously. The relative positions of the lasing modes allow excellent preliminary estimation of the relative periods of the gratings in the two sections.

The independent fits of Fig. 5-9 and Fig. 5-10 each yielded a phase jump of -80° ± 10°. The relative phase jump of a two section laser is responsible for the saw tooth structure (expanded plots, figs. 1 and 2) of the modes on the right-hand side of the spectrum. It can therefore be determined quite accurately. Fits to two section lasers from various different wafers revealed that the size of the phase jump is critical in the performance of the lasers. The phase jump that was determined to be optimal by this method is proprietary to Nortel Networks, Ottawa Ontario.

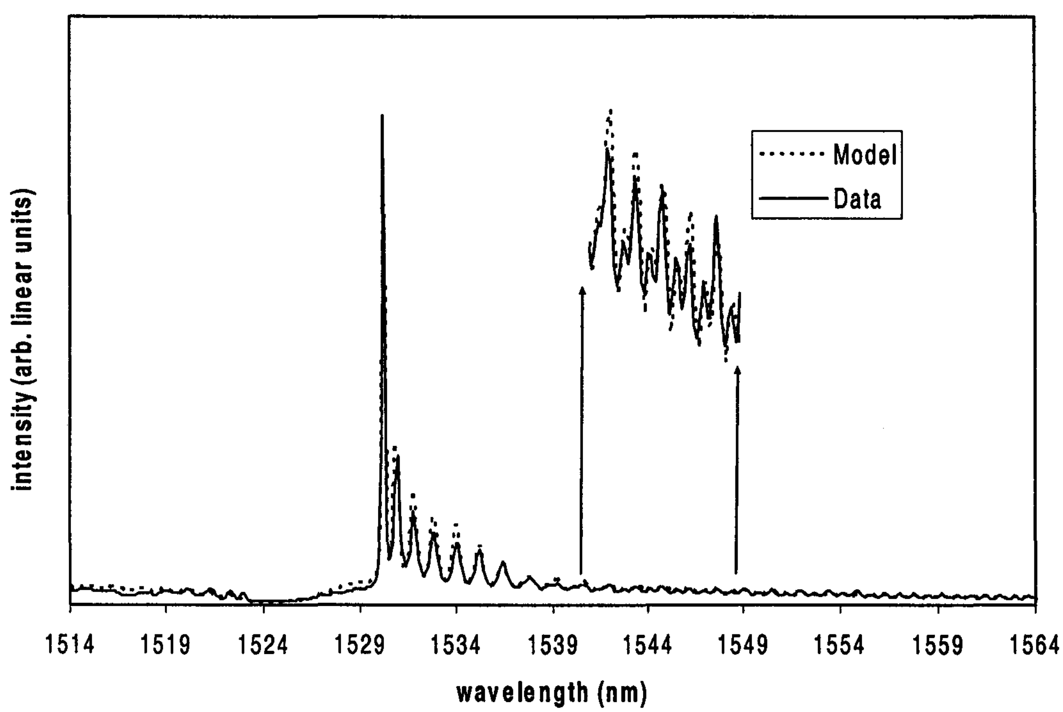

Fig. 5-9 Fitting the model to the front facet of a laser with section 1 activated.

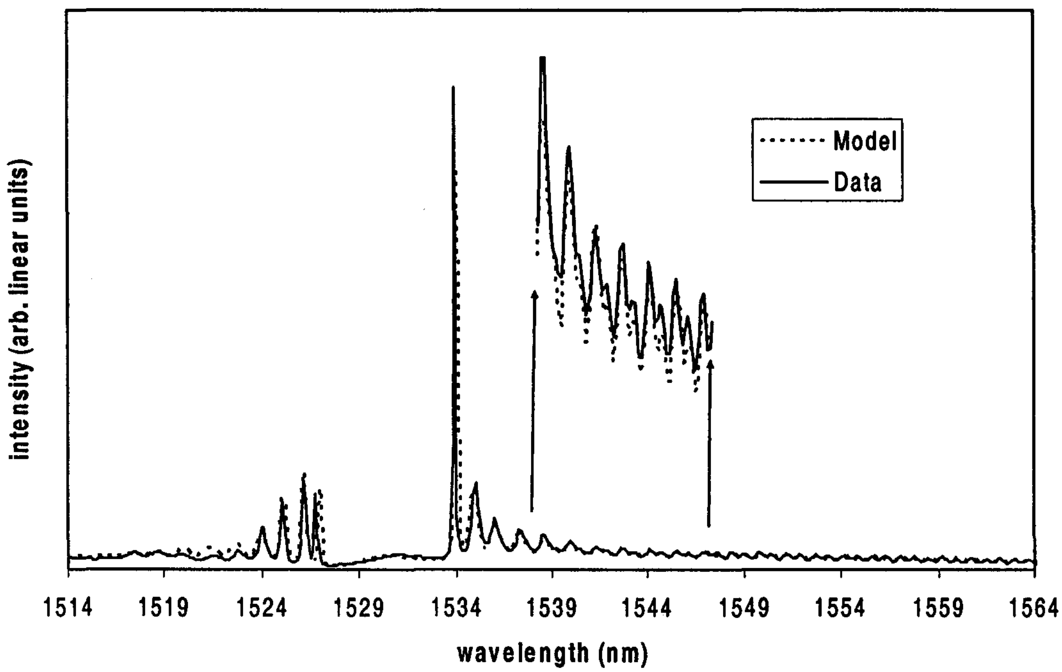

Fig. 5-10 Fitting the model to the rear facet of the laser with section 2 activated.

5.3.4. Summary of the Two Section Tuneable Laser Project

The probability amplitude transfer-matrix model for DFB lasers has been extended for use with two section tuneable DFB lasers. The model was found to fit nicely to spectral data from two section DFBs, and was used to determine the role of phase jump in performance of truncated-well DFB lasers.

5.4. Conclusion

The probability amplitude transfer-matrix model has proved to be an important tool in laser design and research. It has been used to extract experimental evidence of the theoretically predicted enhanced gain coupling in 8:5 ratio truncated quantum well DFB lasers. The probability amplitude transfer-matrix model also proved to be flexible enough to allow easy modification for use with two-section DFBs. The two section DFB model was successfully used to help laser researchers understand the behaviour of multi-section DFB laser devices. I am certain that the probability amplitude transfer-matrix model will continue to prove useful and practical in the field of DFB laser research.

6. LONGITUDINAL INTENSITY DISTRIBUTIONS

6.1. Introduction

The light intensity in a DFB laser varies in magnitude along the length of the cavity [10]. This chapter presents a probability amplitude method for calculating such intensity distributions. Several methods for calculating intensity distributions have been proposed by other research groups in the past, but these usually neglect the standing wave effect, as in [43],[25],[26]. Few are the groups that actually include standing wave effects in their intensity distribution calculations [38],[34],[37]. Furthermore, intensity distributions presented by other research groups usually fail to use spontaneous emission as the source for an existing intensity distribution [25],[43],[38]. One paper that does appear to incorporate properly spontaneous emission into intensity distribution calculations is [26].

Transfer-matrix mathematics for solving transmission and reflection coefficients in a DFB wave guide were discussed in Chapter 2. All variables such as gain, spontaneous emission, and index of refraction are described by the same equations as were presented in Chapter 3. This chapter is therefore only concerned with the mathematics specific to obtaining a longitudinal intensity distribution for a DFB laser. It will be shown that unlike other methods for calculating light intensity distributions in DFB laser cavities, the probability amplitude method considers both standing waves and spontaneous emission in its formulation.

6.2. Derivation of Longitudinal Intensity Distribution

The probability amplitude for a photon at a point of interest due to spontaneous emission from a point source must be calculated to obtain the light intensity at any point in a DFB laser. For the purposes of this discussion, a "point of interest" is defined as any point in the laser cavity for which the intensity is to be calculated. The "source" is defined as a point in the laser from which a spontaneous emission event emanates. Every point in space is potentially a source, but this problem is dealt with by first considering contributions from a single point source, and then integrating throughout the laser. The net probability amplitude at the point of interest will have two components. These are the probability amplitudes for photons originating from sources to the left of the point of interest, and the probability amplitude for photons originating from sources to the right of (and including) the point of interest. An explanation of the use of the term "photon" was given in Chapter 2 of this thesis.

Photons that originated from the right of the point of interest will be travelling to the left when they reach the point of interest. The net probability amplitude at the point of interest, however, must also account for contributions by amplification of these photons during reflections back and forth across the point of interest in Fabry-Perot like resonance. Similar analysis holds for photons that originate from sources that are to the left of the point of interest.

In this chapter, rates of spontaneous emission are considered constant along the length of the cavity (i.e., carrier depletion effects are ignored), and the probability for a photon at a point of interest, or the "intensity" is a normalised value. Inclusion of spontaneous emission rates for absolute photon counting will be discussed in detail in the next chapter.

Summations of probability amplitudes can often be simplified by using the simple formula for a geometric series to simplify infinite series of reflections. This formula is written as

$$\sum_{n=1}^{\infty} ar^{n-1} = \frac{a}{1-r} \qquad |r| < 1.$$

Eq. 6-1

Fig. 6-1 illustrates the case of a spontaneous emission event on the right-hand side of the point of interest. The periodically changing index of refraction is depicted, and the complex reflection and transmission coefficients $r^r{}_l$, $r^r{}_r$, $t^r{}_l$, $t^r{}_r$, are labelled. The reflection and transmission coefficients are labelled with the superscript "r" to identify them as a being associated with a source to the right of the point of interest, and a subscript "r" or "l" to designate the left or right-going probability amplitude respectively. In Fig. 6-1 the terms $t^r{}_l$ and $r^r{}_l$ represent reflection and transmission from/through segments as far to the left as the point of interest. The terms $t^r{}_r$ and $r^r{}_r$ represent reflection or transmission through segments up to and including the facet at the right-hand side of the cavity. The length of the source grating segment is l^r and the position of the source within the grating is x^r. Similarly, the length of the segment containing the point of interest is l, and the position of the point of interest in the segment is x.

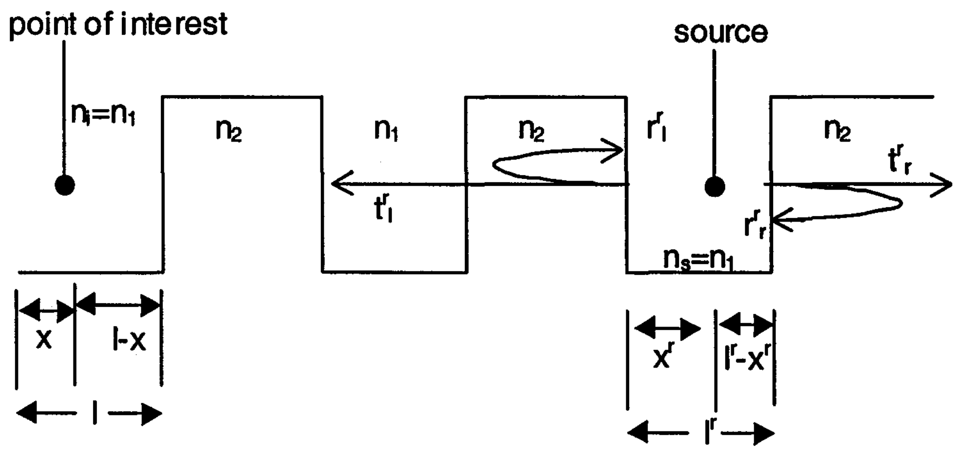

Fig. 6-1 A source to the right of the point of interest in a DFB grating. The index of refraction at the point of interest is labelled n_i and the index at the source is labelled n_s.

Examining the above diagram, one can immediately see that the sum of the probability amplitudes of the paths from the source to the point of interest can be written as

$$\left\langle P_i \middle| right \middle| s_r \right\rangle = \left(e^{-jKn_s x^r} t_l^r \begin{pmatrix} 1 + r_l^r r_r^r e^{-j2Kn_s l^r} \\ + (r_l^r r_r^r e^{-j2Kn_s l^r})^2 \\ + (r_l^r r_r^r e^{-j2Kn_s l^r})^3 \ldots \end{pmatrix} + e^{-jKn_s(2l^r - x^r)} r_r^r t_l^r \begin{pmatrix} 1 + r_l^r r_r^r e^{-j2Kn_s l^r} + \\ (r_l^r r_r^r e^{-j2Kn_s l^r})^2 + \\ (r_l^r r_r^r e^{-j2Kn_s l^r})^3 \ldots \end{pmatrix} \right) e^{-jKn_i(l-x)}$$

Eq. 6-2

which can be simplified using Eq. 6-1 and written as

$$\left\langle P_i \middle| right \middle| s_r \right\rangle = \left(\frac{e^{-jKn_s x^r} t_l^r}{1 - r_l^r r_r^r e^{-j2Kn_s l^r}} + \frac{e^{-jKn_s(2l^r - x^r)} r_r^r t_l^r}{1 - r_l^r r_r^r e^{-j2Kn_s l^r}} \right) e^{-jKn_i(l-x)}$$

Eq. 6-3

where P_i refers to the point of interest, s_r refers to the source that is to the right of the point of interest, and the operator "*right*" is taken to mean all paths that only include the region to the right of the point of interest. This convention is in agreement with the <finish|through|start> notation that is used in [79]. Technically, a factor of ½ should also be included to account for the fact that the probability amplitude for the photon to travel in either one of the two possible initial directions is ½. For simplicity, this is ignored but will be included when spontaneous emission rates and photon counting is introduced in the next chapter.

The total probability amplitude for a photon at the point of interest after emission from the source will be equal to the sum over all the possible routes to the point of interest, including contributions from multiple passes. All routes must begin with $<P_i|right|s_r>$, so $<P_i|s_r>$ will be obtained by multiplying $<P_i|right|s_r><P_i|P_i|P_{il}>$. The second term in the equation represents the sum of the probability amplitudes for routes to $<P_i|$ starting out from $|P_i>$ in the left-hand direction and passing through $|P_i|$ on the way to P_i. This probability amplitude can be calculated with reference to Fig. 6-2.

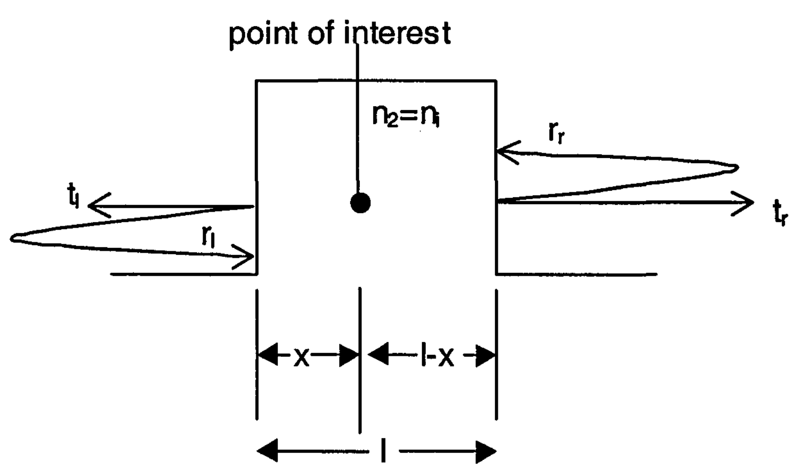

Fig. 6-2 From the point of interest, the probability amplitude can reflect back and forth within the laser in an infinite geometric series.

Given an initial left-going photon at the point of interest, the sum of all the probability amplitudes of the multiple reflection paths is:

$$\left\langle P_i \middle| P_i \middle| P_i^{left} \right\rangle = 1 + r_l e^{-j2Kn_i x} + r_l r_r e^{-j2Kn_i x} e^{-j2Kn_i (l-x)}$$
$$+ r_l r_r r_l e^{-j2Kn_i x} e^{-j2Kn_i (l-x)} e^{-j2Kn_i x} +$$
$$r_l r_r r_l r_r e^{-j2Kn_i x} e^{-j2Kn_i (l-x)} e^{-j2Kn_i x} e^{-j2Kn_i (l-x)} \ldots.$$

Eq. 6-4

which can be broken into the two terms

$$\left\langle P_i \middle| P_i \middle| P_i^{left} \right\rangle = 1 + r_l r_r e^{-j2Kn_i x} e^{-j2Kn_i (l-x)} + \left(r_l r_r e^{-j2Kn_i x} e^{-j2Kn_i (l-x)}\right)^2 \ldots..$$
$$+ r_l e^{-j2Kn_i x}\left(1 + \left(r_l r_r e^{-j2Kn_i x} e^{-j2Kn_i (l-x)}\right) + \left(r_l r_r e^{-j2Kn_i x} e^{-j2Kn_i (l-x)}\right)^2 \ldots..\right)$$

Eq. 6-5

which are further simplified by using Eq. 6-1 such that

$$\left\langle P_i \middle| P_i \middle| P_i^{left} \right\rangle = \frac{1 + r_l e^{-j2Kn_i x}}{1 - r_l r_r e^{-j2Kn_i (l-x)} e^{-j2Kn_i x}} .$$

Eq. 6-6

Thus, given a source to the right of the point of interest, the total probability amplitude for a photon at Pi is

$$\langle P_i | s_r \rangle = \left(\frac{e^{-jKn_s x^r} t_l^r}{1 - r_l^r r_r^r e^{-j2Kn_s l^r}} + \frac{e^{-jKn_s (2l^r - x^r)} r_r^r t_l^r}{1 - r_l^r r_r^r e^{-j2Kn_s l^r}} \right) e^{-jKn_i (l-x)}$$

$$\times \frac{1 + r_l e^{-j2Kn_i x}}{1 - r_l r_r e^{-j2Kn_i (l-x)} e^{-j2Kn_i x}}$$

Eq. 6-7

The above equation is valid only for sources of spontaneous emission that originate in separate segments that lie to the right of the segment containing the point of interest. A slightly different equation will be derived later for sources that are to the right of the point of interest but in the same segment.

The absolute value squared of the equation above can be integrated with respect to x^r, to obtain the intensity at P_i due to all spontaneous emission in a given segment that is to the right of the point of interest. It is important to note that by taking the absolute value of Eq. 6-7, the self interference terms that were discussed in chapter 2 of this thesis are correctly included. The absolute value squared of the term in brackets in Eq. 6-7 can be written as

$$
\begin{aligned}
&= \left| \frac{t_l^r}{1 - r_l^r r_r^r e^{-j2Kn_s l^r}} \right|^2 \left(e^{-jKn_{sR}x^r} e^{Kg_s x^r} + r_r^r e^{-j2Kn_{sR}l^r} e^{2Kg_s l^r} e^{jKn_{sR}x^r} e^{-Kg_s x^r} \right) \\
&\times \left(e^{jKn_{sR}x^r} e^{Kg_s x^r} + r_r^{r*} e^{j2Kn_{sR}l^r} e^{2Kg_s l^r} e^{-jKn_{sR}x^r} e^{-Kg_s x^r} \right) \\
&= \left| \frac{t_l^r}{1 - r_l^r r_r^r e^{-j2Kn_s l^r}} \right|^2 \left(\begin{array}{l} e^{2Kg_s x^r} + r_r^r r_r^{r*} e^{4Kg_s l^r} e^{-2Kg_s x^r} + \\ r_r^{r*} e^{j2Kn_{sR}l^r} e^{2Kg_s l^r} e^{-j2Kn_{sR}x^r} + r_r^r e^{-j2Kn_{sR}l^r} e^{2Kg_s l^r} e^{j2Kn_{sR}x^r} \end{array} \right)
\end{aligned}
$$

Eq. 6-8

where the term g_s is the imaginary part of the source index n_s, and the term n_{sR} is the real part of the source index n_s. Integrating the term in rounded brackets in Eq. 6-8 with respect to x^r yields

$$
\begin{aligned}
&\int_0^l \left(\begin{array}{l} e^{2Kg_s x^r} + r_r^r r_r^{r*} e^{4Kg_s l^r} e^{-2Kg_s x^r} + \\ r_r^{r*} e^{j2Kn_{sR}l^r} e^{2Kg_s l^r} e^{-j2Kn_{sR}x^r} + r_r^r e^{-j2Kn_{sR}l^r} e^{2Kg_s l^r} e^{j2Kn_{sR}x^r} \end{array} \right) dx^r \\
&= \left(\frac{1}{2Kg_s} e^{2Kg_s x^r} + \frac{r_r^r r_r^{r*} e^{4Kg_s l^r}}{-2Kg_s} e^{-2Kg_s x^r} + \frac{r_r^{r*} e^{j2Kn_{sR}l^r} e^{2Kg_s l^r}}{-j2Kn_{sR}} e^{-j2Kn_{sR}x^r} \right. \\
&\left. + \frac{r_r^r e^{-j2Kn_{sR}l^r} e^{2Kg_s l^r}}{j2Kn_{sR}} e^{j2Kn_{sR}x^r} \right) \Bigg|_0^l
\end{aligned}
$$

Eq. 6-9

Evaluating the integral over the limits produces

$$= \left(\begin{array}{l} \dfrac{1}{2Kg_s}\left(e^{2Kg_s l^r}-1\right)+\dfrac{r_r^r r_r^{r*} e^{4Kg_s l^r}}{-2Kg_s}\left(e^{-2Kg_s l^r}-1\right)+ \\ \dfrac{r_r^{r*} e^{j2Kn_{sR}l^r} e^{2Kg_s l^r}}{-j2Kn_{sR}}\left(e^{-j2Kn_{sR}l^r}-1\right)+\dfrac{r_r^r e^{-j2Kn_{sR}l^r} e^{2Kg_s l^r}}{j2Kn_{sR}}\left(e^{j2Kn_{sR}l^r}-1\right) \end{array} \right).$$

Eq. 6-10

And thus, the equation for the total intensity at the point of interest (positioned at x), due to spontaneous emission emitted from a segment to the right of the point of interest, is written as

$$= \left(\begin{array}{l} \dfrac{1}{2Kg_s}\left(e^{2Kg_s l^r}-1\right)+\dfrac{r_r^r r_r^{r*} e^{4Kg_s l^r}}{-2Kg_s}\left(e^{-2Kg_s l^r}-1\right) \\ +\dfrac{r_r^{r*} e^{j2Kn_{sR}l^r} e^{2Kg_s l^r}}{-j2Kn_{sR}}\left(e^{-j2Kn_{sR}l^r}-1\right)+\dfrac{r_r^r e^{-j2Kn_{sR}l^r} e^{2Kg_s l^r}}{j2Kn_{sR}}\left(e^{j2Kn_{sR}l^r}-1\right) \end{array} \right).$$
$$\times \left| \frac{t_l^r}{1-r_l^r r_r^r e^{-j2Kn_s l^r}} \right|^2 \left| e^{-jKn_i(l-x)} \frac{1+r_l e^{-j2Kn_i x}}{1-r_l r_r e^{-j2Kn_i(l-x)} e^{-j2Kn_i x}} \right|^2$$

Eq. 6-11

Very similar equations can be derived for the case when there is a spontaneous emission source to the left of the point of interest, as in Fig. 6-3 .

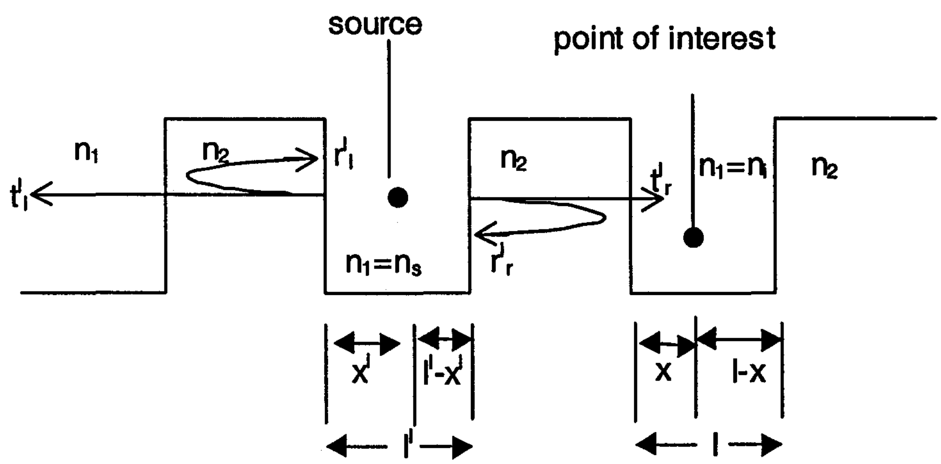

Fig. 6-3 A spontaneous emission source point in a grating segment that is to the left of the point of interest.

The probability amplitude for a photon reaching the point of interest, after having started at a source that is to the left of the point of interest can be written as

$$\langle P_i | left | s_l \rangle = \left(e^{-jKn_s(l^l-x^l)} t_r^l \begin{pmatrix} 1 + r_r^l r_l^l e^{-j2Kn_s l^l} \\ + (r_r^l r_l^l e^{-j2Kn_s l^l})^2 \\ + (r_r^l r_l^l e^{-j2Kn_s l^l})^3 \ldots \end{pmatrix} + e^{-jKn_s(l^l+x^l)} r_l^l t_r^l \begin{pmatrix} 1 + r_r^l r_l^l e^{-j2Kn_s l^l} \\ + (r_r^l r_l^l e^{-j2Kn_s l^l})^2 + \\ (r_r^l r_l^l e^{-j2Kn_s l^l})^3 \ldots \end{pmatrix} \right) e^{-jKn_i x}$$

Eq. 6-12

which can be simplified using Eq. 6-1 and written as

$$\left\langle P_i \middle| left \middle| s_l \right\rangle = \left(\frac{e^{-jKn_s(l^l - x^l)} t_r^l}{1 - r_r^l r_l^l e^{-j2Kn_s l^l}} + \frac{e^{-jKn_s(l^l + x^l)} r_l^l t_r^l}{1 - r_r^l r_l^l e^{-j2Kn_s l^l}} \right) e^{-jKn_i x} .$$

Eq. 6-13

In order to calculate the total probability for a photon to be at the point of interest after emission from the source, the probability amplitudes for all routes to P_i that involve passing through the point P_i one or more times must be summed. All of these routes started off with $<P_i|left|s_l>$ and so can be written $<P_i|s_l>=<P_i|left|s_l><P_i|P_i|P_i^{right}>$. The second term in the equation represents the sum of the probability amplitudes for routes to P_i starting out from P_i in the right-hand direction, and passing through P_i on the way to P_i. The coefficients used in calculating this probability amplitude were illustrated in Fig. 6-2. Given an initially right travelling photon at the point of interest, the sum of all the probability amplitudes of the multiple reflection paths is

$$\left\langle P_i \middle| P_i \middle| P_i^{right} \right\rangle = 1 + r_r e^{-j2Kn_i(l-x)} + r_r r_l e^{-j2Kn_i(l-x)} e^{-j2Kn_i x}$$
$$+ r_r r_l r_r e^{-j2Kn_i(l-x)} e^{-j2Kn_i x} e^{-j2Kn_i(l-x)}$$
$$+ r_r r_l r_r r_l e^{-j2Kn_i(l-x)} e^{-j2Kn_i x} e^{-j2Kn_i(l-x)} e^{-j2Kn_i x} .....$$

Eq. 6-14

which is broken into two parts

$$\left\langle P_i \middle| P_i \middle| P_i^{right} \right\rangle = 1 + r_r r_l e^{-j2Kn_i(l-x)} e^{-j2Kn_i x} + \left(r_r r_l e^{-j2Kn_i(l-x)} e^{-j2Kn_i x}\right)^2 \ldots\ldots$$
$$+ r_r e^{-j2Kn_i(l-x)} \left(1 + r_r r_l e^{-j2Kn_i(l-x)} e^{-j2Kn_i x} + \left(r_r r_l e^{-j2Kn_i(l-x)} e^{-j2Kn_i x}\right)^2 \ldots\ldots\right)$$

Eq. 6-15

and rewritten using Eq. 6-1 as

$$\left\langle P_i \middle| P_i \middle| P_i^{right} \right\rangle = \frac{1 + r_r e^{-j2Kn_i(l-x)}}{1 - r_r r_l e^{-j2Kn_i(l-x)} e^{-j2Kn_i x}} .$$

Eq. 6-16

The total probability amplitude $\langle P_i|s_l\rangle$ is thus

$$\left\langle P_i \middle| s_l \right\rangle = \left(\frac{e^{-jKn_s(l^l - x^l)} t_r^l}{1 - r_r^l r_l^l e^{-j2Kn_s l^l}} + \frac{e^{-jKn_s(l^l + x^l)} r_l^l t_r^l}{1 - r_r^l r_l^l e^{-j2Kn_s l^l}} \right) e^{-jKn_i x}$$
$$\times \frac{1 + r_r e^{-j2Kn_i(l-x)}}{1 - r_r r_l e^{-j2Kn_i(l-x)} e^{-j2Kn_i x}} .$$

Eq. 6-17

The square of the absolute value of the above equation can be integrated with respect to x^l in order to obtain the probability of a photon at the point of interest due to an entire segment that is to the left of the point of interest.

The square of the absolute value of the bracketed term in Eq. 6-17 can be written as

$$=\left|\frac{e^{-jKn_s l^l}t_r^l}{1-r_r^l r_l^l e^{-j2Kn_s l^l}}\right|^2\left(e^{jKn_{sR}x^l}e^{-Kg_s x^l}+r_l^l e^{-jKn_{sR}x^l}e^{Kg_{sR}x^l}\right)$$
$$\times\left(e^{-jKn_{sR}x^l}e^{-Kg_s x^l}+r_l^{l*}e^{jKn_{sR}x^l}e^{Kg_{sR}x^l}\right)$$
$$=\left|\frac{e^{-jKn_s l^l}t_r^l}{1-r_r^l r_l^l e^{-j2Kn_s l^l}}\right|^2\left(e^{-2Kg_s x^l}+r_l^l r_l^{l*}e^{2Kg_{sR}x^l}+r_l^{l*}e^{j2Kn_{sR}x^l}+r_l^l e^{-j2Kn_{sR}x^l}\right)$$

Eq. 6-18

Integrating with respect to x^l yields for the term in the rounded brackets in Eq. 6-18

$$\int_0^l\left(e^{-2Kg_s x^l}+r_l^l r_l^{l*}e^{2Kg_s x^l}+r_l^{l*}e^{j2Kn_{sR}x^l}+r_l^l e^{-j2Kn_{sR}x^l}\right)dx^l$$
$$=\frac{\left(e^{-2Kg_s l^l}-1\right)}{-2Kg_s}+\frac{r_l^l r_l^{l*}\left(e^{2Kg_s l^l}-1\right)}{2Kg_s}+\frac{r_l^{l*}\left(e^{j2Kn_{sR}l^l}-1\right)}{j2Kn_{sR}}+\frac{r_l^l\left(e^{-j2Kn_{sR}l^l}-1\right)}{-j2Kn_{sR}}.$$

Eq. 6-19

Thus the total intensity at the point of interest (located at x), due to all spontaneous emission originating in a segment to the left of the point of interest, can be written as

$$=\left(\frac{\left(e^{-2Kg_s l^l}-1\right)}{-2Kg_s}+\frac{r_l^l r_l^{l*}\left(e^{2Kg_s l^l}-1\right)}{2Kg_s}+\frac{r_l^{l*}\left(e^{j2Kn_{sR}l^l}-1\right)}{j2Kn_{sR}}+\frac{r_l^l\left(e^{-j2Kn_{sR}l^l}-1\right)}{-j2Kn_{sR}}\right)$$
$$\left|\frac{e^{-jKn_s l^l}t_r^l}{1-r_r^l r_l^l e^{-j2Kn_s l^l}}\right|^2\left|e^{-jKn_i x}\frac{1+r_r e^{-j2Kn_i(l-x)}}{1-r_r r_l e^{-j2Kn_i(l-x)}e^{-j2Kn_i x}}\right|^2.$$

Eq. 6-20

It is important to understand that the above equations only apply to situations in which the source and the point of interest are in separate segments. Derivations for situations in which the source is in the same segment as the point of interest will now be presented, starting with the case in which the source is to the left of the point of interest P_i, as in Fig. 6-4.

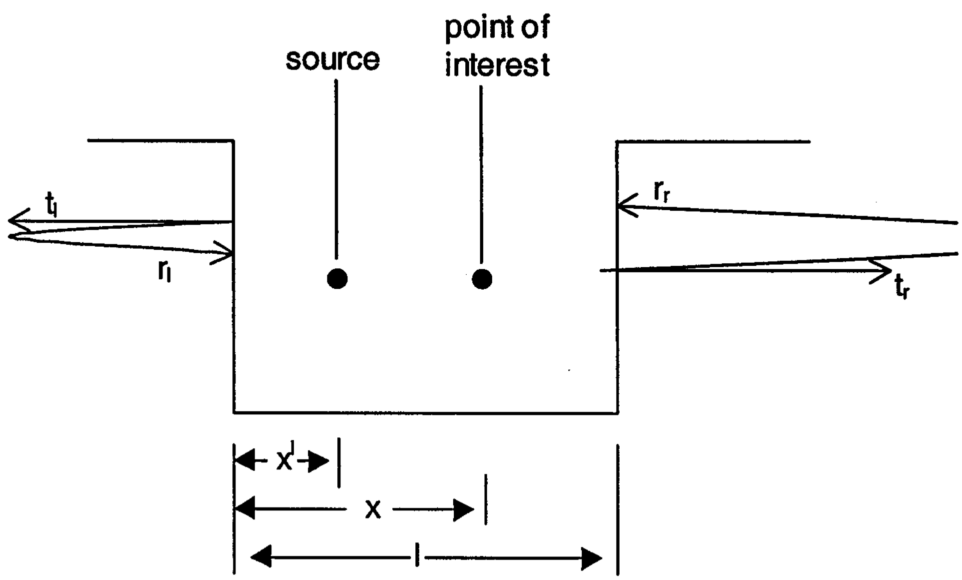

Fig. 6-4 A point source is situated to the left of the point of interest. Both points share a common segment.

The probability amplitude for a photon at the point of interest in the situation depicted in Fig. 6-4 can be written as

$$= \left(e^{-jKn_s(x-x^l)} + e^{-jKn_s x^l} r_l e^{-jKn_s x}\right) \frac{1 + r_r e^{-j2Kn_i(l-x)}}{1 - r_r r_l e^{-j2Kn_i(l-x)} e^{-j2Kn_i x}}$$

Eq. 6-21

The probability for a photon is then

$$\begin{aligned} &= \left(e^{-jKn_{sR}x} e^{jKn_{sR}x^l} e^{Kg_s x} e^{-Kg_s x^l} + e^{-jKn_{sR}x^l} e^{Kg_s x^l} r_l e^{-jKn_{sR}x} e^{Kg_s x}\right) \\ &\times \left(e^{jKn_{sR}x} e^{-jKn_{sR}x^l} e^{Kg_s x} e^{-Kg_s x^l} + e^{jKn_{sR}x^l} e^{Kg_s x^l} r_l^* e^{jKn_{sR}x} e^{Kg_s x}\right) \\ &\times \left| \frac{1 + r_r e^{-j2Kn_i(l-x)}}{1 - r_r r_l e^{-j2Kn_i(l-x)} e^{-j2Kn_i x}} \right|^2 \end{aligned}$$

Eq. 6-22

or, integrating x^l everywhere to the left of the point of interest,

$$\begin{aligned} &= \int_0^x \left(\begin{array}{l} e^{2Kg_s x} e^{-2Kg_s x^l} + r_l r_l^* e^{2Kg_s x^l} e^{2Kg_s x} \\ + e^{-j2Kn_{sR}x^l} r_l e^{2Kg_s x} + e^{j2Kn_{sR}x^l} r_l^* e^{2Kg_s x} \end{array} \right) dx^l \\ &\times \left| \frac{1 + r_r e^{-j2Kn_i(l-x)}}{1 - r_r r_l e^{-j2Kn_i(l-x)} e^{-j2Kn_i x}} \right|^2 \end{aligned}$$

Eq. 6-23

which equates to

$$
= \begin{pmatrix} \dfrac{\left(e^{-2Kg_s x}-1\right)}{-2Kg_s} + \dfrac{r_l r_l^*\left(e^{2Kg_s x}-1\right)}{2Kg_s} \\ + \dfrac{r_l\left(e^{-j2Kn_{sR}x}-1\right)}{-j2Kn_{sR}} + \dfrac{r_l^*\left(e^{j2Kn_{sR}x}-1\right)}{j2Kn_{sR}} \end{pmatrix} e^{2Kg_s x} \left| \frac{1+r_r e^{-j2Kn_l(l-x)}}{1-r_r r_l e^{-j2Kn_l(l-x)} e^{-j2Kn_l x}} \right|^2
$$

Eq. 6-24

The case in which the source is to the right of the point of interest, is illustrated in Fig. 6-5.

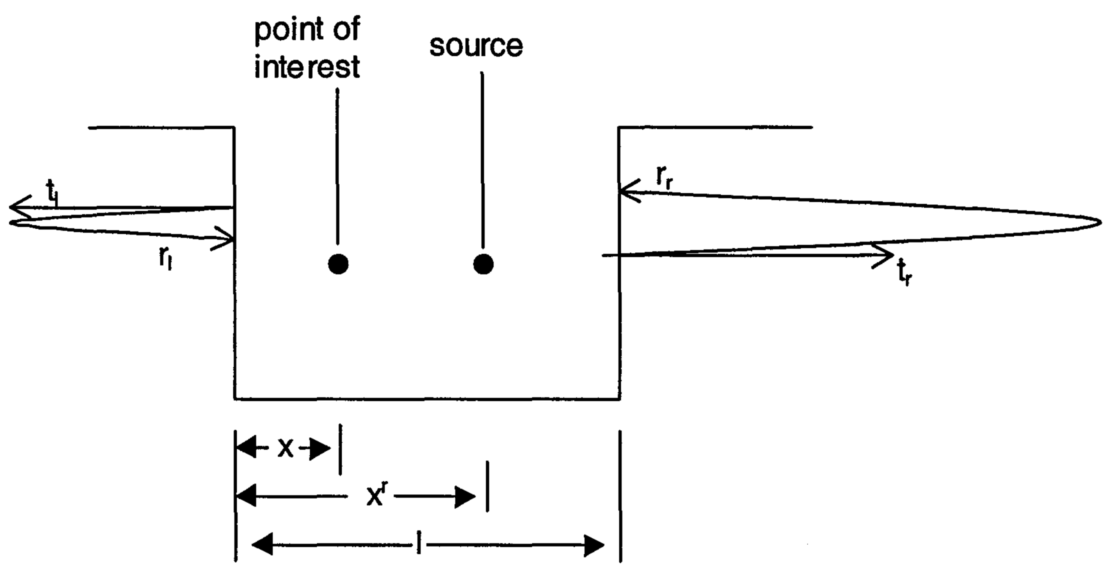

Fig. 6-5 A point source is situated to the right of the point of interest. Both points share a common segment.

The probability amplitude for a photon at the point of interest in Fig. 6-5 can be written as

$$= \left(e^{-jKn_s(x^r-x)} + e^{-jKn_s(2l-x^r-x)} r_r\right) \frac{1 + r_l e^{-j2Kn_i x}}{1 - r_l r_r e^{-j2Kn_i(l-x)} e^{-j2Kn_i x}}$$

Eq. 6-25

so that the probability for a photon that is emitted from the source to be at the point of interest is

$$= \int_x^l \left(e^{-jKn_{sR}(x^r-x)} e^{Kg_s(x^r-x)} + e^{-jKn_{sR}(2l-x^r-x)} e^{Kg_s(2l-x^r-x)} r_r\right)$$
$$\times \left(e^{jKn_{sR}(x^r-x)} e^{Kg_s(x^r-x)} + e^{jKn_{sR}(2l-x^r-x)} e^{Kg_s(2l-x^r-x)} r_r^*\right)$$
$$\left| \frac{1 + r_l e^{-j2Kn_i x}}{1 - r_l r_r e^{-j2Kn_i(l-x)} e^{-j2Kn_i x}} \right|^2 dx^r$$

Eq. 6-26

which simplifies to

$$= \int_x^l \left(\begin{array}{l} e^{2Kg_s x^r} e^{-2Kg_s x} + e^{2Kg_s(2l-x^r-x)} r_r r_r^* + \\ e^{Kg_s(2l-2x)} e^{jKn_{sR}(2l-2x^r)} r_r^* + e^{-jKn_{sR}(2l-2x^r)} e^{Kg_s(2l-2x)} r_r \end{array} \right)$$
$$\times \left| \frac{1 + r_l e^{-j2Kn_i x}}{1 - r_l r_r e^{-j2Kn_i(l-x)} e^{-j2Kn_i x}} \right|^2 dx^r$$

Eq. 6-27

$$= \int_x^l \begin{pmatrix} e^{2Kg_s x^r} + e^{2Kg_s 2l} e^{-2Kg_s x^r} r_r r_r^* + \\ e^{Kg_s 2l} e^{jKn_{sR} 2l} e^{-jKn_{sR} 2x^r} r_r^* + e^{-jKn_{sR} 2l} e^{jKn_{sR} 2x^r} e^{Kg_s 2l} r_r \end{pmatrix}$$

$$\times e^{-2Kg_s x} \left| \frac{1 + r_l e^{-j2Kn_i x}}{1 - r_l r_r e^{-j2Kn_i (l-x)} e^{-j2Kn_i x}} \right|^2 dx^r$$

Eq. 6-28

Performing the integration yields

$$= \begin{pmatrix} \dfrac{\left(e^{2Kg_s l} - e^{2Kg_s x}\right)}{2Kg_s} + r_r r_r^* e^{2Kg_s 2l} \dfrac{\left(e^{-2Kg_s l} - e^{-2Kg_s x}\right)}{-2Kg_s} \\ + r_r^* e^{Kg_s 2l} e^{jKn_{sR} 2l} \dfrac{\left(e^{-j2Kn_{sR} l} - e^{-j2Kn_{sR} x}\right)}{-j2Kn_{sR}} \\ + r_r e^{-jKn_{sR} 2l} e^{Kg_s 2l} \dfrac{\left(e^{j2Kn_{sR} l} - e^{j2Kn_{sR} x}\right)}{j2Kn_{sR}} \end{pmatrix}$$

$$\times e^{-2Kg_s x} \left| \frac{1 + r_l e^{-j2Kn_i x}}{1 - r_l r_r e^{-j2Kn_i (l-x)} e^{-j2Kn_i x}} \right|^2$$

Eq. 6-29

The formulas given in Eq. 6-11, Eq. 6-20, Eq. 6-24, and Eq. 6-29 allow calculation of the probability for a photon to be at any point of interest x, due to spontaneous emission everywhere in the laser cavity. Note that Eq. 6-11 and Eq. 6-20 must be repeatedly summed to account for every segment to the right of the point of interest, and every segment to the left of the point of interest, respectively. Furthermore, the rates of spontaneous emission have not been included. Thus, the above equations yield relative intensities, but the scale is in arbitrary units. With proper weighting of the equations with respect to spontaneous emission rates, meaningful values for the intensity distribution can be obtained. This will be further discussed in the next chapter.

6.3. Simulations of Longitudinal Intensity Distributions in Lasers

Using the equations of section 6.2, a computer program was developed to generate the intensity distribution in DFB laser structures as a function of position in the laser cavity. This section examines some of the basic properties of these simulations.

6.3.1. Parameters for Laser Intensity Distribution Simulations

The parameters used for the simulations in this chapter were obtained by fitting a below-threshold model to data from a gain-coupled DFB laser. The spectra from this laser and the best fits to it are shown in Fig. 6-6. Important parameters that were extracted from this laser are listed in Table 6-1. Observations of the front/back power magnitudes at certain wavelengths in Fig. 6-6 will be useful for comparison with intensity distributions near the facets in section 6.3.3 of this chapter.

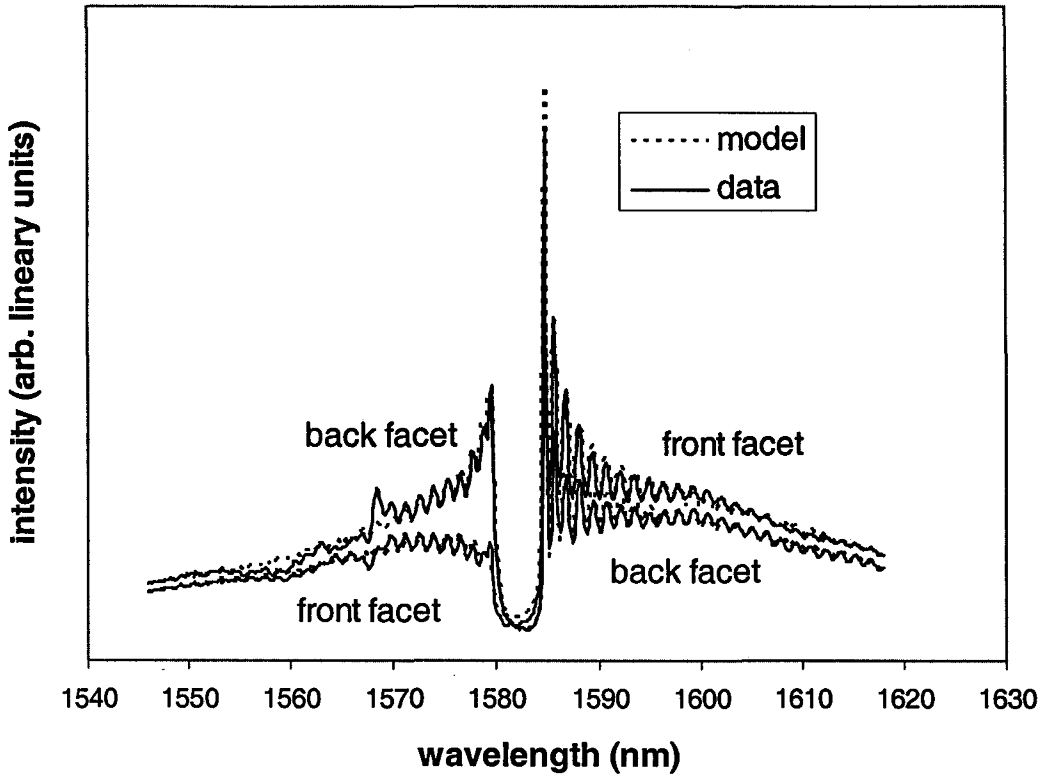

Fig. 6-6 Front and back facet spectra from a gain-coupled DFB laser (solid lines), and best fits by computer model (dashed lines). For visual clarity, the spectra have been labelled on both sides of the stop band.

Table 6-1 Laser parameters that were extracted from the fit shown in Fig. 6-6 and used in the simulations of intensity distributions in this chapter.

Front Facet Reflectance	0.2 %
Front Facet Phase	-33°
Back Facet Reflectance	31.1 %

Back Facet Phase	175°
Real Index Step of Grating	0.01676
Real Coupling Coefficient κ_r	211.8 cm^{-1}
Average Modal Effective Index	3.2049
Average Modal Group Index	3.5240
Length of Grating Period	246.8 nm
Length of Laser	250 μm

6.3.2. Intensity Distribution in a Fabry Perot Cavity

A Fabry-Perot laser is simulated as a first test of the intensity distribution algorithm described in section 6.2. The simulation of a Fabry-Perot laser is easily accomplished by setting the coupling coefficient in Table 6-1 to 0 cm^{-1}. In addition to setting the coupling coefficient to 0, the reflectance has been set to 31.1% (as cleaved) at both facets for symmetry. In Fig. 6-7 a simulated Fabry-Perot spectrum with a field gain of 0.5 cm^{-1} is shown. This spectrum is for a laser far below-threshold operation.

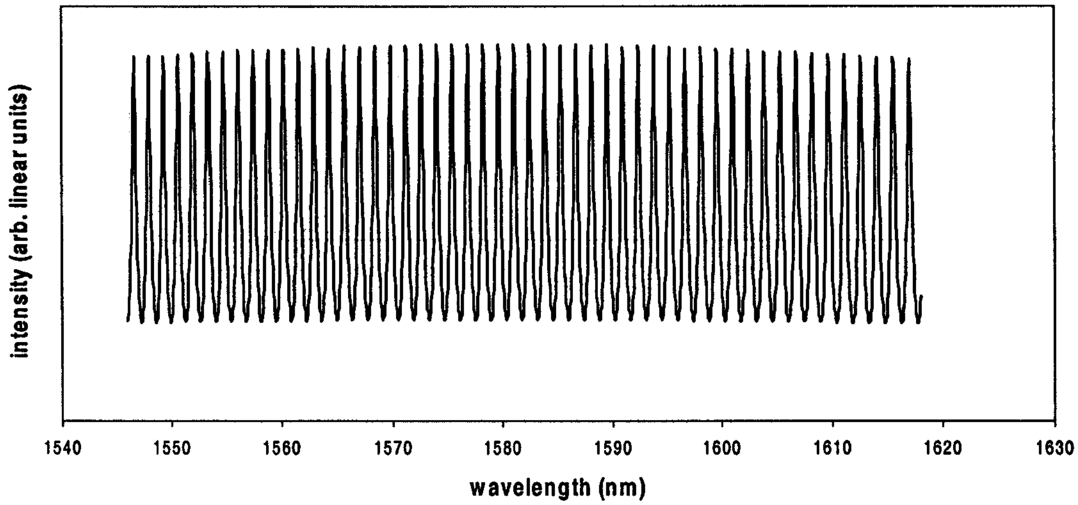

Fig. 6-7 A simple Fabry-Perot spectrum, far below-threshold.

The simulation that produces the spectrum of Fig. 6-7 also produced the intensity distribution shown in Fig. 6-8. The standing wave profile in Fig. 6-8 is seen as solid black because it has a period that is approximately three orders of magnitude smaller than the cavity length. The standing wave magnitude is constant throughout the cavity. The intensity distribution was simulated at a wavelength of 1586.66 nm, which was a mode maximum.

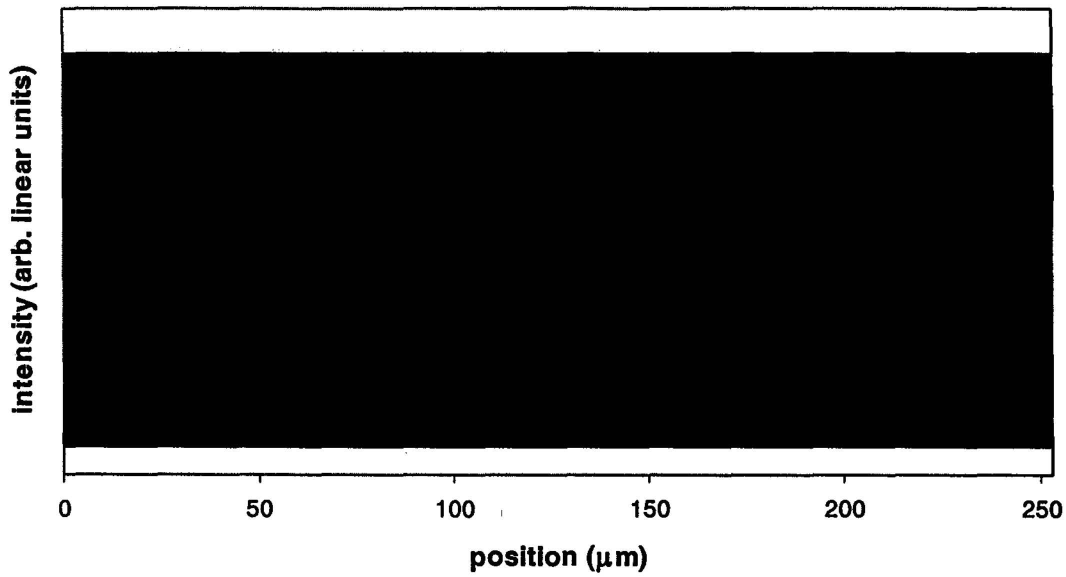

Fig. 6-8 A below-threshold standing wave profile for 1586.66 nm (mode maximum) in a Fabry-Perot cavity. The purpose of this figure is to demonstrate the uniform intensity in the laser, when operating below threshold.

The standing wave magnitude for a Fabry-Perot peak is constant, but this raises the question as to what the intensity distribution should look like for a wavelength that produces a minimum in the Fabry-Perot spectrum. For a peak wavelength, the resonance condition is met, and the standing waves created by each of the facets are in phase. For a minimum wavelength, the resonance condition is not met, and thus a less uniform standing wave profile is expected. The intensity distribution for a modal minimum, at 1581.82 nm is shown in Fig. 6-9. For comparison, it has been plotted on the same scale as Fig. 6-8.

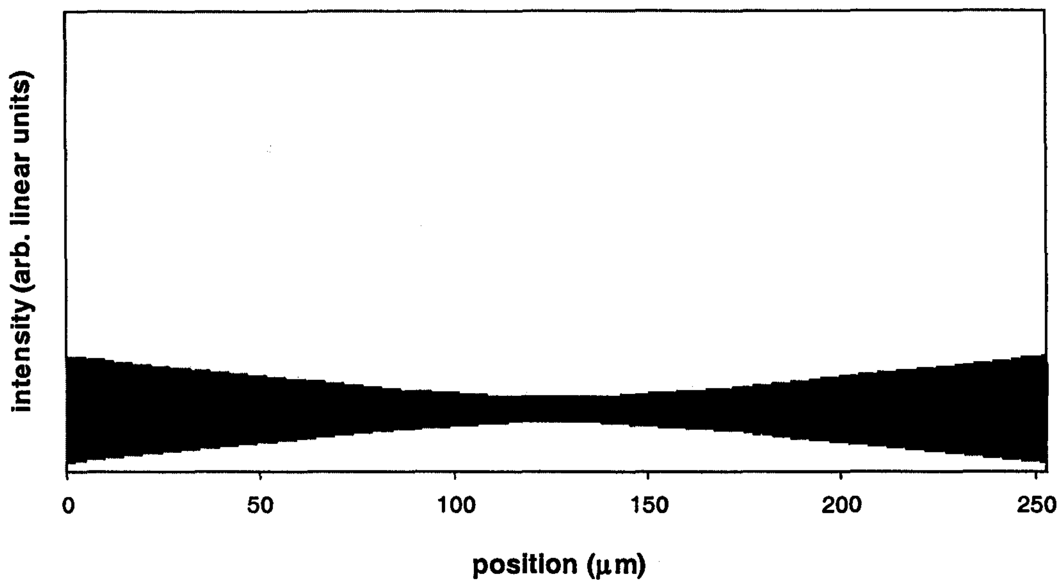

Fig. 6-9 An intensity distribution at a wavelength of 1581.82 nm, which is a minimum of the Fabry-Perot spectrum.

The intensity distribution of Fig. 6-9 indicates that the standing wave profile becomes much smaller near the centre of the cavity, though the average intensity distribution remains the same throughout. Note also that the intensity everywhere is smaller than in Fig. 6-8, as is expected based on the relative magnitudes of the intensities in Fig. 6-7. Because a round trip in the cavity does not equal an integer number of wavelengths, a probability amplitude wave cancels itself out after more than a single round trip from its point of origin (source) by destructive interference. Standing waves formed by reflection at the right-hand facet are exactly out of phase with standing waves formed by reflection at the left-hand facet. Each standing wave diminishes in magnitude, due to destructive interference, the further it is from the reflector that created it. As a result, the standing waves at each facet are large, but at the center of the cavity, the two standing waves are out of phase and of equal magnitude and therefore cancel. Note that in Fig. 6-9, the standing wave is not completely diminished at the center of the cavity. This indicates that 1581.82 nm is near a spectral minimum, but is not an exact minimum. The exact minimum would produce complete cancellation of the standing wave at the center of the cavity.

Intensity distributions in Fabry-Perot lasers are not longitudinally constant in a laser that is near or above-threshold. By increasing the field gain in the simulations to 23 cm^{-1}, the above-threshold case can be examined, as shown in Fig. 6-10.

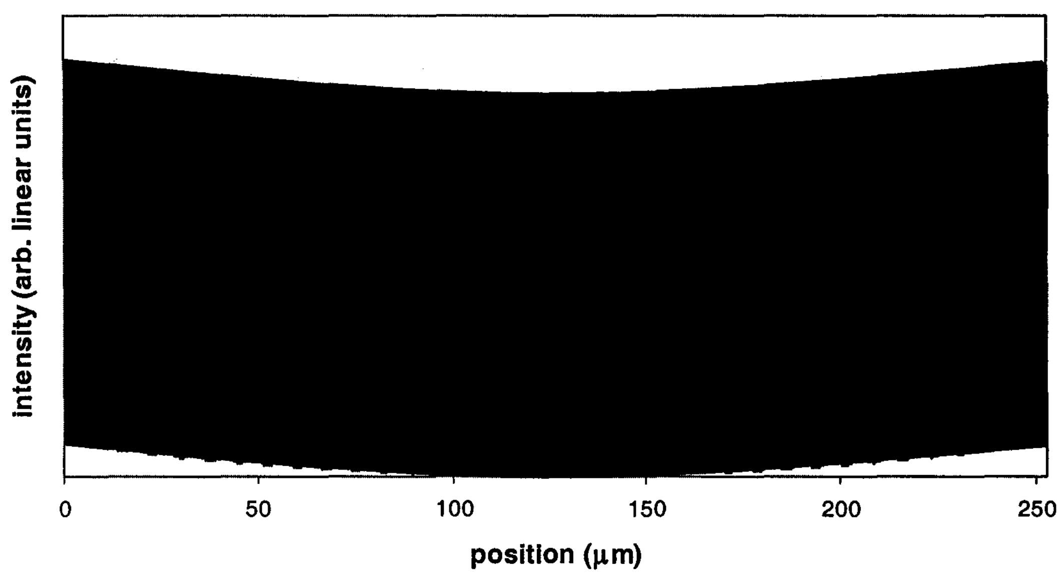

Fig. 6-10 An above-threshold intensity distribution for 1586.66 nm.

In Fig. 6-10 the standing wave in the Fabry-Perot cavity is of constant size because the resonance condition is met for a wavelength of 1586.66 nm however, the average intensity in the laser varies throughout the cavity. This result is expected because light reflected from either facet grows exponentially as it passes through the gain medium to the other facet. Thus, the light intensity at the facets is larger than in the centre of the laser.

6.3.3. Intensity Distributions in Distributed Feedback Lasers.

Intensity distributions in DFB lasers are complicated by the Bragg grating in the waveguide of the laser. Different modes have significantly different longitudinal intensity profiles, and the alignment of the standing wave with respect to the internal grating is especially important in gain-coupled lasers [23]. Gain-coupled lasers make use of the fact that the long wavelength Bragg mode standing wave tends to be in phase with the high index grating segments, and the short wavelength Bragg mode standing wave tends to be in phase with the low index grating segments. In a gain-coupled laser, the long wavelength Bragg mode can be selected by designing a laser that exhibits more gain in the high index segments. Conversely, the short wavelength Bragg mode can be selected by designing a laser that exhibits more gain in the low index segments.

The intensity distributions shown in Fig. 6-11 and Fig. 6-12 are for the long (1584.704 nm) and short (1579.416 nm) wavelengths of the gain-coupled laser described in Table 6-1. The intensities for the short wavelength are much lower than for the long wavelengths, in agreement with the intensities shown in Fig. 6-6. The relative front-back intensity ratios are also consistent with Fig. 6-6. Another noteworthy observation is that the high facet reflectance at the back facet has a strong influence on the intensity distribution near the back facet. The overall power distributions for the Bragg modes are similar to those originally obtained by [10] using their coupled mode theory. Unfortunately, the coupled mode theory did not examine the standing wave.

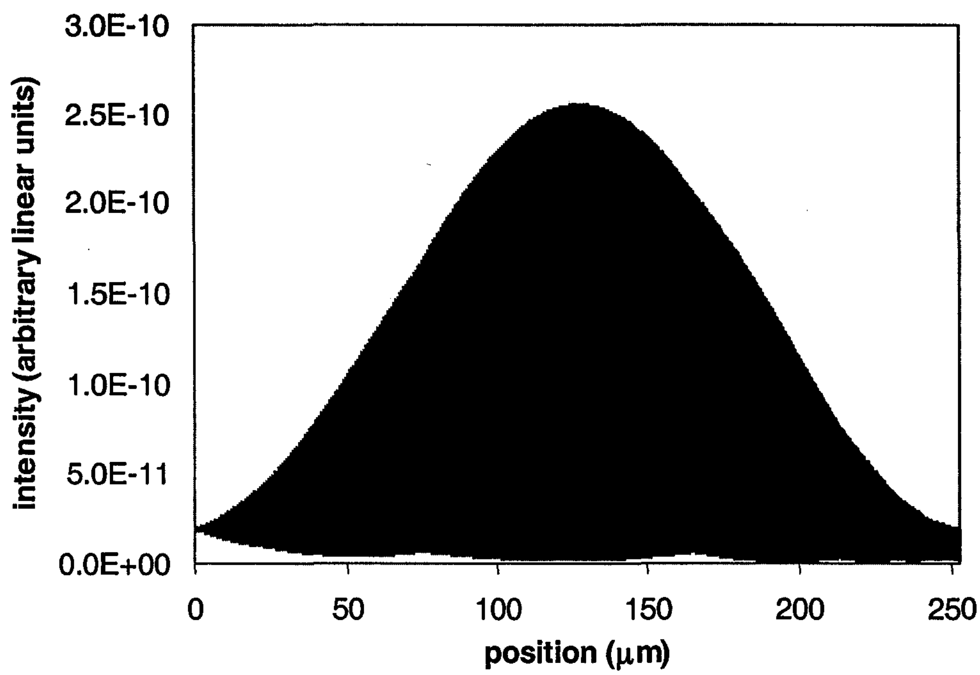

Fig. 6-11 Intensity distribution for the long wavelength mode of Fig. 6-6.

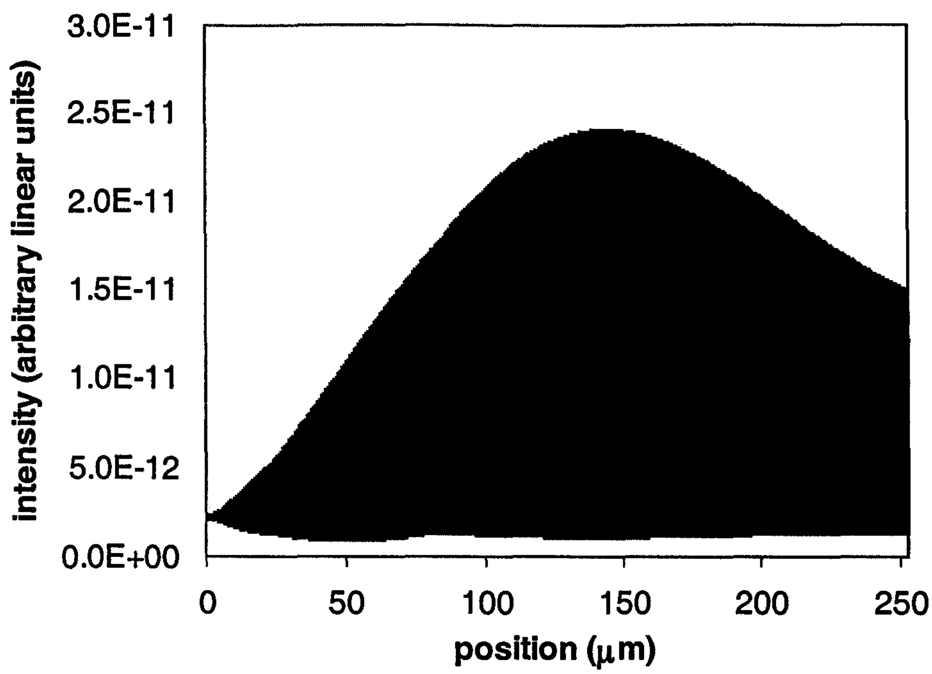

Fig. 6-12 Intensity distribution for the short wavelength mode of Fig. 6-6.

The high frequency of the standing waves in Fig. 6-11 and Fig. 6-12 prevents visual inspection of individual standing waves. To examine closely the relationship between standing waves and the internal Bragg grating of the DFB laser, Fig. 6-13 and Fig. 6-14 show the standing waves over a very small section of the laser near the middle of the cavity. A square wave is used to describe the index profile in the grating. As expected, the long wavelength standing wave maxima occur in the high index sections, and the short wavelength standing wave maxima occur in the low index sections. This alignment of the standing waves is true in general near the middle of the laser cavity.

Near the facets, standing wave alignment with the grating is dominated by the position of the reflective facet with respect to the phase of the grating.

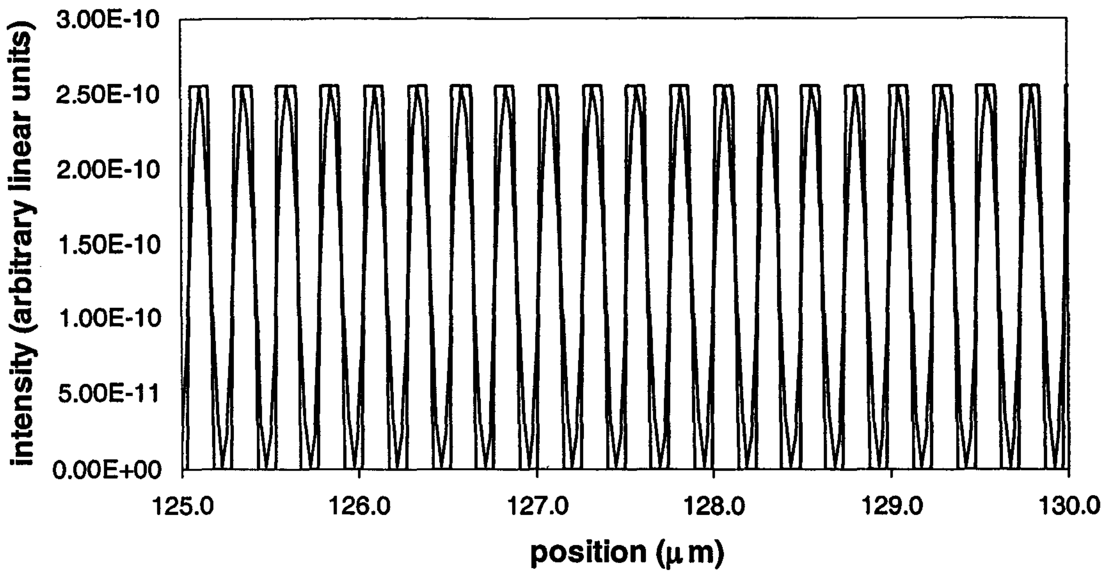

Fig. 6-13 Expanded view of the long Bragg mode intensity distribution of Fig. 6-11.

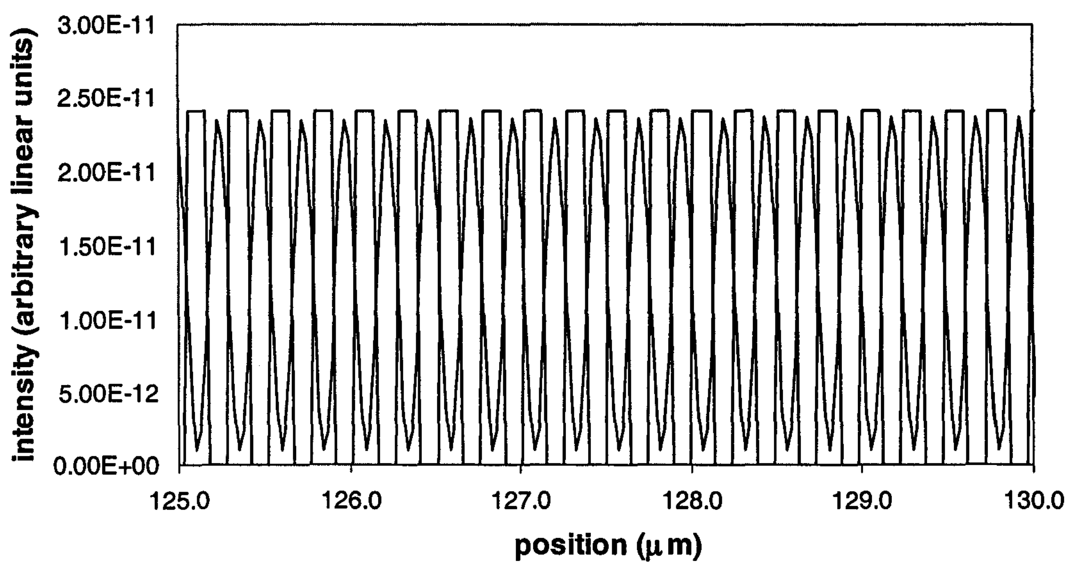

Fig. 6-14 Expanded view of the short Bragg mode intensity distribution of Fig. 6-12.

The tendency for long wavelength Bragg mode standing wave to align itself over the high index segments, and the short Bragg mode standing wave to align itself over the low index segments, can be explained by considering that all standing waves are generated by a reflection from an interface, and therefore all standing waves start off aligned with interfaces. A long wavelength standing wave, however, is slightly longer than a grating period, and therefore gradually shifts into phase with the high index segments of the grating. Similarly, the short wavelength will gradually shift into phase with the low index segments of the grating. The grating coupling prevents either standing wave from propagating far enough to shift through a full 360 degree phase change with respect to the internal grating. Thus, on average, the long wavelength standing wave overlaps the high index segments, and the short wavelength standing wave overlaps the low index modes.

Another interesting phenomenon is the effect that wavelength has on intensity distribution. The intensity distributions for modes further from the stop band each have a series of standing wave envelope maxima. For example, the fourth mode out from the stop band has four standing wave envelope maxima. This phenomenon is clearly demonstrated in Fig. 6-15, which shows intensity distributions for the ninth (1594.96 nm) and tenth (1596.40 nm) maxima on the long wavelength side of the stop band of the spectrum of Fig. 6-6. Also shown is the intensity distribution for the minimum between the two modes, with a wavelength of 1595.68 nm.

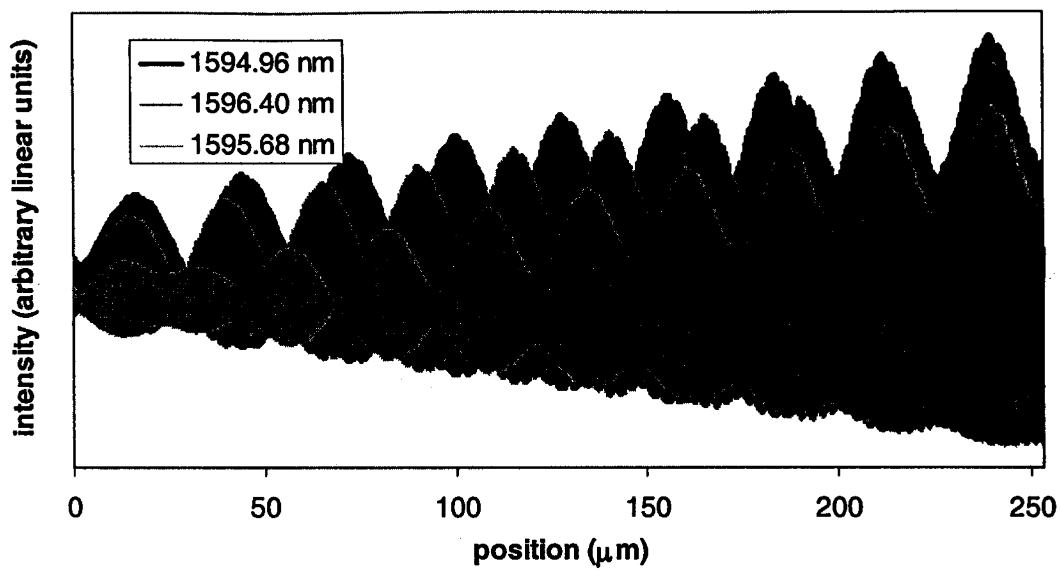

Fig. 6-15 Intensity distributions for various different long wavelength modes.

For each wavelength of Fig. 6-15, the standing waves are in phase with the high index segments near the standing wave envelope maxima, and are in phase with the low index segments near the standing wave envelope minima. This phenomenon can be also seen in Fig. 6-16, which shows the standing wave over a part of the cavity that spans from an envelope minimum to an envelope maximum.

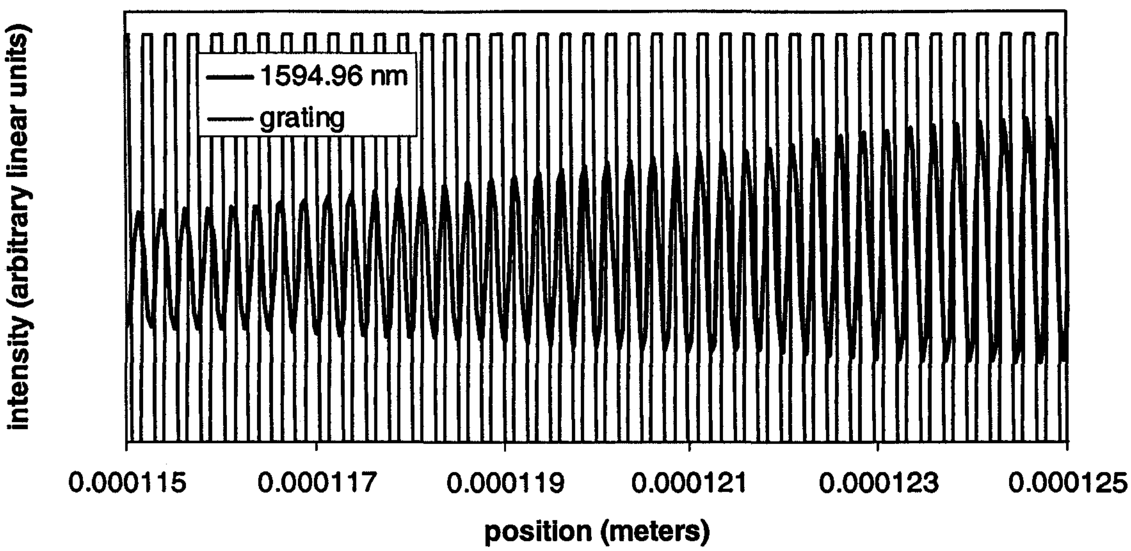

Fig. 6-16 A standing wave intensity distribution showing the evolution of a standing wave phase with respect to the phase of the internal grating.

6.4. Conclusion

The intensity distribution examples presented in the past two sections make intuitive sense. Furthermore, the average intensities for the distributed feedback laser match simulations originally made by [10] that neglect the standing wave. Finally, the phase of the standing waves with respect to the Bragg grating has been shown to agree with current understanding of the gain coupling phenomena [23]. The consistency of the results with intuitive expectations, and with other work in the literature, validates the probability amplitude model for intensity distributions. The probability amplitude transfer-matrix model for intensity distributions that has been presented in this chapter will play an important role in the above-threshold model that is described in the next chapter.

7. ABOVE-THRESHOLD MODEL

7.1. Introduction

The behaviour of DFB lasers above-threshold is more complicated than the behaviour below-threshold. The relationship between gain and light intensity becomes very non-linear above-threshold, and the interactions between photons and carriers must be considered in a self-consistent manner. Carrier density affects the complex index of refraction within the laser, and therefore significantly affects laser performance. The photon density in a laser cavity is non-uniform longitudinally, thus the carrier density also becomes non-uniform longitudinally. This above-threshold effect is called "spatial hole burning". The modified carrier density directly affects the photon density in the laser cavity, which results in a new carrier distribution and so on and so on. The overall system becomes quite complex, and is usually modelled numerically. Many research groups have proposed dynamic and steady state models for above-threshold lasers, but only a few include the effect of standing waves [38], or incorporate spontaneous emission sources into the intensity distribution calculation [26]. The probability amplitude model, which was developed in the course of research for this PhD, allows development of an above-threshold model that includes both of these phenomena.

Most above-threshold DFB laser models in the literature do not make direct comparisons between simulated spectra and real data [26],[38], [32], [35],[80],[81]. Those that do make direct comparisons often present results in which the lasing modes of the data and the simulation differ in power by several orders of magnitude, or in which the lasing modes are not comparable due to the response function of the data [43],[30]. Other models present spectra with non-physical lasing modes of infinite peak power [25]. Much of the work on above threshold spectral modelling has been performed only for quarter wavelength shifted DFB lasers [82]. The probability amplitude model for above-threshold DFB laser spectra has been developed with the final goal of fitting the model to real spectral data from gain-coupled DFB lasers.

This chapter first explains methods and algorithms for efficiently processing the complicated probability amplitude equations that describe the above-threshold DFB laser. The chapter then presents the mathematics of the rate equations that relate carrier density to gain and intensity distribution. Finally, a method for finding an equilibrium solution to the rate equations is discussed.

7.2. Rapid Computing of Probability Amplitudes in DFB Lasers

7.2.1. Collecting Common Terms

The probability amplitude method for calculating intensity distributions and laser spectra can consume extremely large amounts of time. The efficiency of a probability amplitude computer algorithm can be greatly increased by storing numerical results in memory if they are to be used repeatedly. For instance, when calculating intensity distributions, a loop must be coded that sums the intensity contributions from all the different grating segments in the laser. Many of the terms that must be calculated for a single point in a segment are identical, regardless of the source, and these terms should be calculated only once, outside of the loop that sums all sources, in order to maximize efficiency.

7.2.2. Homogeneous Gratings

In a sub-threshold DFB laser, all periods in the grating are considered to be identical. The active region grating is, in approximation, longitudinally homogeneous (i.e., spatial hole burning is negligible). Thus, after the calculation of two plane wave propagation matrices and two interface matrices (see chapter 2), the reflectivity and transmission coefficients for any number of periods can be calculated easily. As an example, in a laser with 1024 periods, there is only a need to store 4056 different transfer matrices to completely describe probability amplitude propagation from any one grating segment to any other.

7.2.3. Inhomogeneous Gratings

Above-threshold, light intensity varies from grating segment to grating segment. The varying light intensity is intense enough to cause a varying carrier density (spatial hole burning), which in turn results in a varying complex index of refraction. Thus, the grating in the DFB laser cavity is longitudinally inhomogeneous. Each period of the inhomogeneous grating must then be described by its own unique transfer-matrix. To take once again the example of a 1024 period DFB laser, the number of transfer matrices necessary to describe the propagation of probability amplitude from any one interface or segment to any other, is 4n×(4n-1)= 16,773,120 where n is equal to the number of periods. This relationship between the number of grating periods and the number of necessary transfer matrices is quite clear if one considers that any one grating segment or interface needs an individual transfer-matrix to describe its relationship with each of the other 4n-1 grating segments or interfaces. Obviously, this grossly complicates the number of transfer-matrix calculations that must be performed. The propagation matrices are especially slow to calculate as they include two base *e* complex exponents each.

The most convenient method for dealing with the large number of relationships between different grating segments is as follows:

1. Calculate each propagation matrix P and each interface matrix R.
2. Multiply these matrices, in order, from the front facet to the rear facet.
3. Store the 2×2 matrix result of each multiplication in an array of matrices. The array will be of length 4n, where n is equal to the number of grating periods. These matrices will be referred to as **F1** to **F4n**.
4. Create a second array of matrices containing the inverse of each matrix in the first array [56]. These matrices will be called **Inv1** to **Inv4n**.

The reflection and transmission coefficients between any two segments or interfaces can be derived with these two arrays of matrices. As an example of how these arrays of matrices should be used, consider the relationships between two segments somewhere within a laser cavity, as shown in Fig. 7-1

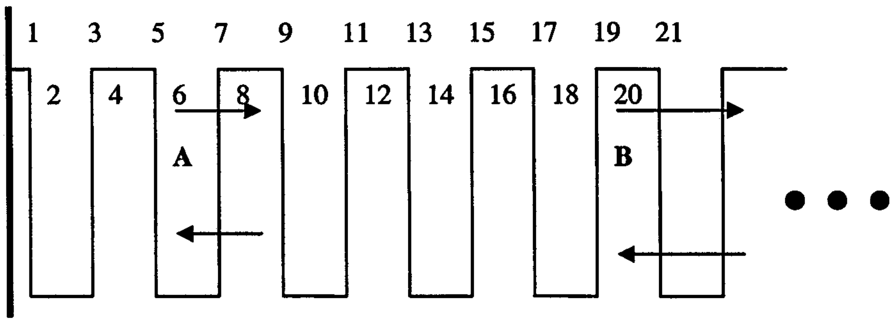

$$\begin{bmatrix} E_A^+ \\ E_A^- \end{bmatrix} = \begin{bmatrix} T_{11} & T_{12} \\ T_{21} & T_{22} \end{bmatrix} \begin{bmatrix} E_B^+ \\ E_B^- \end{bmatrix}$$

Fig. 7-1 Two segments in a grating near the left-hand (front, by convention) facet, and the mathematical relationship between probability amplitudes propagating within them. Propagation directions are indicated by the arrows.

The convention for laser grating numbering in Fig. 7-1 starts at the left-hand, front facet (see Fig. 7-1) at the first interface between a high index segment and a low index segment. This first interface is labelled 1. The transfer-matrix for this interface, that transforms amplitudes on the right to amplitudes on the left, is **F1**. Wave directions are defined by the arrows in Figure 1-1. The first, low index segment is labelled 2 in Fig. 7-1. The transfer-matrix that transforms amplitudes on the right-hand side of low index segment 2, to the left-hand side of interface 1 is **F2**.

The transfer-matrix relating probability amplitudes at the right-hand side of A to the right-hand side of B in Fig. 7-1 can now be obtained. The relationship between the left-hand side of interface 1, and the right-hand interface of high index segment B is written as

$$\begin{bmatrix} E_0^+ \\ E_0^- \end{bmatrix} = \begin{bmatrix} F20_{11} & F20_{12} \\ F20_{21} & F20_{22} \end{bmatrix} \begin{bmatrix} E_{20}^+ \\ E_{20}^- \end{bmatrix}.$$

Eq. 7-1

Furthermore the inverse matrix **Inv6** is used as

$$\begin{bmatrix} E_6^+ \\ E_6^- \end{bmatrix} = \begin{bmatrix} Inv6_{11} & Inv6_{12} \\ Inv6_{21} & Inv6_{22} \end{bmatrix} \begin{bmatrix} E_0^+ \\ E_0^- \end{bmatrix}.$$

Eq. 7-2

The matrix **T** of Fig. 7-1 can then be determined by substituting Eq. 7-1 into Eq. 7-2 to obtain

$$\begin{bmatrix} E_6^+ \\ E_6^- \end{bmatrix} = \begin{bmatrix} Inv6_{11} & Inv6_{12} \\ Inv6_{21} & Inv6_{22} \end{bmatrix} \begin{bmatrix} F20_{11} & F20_{12} \\ F20_{21} & F20_{22} \end{bmatrix} \begin{bmatrix} E_{20}^+ \\ E_{20}^- \end{bmatrix} = \begin{bmatrix} T_{11} & T_{12} \\ T_{21} & T_{22} \end{bmatrix} \begin{bmatrix} E_{20}^+ \\ E_{20}^- \end{bmatrix}.$$

Eq. 7-3

Now the reflection and transmission coefficients from A to B are clearly

$$t = \frac{1}{T_{11}} \quad r = \frac{T_{21}}{T_{11}}$$

Eq. 7-4

Similarily, a relationship looking from the right-hand side of section B to the right-hand side of section A can be written as

$$\begin{bmatrix} E_{20}^{+} \\ E_{20}^{-} \end{bmatrix} = \begin{bmatrix} Inv20_{11} & Inv20_{12} \\ Inv20_{21} & Inv20_{22} \end{bmatrix} \begin{bmatrix} F6_{11} & F6_{12} \\ F6_{21} & F6_{22} \end{bmatrix} \begin{bmatrix} E_{6}^{+} \\ E_{6}^{-} \end{bmatrix} = \begin{bmatrix} U_{11} & U_{12} \\ U_{21} & U_{22} \end{bmatrix} \begin{bmatrix} E_{20}^{+} \\ E_{20}^{-} \end{bmatrix}.$$

Eq. 7-5

In order to preserve the convention of Eq. 7-3, where the upper term in each vector has a direction pointing from starting point (i.e., B in this case) to finishing point (i.e., A in this case), Eq. 7-5 is rewritten in the form

$$\begin{bmatrix} E_{20}^{-} \\ E_{20}^{+} \end{bmatrix} = \begin{bmatrix} W_{11} & W_{12} \\ W_{21} & W_{22} \end{bmatrix} \begin{bmatrix} E_{20}^{-} \\ E_{20}^{+} \end{bmatrix}$$

Eq. 7-6

where

$$W_{11} = U_{22},\ W_{12} = U_{21},\ W_{21} = U_{12},\ W_{22} = U_{11}.$$

Eq. 7-7

In analogy with Eq. 7-4 the transmission and reflection coefficients looking from B to A are now

$$t = \frac{1}{W_{11}} \quad r = \frac{W_{21}}{W_{11}}.$$

Eq. 7-8

The above equations clearly indicate that reflection and transmission coefficients in any direction, between any two segments in a laser, can be readily calculated with just a few multiplications and divisions using pre-calculated F matrices and Inv matrices. A computer program designed to calculate photon distribution within a laser cavity should always begin by generating and storing in memory all **F** matrices and all **Inv** matrices. These matrices can then be used when needed to calculate any desired reflection or transmission coefficient. If transfer matrices between any two segments are calculated on demand, instead of using the above method, the computer processing time increases exponentially. Computing time is one of the main reasons that standing waves and spontaneous emission are neglected in other above-threshold models.

7.3. Introduction of Rate Equations

In a DFB laser, relationships between light intensity and the gain, spontaneous emission, and refractive index are very critical. At points in the DFB active region where the light intensity is strongest, electrons and holes are rapidly recombined through stimulated emission. Where light intensity is weaker, the electrons and holes recombine at a reduced rate. To complicate matters further, the density of electrons and holes has a strong effect on the index of refraction, gain, and spontaneous emission. Gain and spontaneous emission, in turn, can greatly affect the light intensity, and changes in refractive index correspond to a shifting of the lasing wavelength, and to small changes in the shape of the intensity distribution. Recombination of electrons and holes also occur at material defects, and through spontaneous emission and Auger recombination.

7.3.1. The Rate Equation

The complex relationships between carrier density and light intensity and laser parameters are usually described using a rate equation. At any axial point in the laser, the rate at which carriers recombine must be balanced with the injection current. The steady state rate equation used in this above-threshold model is detailed in Eq. 7-9. It is based on the standard equations used by [26], [25], [36], with the inclusion of a few extra details to account for the fact that most modern laser active regions derive gain from quantum wells, rather than from bulk material.

$$\frac{I\eta}{Vq}(1+D\chi)=2\frac{dn_i}{dN}k\left(\sum_{w=1}^{W}N_w-WN_t\right)\Gamma S\frac{1}{1+\varepsilon\frac{n_r}{c}\Gamma S}+A\sum_{w=1}^{W}N_w+B\left(\sum_{w=1}^{W}N_w^{\,2}\right)+C\left(\sum_{w=1}^{W}N_w^{\,3}\right)$$

Eq. 7-9

Note that Eq. 1-9 must be solved once in each grating segment. The number of wells, W, can be different in the low and high index segments. A more detailed description of Eq. 7-9 is presented in Table 7-1.

Table 7-1 Definition of symbols used in the rate equation.

I	Injection current, in Amps.
η	Current injection efficiency (not all the current goes into the quantum wells).
V	Net volume of quantum wells. Units=cm^3
q	Electron charge = 1.6022E-19 Coulombs.

D	In cases where there are a different number of wells in the high index segments than in the low index segments (i.e. truncated quantum well gain coupling), this term approximates lateral carrier injection. Otherwise this term is set to zero.
χ	If the rate equation is being applied to a high index segment, then this term is the ratio of the length of a high index segment to the length of a low index segment. In a high index-high gain truncated-well laser, it is POSITIVE in a high index segment to indicate lateral injection INTO the segment. If the rate equation is being applied to a low index segment, then this term is the ratio of the length of a low index segment to the length of a high index segment, and is NEGATIVE in value to indicate lateral injection OUT of the segment.
dn_i/dN	The differential imaginary index. This term is the rate of change in imaginary index with respect to change in carrier concentration. Units = cm^3.
K	The wavenumber = $2*\pi/\lambda$. Units = cm^{-1}.
N_w	The carrier concentration in the w^{th} quantum well. Units = cm^{-3}.
W	The number of quantum wells. This number is different for low index segments and high index segments in a truncated quantum well gain-coupled DFB laser.
N_t	The transparency carrier concentration.

Γ	The effective optical overlap with the quantum wells.
S	Average photon flux, in $cm^{-2}s^{-1}$.
ε	Nonlinear gain suppression coefficient. Units = cm^3.
n_r	Real part of the index.
c	Speed of light in vacuum. Units = cm/s.
A	Linear recombination coefficient often associated with material defects. Units=s^{-1}.
B	Spontaneous emission coefficient. Units=cm^3/s.
C	Auger recombination coefficient. Units = cm^6/s.

The carrier densities in the quantum wells, N_w, are assumed to be linearly related to each other. The linear relationship is defined by N_W/N_1, i.e., the ratio between the bottom (n-side) well and the top (p-side) well, as in Eq. 7-10. This is a rough approximation, but it allows consideration of non-uniform carrier distribution due to poor hole mobility [72]. Many models in the literature present results that either neglect non uniform carrier distribution, or conclude that the carrier distribution is uniform [83].

$$N_w = N_1\left(1 - w\left(\frac{1 - \frac{N_W}{N_1}}{W - 1}\right)\right)$$

Eq. 7-10

The solution of Eq. 7-9 is found in terms of the variable N_1, i.e., the carrier distribution in the top well of the segment. The computer uses a simple bisection method to find the root.

7.3.2. Calculating Photon Flux in a Lasing Mode

The term *S* in Eq. 7-9 is obtained using the probability amplitude method of the previous chapter, and the computing techniques described in section 7.2. The rate of spontaneous emission is given by the third term on the right-hand side of Eq. 7-9, in units of cm^{-3}/s. This term must be modified to account for the spatial spontaneous emission factor, and for the TE and TM modes. Furthermore, the total spontaneous emission rate is spread out over a range of wavelengths. The equation describing rate of spontaneous emission at any given wavelength is then

$$Spont = \frac{\frac{1}{2}B\left(\sum_{w=1}^{W} N_w^{\ 2}\right)\beta_g}{span}$$

Eq. 7-11

where

$$\beta_g = \frac{\int I(\theta,\phi)d\Omega}{4\pi\, I_o}$$

Eq. 7-12

and *span* is the approximate bandwidth of the spontaneous emission spectrum. The geometric spontaneous emission factor of Eq. 7-12 is simply a ratio of the total number of plane waves coupled into the lasing mode, divided by the total number of plane waves emitted [84]. The term B is the spontaneous emission coefficient, and N_w is the carrier density in the wth well of the segment from which the spontaneous emission originates. The normalised photon density at any given point in a laser is determined by the probability amplitude method which sums contributions from all source points (by integration) within the laser cavity, as described in the previous chapter. Photon counting can be carried out by weighting the sources of the normalised photon density with the spontaneous emission rate of Eq. 7-8, which has units of cm^{-3}/s/nm (i.e. per unit volume, per second, per unit wavelength). The result of this axially integrated amplified spontaneous emission is a photon flux per unit wavelength, with units in cm^{-2}/s/nm. The term "flux" is used here in the sense of a rate at which photons (moving either to the left or to the right) pass a point x in the laser. For the sake of simplicity the phrase "intensity distribution" will be taken as meaning the longitudinal distribution of photon flux in the laser throughout the rest of this thesis.

To find the total photon flux at a point in the laser cavity, one must integrate over all wavelengths. When a laser is above-threshold, the approximation can be made that all stimulated emission at frequencies other than the lasing mode is negligible, and thus integration is only necessary over the free spectral range of the lasing mode. In theory, numerical integration could be performed by calculating the photon flux for a large number of wavelengths within the span of the lasing mode. This is not feasible in practice, however, because the lasing mode is extremely narrow, and the flux per unit wavelength would need to be calculated at a very large number of wavelengths to obtain accurate results. A more efficient method for integration over the mode is necessary.

A lasing mode is often approximated as having a Lorentzian line shape [85]. The area under a random Lorentzian [86] shaped mode has the analytic form

$$Z\int_{-\infty}^{\infty}\frac{1}{x^2+a^2}dx=\frac{Z}{a}\tan^{-1}\left(\frac{x}{a}\right)\Big|_{-\infty}^{\infty}=Z\frac{\pi}{a}$$

Eq. 7-13

where a is the halfwidth of the curve at half maximum, and Z is a random variable modifying the amplitude. Examination of Eq. 7-13 reveals that the peak of the Lorentzian at x=0 has a magnitude of Z/a^2. Thus, if the peak of a Lorentzian is found to have magnitude A, then $Z=A\times a^2$. The area under the Lorentzian will then be, using Eq. 7-13,

$$S=A\times a^2\frac{\pi}{a}=A\times a\times\pi.$$

Eq. 7-14

Using Eq. 7-14, one is able to integrate the flux per unit wavelength over the free spectral range of a mode using only the mode peak and halfwidth.

7.3.3. Finding a Mode Peak and Halfwidth

To find the rate of photons passing through a point in the laser using Eq. 7-14, one must know the peak of the lasing mode, and the halfwidth. Finding the peak of a lasing mode is a difficult task that requires double precision arithmetic. The extremely narrow linewidth of a lasing mode can be more than seven orders of magnitude smaller than the free spectral range of the mode, and thus a search algorithm is necessary to find the peak. A quick method for finding the peak of a lasing mode is to use the fact that the power transmission function of the laser should have a peak wavelength at the same frequency as the lasing mode. The power transmission function for a laser is simply $1/T_{11}$, where **T** is the 2×2 transfer-matrix for the entire laser (see chapter 2), and can be calculated very quickly. The transmission function of the laser will also have a halfwidth that is approximately the same as the halfwidth of the lasing mode. The wavelength that maximizes power transmission is readily calculated by searching for a point where the derivative of T with respect to wavelength is zero. A bisectional search algorithm was successfully implemented to find the zero-derivative point. Once the peak wavelength is found, a second bisectional search algorithm is used to find the wavelength of the half maximum. Integration of the Lorentzian mode by the methods of section 7.3.2 is then trivial.

7.3.4. Parameter Modification

When a new carrier distribution is obtained by substituting an intensity distribution into the rate equation (Eq. 7-9), new values must be assigned to the index, gain, and spontaneous emission rates for each segment in the laser. The spontaneous emission rate for each segment was described by Eq. 7-11. The new values for gain and index of refraction are based on the new carrier distribution, and are defined as

$$gain = \frac{dn_i}{dN}\left(\sum_{w=1}^{w=W} N_w - WN_t\right)\Gamma S \frac{1}{1+\varepsilon \frac{n_r}{c}\Gamma S} + \frac{\alpha(\lambda)}{k}$$

Eq. 7-15

$$index = n_t(\lambda) + \frac{dn_R}{dN}\left(\sum_{w=1}^{w=W} N_w - WN_t\right)$$

Eq. 7-16

where λ is the wavelength, α is the field loss per cm of the waveguide, n_t is the transparency index of refraction, and dn_R/dN is the differential index.

The wavelength dependence in the loss and index terms is useful in making realistic fits to data, but it can make searching for the peak wavelength impossible. The peak of the above-threshold lasing mode is extremely sensitive to gain and is very non-linear. Therefore, if the lasing wavelength is changed even slightly, and there is a wavelength dependent term for the gain, the new gain associated with the new wavelength could be completely unphysical. This problem is especially apparent when trying to find the derivative of the lasing mode height with respect to wavelength, or the derivative of the mode height with respect to carrier density. The solution to these problems is to approximate all parameters as being wavelength independent over the width of the lasing mode. The values used for the wavelength independent parameter approximations around the lasing mode are recalculated at the beginning of each iteration of intensity distribution calculation. This necessary approximation is of little consequence to the overall fit of the laser because it is made only over the very small bandwidth of the lasing mode.

7.4. Finding Equilibrium for the Rate Equations and Photon Distributions

Solving the rate equation for each segment in a DFB laser is not difficult, but once a solution is found the new carrier distributions will alter the physical properties (i.e., gain, spontaneous emission rate, index of refraction) of the laser, and a new intensity distribution will result. This new intensity distribution will then have to be substituted into the rate equation, and the entire process is repeated. Unfortunately, the new intensity distribution will often be so far from equilibrium that convergence, (or equilibrium) does not occur. The solutions will oscillate between extremely high intensity and extremely low intensity, or worse yet the algorithm gets stuck in a regime of non-physical (overly large) values for of gain. These oscillations and instabilities occur because the simulation attempts to balance carrier distribution with intensity distribution in discrete steps. In a real laser, of course, the balance between carrier distribution and intensity distribution is constantly being adjusted in real time.

Fabry-Perot models can attempt to dampen oscillations in solution space by applying a low pass filtering mechanism to solutions obtained after each iteration. It seems reasonable then, that a similar method might be used to obtain equilibrium in a DFB laser model. The term "equilibrium" will be used in this thesis to describe the situation where an intensity distribution can be substituted into the rate equations to produce a carrier distribution, which in turn yields the original intensity distribution.

7.4.1. Attempting to Dampen Oscillations in Solution Space

Two different dampening mechanisms were tested, each with the goal of reducing oscillations between high intensity-low carrier distribution solutions, and low intensity-high carrier distribution solutions. Neither method was found to work satisfactorily. The first method tried dampening the system by using a weighted average of the intensity distribution from the previous iteration with the newly calculated intensity distribution. Unfortunately, the non-linear behaviour of the lasing mode power when above-threshold necessitated unacceptable trade-offs between stability and convergence times (i.e., very heavy weighting in favour of the intensity distribution from the previous iteration could produce reasonable stability, but convergence was then too slow to be useful). Furthermore, very high, non-physical carrier densities (due to low initial intensity estimates) could occur, which also created instability and prevented convergence on a physically sensible solution.

The second method that was tried attempted to dampen the oscillations of the system of equations by using a weighted average of the carrier distributions from the previous iteration. This method was more successful because the carrier distributions do not behave in a non-linear manner. One problem with averaging successive carrier distribution solutions, however, was that the shape of the carrier distribution was then slow to change. As a starting point, the carrier distribution was assumed to be longitudinally constant, and thus the carrier distribution tended to be too flat as equilibrium was approached. Convergence was made very difficult because the shape of the carrier distribution was usually incorrect, even if it was producing a gain that appeared to be allowing equilibrium with the intensity distribution. The system also remained very unstable because the carrier distribution could overshoot far into non-physical space (i.e., where the round trip reflectivity gain product, RRG^2, is greater than 1), unless extremely heavy weighting with previous solutions was used. In fact, very different solutions were often obtained when different starting values were used for the carrier distribution. Results obtained by this method were therefore considered spurious.

7.4.2. The Iterative Trial and Error Approach

Attempting to dampen oscillations between high and low intensity solutions by applying a low pass filter to the carrier distribution or intensity distribution did not result in stable or consistent equilibrium solutions. The main problems were corruption of the converging algorithm by entering into non-physical solution space (round trip reflectivity gain product RRG^2 greater than 1) and the extremely non-linear behaviour of the power in the lasing mode. A new, more complicated algorithm, based on a simple trial and error approach was therefore developed. The basic flow of the algorithm is shown in Fig. 7-2, and will be discussed in detail in the remaining sections of this chapter.

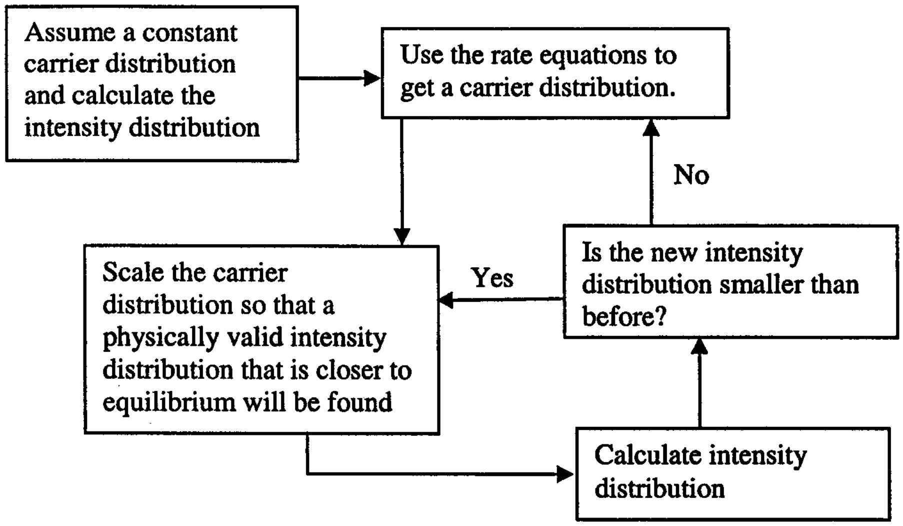

Fig. 7-2 Basic flow chart of the above-threshold model that is discussed in the rest of this chapter.

In the trial and error method, a flat carrier distribution is initially assumed. The laser parameters are calculated based on this carrier distribution, and an intensity distribution is then obtained. A new carrier distribution is obtained by substituting the new intensity distribution into the rate equations. Laser parameters are modified according to the new distribution of carriers, and spatial hole burning is thereby simulated. Often, the new parameters will be unphysical, and the RRG^2 product of the laser breaks the condition that $RRG^2<1$. Unphysical solutions are unacceptable. Therefore, whenever a new carrier distribution is obtained, an algorithm is invoked that checks RRG^2 for each segment in the DFB laser is invoked. The RRG^2 test for each segment is of the form

$$RRG = r_r r_l e^{j2knl}$$

Eq. 7-17

where r_r is the reflection in the right-hand direction from inside the grating segment, and r_l is the reflection in the left-hand direction from inside the grating segment. It is vital that the calculation of Eq. 7-17 should be performed at the lasing wavelength, where the reflectivity gain product is the largest (due to constructive interference), and is expected to have a real value. Thus the peak search algorithm, as described in section 7.3.3, must be used to find the peak transmission wavelength prior to calculating the RRG^2. Testing the RRG^2 does not always produce useful information, however, because changes in the gain of the laser due to the new carrier distribution can result in a small shift in lasing wavelength, and/or a complete lack of modal structure in the spectrum around the lasing mode (i.e., the new gain is much too small or much too large). The maximum is then hard to find. It was also found that when far from equilibrium tests of the RRG^2 yield no useful information because there is nothing to distinguish the RRG^2 values that are far below-threshold from the RRG^2 values obtained using an unphysical, overly large gain. The RRG^2 test is only useful when a distinct lasing mode exists, and the laser is near equilibrium.

A useful approximation for checking whether the simulated gain is unphysical is to find the derivative dT/dN, where N is the carrier distribution and T is the power transmission coefficient for the laser, which is obtained using transfer-matrix multiplication (see chapter 2). In the physically valid regime, the derivative *dT/dN* should be positive (i.e., increasing the carrier density increases the gain, which in turn increases the power transmission - see Fig. 7-3). In the unphysical regime, where gain is too high, *dT/dN* is negative. A major asset of the term *dT/dN* is that it has the correct sign regardless of whether it is calculated at the peak of the mode or not. Thus it is possible to test for a physical solution even if the exact position of the lasing peak is unknown.

Calculation of *dT/dN* is difficult because its value varies between two extremes. Far above-threshold, at wavelengths near the lasing mode peak, *dT/dN* has very large values, and there is a discontinuity at the point where $RRG^2=1$, as depicted in Fig. 7-3. In this region very small values of *dN* should be used (e.g., 10^{-10} of N). If the laser is far above or below-threshold however, a much larger value for *dN* must be used to avoid obtaining a slope of 0. The slope *dT/dN* must often be calculated several times, each with an incrementally larger value for *dN*, to avoid floating point error due to negligible values of *dT* while at the same time avoiding a numerical derivative across the discontinuity. The calculation of *dT/dN* is made by first calculating *T*, and then recalculating *T* again after having incremented the carrier density *N* (by a very tiny amount), in each segment, (usually starting with $dN = 10^8$, where N_t has a value in the order of 1.5×10^{18}).

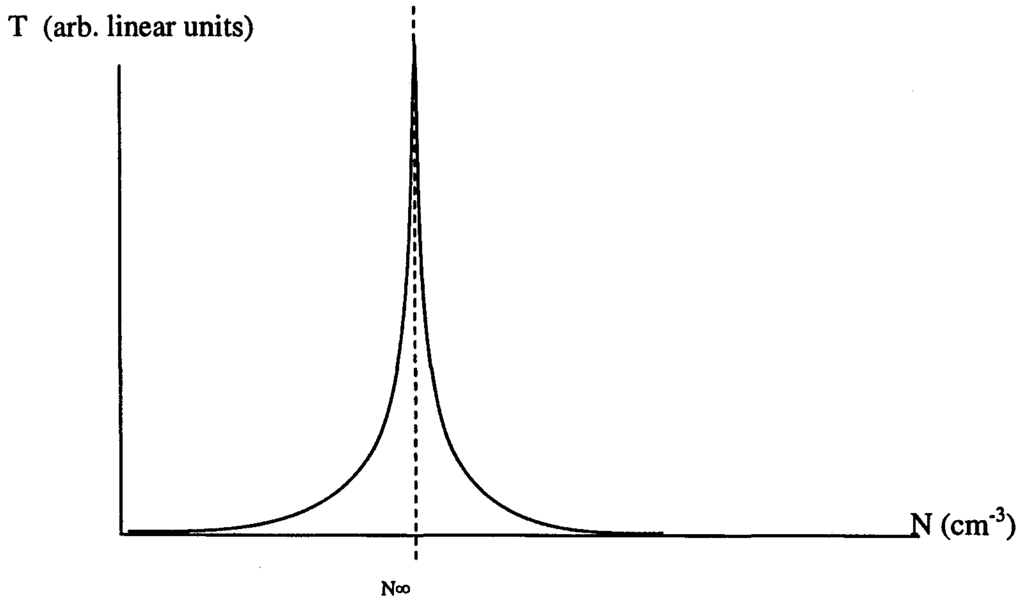

Fig. 7-3 Power transmission vs carrier density. The region to the right of N_∞ is non-physical.

Once it is established whether a new carrier distribution is too large or too small to be realistic, rather than trying to dampen the change in carrier distribution by averaging it with the previous distribution, the new distribution is scaled by an appropriate factor so that the new light intensity will be closer to creating equilibrium between the intensity distribution and the carrier density. The method for determining an intensity that is nearer equilibrium is discussed in section 7.4.3. The method for determining an appropriate scaling factor will be discussed in section 7.4.4.

Scaling of the carrier distribution is accomplished using the equation

$$N_{new} = \gamma\left(N_{old} - WN_t\right) + WN_t$$

Eq. 7-18

where γ is an appropriate scaling factor, N_{old} is the sum of the carrier densities that were assumed to be in the W wells of the segment, and N_{new} is the sum of the W carrier densities in the segment after the scaling operation. This scaling operation is applied to every segment in the laser. The new carrier distribution can then be used to generate a new intensity distribution, and the entire process is repeated. Every iteration will require a smaller scaling value than the previous one, and equilibrium is eventually obtained.

7.4.3. Using the Power Transmission Coefficient to Bound Equilibrium Space

The previous section described a method whereby the longitudinal intensity distribution in a laser is calculated using a carrier distribution that is obtained by solving a series of rate equations and scaling the result. A new carrier distribution can then be calculated from the intensity distribution, and scaled appropriately. This process is repeated until equilibrium is obtained. In the previous section, details were given on how to avoid non-physical solutions (i.e., carrier densities that are too large), but no explanation was given for how to make each iteration closer to equilibrium than the last.

The initial carrier concentration is assumed to be constant throughout the laser cavity, and is given a reasonable value based on the gain that was needed to generate a below-threshold spectrum. This distribution is referred to as the "seed" carrier distribution. Associated with this carrier distribution is a power transmission coefficient

T for the peak wavelength of the dominant mode. It was shown in chapter 2 that the transmission coefficient near the lasing mode is closely related to the output intensity of the laser. Obviously the intensity distribution within the laser must have a magnitude proportional to the output intensity of the laser. The power transmission coefficient *T* can therefore be used as a test variable that describes allowable solution space for the intensity distribution. This is a very important because *T* and is several orders of magnitude faster to calculate than the actual intensity distribution.

The carrier densities that are obtained from the below-threshold intensity distribution (i.e., from the seed carrier distribution) will inevitably be much larger than is physically realistic in order to solve the rate equations far above-threshold. This is because the relationship between carrier density and light intensity is highly non-linear. Clearly, a new carrier distribution should be tried, but this new carrier distribution should properly reflect the fact that longitudinally varying intensity distributions are causing longitudinally varying carrier distributions. Thus, the new carrier distribution should be a scaled version of the one that was obtained using rate equations with the below-threshold intensity distribution. Furthermore, the new carrier distribution should produce a gain that will create a larger intensity (or larger *T*) in the laser cavity. Creating a larger intensity in the laser cavity will allow the next iteration of rate equations (Eq. 7-9) to produce a carrier distribution that is more realistic than the previous iteration. Note that every calculation of *T* requires a derivative based bisectional search for the peak ($dT/d\lambda=0$) of the power transmission spectrum (as was explained in section 7.3.3).

A distribution can be chosen to make the intensity of a laser arbitrarily large (see Fig. 7-3). The question then arises as to how much larger the new, scaled carrier distribution should make the intensity distribution. If the intensity distribution is too large, then the rate equations will produce a new carrier distribution that yields a T smaller than that of the carrier distribution that was initially used to calculate the intensity distribution. This scenario indicates that an upper boundary for the intensity distribution has been discovered. A computer can store this upper boundary for the intensity distribution as the single variable T_{max} and disregard the new carrier distribution, as it was obtained from a non-physical (overly large) intensity distribution. The previous carrier distribution, from the previous iteration, should be reused and rescaled, this time to produce an intensity distribution that is smaller than the last (i.e., the new T should be smaller than T_{max}). Should any single iteration not produce a maximum limit, T_{max}, then it must have produced a minimum boundary, T_{min}, for the intensity distribution. As the iterative process is continuously repeated, the solution space between T_{max} and T_{min} becomes smaller and smaller, and eventually, equilibrium is reached.

7.4.4. A Method for Finding the Carrier Concentration Scaling Factor

A consistent method is necessary for scaling the carrier distribution so that it produces a T that lies between T_{max} and T_{min}. This can be accomplished by using a bisectional search algorithm to find the scaling factor that produces the desired T (i.e., one that lies somewhere between T_{max} and T_{min}). Unfortunately, the extremely non-linear nature of the relationship between T and the carrier density makes this search algorithm very slow. Furthermore, the search often produces a new *T* that is very close to one of the boundaries (T_{maz} or T_{min}). Alternatively, the search could be made for a carrier distribution that produces a *T* that approximately bisects T_{max} and T_{min}, however, as the algorithm is in this case searching for a more specific value of T, each iteration takes much longer. Equilibrium was eventually obtained by these methods, but in a painfully slow manner.

Repeated searches for appropriate values of *T* led to a better understanding of the relationship between *T* and *N* (carrier distribution). Knowledge of the basic relationship between T and N improved the ability to estimate an appropriate scaling factor. The relationship between *T* and *N* is depicted in Fig. 7-3, section 7.4.2, and appears to have a form that can be approximated by the equation

$$T = \frac{A}{(N - N_\infty)^2}$$

Eq. 7-19

where *A* is an arbitrary magnitude scaling factor, *N* is the sum of the carrier densities in the quantum wells, and N_∞ is the carrier density at which *T* reaches infinity and *dT/dN* is discontinuous. The carrier density varies longitudinally throughout the cavity, but the scaling of the overall distribution can be represented by the value of N in any one segment. A segment at the center of the DFB cavity is chosen for this purpose.

The quality of the approximation of Eq. 7-19 was tested by plotting T vs N based on points calculated during a single iteration of the bisectional search algorithm, and then adjusting A to obtain the best fit. Examples of the excellent agreement with the simulated T vs N relationship are shown in Fig. 7-4 and Fig. 7-5.

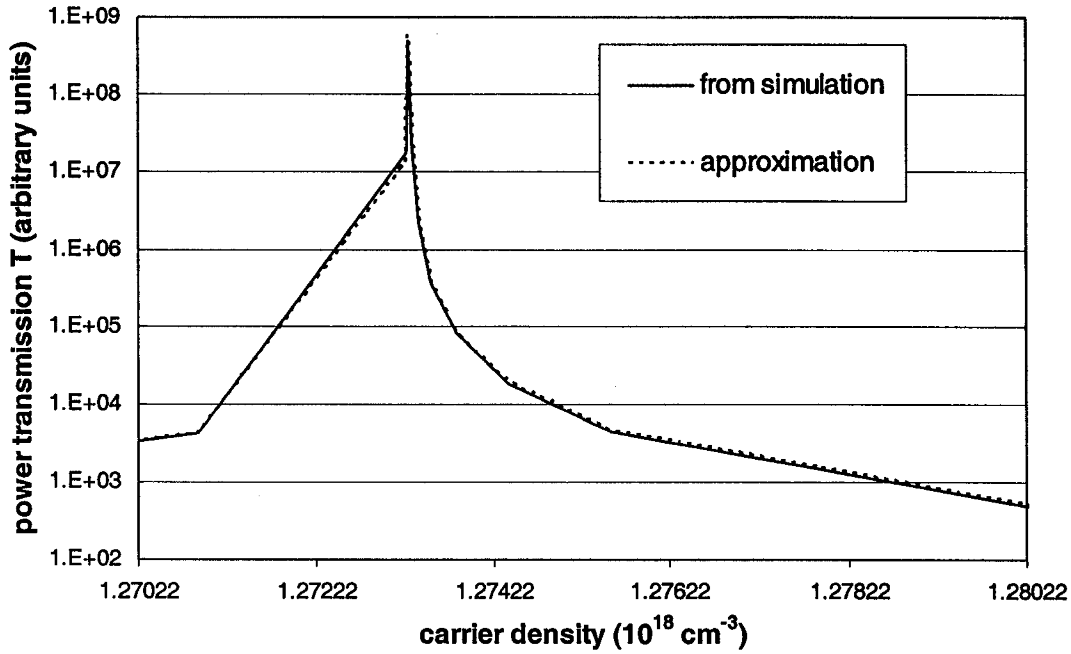

Fig. 7-4 The approximation of Eq. 7-19 compared to actual simulations. In this case A=0.024 and N_{∞}= 1.273257.

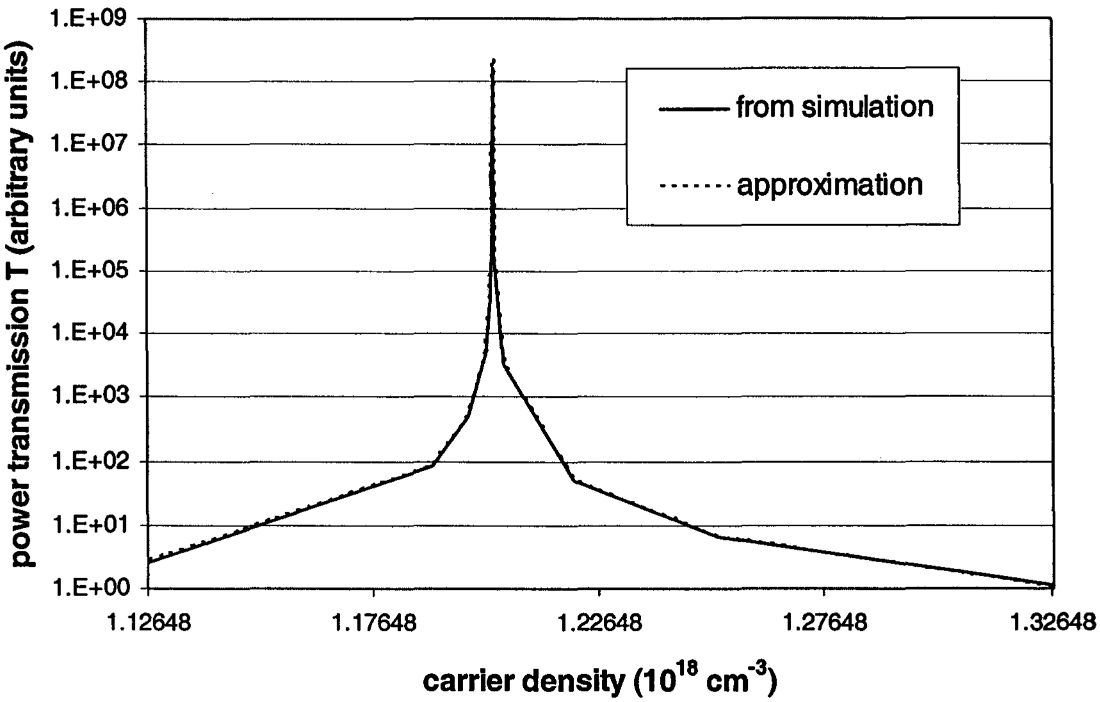

Fig. 7-5 The approximation of Eq. 7-19 compared to actual simulations. In this case A=0.016 and N_{∞}= 1.203258e18.

The approximation in Eq. 7-19 appears reasonable. It therefore allows great increases in the speed with which an appropriate carrier distribution can be found for generation of a desired T. Given two transmission coefficients T_1 and T_2 at two arbitrarily chosen carrier distributions, N_1 and N_2, a carrier distribution N_3 can be found for any desired point T_3 by way of Eq. 7-19. Specifically, using the known points, T_1,N_1 and T_2,$N2$, and Eq. 7-19, the term N_{∞} is found as

$$N_\infty = \frac{\left(\sigma\sqrt{\frac{T_1}{T_2}}N_1 - N_2\right)}{\left(\sigma\sqrt{\frac{T_1}{T_2}} - 1\right)}$$

Eq. 7-20

and N_3 is then

$$N_3 = N_\infty + \rho\sqrt{\frac{T_1}{T_3}}(N_1 - N_\infty).$$

Eq. 7-21

where

$$\sigma = \frac{\frac{dT_1}{dN_1} \Big/ \left|\frac{dT_1}{dN_1}\right|}{\frac{dT_2}{dN_2} \Big/ \left|\frac{dT_2}{dN_2}\right|}$$

Eq. 7-22

and

$$\rho = \frac{dT_1}{dN_1} \Big/ \left|\frac{dT_1}{dN_1}\right|$$

Eq. 7-23

The term σ will have the value -1 if N_1 and N_2 are on opposite sides of the cusp (N_∞) in Fig. 7-3. Otherwise it will have the value +1. The term ρ will have the value +1 if N_1 is on the left-hand side of the cusp, and will have the value -1 if N_1 is on the right-hand side of the cusp. Once a value is obtained for N_3, the scaling factor γ of Eq. 7-18 can be written as

$$\gamma = \frac{N_3 - WN_t}{N_{old} - WN_t}.$$

Eq. 7-24

The algorithm described in Eq. 7-20 through Eq. 7-24 is entirely based on the approximation of Eq. 7-19, so it usually must be repeated a few times to obtain the desired accuracy. The accuracy of the approximation improves as the proximity of N_1 and N_2 to N_3 increases. Thus, if the value for T obtained using the scaled carrier distribution turns out to be a poor approximation for the desired value T_3, then the entire procedure should be repeated after making the substitutions N_1=N_2, N_2=N_3, T_1=T_2, and T_2=T.

The time necessary for finding equilibrium between intensity distribution and carrier distribution can be further decreased by choosing sensible methods for collapsing the boundaries T_{max} and T_{min} on the equilibrium value of T. Initially, no value for T_{max} exists, and so T is increased by a factor of 10000 in each iteration. Once a maximum is found, a point at $100T_{min}$ is tried, and the next iteration is at $10T_{min}$. When the two values are within a single order of magnitude, a bisectional search is used. The computing time using the above methods is roughly 1/10 that which was necessary without Eq. 7-19.

7.4.5. Tracking the wavelength and Adjusting the Effective Index

In addition to the problems that are created by the non-linear relationship between carrier density and intensity distribution, changes in carrier density modify the effective index, thus causing a shift in the lasing wavelength. Often, upon solving the rate equations (Eq. 7-9) for each segment in the laser, the new carrier distribution results in a large shift in the index of refraction. The new carrier distribution will also result in a gain that is either so weak that no single mode dominates, or a gain that is non-physically high (i.e. the threshold condition that round trip reflectivity gain product=$R_1R_2G^2<1$ is broken, where R is the facet reflectivity and G is the single pass field gain), so that a side mode dominates. Theoretically the Bragg mode intensity should be infinite for an excessively high (i.e., non-physical) gain, but the geometric series approximations that are used to calculate intensity are not valid in such situations (i.e., the approximation $1/(1-x)$ is only valid if $|x|<1$). With substantial changes in wavelength possible for the lasing mode, and possible non-dominance of the lasing mode, there is no simple way to keep track of the lasing mode wavelength. On the other hand, the search for equilibrium between the carrier distribution and intensity distribution becomes impossible if different modes are used in different iterations, because the intensity distribution for each mode is very different. Moreover, the algorithms discussed in sections 7.4.3 and 7.4.4 are absolutely dependant on being able to find the peak wavelength for the power transmission coefficient T.

To prevent widespread shifting of the lasing mode when the carrier concentration is scaled, the longitudinally varying part of the carrier concentration is separated from the longitudinally constant part of the carrier concentration. That is,

$$N_{tot}(x) = N(x) + N_{const} .$$

Eq. 7-25

Substituting Eq. 7-25 into Eq. 7-16 yields

$$n = n_t(\lambda) + \frac{dn_R}{dN}\left(N(x) + N_{const} - WN_t\right)$$

Eq. 7-26

so that the change in index due to a carrier concentration that is above transparency is

$$\delta n = \frac{dn_R}{dN} N(x) + \frac{dn_R}{dN}\left(N_{const} - WN_t\right)$$

Eq. 7-27

The second term in Eq. 7-27 is much larger than the first, for everywhere in the laser cavity. Thus, the second term is primarily responsible for wavelength shifting when carrier distribution is modified. By neglecting the second term, the longitudinally varying index is properly included in the laser model, but the large wavelength shifting offset is eliminated. At the end of each iteration, the intensity distribution can be recalculated, with the full index of refraction incorporated. The wavelength will shift, but the carrier distribution will not be unrealistically large or small. Thus the lasing mode will dominate the spectrum, and a course search through the spectrum of T can be used to identify its position. Once its position is known, the standard derivative based bisectional search method can be used to find the peak wavelength. This new wavelength can be used throughout the next iteration.

7.5. Conclusion

The above-threshold model that is described in this chapter is relatively quick at finding an equilibrium solution for the longitudinal intensity and carrier distributions in the laser cavity. A Pentium IIII 750MHz machine is capable of modeling an above-threshold laser in under 20 minutes. The rapid approach to equilibrium of a simulated laser is demonstrated in Fig. 7-6 below. As expected, sudden drops in the carrier distribution are correlated with increases in T that do not result in a new T_{max} value.

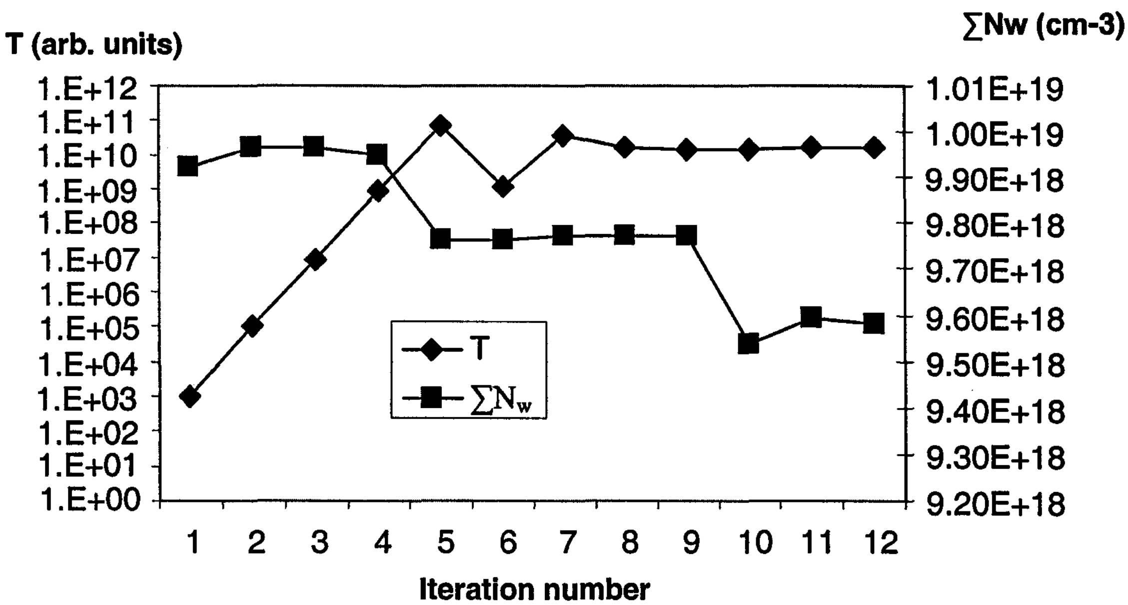

Fig. 7-6 The power transmission coefficient plotted on a logarithmic scale approaches equilibrium as the number of iterations of the searching algorithm increases. The sum of the carrier densities in the quantum wells of a high index segment near the center of a truncated-well laser, plotted as a function of iterations through the intensity distribution/rate equation loop.

The above-threshold model, as described in this chapter, has been used to successfully predict DFB laser performance. Methods for fitting the spectral output to data are discussed in the next chapter and several good fits are demonstrated. The effects of spatial hole burning that are predicted by this model will be discussed, and will be shown to match data extremely well.

8. FITTING TO THE ABOVE-THRESHOLD SPECTRA OF TRUNCATED-WELL DFB LASERS

8.1. Introduction

An above-threshold model for DFB lasers is only useful if it can correctly predict the "real life" behaviour of a device. The spectral predictions of above-threshold models are rarely compared to spectral data, and where comparisons have been made, the predicted lasing mode power is not comparable to the experimental data [30], [43], [25]. The effects of spatial hole burning on line width are usually considered in detail [25], [35], [26], [87], [88], [89] but the effect of spatial hole burning on mode spacing in the spectra is often not addressed. Facet reflectances are often neglected in above-threshold models, making direct comparison with real data quite difficult [25], [90]. Work that has examined evolution of above-threshold spectra over a range of injection currents has been primarily performed for index-coupled $\lambda/4$ phase-shifted DFB lasers (e.g. [25], [89], [87], [91], [33]). However, $\lambda/4$ phase shifted DFBs are no longer a dominant device in the world of telecommunications owing to the large spectral hole burning effects that are associated with them.

This chapter explains important methods for accounting for the response function (resolution) of the optical spectrum analyser prior to fitting above-threshold models to data. A method for eliminating thermal effects from the problem of fitting to above-threshold data is also presented. Important differences are identified between the above-threshold and below-threshold spectral data collected from truncated-well DFB lasers. The above-threshold model, which includes spatial hole burning, will be shown to fit to above-threshold data (with a precision that is unobtainable using a below-threshold model), and will be used to identify spatial hole burning effects on the spectra. Explanations for spatial hole burning effects on spectra will be given, and the role of standing waves in spatial hole burning will be examined.

8.2. Separating Thermal Effects from Spatial Hole Burning Effects

The above-threshold model that was presented in the previous chapter does not include thermal effects, so data used for comparison is taken using temperature compensation of the active region. In this procedure, an assumption is being made that if temperature is kept constant in the laser active region, then the wavelength of the lasing mode will remain the same. Thus, as injection currents are increased, the temperature of the laser mount is reduced, so that heating due to higher injection currents is countered by the cooling effect of the mount. All spectral data then has a lasing mode at approximately the same wavelength. Unfortunately, shifts in the position of the lasing mode that are due to carrier concentrations will be hidden by compensations in temperature.

Increasing the temperature of a DFB laser shifts the entire spectrum to longer wavelengths. The relative positions of the modes in the spectrum, and the width of the stop band, remain unchanged. The effects of temperature on the wavelength of the lasing mode can be modelled as a change in effective index for the laser [43]. A spectral shift caused by a change in effective index is often approximated for small perturbations using the equation $\lambda_1/\lambda_2 = n_{eff1}/n_{eff2}$, where n_{eff} is the average modal effective index of the laser, and λ is the lasing wavelength of the spectrum. Thus, any temperature shifting of the spectrum can be easily modelled by changing the effective index that is being used in the simulation.

The computer simulation starts an above-threshold simulation with a fit that was made to sub-threshold spectra. When a wavelength shift of the lasing mode occurs (due to the dependence of the index of refraction on carrier concentration), the effective index is adjusted using a Newton-Raphson solver so that the lasing mode of the simulation remains aligned with the lasing mode of the data. In this step, the simulated laser is effectively being temperature tuned just as the real laser was in data collection process. Thus the effect of temperature compensation for carrier induced wavelength shifting that occurs in the laboratory is correctly incorporated into the model.

8.3. The Resolution of the Lasing Mode

A major problem with comparing spectral data to simulated spectra is that the spectral data is modified by the response function of the Optical Spectrum Analyser (OSA) that collected it. Another problem is that the linewidth of a laser is so narrow that a simulation will miss most of the power in the lasing mode unless the sampling frequency is very high (e.g., sampling points at wavelengths separated by at most 10^{-14} m would be needed to capture the peak of the lasing mode). But simulating a spectrum at such a high resolution would mean a massive number of simulated wavelengths. This is unfeasible given the processing speeds of modern computers. These problems will be addressed in the following sections.

8.3.1. Simulating the High Power, Narrow Linewidth of a DFB Laser

The power in the lasing mode can be estimated by analysing the power transmission coefficient as a function of wavelength. The power transmission coefficient is simply $T_{11}^{-1}(\lambda)$ where T_{11} is the upper left-hand term in the 2×2 transfer-matrix that describes the optics of the DFB laser device (see chapter 2). The peak wavelength for the largest mode in the power transmission coefficient spectrum can be found using a bisectional search algorithm to find the $dT/d\lambda = 0$ point. A second bisectional search can then be used to find the half-maximum point. A similar algorithm was described in section 3.2 of the previous chapter.

Once the peak wavelength is found, the spectral output from a facet of the laser can be calculated. The peak magnitude and full-width-half-maximum are all that are needed for a complete mathematical description of a Lorentzian line shape, as was discussed in the previous chapter. The shape of the lasing mode will be a scaled value of the power transmission mode, and thus the halfwidth and power of the lasing mode can be calculated by the same methods as were used in the last chapter to calculate the photon density at a point in the laser. The basic equation for the area under a portion of a Lorentzian mode shape is

$$Z\int_{x1}^{x2}\frac{1}{x^2+a^2}dx=\frac{Z}{a}\left(\tan^{-1}\left(\frac{x2}{a}\right)-\tan^{-1}\left(\frac{x1}{a}\right)\right)$$

Eq. 8-1

where Z is an arbitrary scaling factor, a is the halfwidth of the mode, and x is λ-λ_{peak}. If the lasing mode peak is calculated to have power spectral density peak A, then $Z=a^2\times A$, so that the power in a wavelength range of width x_2-x_1 can be written as

$$P=a\times A\left(\tan^{-1}\left(\frac{x2}{a}\right)-\tan^{-1}\left(\frac{x1}{a}\right)\right).$$

Eq. 8-2

The sampling frequency for the simulated spectrum is high enough that the discrete representation of the continuous spectrum is very accurate everywhere other than the lasing mode. The implicit approximation is that power spectral density is constant over a width of one sampling unit, and that the power spectral density at any wavelength is represented by the nearest sampling point. Thus, the power calculated in Eq. 8-2 for wavelength width x_2-x_1 must be converted into an effective power spectral density (i.e., psd=P/(x_2-x_1)). This special treatment is given to all points that fall near the maximum of the lasing mode.

8.3.2. Dealing with the Response Function of the OSA

The response function of the OSA limits the resolution of the data. The response function was measured to have a half-width of 0.058 nm, and is known to have a dynamic range of approximately 70dB over a range of 1 nm and approximately 58dB over a range of 0.5 nm [92]. The best analytic description for the response function near the lasing peak was obtained by fitting that part of the response function to data. The dynamic range limit far from the response peak (most likely due to scattered light from the OSA grating) was found by fitting to data. An empirical analytic function for the OSA response function was thereby discovered to be

$$F(x) = 10^{-\left(7.473 + \frac{-7.473}{1+\left|\frac{x}{0.15\times10^{-9}}\right|^{3/2}}\right)}.$$

Eq. 8-3

This function is shown in Fig. 8-1 below, where it is compared to an OSA measurement of the lasing mode.

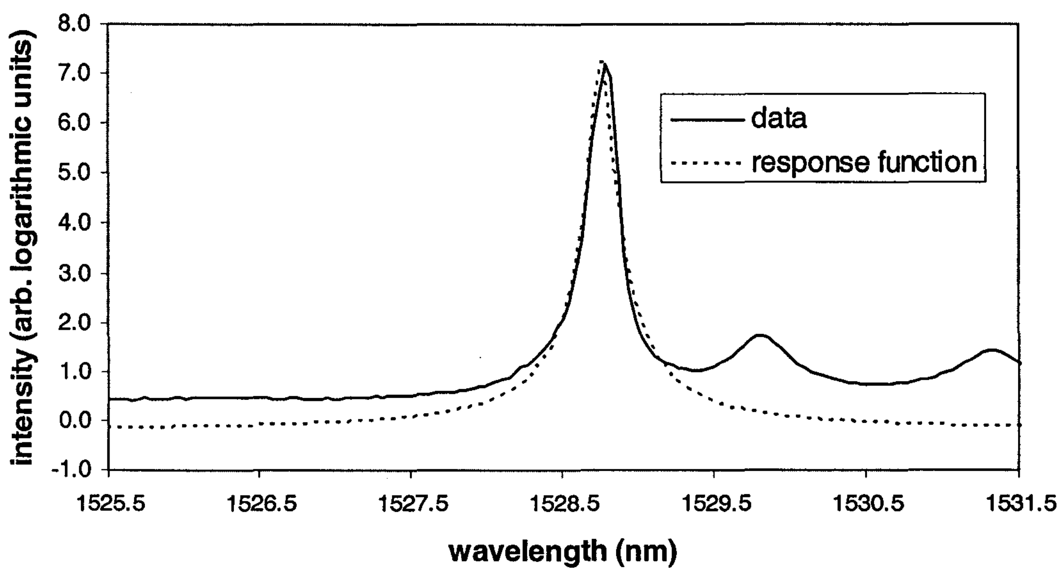

Fig. 8-1 The response function of the OSA is compared to a lasing mode that was collected using the OSA.

The effect of the response function must be taken into consideration if a model is to be compared to data. The usual solution for below-threshold spectra [42] is to convolve the OSA response function with the simulated laser spectrum prior to comparison with data. This method was attempted for above-threshold data. Unfortunately, the side modes of the simulated spectrum are heavily dependant on the height of the simulated lasing mode due to the wide tails of the response function. It is therefore extremely difficult to compare any of the features of the data with the simulation unless the simulated lasing mode has approximately the same power as in the data. That the simulated mode should have the same power as the data is obviously a desirable end result, but maintaining a correct lasing mode power throughout the fitting process is impossible. The power in the simulated lasing mode is extremely sensitive to all the variables in the model, especially facet phase, facet reflectivity, coupling coefficient, and differential gain. The task of adjusting variables so that the model matches the data is made extremely difficult if the two spectra are only aligned for comparison when the power in the lasing mode is correct. Furthermore, an automated fitting algorithm [57],[58] is totally useless if alignment of the two spectra is entirely dependant on the height of the very sensitive simulated lasing mode.

An alternative to convolving the model with the response function is deconvolving the data with respect to the response function. Deconvolving the data using the response function of the OSA will result in a very narrow delta-function-like lasing mode. The resulting spectrum violates the Nyquist sampling theorem. Side effects of this include misplacement of the delta function and ringing (subsidiary oscillations) around the base of the lasing mode [93],[94],[95].

The problems associated with deconvolution of discretely sampled intensities are common in the field of astronomy, where optical considerations limit the resolution of point sources (stars), and the image is recorded using a CCD. A new method has recently been developed and successfully tested by astronomers for partially deconvolving data and thereby avoiding the usual errors that arise from violating the sampling theorem [93],[94]. This new method breaks the known (or estimated) response function into a convolution of a desired response function with a residual function. That is, if $F(x)$ is the response function then

$$F(x) = S(x) * R(x)$$

Eq. 8-4

where $R(x)$ is the desired response, or resolution, and $S(x)$ is the residual response. By deconvolving the actual response function with the desired response function, the residual response function is obtained. Thus, in order to obtain data with a resolution that does not defy the sampling theorem, and yet doesn't have the wide tails associated with $F(x)$, the data should be deconvolved with $S(x)$ (the residual response function). In turn, the model should be convolved with the desired response function $R(x)$, so that both the model and the data have the same resolution. The unwanted effects of the wide tails of *F(x)* are thereby eliminated, and fitting the model to data is a relatively simple matter. Convolution and deconvolution operations can be efficiently implemented on a computer by first performing a Fast Fourier Transform on all spectra and response functions [96]. Convolution is then simply a matter of multiplication and division, after which an inverse Fast Fourier Transform returns the spectra back to their wavelength domain.

8.4. Comparison with Data

The above-threshold model that has been described in the previous two chapters has been compared with above-threshold spectral data. Spatial hole burning effects in the spectra are identified by comparison with below-threshold spectra, and explanations for these effects are presented. The above-threshold model is shown to predict correctly the above-threshold spectra, using parameters that were obtained by fitting to below-threshold data with a below-threshold model. The role of facet phase in spatial hole burning phenomena is examined, and the importance of the standing wave effect in spatial hole burning is demonstrated. The longitudinal profiles of carrier distribution, spontaneous emission, gain, and index of refraction will also be discussed. The lasers used in this chapter are truncated-well DFB lasers, with a 5:0 quantum well ratio between the high index and low index areas as shown in Fig. 8-2 below.

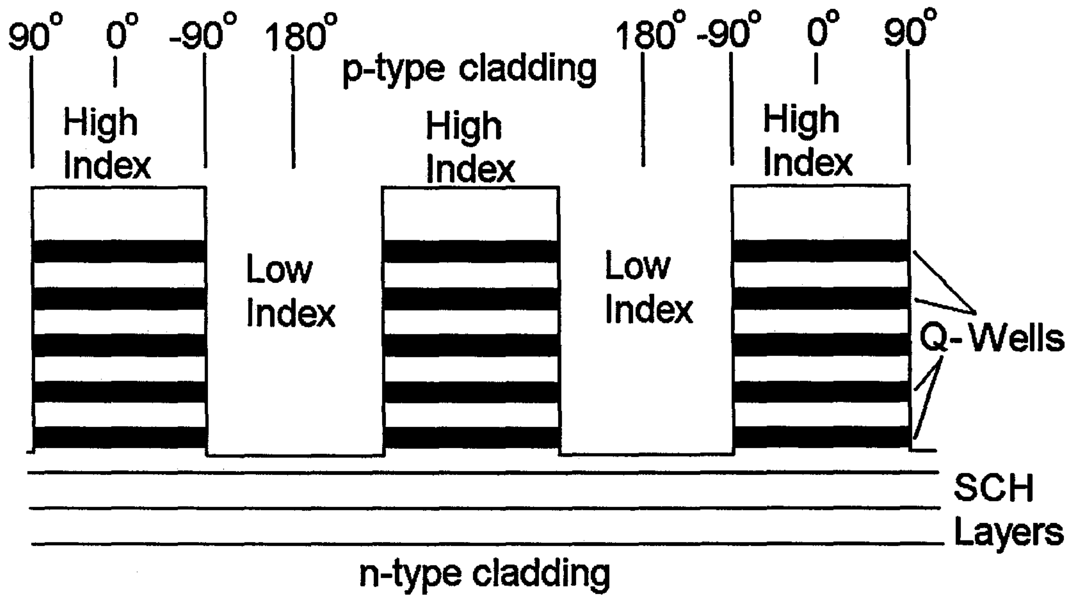

Fig. 8-2 Schematic of a 5:0 truncated-well laser grating. Phase convention is included.

8.4.1. Comparison of Below-threshold Data with Above-threshold Data

Other than the exponential increase in the power of the lasing mode, the differences between above-threshold and below-threshold spectra are subtle in truncated-well gain-coupled lasers. To compare above-threshold data with below-threshold data, the two spectra must be overlaid on a graph with two separate vertical axes. The vertical axis for the above-threshold data is logarithmic, while the axis for the below-threshold data is linear. Comparisons of below-threshold data and above-threshold data are made for two different lasers in Fig. 8-3, Fig. 8-4, Fig. 8-5, and Fig. 8-6. All the above-threshold simulations and data are for a 60 mA input current. Threshold for these lasers was in the vicinity of 12 mA.

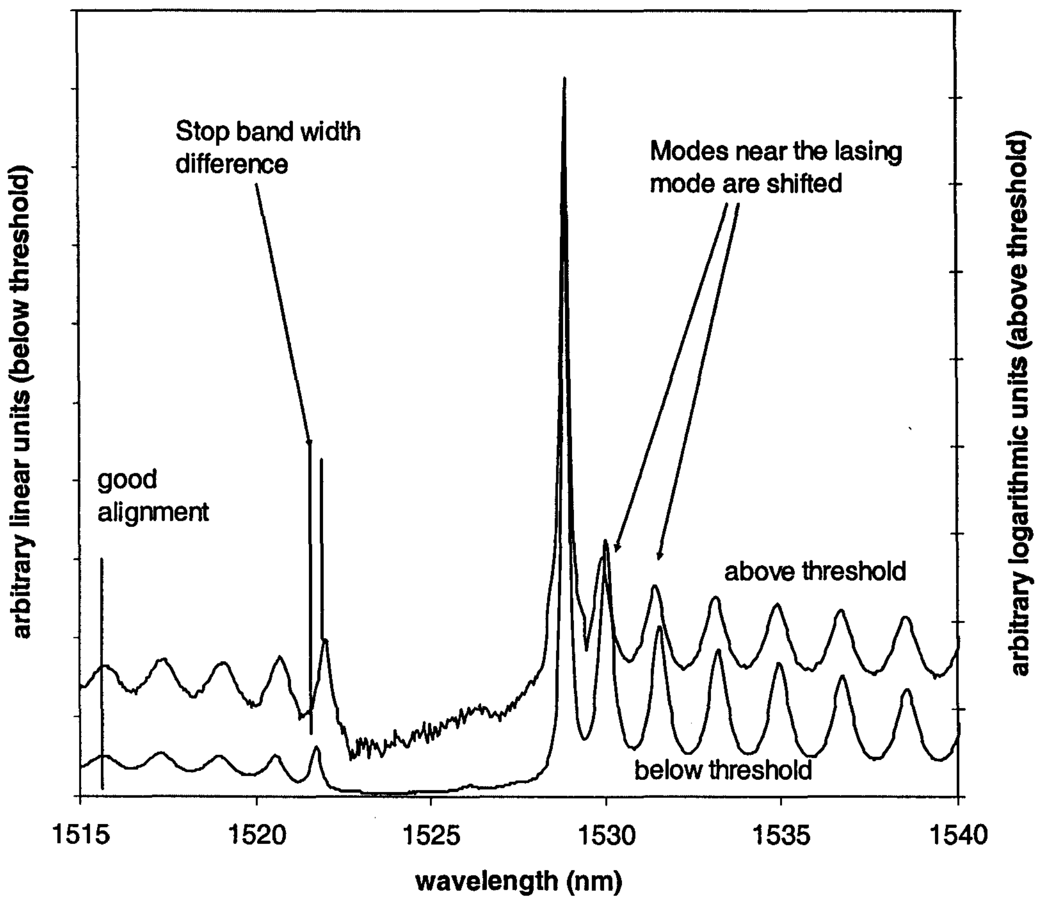

Fig. 8-3 Below-threshold data and above-threshold data from the front facet of a gain-coupled DFB laser (laser 1). Differences in the shape of the spectrum are labelled.

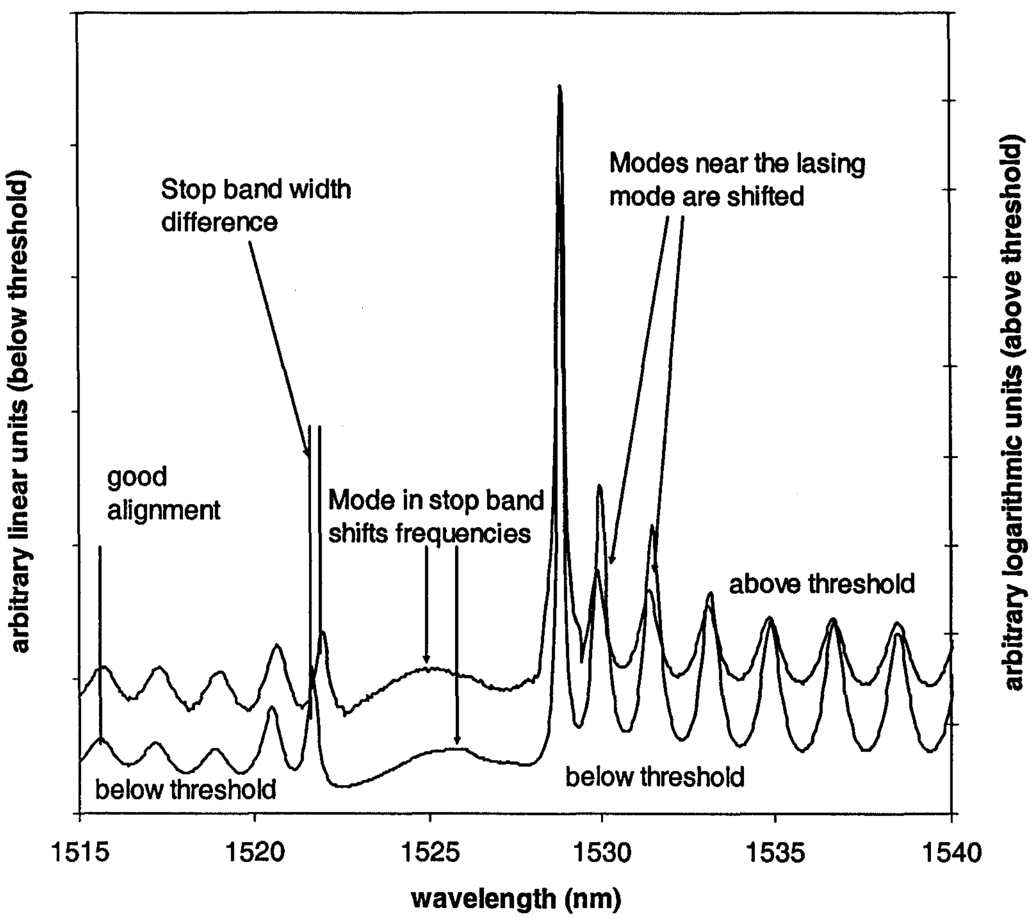

Fig. 8-4 Below-threshold data and above-threshold data from the back facet of a gain-coupled DFB laser (Laser 1). Differences in the shapes of the spectra are labelled.

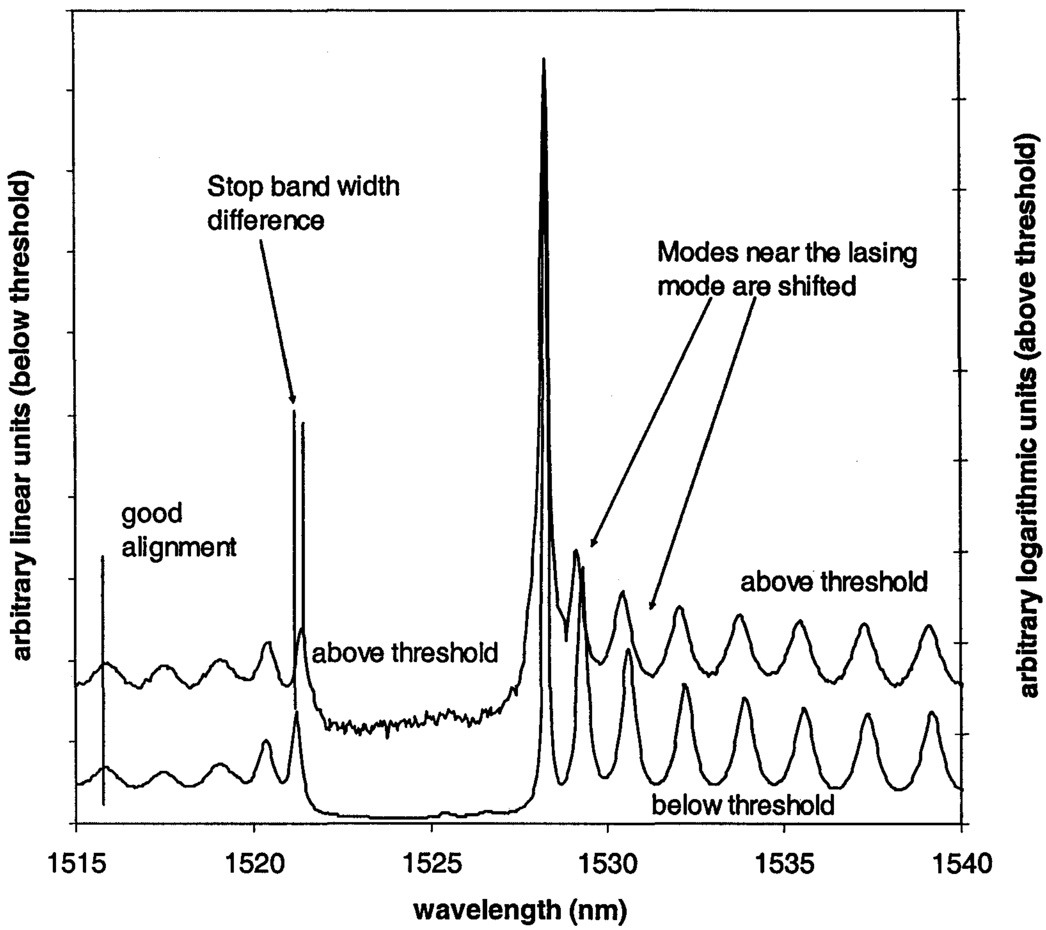

Fig. 8-5 Below-threshold data and above-threshold data from the front facet of a gain-coupled DFB laser (laser 3). Differences in the shapes of the spectra are labelled.

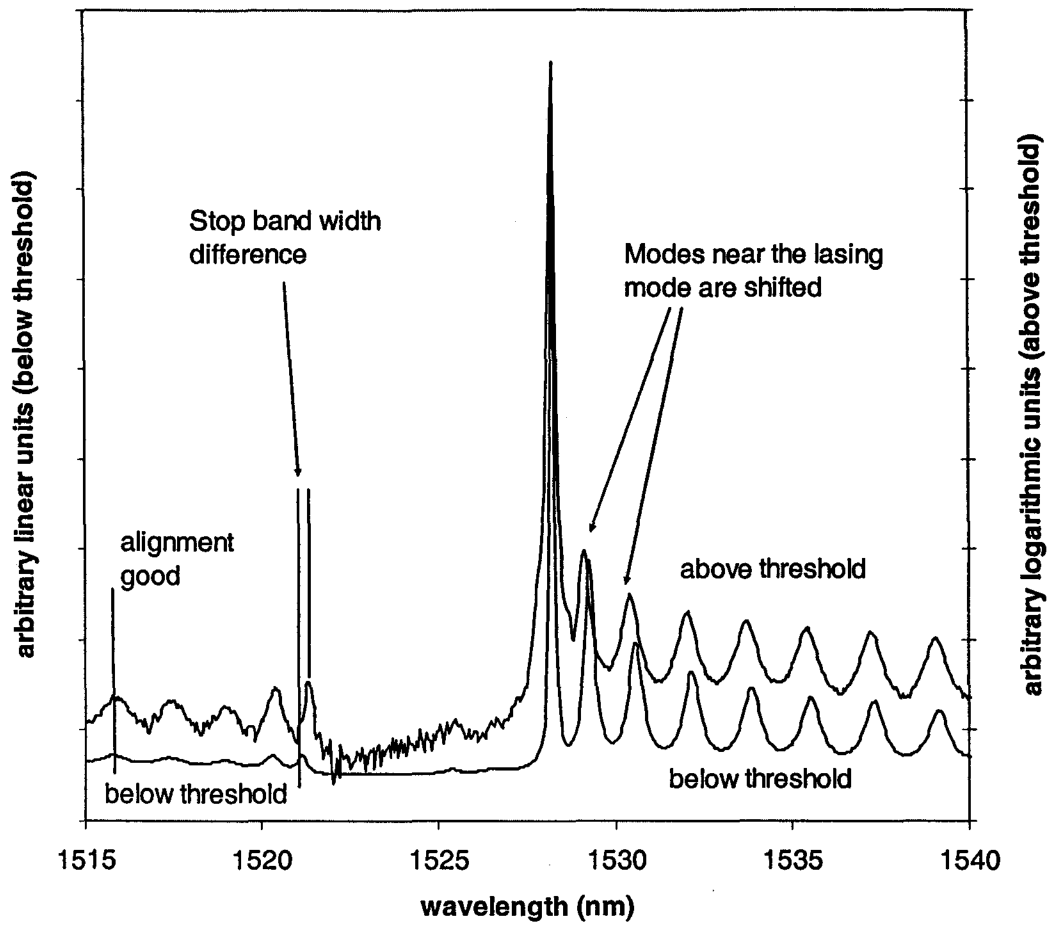

Fig. 8-6 Below-threshold data and above-threshold data from the back facet of a gain-coupled DFB laser (Laser 3). Differences in the shapes of the spectra are labelled.

The spectra in the above figures are plotted over a 25 nm range, though data over a range of 72 nm is used for the fits that are presented later in this chapter. The shortened wavelength range in the graphs facilitates comparison of small wavelength shifts. Both facets were fitted simultaneously. The main differences between below-threshold and above-threshold data are labelled. In both lasers, the stop band becomes narrower, but short wavelength modes that are not especially close to the stop band remain in the same position. Also in both lasers, the modes near the long wavelength Bragg mode move to shorter wavelengths, but further from the stop band the modes do not change position. In laser 1, there is an extra mode within the stop band of the back facet spectrum [17],[18]. This band gap mode is caused by the phase of the back facet reflection with respect to the internal grating, and has shifted in position with increased injection current. These above-threshold characteristics can be used to test the validity of the above-threshold model.

8.4.2. Below-threshold and Above-threshold Fits

Below-threshold fits for both fits are show in Fig. 8-7, Fig. 8-8, Fig. 8-9, and Fig. 8-10 below. Estimates of laser parameters that were obtained by fitting to the below-threshold data were later used for above-threshold fits. Expanded views around the stop band are included in each figure for better comparison of detail. The front and back facets were fitted simultaneously, over a wavelength range of 72 nm.

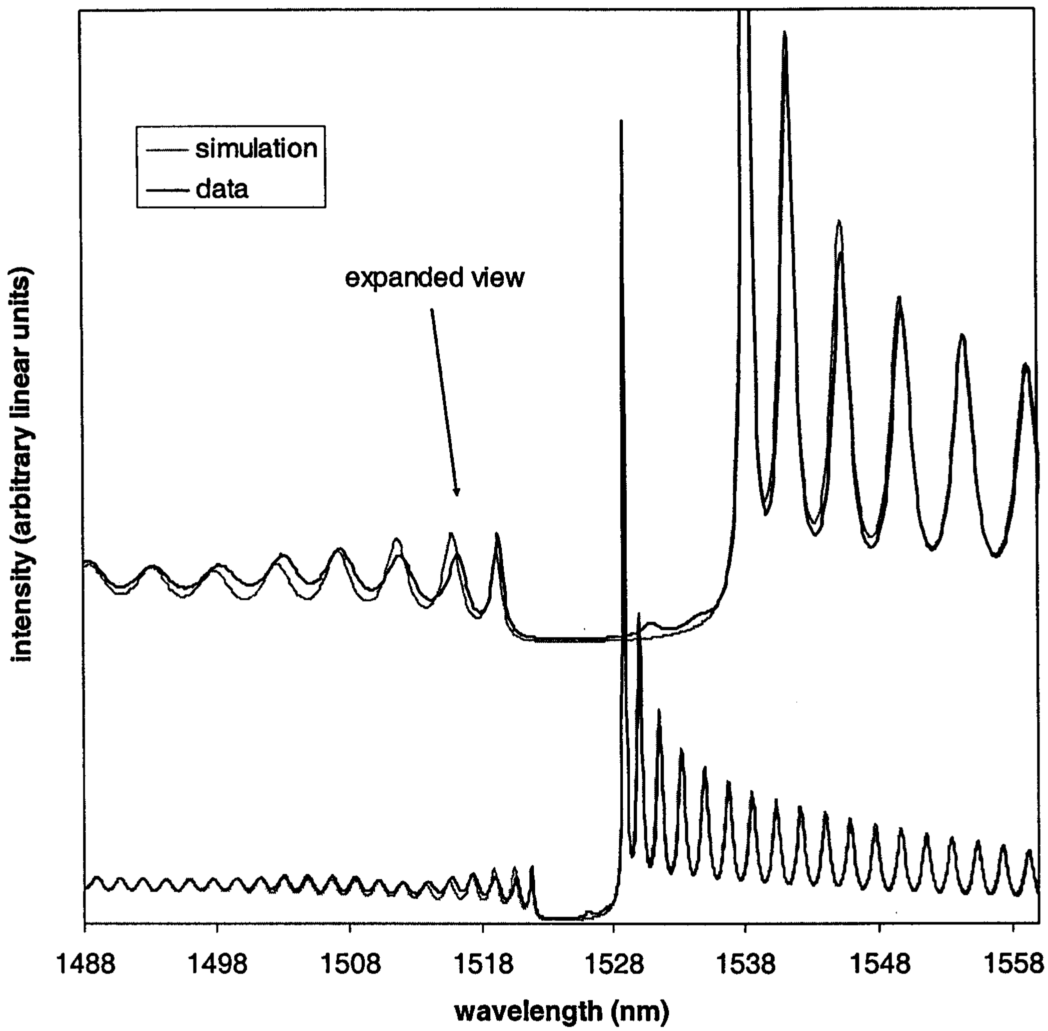

Fig. 8-7 A fit to the below-threshold spectrum from the front facet of laser 1, using the below-threshold model. An expanded view is included. Front and rear facet data were fitted simultaneously.

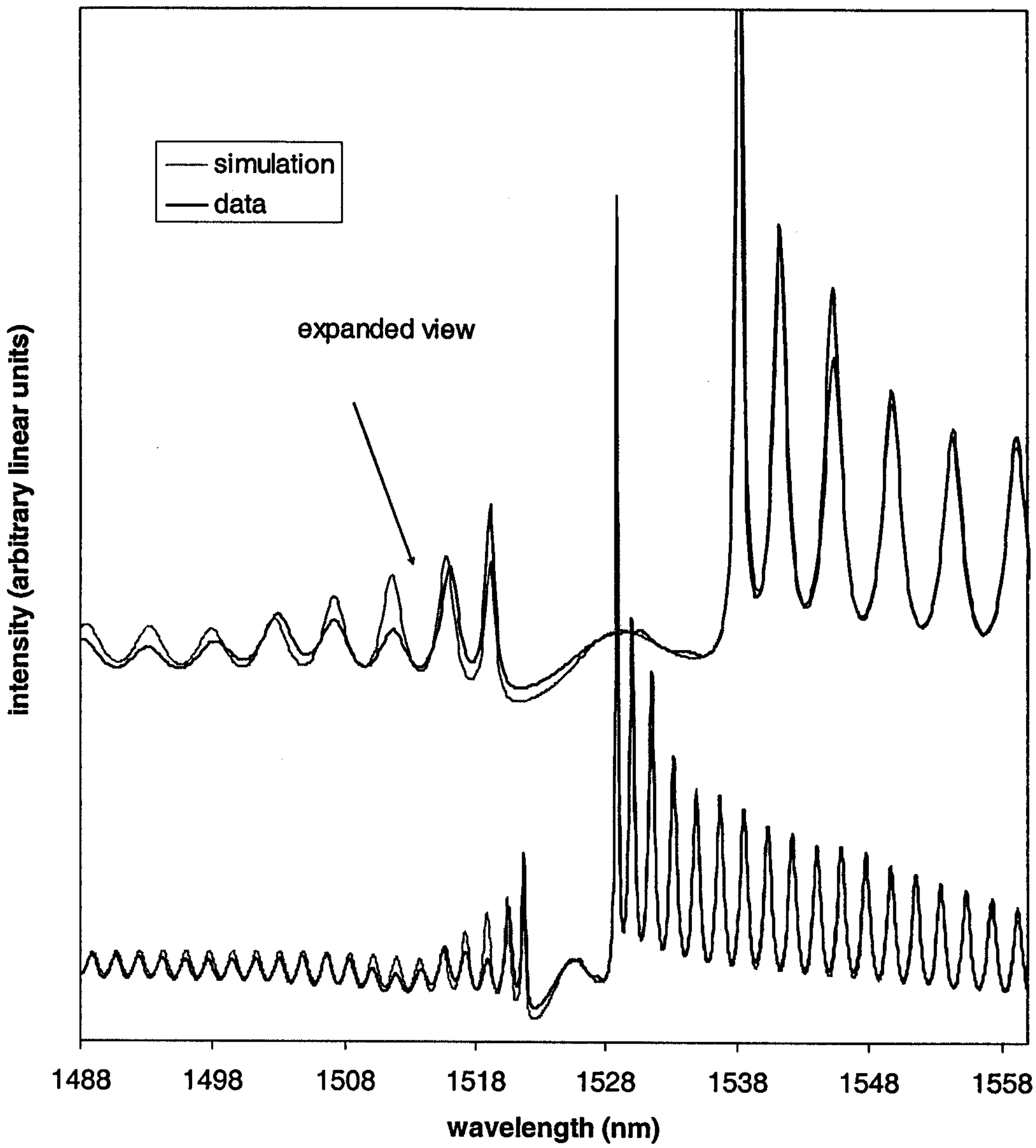

Fig. 8-8 A fit to the below-threshold spectrum from the back facet of laser 1, using the below-threshold model. An expanded view is included. Front and rear facet data were fitted simultaneously.

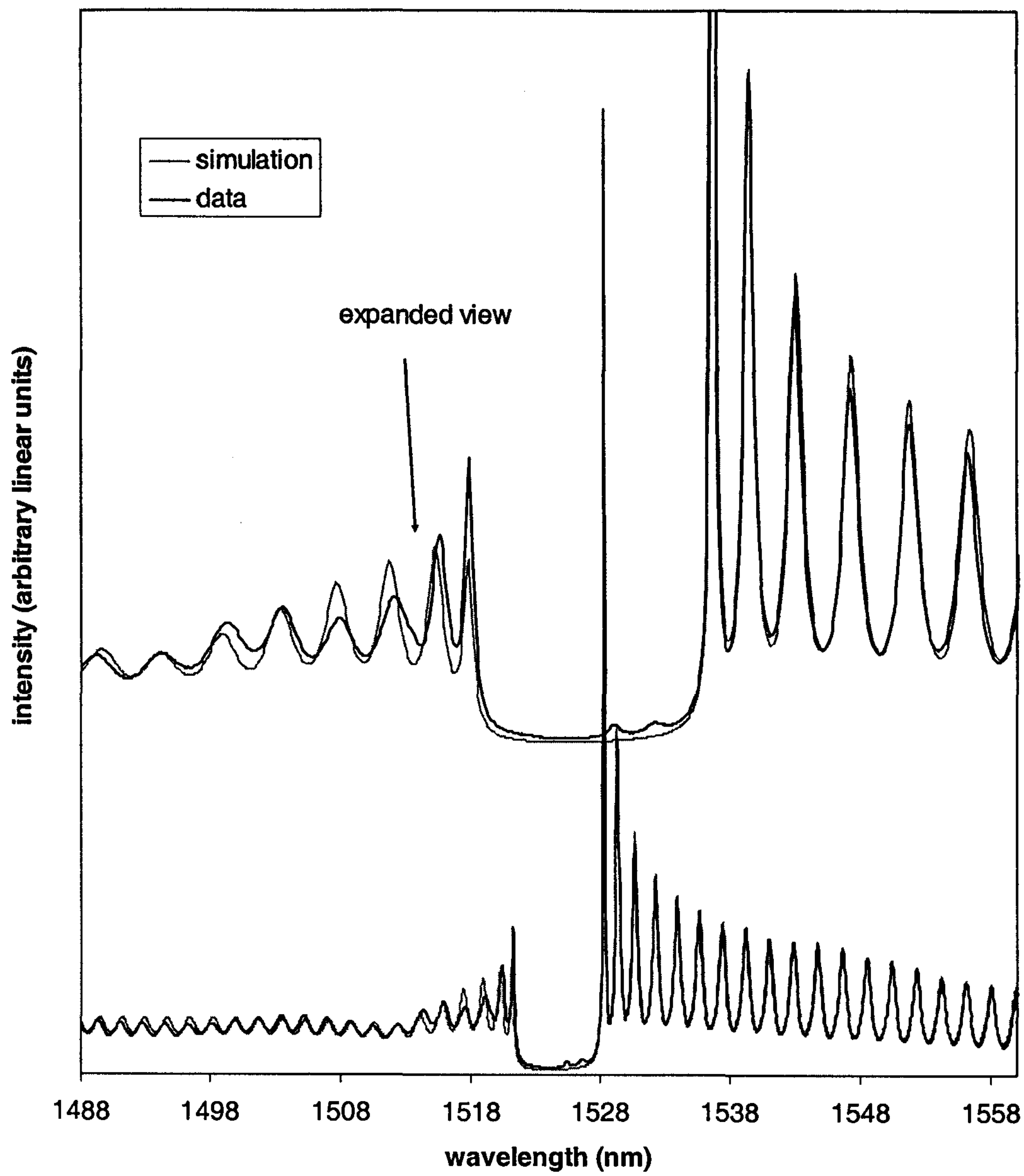

Fig. 8-9 A fit to the below-threshold spectrum from the front facet of laser 3, using the below-threshold model. An expanded view is included. Front and rear facet data were fitted simultaneously.

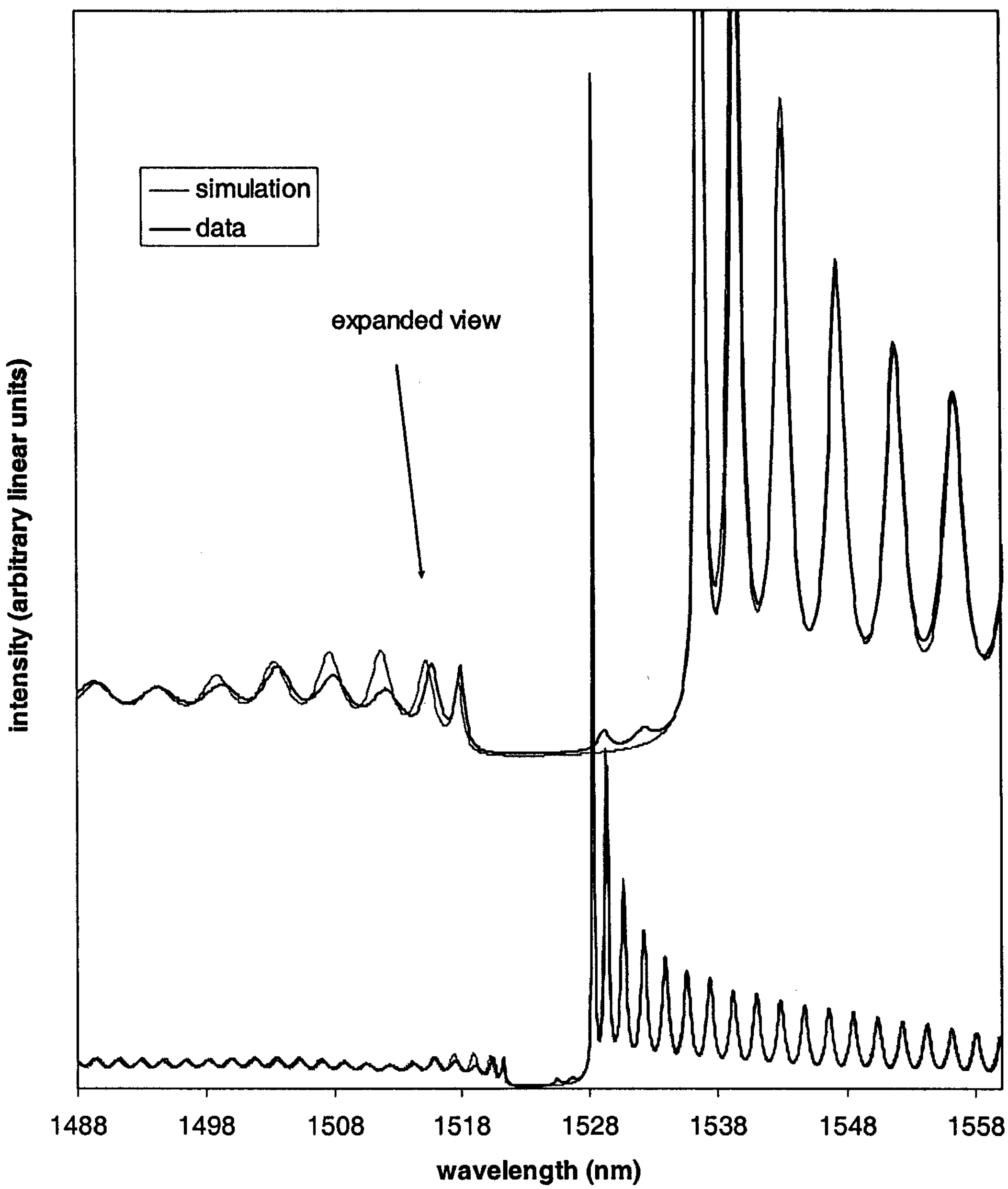

Fig. 8-10 A fit to the below-threshold spectrum from the back facet of laser 3, using the below-threshold model. An expanded view is included. Front and rear facet data were fitted simultaneously.

The parameters that were obtained from the below-threshold fits were used in the above-threshold model. The above-threshold model is able to modify the effective index to compensate for thermal effects, and also modifies the index of refraction, spontaneous emission rate, and gain, in each grating tooth based on the solution of the photon-carrier rate equations. All other parameters are held constant based on the values obtained from the below-threshold fit. Above-threshold simulations and data are shown in Fig. 8-11, Fig. 8-12, Fig. 8-13, and Fig. 8-14 below. Of special interest is the very good alignment of the modes next to the long wavelength Bragg mode. Also note the good alignment of the fit with data for the mode that is inside the stop band. A final point of interest is that the simulated stop band width is correct. All of these features result from higher carrier density or spatial hole burning (see section 8.4.3). Referring back to Fig. 8-3, Fig. 8-4, Fig. 8-5, and Fig. 8-6, which compare above-threshold data with below-threshold data, it is clear that the above-threshold model has predicted correctly the above-threshold features. In Fig. 8-13 and Fig. 8-14, noise in the stop band resulted in a poor fit in the stop band region. It is important to keep in mind, however, that the plots are on a logarithmic scale, and small differences around the stop band are therefore grossly exaggerated.

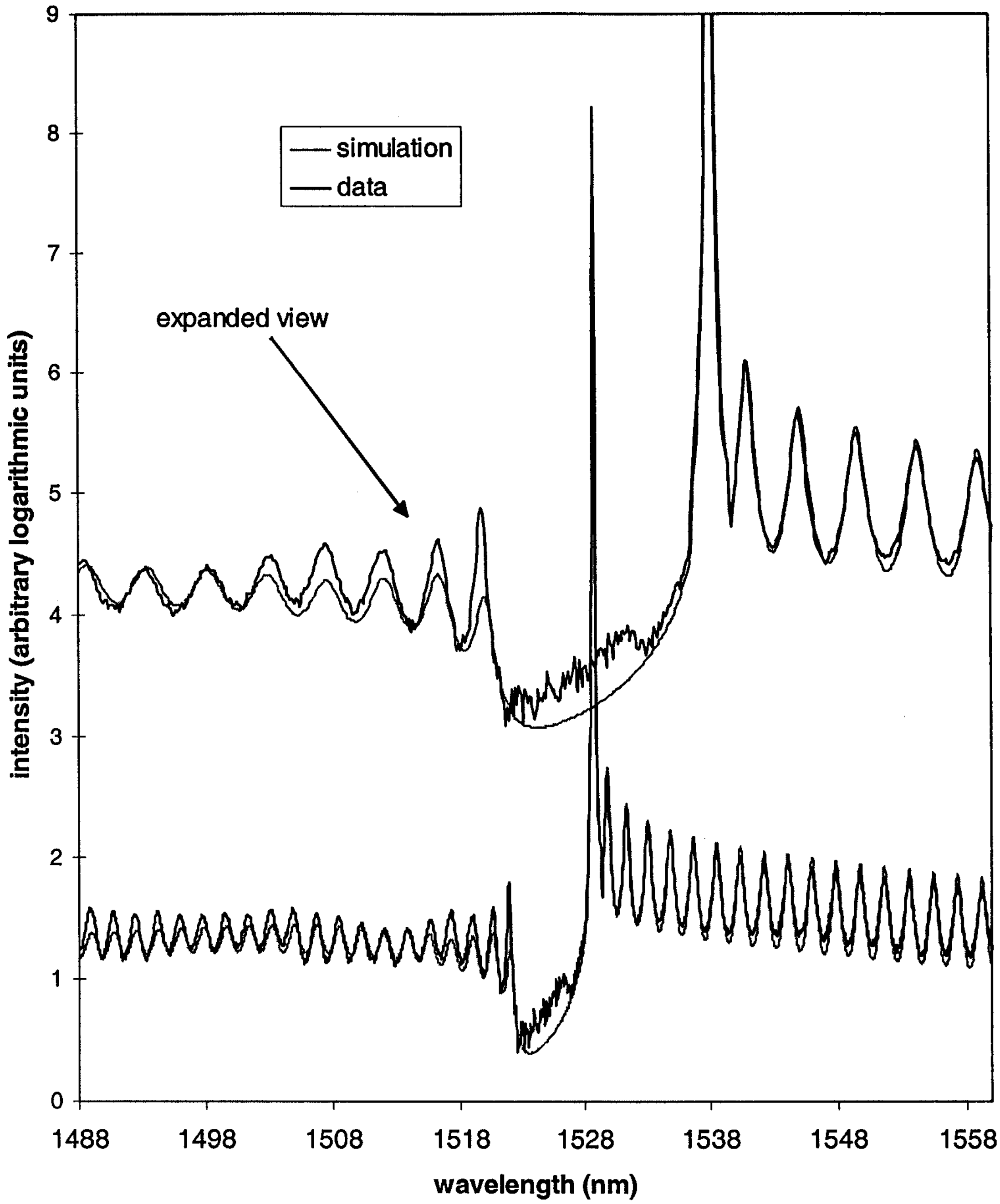

Fig. 8-11 A simulation of the above-threshold spectrum from the front facet of laser 1, using the above-threshold model. An expanded view is included. The values of all variables used in the front and back facet simulations are identical.

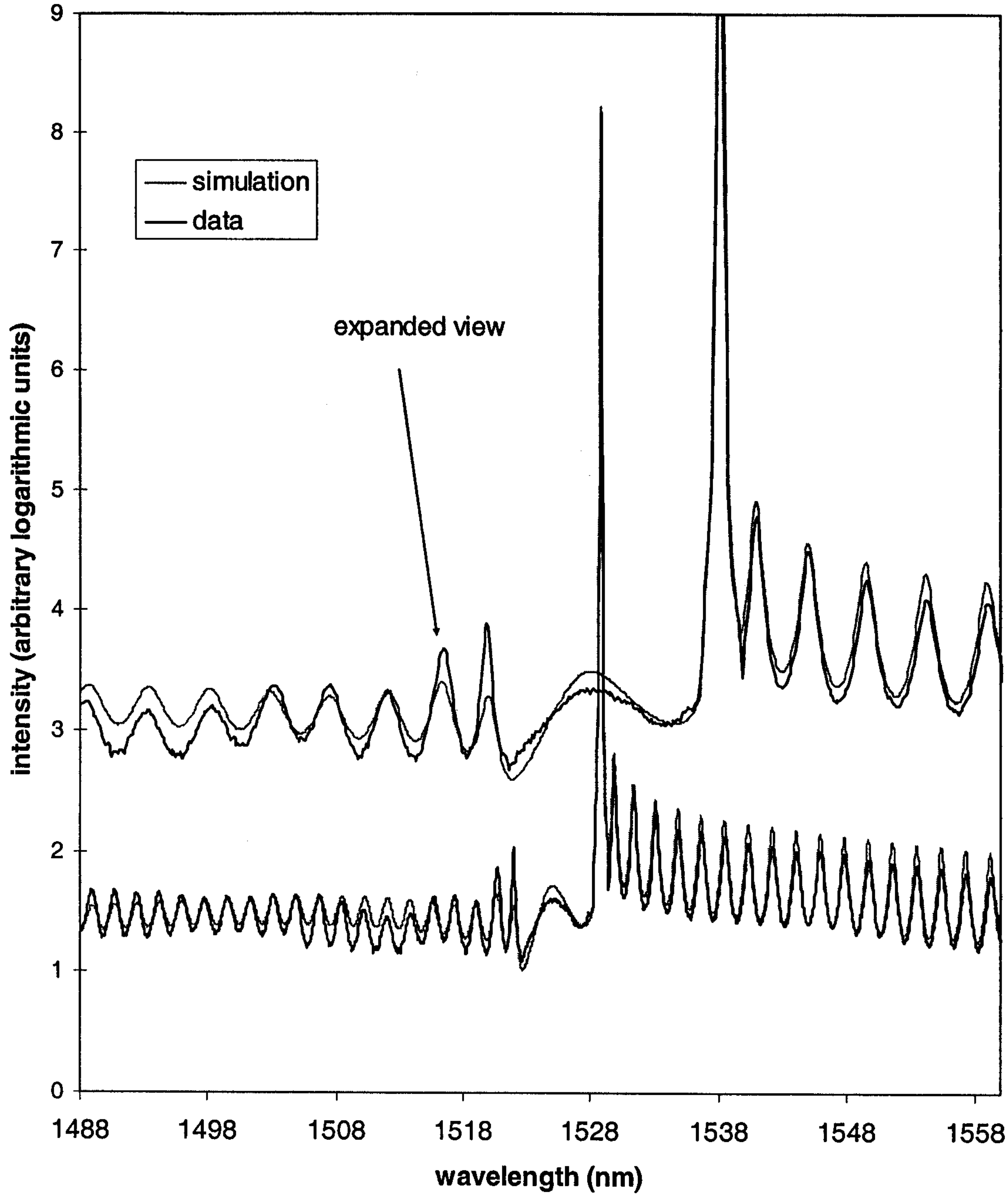

Fig. 8-12 A simulation of the above-threshold spectrum from the back facet of laser 1, using the above-threshold model. An expanded view is included. The values of all variables used in the front and back facet simulations are identical.

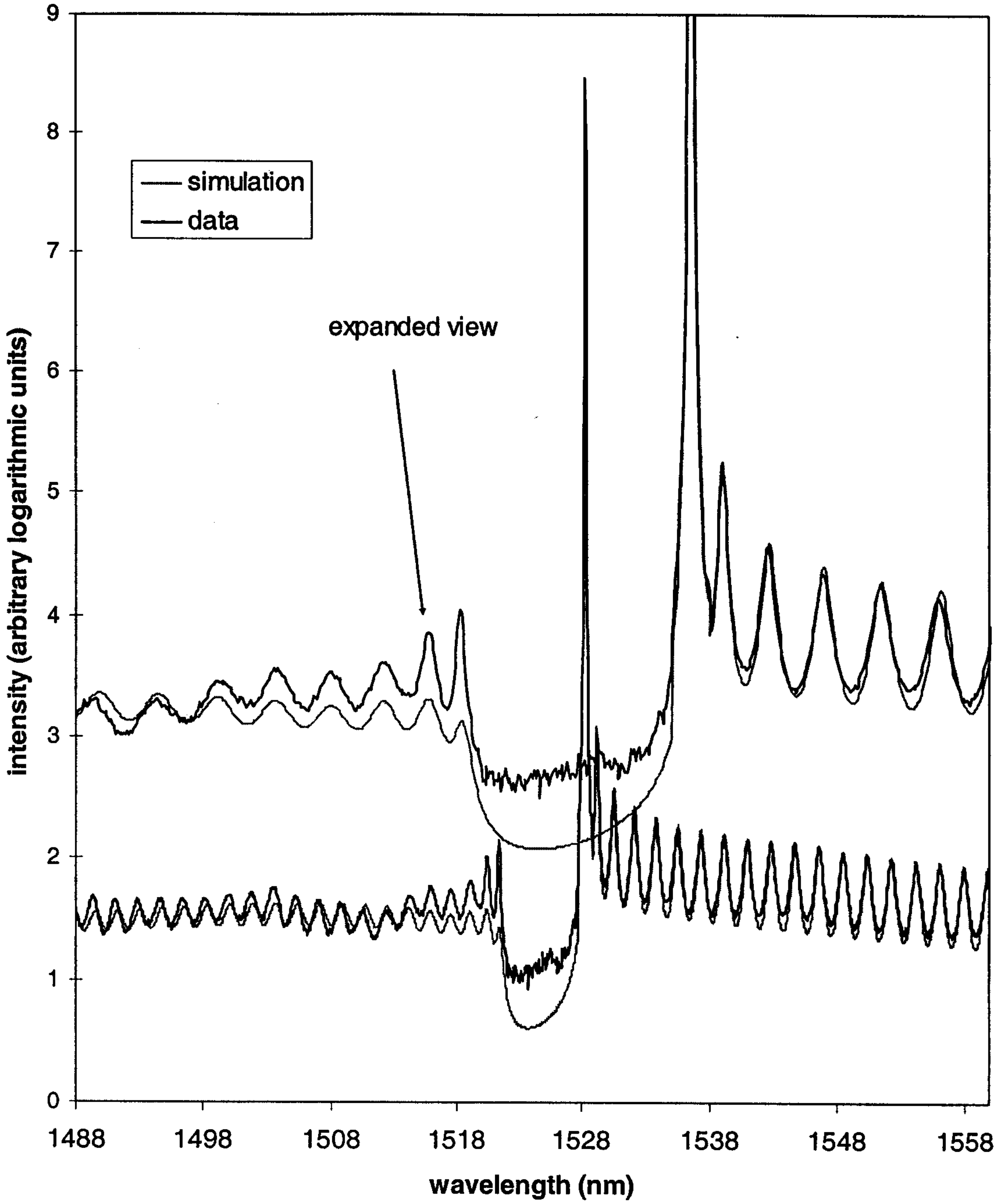

Fig. 8-13 A simulation of the above-threshold spectrum from the front facet of laser 3, using the above-threshold model. An expanded view is included. The values of all parameters for the front and back facet simulations are identical.

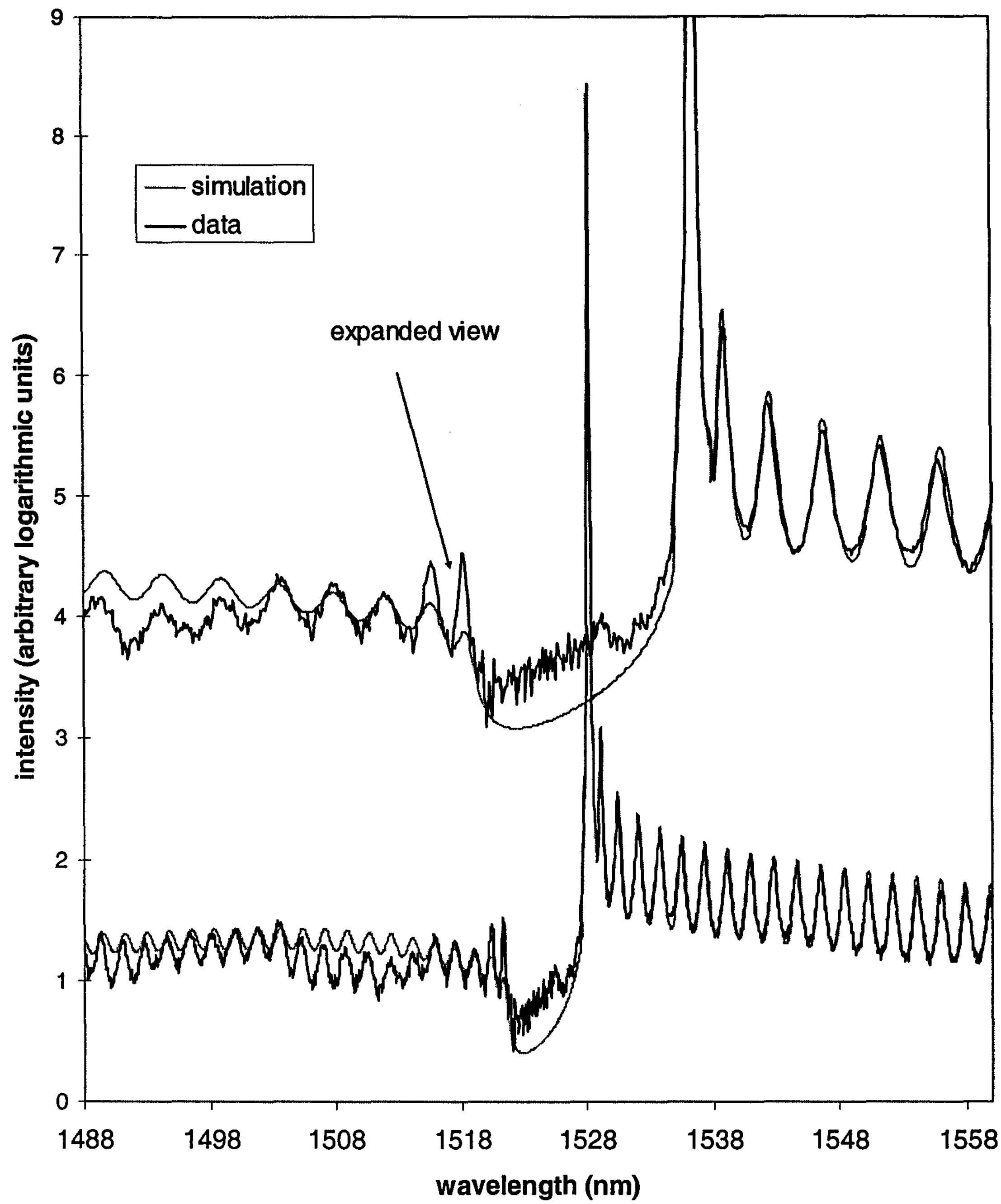

Fig. 8-14 A simulation of the above-threshold spectrum from the front facet of laser 3, using the above-threshold model. An expanded view is included. The values of all parameters for the front and back facet simulations are identical.

8.4.3. Explanation of Above-threshold Phenomena

The above-threshold fits, using the above-threshold model, are of good quality in the sense that they correctly predict the height of the lasing mode, and correctly predict above-threshold spectral phenomena. The fact that a good fit is made to the data does not in itself prove that spatial hole burning is responsible for the phenomena being seen in the above-threshold spectra. To show that the rate equations and intensity distribution calculations are needed in the above-threshold model, a fit to data should be attempted without the rate equations and intensity distribution calculation results. A simple method for ignoring many of the effects of spatial hole burning is to set the differential index (dn_R/dN) to zero. Setting the differential index to zero creates a model with a longitudinally homogeneous grating profile for the real part of the refractive index (i.e., the effects of increased carrier concentration and spatial holeburning on refractive index are removed). Comparing this simplified model to the full above-threshold model will highlight the effects of an inhomogeneous refractive index on above-threshold spectra (i.e, it will highlight the effects of spatial hole burning).

The simulation that was obtained when neglecting spatial hole burning effects on local refractive index, is compared to the data in Fig. 8-15 and Fig. 8-16. The stop band is too wide, the position of the band gap mode is incorrect, and the side modes near the lasing mode are misaligned and too large. Clearly, these details can only be explained by the effects of carrier density on refractive index. As a second comparison, the simulated spectra with and without (dn_R/dN) = 0 are shown in Fig. 8-17 and Fig. 8-18.

These two figures are useful when compared to Fig. 8-3 and Fig. 8-4 because the differences between the simulations are similar to the differences between above-threshold and below-threshold data. The importance of the full above-threshold model is thereby highlighted.

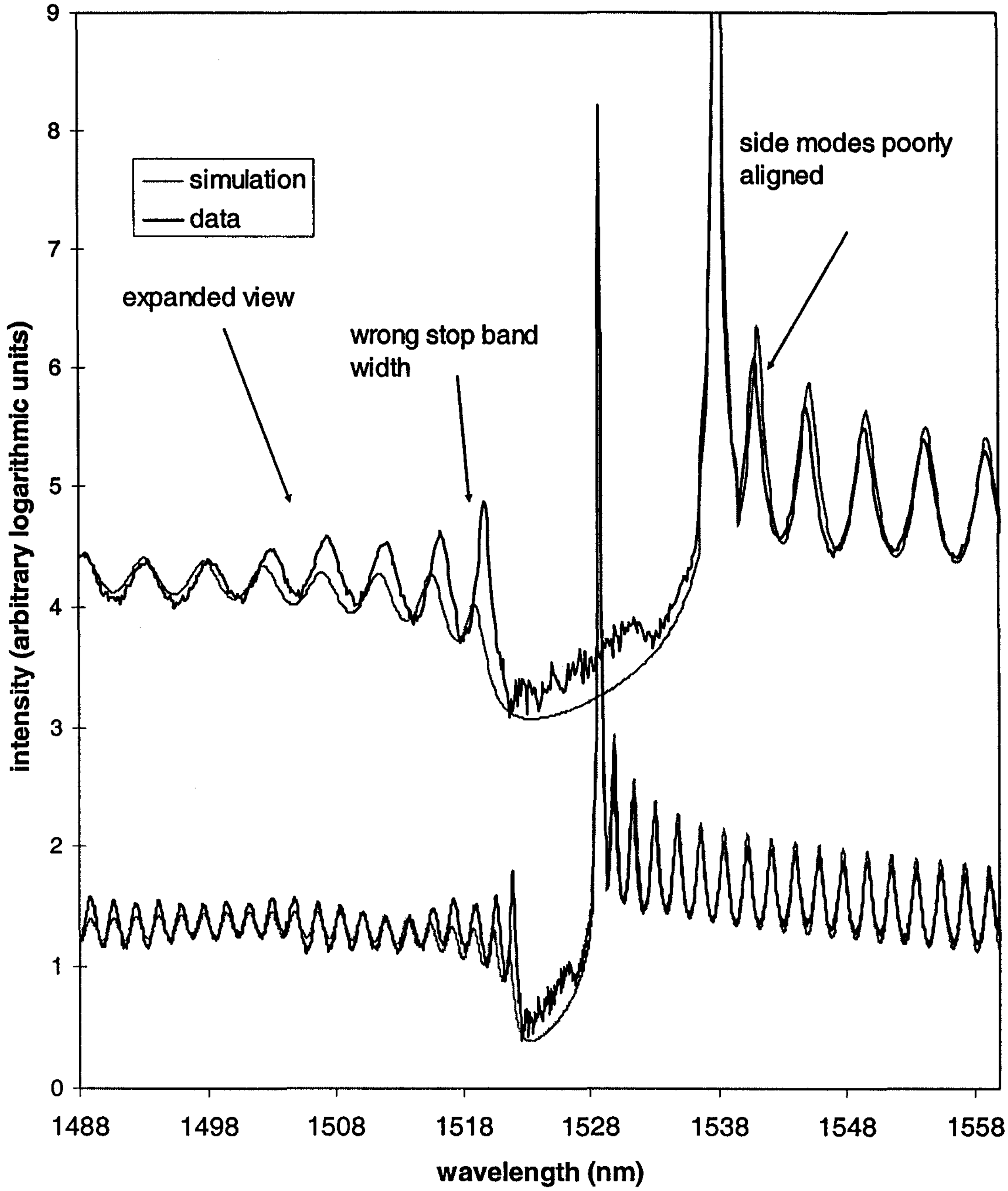

Fig. 8-15 Comparison of a simulation with data for the front facet of laser 1, when the differential index of refraction (dn_R/dN) is neglected.

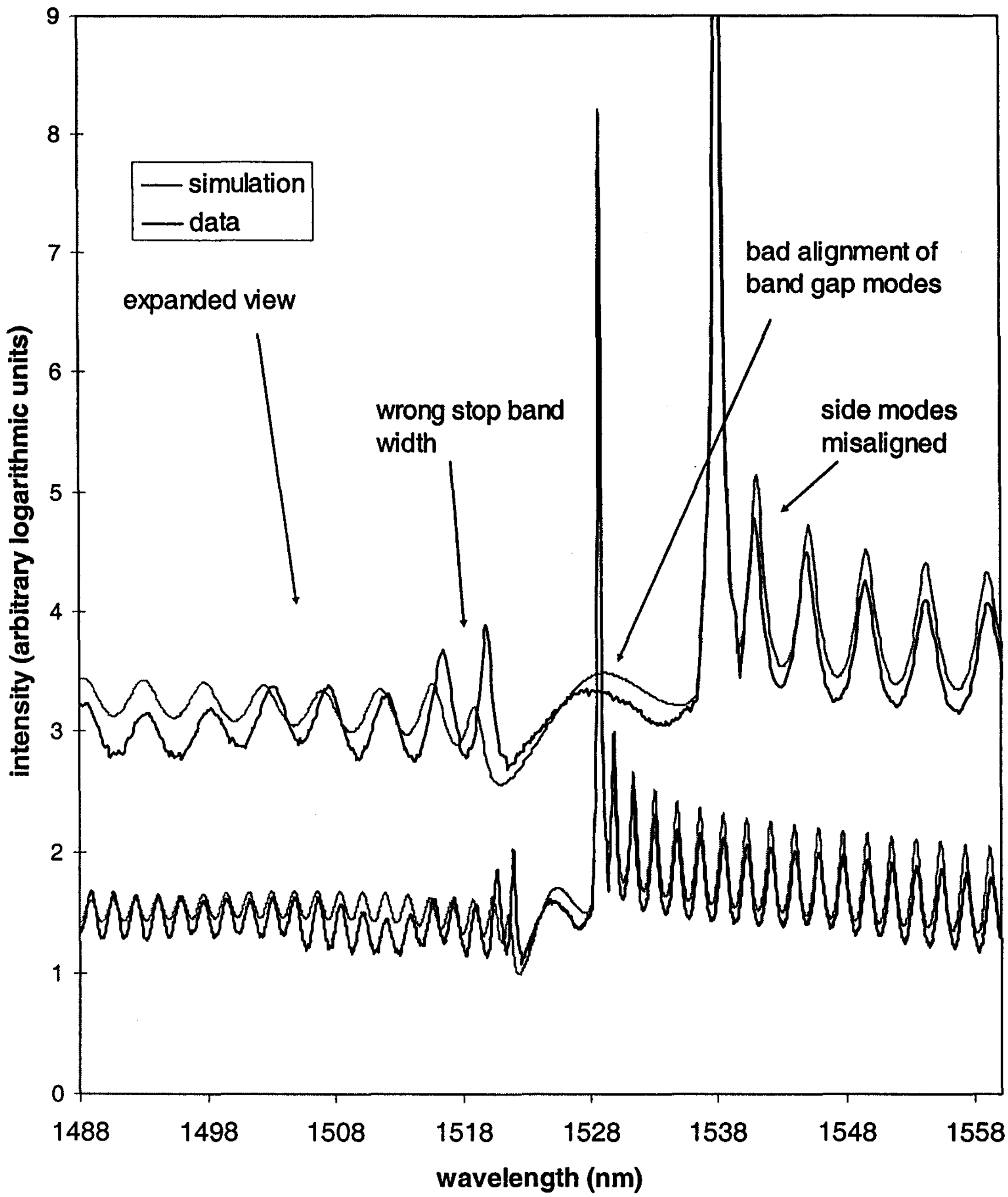

Fig. 8-16 Comparison of a simulation with data from the back facet of laser 1, when the differential index of refraction (dn_R/dN) is neglected.

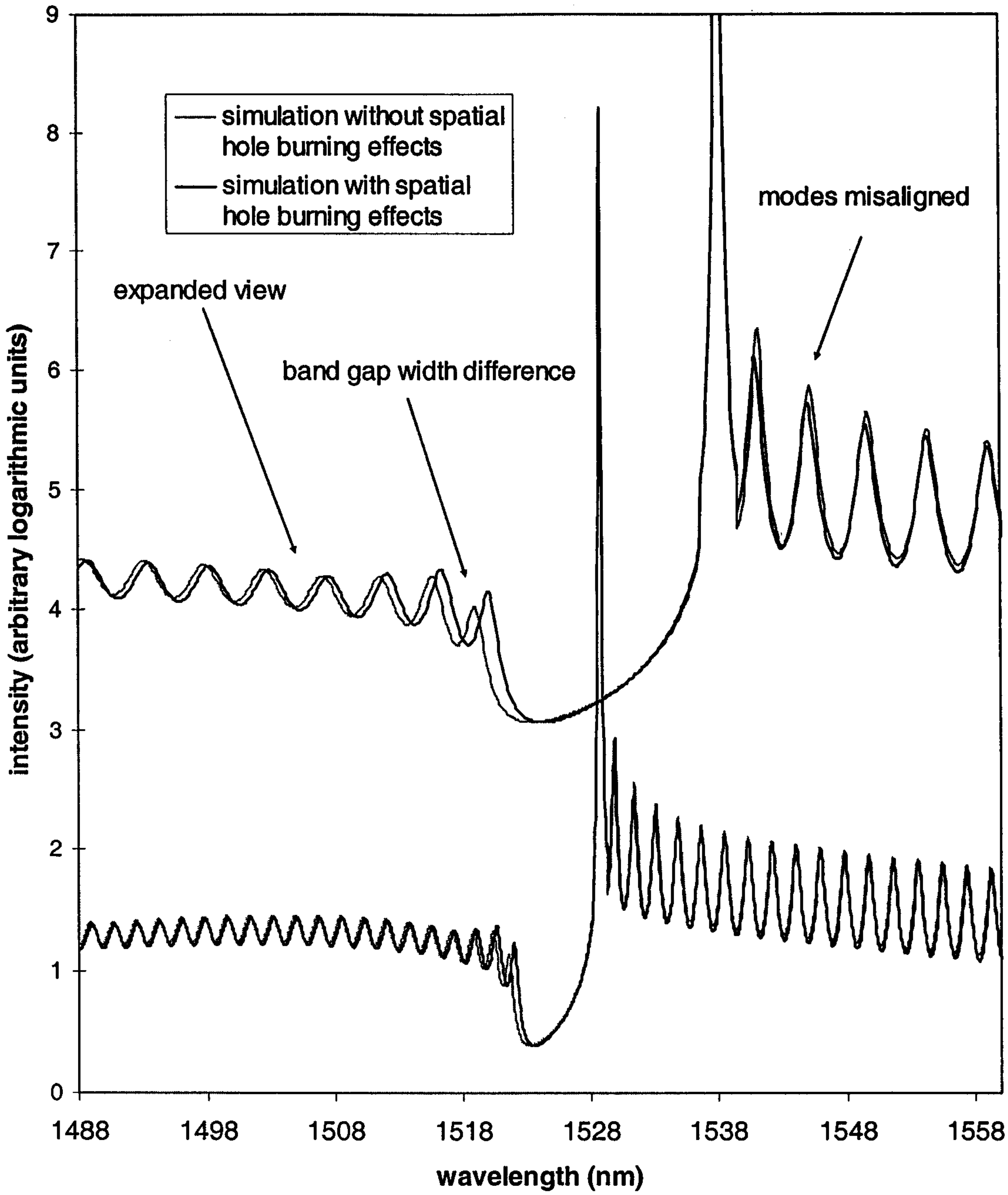

Fig. 8-17 Comparison of above-threshold simulations for the front facet of laser 1, one with the differential index of refraction (dn_R/dN) neglected (grey line), and one with complete spatial hole burning and carrier effects.

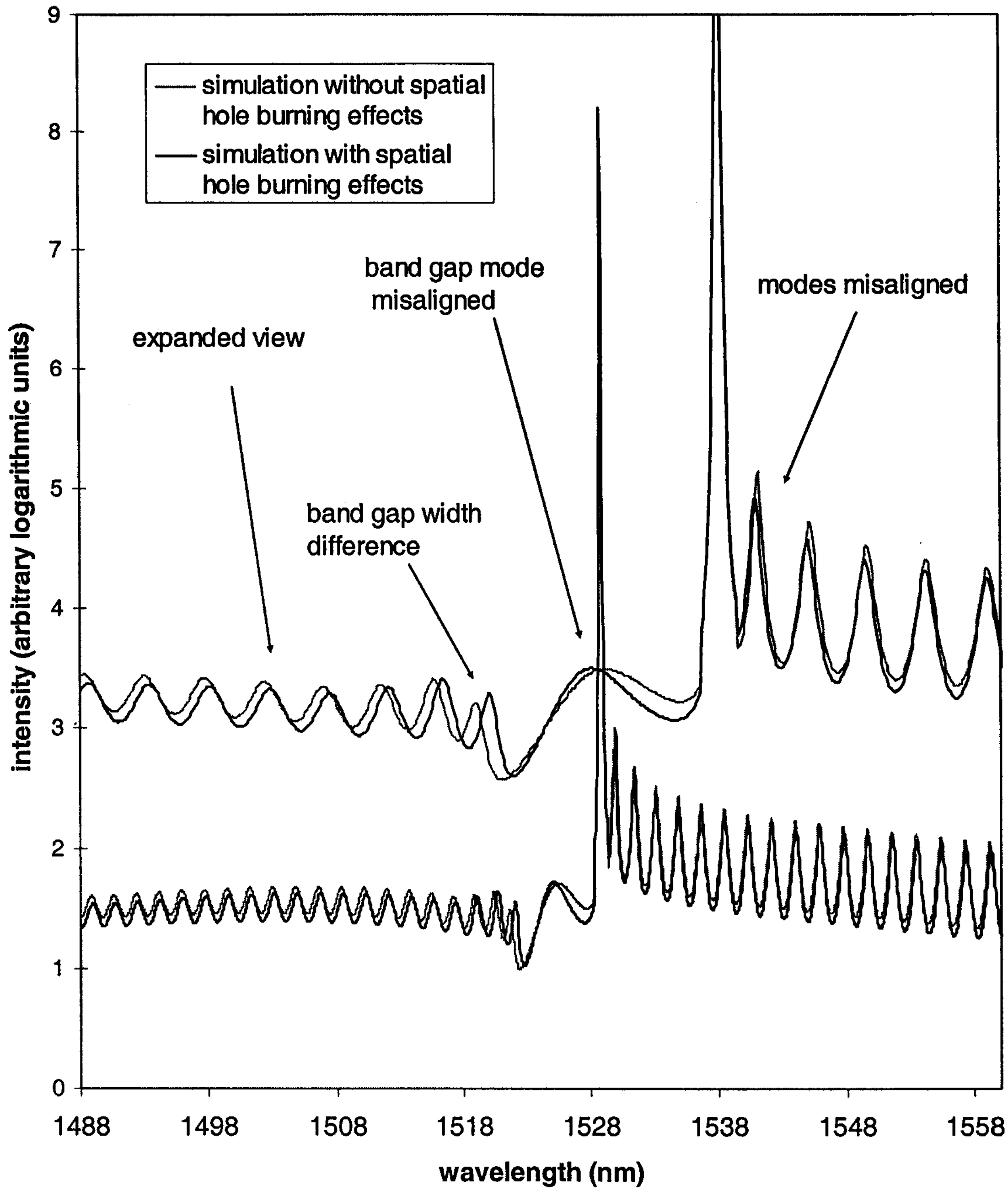

Fig. 8-18 Comparison of above-threshold simulations for the back facet of laser 1, one with the differential index of refraction (dn_R/dN) neglected (grey line), and one with complete spatial hole burning and carrier effects.

The stop band narrows above-threshold because an increased injection current causes an increased average carrier density in the quantum wells of the high index area. The higher carrier density reduces the index of refraction, and so the index step between the high index segments and the low index segments is reduced in magnitude. A reduced coupling coefficient results in a narrower stop band. This is not a spatial hole burning effect, but it is important to note that the differential index dn_R/dN can be set by this change. The magnitude of the spatial hole burning effects that are determined by the rate equation must therefore be accurately predicted in order for the simulated spatial hole burning effects to fit well to the spatial hole burning effects in the data.

With increased injection current, long wavelength side modes move towards the long wavelength mode (shorter wavelengths). This phenomenon can be modelled using a sub threshold model by decreasing the front facet phase. A smaller facet phase is also consistent with the reduced long wavelength side mode height caused by spatial hole burning (as seen in Fig. 8-17 and Fig. 8-18). Above-threshold, the band gap mode that is present in the back facet spectrum of laser 1 drifts toward shorter wavelengths. This phenomenon, too, can be modelled by decreasing the back facet phase. It appears that the spatial hole burning effects are partly similar to small changes (decreases) in facet phase.

The above-threshold longitudinal carrier distribution, gain, index of refraction, and spontaneous emission rates for laser 1 are shown in Fig. 8-19, Fig. 8-20, Fig. 8-21, and Fig. 8-22, respectively. The longitudinal photon density that is responsible for these physical distributions is shown in Fig. 8-23. Examination of the index of refraction in the high index areas clearly shows that at each facet, the index of refraction is reduced in the high index area. From the perspective of gratings deeper within the laser cavity, this has the effect of shifting the facet reflector towards them (just fractionally). As a result, above-threshold spectral phenomena caused by spatial hole burning resemble the effects of reduced facet phases.

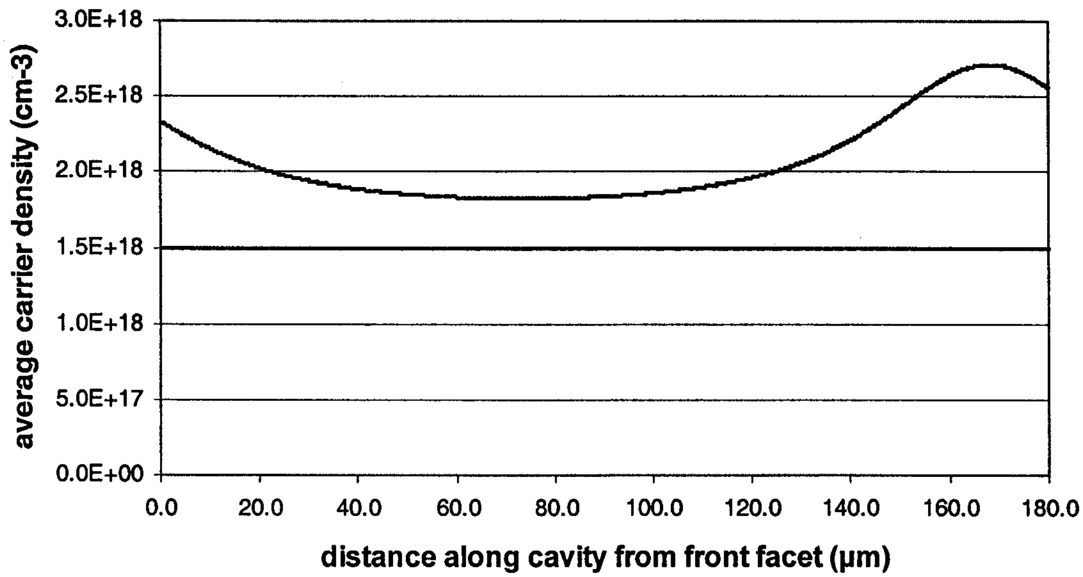

Fig. 8-19 The average carrier density per quantum well in the high index sections as a function of position in the laser cavity for laser 1. The constant line marks the transparency carrier density.

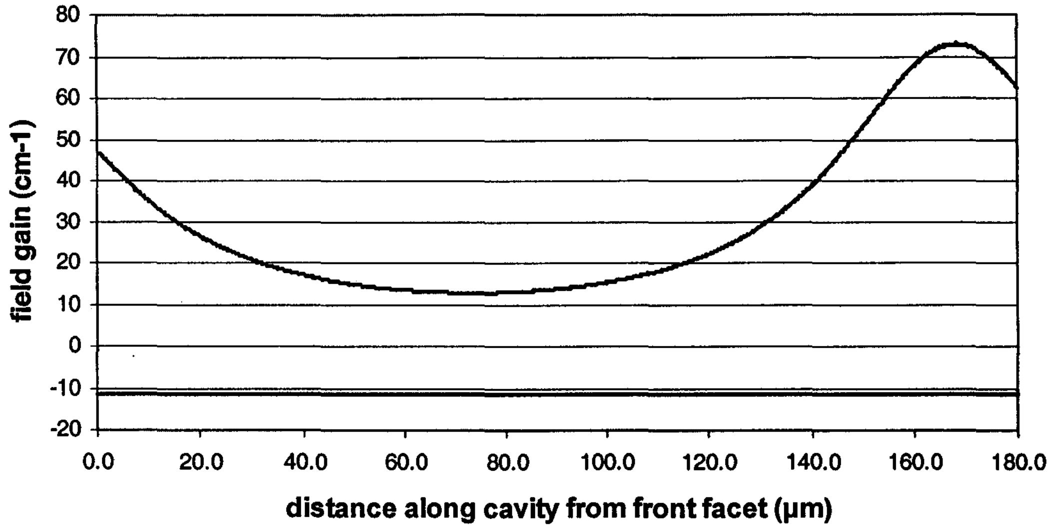

Fig. 8-20 Modal field gain distribution in the high index segments of the cavity of laser 1. The lower, constant line indicates the scattering loss in the low index segments.

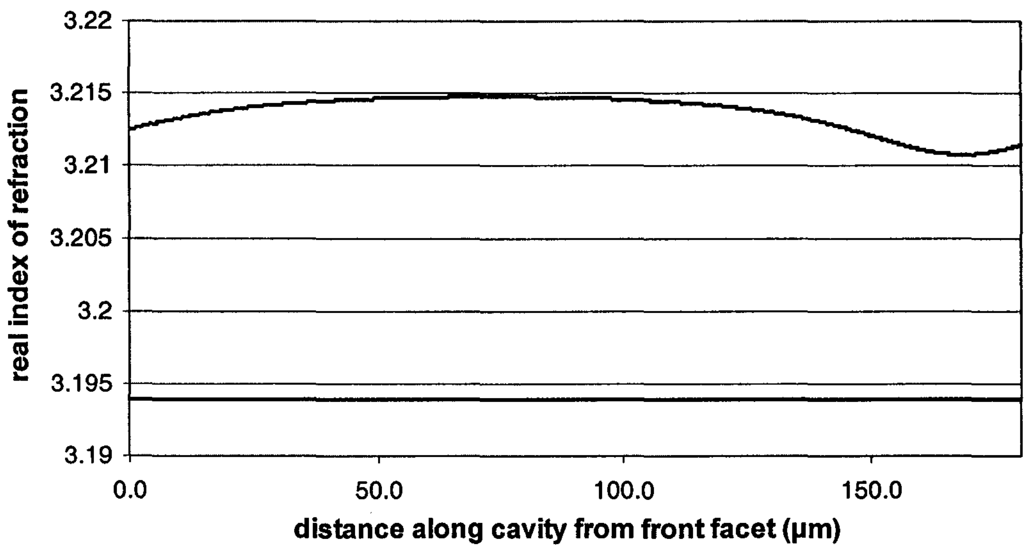

Fig. 8-21 Index of refraction in the laser 1 cavity. Top line represents index of refraction in the high index segments. Bottom line represents the index of refraction in the low index segments.

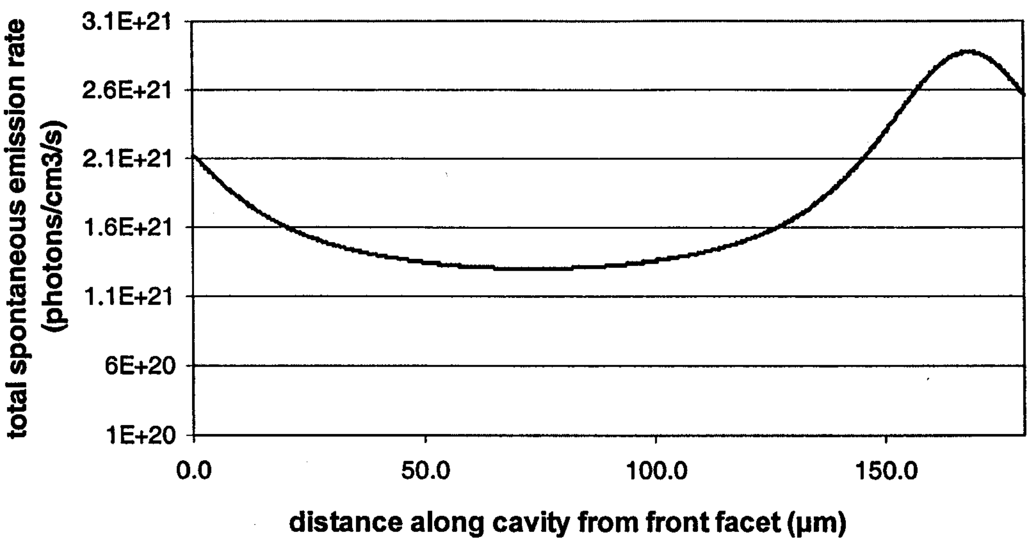

Fig. 8-22 Total rate of spontaneous emission in the high index segments as a function of position in laser cavity.

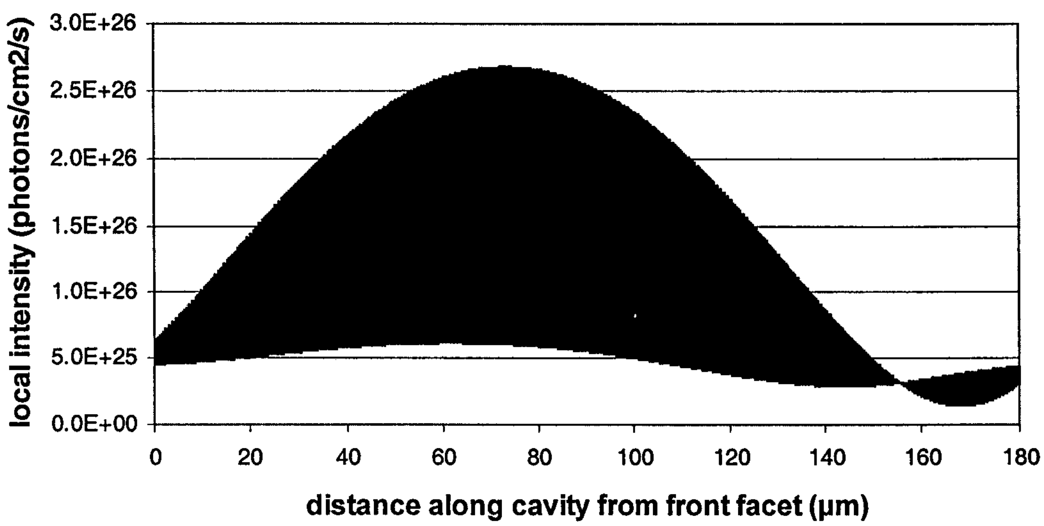

Fig. 8-23 The intensity distribution in the cavity of laser 1. The standing waves form a solid black shape at the low resolution that is required to fit the image on the page.

The intensity distribution shown in Fig. 8-23 clearly demonstrates the effect of facet phase on intensity distribution. At the back facet (right-hand side in Fig. 8-23) of the cavity, the standing waves become completely out of phase with the grating, and have a noticeably different envelope shape than at the front facet. This asymmetry causes the asymmetry in carrier distribution that is seen in Fig. 8-19, and the carrier distribution, in turn, is responsible for the parameter distributions shown in Fig. 8-20, Fig. 8-21, and Fig. 8-22. The larger degree of spatial hole burning that is apparent near the back facet, as compared to the front facet, is responsible for the comparatively large shift in wavelength of the back facet band gap mode (Fig. 8-12).

8.4.4. Examination of the Standing Wave in Gain-coupled Lasers

The standing wave in a DFB laser cavity is often not included in DFB laser models [25],[26],[43]. This approximation is sometimes justified on the grounds that diffusion of carriers prevents spatial hole burning over distances that are as short as a half wavelength of the lasing mode. However, in truncated quantum well structures such as those being studied in this chapter, diffusion between quantum wells in separate high index segments is inhibited by the low index segment barrier material. Thus the standing wave effect is important, and needs to be included in an above-threshold model. Previous work has presented this idea on a theoretical basis [34], [38], but the impact of standing wave induced spatial hole burning on laser spectra has not been considered in detail.

Simulations neglecting the standing wave effect were obtained by making the threshold model average the intensity in each period of the Bragg grating. The resulting fit to the back facet spectrum of laser 1 is shown in Fig. 8-24. Comparison of this fit with the fit of Fig. 8-12 indicates that the lasing mode is expected to have more power if the standing wave effect is neglected. Furthermore, a worse fit is made to the band gap mode in that it has not shifted far enough to the short wavelength side of the stop band. These two subtle differences indicate a definite impact of the standing wave on laser spectra. Although the fit could be improved by guessing a higher loss in the cavity, or by decreasing the injection efficiency (thereby reducing the height of the lasing mode), it is not obvious how one should go about increasing the degree of spatial hole burning at the same time, so that the band gap mode would remain properly positioned in the stop band. Increasing the differential index, for instance, would result in an incorrect narrowing of the stop band width. To further examine the effect of inclusion of the standing wave in the above-threshold model, Fig. 8-25 compares simulations with and without the standing wave. Finally, the effect of the standing wave on the refractive index distribution is shown in Fig. 8-26.

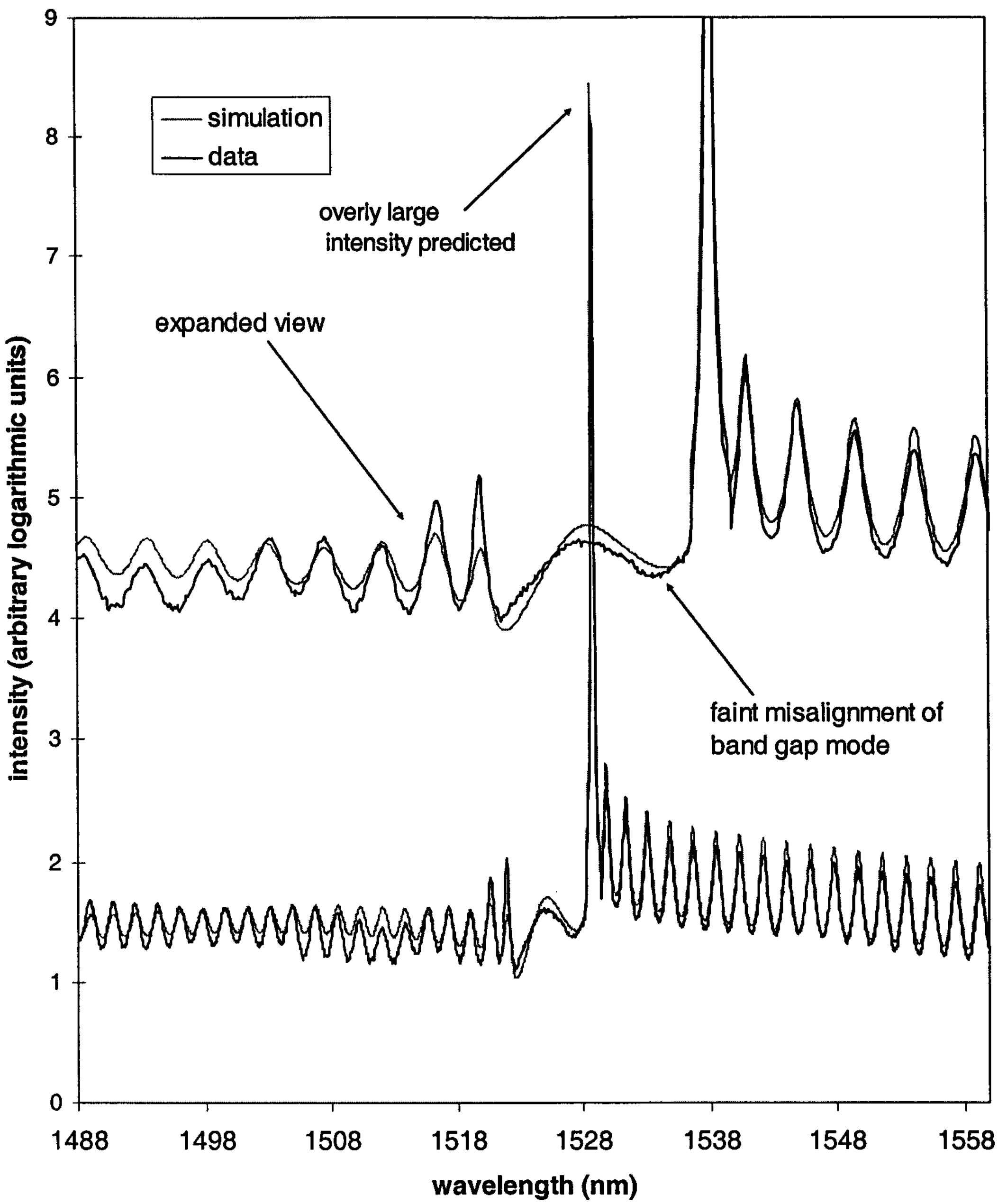

Fig. 8-24 A simulation that neglects the standing wave effect is compared to data. The overall fit is good, but is not as impressive as in Fig. 8-12.

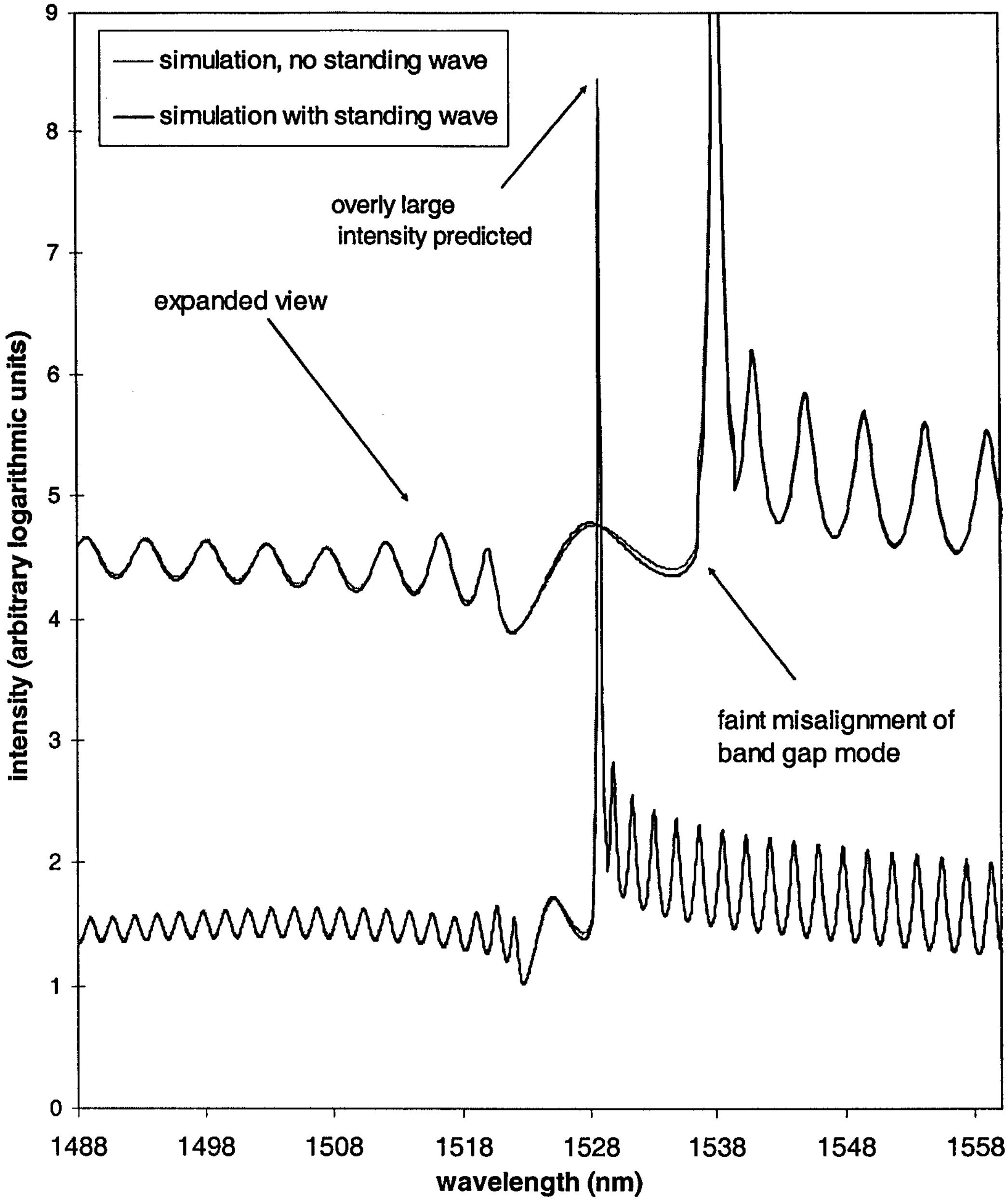

Fig. 8-25 A comparison of simulations including, and not including, the standing wave effect.

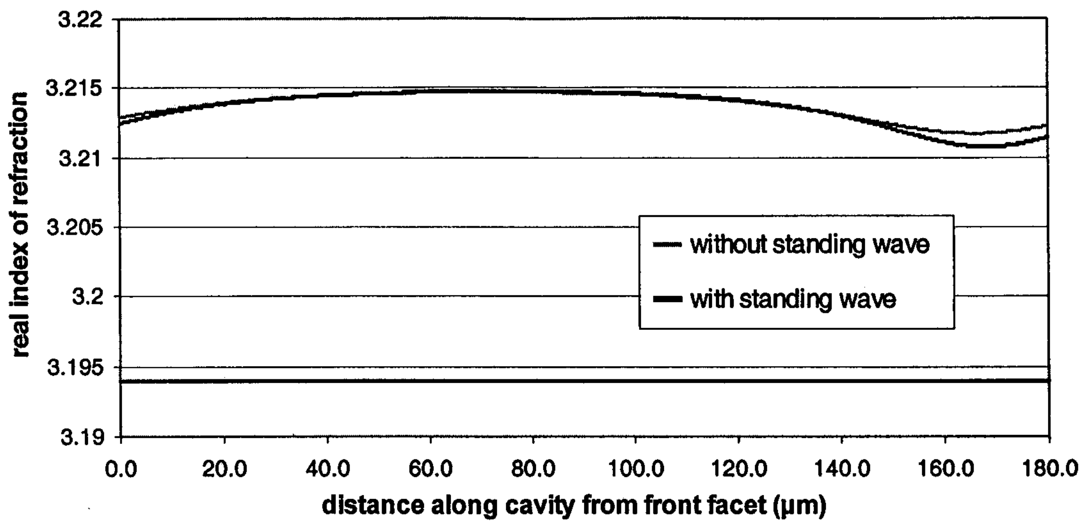

Fig. 8-26 Black: calculated with standing wave. Grey: No standing wave.

The standing wave effect is shown in Fig. 8-24 and Fig. 8-25 to have a noticeable effect at the back facet. This is because the standing wave is entirely out of phase with the grating at the back facet. Clearly spatial hole burning is increased by the standing wave, and the side mode suppression ratio is decreased.

8.5. Conclusions

The above-threshold model, which was developed in the previous two chapters, has been shown to accurately predict spatial hole burning features in truncated-well gain-coupled lasers. Effects of facet phase on degree of spatial hole burning have been demonstrated, and the importance of the standing wave for calculating spatial hole burning effects has been highlighted. Longitudinal variances of carrier densities, induced by spatial hole burning, have been calculated. From the carrier density distributions, gain, spontaneous emission, and refractive index variances within the laser cavity were easily calculated.

9. Conclusion

9.1. Suggestions for Future Work

Distributed feedback lasers are the preferred light source for modern fibre optic communications systems. New designs are constantly being proposed, and consumers continually demand higher power, higher efficiency, and broader tuning range. The probability amplitude DFB laser model will therefore continue to be a useful tool in evaluating new designs, and helping to diagnose limitations in current designs.

9.1.1. Future Projects

An ongoing project in laser design is life time analysis. No laser will last forever, but naturally researchers try to design their lasers to work for as many years as possible. Analysis of the changes that occur in a DFB laser over time is difficult because of its microscopic size. Thus a potential application for a DFB model is as a non-destructive diagnostic tool in life time tests. The deterioration of laser performance with time might well be correlated with a change in laser parameter, such as facet reflectivity, or gain coupling.

The probability amplitude model has primarily been applied to index-coupled and gain-coupled DFB lasers of relatively low power. Very high power, weakly index-coupled lasers with significantly longer cavity lengths are now being designed for long-haul fibre optic systems. The very high power of these new DFB lasers inherently induces a high susceptibility to spatial hole burning. Adapting the probability amplitude model for high power, long cavity length, weakly coupled DFB lasers could prove to be an interesting and rewarding project. The degree of influence of facet phase on these lasers is not well known.

The influence of facet phase on spatial hole burning phenomena has not been studied in detail. The effects of facet phase on spatial hole burning is expected to be different for different degrees of index coupling, gain coupling, and facet reflectivity, but the exact relationships could certainly be modelled in greater detail.

Non-linear gain due to spectral hole burning in DFB lasers is often cited as playing a major role in DFB laser characteristics such as side mode suppression ratio and linewidth. For the lasers studied at above-threshold injection currents in this thesis, however, spectral hole burning was found to be unimportant. The effect of the spectral hole burning parameter on simulated laser spectra was to decrease side mode suppression. Further analysis of the degree of spectral hole burning in various different laser designs will be very interesting.

9.1.2. Extension of the Model.

The below-threshold model, while extremely robust, is not particularly user friendly. Fitting the model to data is difficult without a working knowledge of the relationship of DFB laser spectra to various laser parameters. Being able to estimate sensible starting values for the automated fitting routine is of fundamental importance in the quest to obtain a reasonable fit to data. The model could therefore be greatly improved with a graphical user interface, and with some degree of artificial intelligence based on the observations of the influences of coupling coefficient, facet phase, and facet reflectivity that were made in chapters 3 and 4 of this thesis.

The above-threshold version of the truncated quantum well laser will benefit from further revision and testing. The model is not perfectly stable, and often needs careful supervision during a simulation. The "seed" value discussed in chapter 7 often needs to be changed for different lasers, and occasionally the rate equations produce a carrier distribution that is so far from equilibrium that the basic algorithms for tracking the lasing mode fail. Furthermore, the work in this thesis has been limited to treatment of a single lasing mode. These problems are by no means insurmountable, but a bit of time and thought will be required to optimize the code so that it can operate reliably for a wide range of laser designs without close supervision.

Currently, an above-threshold spectrum can be generated in about 13 minutes on a 1.7 GHz Pentium IV. One of the major bottle-necks in the current algorithm is the constant recalculation of the intensity distribution. In many lasers, the effect of spatial hole burning has been found to be quite small on the overall shape of the intensity distribution, so a large shortcut could conceivably be implemented in which the intensity distribution is calculated just once, and then scaled upwards incrementally to a magnitude that satisfies the rate equations. Once equilibrium is found, the parameters of the laser could be recalculated and small modifications would be made to the intensity distribution. This may significantly increase the speed with which the model operates, and could also improve the stability of the program.

Another exciting project for the above-threshold model involves analysis of DFB performance over a wide range of injection currents. The model should be optimized to solve the problem of above-threshold performance at multiple different injection currents. The above-threshold probability amplitude model properly predicts the power of the lasing mode at a given injection current. When compared to data from a DFB laser at a range of different above-threshold currents, it should be possible to make an interesting analysis of the relative magnitudes of the different carrier and photonic loss mechanisms in the laser. The roles of spectral hole burning, spatial hole burning, spontaneous emission, leakage current, and Auger recombination are always important in DFB laser design.

Finally, the model presented in this thesis would certainly benefit from more careful calculation of carrier dynamics. A mathematically rigorous Poisson solver such as that used by [38], could be incorporated. Alternatively, a simpler, experimentally rigorous rate equation model for carrier distribution, such as the one proposed by Hamp *et. al.* [5] might be more practical.

9.2. Summary

This thesis has developed and implemented a numerical model for distributed feedback laser spectra. The model makes use of probability amplitude waves for spontaneous emissions of radiation in DFB laser cavities. By allowing the probability amplitude wave to propagate coherently in two directions simultaneously, an additional self-interference term is obtained. This additional term has been shown to have significant impact on simulations for spectra of truncated quantum well DFB lasers, and simulations which include the self-interference term have been shown to make better fits to spectral data.

The importance of fitting a DFB laser model over a wide bandwidth and to spectra from both facets simultaneously has also been demonstrated. Easily identifiable spectral features that are useful in finding initial facet phase parameters for an automated fitting algorithm have been documented. Intuitive explanations for many of these features have been given, and the validity of the probability amplitude transfer-matrix model for extraction of facet phase has been experimentally verified.

The practical nature of the probability amplitude transfer-matrix model has been demonstrated by extracting gain parameters over a range of below-threshold injection currents for an explanation of truncated-well DFB laser performance. A modified version of the model was also successfully used for diagnostic analysis of two-section tuneable DFB lasers.

Finally, the probability amplitude transfer-matrix model has been used for prediction of intensity distributions in DFB laser cavities. Combined with the carrier rate equations, which balance the rates of spontaneous emission and stimulated emission with injection current, an above-threshold model has been proposed. The model has been demonstrated to correctly predict above-threshold DFB laser spectra, using parameters extracted from below-threshold spectra.

9.3. Conclusion

Distributed feedback lasers are incredibly complicated and interesting devices. The past four years of modelling DFB laser spectra have been fascinating and rewarding for me. The bizarre quantum nature of light cannot be ignored in DFB lasers. For instance, the rate equations used to model spatial hole burning require the treatment of light as a collection of quantized units, or photons, the production of which are balanced against a rate of carrier recombination. At the same time however, the wave nature of light must be considered in order to understand the constructive and destructive interference that determines DFB laser spectra.

This paradox is especially dumbfounding when considering the amplification of spontaneous emission: a quantized unit of energy, or photon, or boson particle with zero rest mass, is released by recombination of electrons and holes in the active region. The quantized unit must be modelled by a probability amplitude wave that initially starts in two different directions (in a one dimensional approximation) simultaneously, and is then reflected back and forth such that it can interfere with itself. Finally, the quantized unit of energy, or photon, or boson particle with zero rest mass, is detected outside the laser, at one of the two facets.

While some may consider the phenomenon described in the above sentences to be a trivial, or mundane example of quantum behaviour, this thesis has demonstrated that even the best of researchers can sometimes overlook the fundamental quantum mechanical nature of light in their laser models. Einstein once made the famous comment "God doesn't roll dice". That statement may very well be true, but distributed feedback lasers have certainly made it appear, to me at least, that there is a heavenly coin being flipped where photons are concerned.

10. REFERENCES

[1] Charles H. Henry., 1993, *Quantum Well Lasers*, ed. P. S. Zory Jr., (San Diego, CA: Academic Press).

[2] S. W. Corzine, R. Yan, L. A. Coldren, 1993, *Quantum Well Lasers*, ed. P. S. Zory Jr., (San Diego, CA: Academic Press).

[3] A. R. Adams, E. P. O'Reilly, M. Silver, 1999, *Semiconductor Lasers I – Fundamentals*, ed. E. Kapon, (San Diego, CA: Academic Press).

[4] S. L. Chuang, 1995, *Physics of Optoelectronic Devices*, (New York, NY: John Wiley & Sons).

[5] M. J. Hamp, *Asymmetric Multiple Quantum Well Lasers*, 2000, (Hamilton ON: McMaster University)

[6] E.G. Steward, *Fourier Optics, an Introduction, second edition*, 1987, (Rexdale, ON: John Wiley & Sons).

[7] P.W. Milonni, J. H. Eberly, *Lasers*, p. 1, 1988, (Toronto, ON: John Wiley & Sons)

[8] E. Kapon, *Semiconductor Lasers I – Fundamentals*, Preface. ed. E. Kapon, 1999 (San Diego, CA: Academic Press)

[9] H. Kogelnik, C. V. Shank, "Stimulated emission in a periodic structure", Applied Physics Letters, Vol. 18, pp. 152-154, 1971.

[10] H. Kogelnik, C. V. Shank, "Coupled-Wave Theory of Distributed Feedback Lasers", Journal of Applied Physics, Vol. 43, pp 2327-2335, 1972.

[11] B. G. Kim, E. Garmire, "Comparison between the matrix method and the coupled-wave method in the analysis of Bragg reflector structures", Journal of the Optical Society of America A, Vol. 9, pp. 132-136, 1992.

[12] J. Hong, W. Huang, T. Makino, "On the Transfer-matrix Method for Distributed-Feedback Waveguide Devices", Journal of Lightwave Technology, Vol. 10, pp. 1860-1868, 1992.

[13] T. Nakura, Y. Nakano, "LAPAREX- An Automatic Parameter Extracton Program for Gain- and Index-Coupled Distributed Feedback Semiconductor Lasers, and Its Application to Observation of Changing Coupling Coefficients with Currents", IEICE Trans. Electron., BOL E83-C, pp. 488-495, 2000.

[14] S. Wang, "Principles of distributed feedback and distributed Bragg-reflector lasers," IEEE Journal of Quantum Electronics, vol. QE-10, pp. 413-427, 1974.

[15] J-P Weber, S. Wang, "A New Method for the Calculation of the Emission Spectrum of DFB and DBR Lasers", IEEE Journal of Quantum Electronics, Vol. 27, pp. 2256-2266, 1991.

[16] W. Striefer, R. D. Burnham, D. R. Scifres, "Effect of external reflectors on longitudinal modes of distributed feedback lasers", IEEE Journal of Quantum Electronics, vol. QE-11, pp. 154-156, 1975.

[17] C. H. Henry, "Performance of Distributed Feedback Lasers Designed to Favor the Energy Gap Mode", IEEE Journal of Quantum Electronics, Vol. QE-21, pp 1913-1918, 1985.

[18] S. L. McCall, P. M. Platzman, "An Optimized PI/2 Distributed Feedback Laser", IEEE Journal of Quantum Electronics, Vol. QE-21, pp 1899-1904, 1985.

[19] D. M. Adams, D. T. Cassidy, and D. M. Bruce, "Scanning Photoluminescence Technique to Determine the Phase of the Grating at the Facets of Gain-Coupled DFB's", IEEE Journal of Quantum Electronics, Vol. 32, pp. 1237-1242, 1996.

[20] H. Soda and H. Imai, "Analysis of the Spectrum Behavior Below the Threshold in DFB Lasers", IEEE Journal of Quantum Electronics, Vol. QE-22, 1986, pp. 637-641.

[21] G. Björk, O. Nilsson, "A new exact and Efficient Numerical Matrix Theory of Complicated Laser Structures: Properties of Asymmetric Phase-Shifted DFB Lasers", Journal of Lightwave Technology, Vol. LT-5., pp. 140-146, 1987.

[22] T. Makino, J. Glinski, "Transfer-matrix Analysis of the Amplified Spontaneous Emission of DFB Semiconductor Laser Amplifiers", IEEE Journal of Quantum Electronics, Vol. 24, pp. 1507-1518, 1988.

[23] J. Hamasaki, T. Iwashima, "A Single-Wavelength DFB Structure with a Synchronized Gain Profile", IEEE Journal of Quantum Electronics, Vol. 24, pp.1864-1872, 1988.

[24] E. Berglind and L. Gillner, "Optical Quantum Noise Treated with Classical Electrical Network Theory", Vol. 30, pp 845-853, 1994.

[25] J. E. Whiteaway, G. H. B. Thompson, A. J. Collar, C. J. Armistead, "The Design and Assessment of $\lambda/4$ Phase-Shifted DFB Laser Structures", IEEE Journal of Quantum Electronics, vol. 25, pp. 1261-1279, 1989.

[26] P. Vankwikelberge, G. Morthier, R. Baets, "CLADISS-A Longitudinal Multimode Model for the Analysis of the Static, Dynamic, and Stochastic Behaviour of Diode Lasers with Distributed Feedback", IEEE Journal of Quantum Electronics, Vol. 26, pp. 1728-1741.

[27] K. David, G. Morthier, P. Vankwikelberge, R. G. Baets, T. Wolf, B. Borchert, "Gain-Coupled DFB Lasers Versus Index-Coupled Phase-Shifted DFB Lasers: A Comparison Based on Spatial Hole Burning Corrected Yield", IEEE Journal of Quantum Electronics, pp 1714 -1723, 1991.

[28] G. Morthier, P. Vankwikelberge *Handbook of Distributed Feedback Laser Diodes*, 1997, (Norwood, MA: Artech House Inc.).

[29] J. E. Whiteaway, G. H. B. Thompson, A. J. Collar, C. J. Armistead, M. J. Fice, "The Static and Dynamic Characteristics of Single and Multiple Phase-Shifted DFB Laser Structures", IEEE Journal of Quantum Electronics, Vol. 28, pp 1277-1293.

[30] S. Hansmann, "Transfer-matrix Analysis of the Spectral Properties of Complex Distributed Feedback Laser Structures", IEEE Journal of Quantum Electronics, Vol. 28, pp. 2589-2595, 1992.

[31] S. Hansmann, H. Walter, H. Hillmer, H. Burkhard, "Static and Dynamic Properties of InGaAsP-InP Distributed Feedback Lasers—A Detailed Comparison

Between Experiment and Theory", IEEE Journal of Quantum Electronics, Vol. 30, pp. 2477-2484, 1994.

[32] R. Schatz, "Dynamics of Spatial Hole Burning Effects in DFB Lasers", IEEE Journal of Quantum Electronics, Vol. 31, pp. 1981-1996, 1995.

[33] A. J. Lowery, A. Keating, C. N. Murtonen, "Modeling the Static and dynamic Behavior of Quarter-Wave-Shifted DFB Lasers", IEEE Journal of Quantum Electronics, Vol. 28, pp1874-1215, 1992.

[34] X. Pan, H. Olesen, B. Tromborg, H.E. Lassen, "Analytic description of the standing wave effect in DFB lasers", IEE Proceedings-J Vol. 139, pp. 189-193, 1992.

[35] B. Tromborg, H. Olesen, X. Pan, "Theory of Linewidth for Multielectrode Laser Diodes with Spatially Distributed Noise Sources", IEEE Journal of Quantum Electronics, Vol. 27, pp. 178-192, 1991.

[36] R. Bonello, I. Montrosset, "Analysis of Multisection and Multielectrode Semiconductor Lasers", IEEE Journal of Quantum Electronics, Vol. 10pp. 1890-1900, 1992.

[37] F. Randone and I. Montrosset, "Analysis and Simulation of Gain-Coupled Distributed Feedback Semiconductor Lasers", IEEE Journal of Quantum Electronics, Vol. 31, pp. 1964-1973, 1995.

[38] A. Champagne, R. M. Maciejko, D. M. Adams, G. Pakulski, B. Takasaki, T. Makino, " Global and Local Effects in Gain-Coupled Multiple Quantum-Well DFB Lasers", IEEE Journal of Quantum Electronics, Vol. 35, pp. 1390-1401, 1999.

[39] R. Schatz, E. Berglind, L. Gillner, "Parameter Extraction from DFB Lasers by Means of a Simple Expression for the Spontaneous Emission Spectrum", IEEE Photonics Technology Letters, Vol. 6, pp1182-1184, 1994.

[40] G. Morthier, K. Sato, R. Baets, T. Sudoh, Y. Nakano, K. Tada, "Parameter extraction from subthreshold spectra in cleaved gain-and index-coupled DFB LDs", OFC '95 Technical Digest, pp 309-310, 1995.

[41] H. Hillmer, S. Hansmann, H. Burkhard, H. Walter, A. Krost, D. Bimberg, "Study of Wavelength Shift in InGaAs/InAlGaAs QW DFB Lasers Based ON Laser Parameters From a Comparison of Experiment and Theory", IEEE Journal of Quantum Electronics, Vol. 30, pp. 2251-2261, 1994.

[42] J. Skagerlund, F. Pusa, O Sahlén, L. Gillner, R. Schatz, P. Ganestrnd, L. Lundqvist, B. Stoltz, J. Terlecki, F. Wahlin, A-C Mörner, Johan Wallin, O. Öberg, "Evaluation of an Automatic Method to Extract the Grating Coupling Coefficient in Different Types of Fabricated DFB Lasers", IEEE Journal of Quantum Electronics, Vol. 34, pp. 141-146, 1998.

[43] W. Fang, A. Hsu, S. L. Chuang, T. Tanbuk-Ek, A. M. Sergent, "Measurement and Modeling of Distributed-Feedback Lasers with Spatial Hole Burning", IEEE Journal of Selected Topics in Quantum Electronics, Vol. 3, pp 547-554, 1997.

[44] G.B Morrison, D.T. Cassidy, D. M. Bruce, "Facet Phases and Sub-Threshold Spectra of DFB Lasers: Spectral Extraction, Features, Explanations, and Verification", IEEE Journal of Quantum Electronics, Vol. 37, pp762-769, 2001.

[45] G. B. Morrison, D. T. Cassidy, "Improving the Ability of a Distributed Feedback Laser Transfer-Matrix Model to Fit to Spectra from Distributed Feedback Lasers", IEEE Photonics Technology Letters, Vol. 12, pp 768-770, 2000.

[46] G. B. Morrison, D. T. Cassidy, D. M. Bruce, "Accuracy of a probability-amplitude model for extracting facet phases from truncated-well DFB lasers", Technical Digest, OESC 2001, pp. 30-31.

[47] A. Nicolas, G. B. Morrison, D. T. Cassidy, "A Sub-threshold Model for Two-section Tunable Gain Coupled DFB Lasers", Technical Digest, OESC 2001, pp. 40-41.

[48] W. E. Lamb, Jr., "Anti-Photon", Applied Physics B, Vol. 60, pp 77-84, 1995.

[49] Richard P. Feynman, Robert B. Leighton, and Matthew Sands, "The Feynman Lectures on Physics", Vol. III, Reading Massachusetts: Addison-Wesley Publishing Company 1965 pp. 3.1-3.7.

[50] Robert Eisberg and Robert Resnick, "Quantum Physics of Atoms, Molecules, Solids, Nuclei, and Particles", 2^{nd} Ed., Toronto: John Wiley and Sons, 1985, pp. 56-80.

[51] T. Makino, "Transfer-Matrix Formulation of Spontaneous Emission Noise of DFB Semiconductor Lasers", Journal of Lightwave Technology, Vol. 9, pp. 84-91, 1991

[52] C.H. Henry, "Theory of Spontaneous Emission Noise in Open Resonators and its Application to Lasers and Optical Amplifiers", Journal of Lightwave Technology Vol. LT-4, 1986, pp. 289-297.

[53] K. Petermann, "Calculated spontaneous emission factor for double-heterostructure injection lasers with gain-induced waveguideing", IEEE Journal of Quantum Electronics, vol. QE-15, pp. 566-570, July 1979.

[54] M. Newstein, "The Spontaneous Emission Factor for Lasers with Gain Induced Waveguiding", IEEE Journal of Quantum Electronics, Vol. QE-20, pp. 1270-1276, 1984.

[55] G.B. Morrison, David M. Adams, and D.T. Cassidy, "Extraction of Gain Parameters for Truncated-Well Gain-Coupled DFB Lasers", IEEE Photonics Technology Letters, Vol 11, pp 1566-1568, 1999.

[56] P.R. Bevington and D.K. Robinson, *Data Reductions and Error Analysis for the Physical Sciences,* 2nd ed. New York: McGraw Hill, 1969, pp161-164.

[57] K. Levenberg, "A method for the solution of certain non-linear problems in least squares", Quart. Appl. Math., Vol 2., pp. 164-168, 1944.

[58] D. W. Marquardt, "An Algorithm for Least-Squares Estimation of Nonlinear Parameters", J. Soc. Indust. Appl. Math., Vol. 11, pp. 431-441, 1963.

[59] G.P. Agrawal, N.K. Dutta, and P.J. Anthony, "Linewidth of distributed feedback semiconductor lasers with partially reflecting facets", Applied Physics Letters, Vol. 48, pp. 453-455, 1986.

[60] F. Favre, "Sensitivity to external feedback for gain-coupled DFB semiconductor lasers," Electronics Letters, Vol. 27, pp. 433-455, 1991.

[61] G.H.B. Thompson, *Physics of Semiconductor Laser Devices.* New York:Wiley, 1980.

[62] S. Akiba, K. Utaka, K. Sakai, Y Matsushima, “Asymmetry in output power of InGaAsP/InP DFB lasers”, Japan Journal of Applied Physics, Vol. 23, pp. 1054-1059, 1984.

[63] T. Makino, and H.Lu, “Wide temperature range singlemode operation of MQW gain-coupled DFB lasers”, Electronics Letters, Vol. 30, pp. 1948-1949, 1994.

[64] G.P. Li and T. Makino, “Single mode yield analysis of partly gain-coupled multi-quantum well DFB lasers”, IEEE Photonics Technology Letters, Vol. 5, pp. 1282-1284, 1993.

[65] T. Matsuoka, Y. Yoshikuni, and H. Nagai, “Verification of the Light Phase Effect at the Facet on DFB Laser Properties”, IEEE Journal of Quantum Electronics, Vol. QE-21, pp. 1880-1886, 1985.

[66] G.B. Morrison and D.T. Cassidy, “A Probability-Amplitude Transfer Matrix Model for Distributed-Feedback Laser Structures”, IEEE Journal of Quantum Electronics, Vol. 36, pp. 633-640, 2000.

[67] D. M. Adams, D. T. Cassity, D. M. Bruce, “Scanning photoluminescence technique to determine the phase of the grating at the facets of gain-coupled DFBs”, CLEO ’96 proceedings, paper CFM8, pp38-39, 1996.

[68] G.P. Li, T. Makino, R. Moore, N. Puetz, K. Leong, and H Lu, “Partly Gain-Coupled 1.55 μm Strained-Layer Multiquantum-Well DFB Lasers”, IEEE J. Quantum Electron., vol. 29, pp. 1736-1742, 1993.

[69] H. Lu, C. Blaauw, B. Benyon,, G.P. Li., and T. Makino, "High power and high speed performance of 1.3 μm strained MQW gain-coupled DFB lasers", IEEE Journal of Selected Topics of Quantum Electronics, vol. 1, pp375-380, 1995.

[70] H. Lu, G.P. Li., and T. Makino, "High-Speed performance of partly gain-coupled 1.55 μm strained layer multiple quantum well DFB lasers", IEEE Photon. Tehnol. Lett., vol. 5, pp. 861-863, 1993.

[71] D.M. Adams and T. Makino, "Mechanism for enhanced gain-periodicity in truncated-well gain-coupled DFB lasers", Electronics Letters, Vol 31, No. 12, pp. 976-977, 1995.

[72] D. M. Adams, A. Champagne, J. Chen, R. Maciejko, "Yield enhancement due to carrier injection behaviour in truncated–well gain-coupled DFB's", CLEO 96, Paper CMF3, Proceedings p. 34.

[73] A. Champagne, R. Maciejko, and T Makino, "Enhanced carrier injection efficiency from lateral current injection in multiple-quantum-well DFB lasers", IEEE Photon. Technol. Lett., Vol. 8, pp 749-751, 1996.

[74] G.C. Crow and R.A Abram, "Monte Carlo simulations of charge transport in high speed lasers", IEEE J. Quantum Electron., vol. 33, pp. 1190-1196, 1997.

[75] H. Yamazaki, A. Tomita, M.Yamaguchi, and Y.Sasaki, "Evidence of nonuniform carrier distribution in multiple quantum well lasers", Appl. Phys. Lett., vol. 71, pp 767-769, 1997.

[76] M.J. Hamp, D.T. Cassidy, B.J. Robinson, Q.C Zhao, and D.A. Thompson, "Nonuniform carrier distribution in asymmetric multiple-quantum-well InGaAsP laser structures with different numbers of quantum wells", Applied Physics Letters, Vol. 74, No. 5, pp. 744-746, 1999.

[77] D.M. Adams, C. Gamache, R.Finlay, M. Cyr, K.M. Burt, J. Evans, E. Jamroz, S. Wallace, I. Woods, L. Doran, P. Ayliffe, D. Goodchild and C. Rogers, "Module-packaged tunable laser and wavelength locker delivering 40 mW of fibre-coupled power on 34 channels", Electonics Letters, Vol. 37, 691-693, 2001.

[78] W. Li, W.-P. Huang, S. Li, and J. Hong, "Multiwavelength Gain-Coupled DFB Laser Cascade: Design Modeling and Simulation", IEEE J. Quantum Electron., Vol **36**, 1110-1116, (2000).

[79] Richard P. Feynman, Robert B. Leighton, and Matthew Sands, "The Feynman Lectures on Physics", Vol. III, Reading Massachusetts: Addison-Wesley Publishing Company 1965 p. 5.29.

[80] J. Kinoshita, "Modeling of High Speed DFB Lasers Considering the Spatial Holeburning Effect Using Three Rate Equations", IEEE Journal of Quantum Electronics, Vol. 30 pp. 929-938, 1994.

[81] M. Aoki, K. Uomi, T. Tsuchiya, S. Sasaki, M. Okai, N. Chinone, "Quantum Size Effect on Longitudinal Spatial Hole Burning in MQW $\lambda/4$-Shifted DFB lasers", IEEE Journal of Quantum Electronics, Vol. 27, pp. 1782-1789, 1991.

[82] F. Girardin, G-H. Duan, A Talneau, "Modeling and Measurement of Spatial-Hole-Burning Applied to Amplitude Modulated Coupling Distributed Feedback Lasers", IEEE Journal of Quantum Electronics, Vol. 31, pp.834-841, 1995.

[83] J. Piprek, P. Abraham, J. E. Bowers, "Self-Consistent Analysis of High-Temperature Effects on Strained-Layer Multiquantum-Well InGaAsP-InP Lasers", IEEE Journal of Quantum Electronics, Vol. 36, pp366-374, 2000.

[84] D. T. Cassidy, "Spontaneous-emission factor of semiconductor diode lasers", J. Opt. Soc. Am. B, Vol. 8, pp. 747-752, 1991.

[85] P. W. Milonni, J. H. Eberly, *Lasers*, pp. 86-88, John Wiley & Sons, Toronto, 1988.

[86] M. R. Spiegel, *Schaum's Outline Series, Mathematical Handbook of Formulas and Tables*, pp. 64, McGraw-Hill Inc., Toronto, 1968.

[87] H.J. Wünsche, U. Bandelow, H Wenzel, "Calculation of Combined Lateral and Longitudinal Spatial Hole Burning in $\lambda/4$ Shifted DFB Lasers", IEEE Journal of Quantum Electronics, Vol. 29, pp. 1751-1760, 1993.

[88] Udo Krüger, K. Petermann, "The Semiconductor Laser Linewidth Due to the Presence of Side Modes", IEEE Journal of Quantum Electronics, Vol. 24, pp 2355-2358, 1988.

[89] X. Pan, B. Tromborg, H. Oelsen, "Linewidth Rebroadening in DFB Lasers Due to Weak Side Modes", IEEE Photonics Technology Letters, Vol. 3, pp. 112-114, 1991.

[90] J-Y. Wang, M. Cada, "Analysis and Optimum Design of Distributed Feedback Lasers Using Coupled-Power Theory", IEEE Journal of Quantum Electronics, Vol. 36 pp. 52-58, 2000.

[91] K. Yokoyama, T. Yamanaka, S Seki, W. Lui, "Static Wavelength Shift for Multielectrode DFB Lasers with Longitudinal Mode Spatial Hole Burning Using a Two-Dimensional Numerical Simulator", IEEE Journal of Quantum Electronics, Vol. 29, pp. 1761-1768, 1993.

[92] Anritsu MS9710 B Technical Manual, Specifications sheet pp. 73. www.anritsu.com (2002).

[93] P. Magain, F. Courbin, S. Sohy, "Deconvolution with correct sampling", Astrophysical Journal, Vol. 494, p. 472, 1998.

[94] P. Magain, F. Courbin, S. Sohy, "Deconvolution with correct sampling", The Messenger, Vol. 88, pp. 28-31, 1997.

[95] F. Courbin, P. Magain, M. Kirkove, S. Sohy, "The Sstrophysical Journal, Volume 529, pp. 1136-1144, 1998.

[96] W. H. Press, S. A. Teukolsky, W. T. Vetterling, B. P. Flannery, *Numerical Recipes in C, Second Edition*, pp. 504-514, Cambridge University Press, New York, NY 1997.